

**DOCTORAL THESIS**

Biomimicry and Novel  
Structures: Advancing the  
Design Paradigm of Bone  
Implants

Mansoureh Rezapourianghahfarokhi

TALLINN UNIVERSITY OF TECHNOLOGY  
DOCTORAL THESIS  
9/2024

# **Biomimicry and Novel Structures: Advancing the Design Paradigm of Bone Implants**

MANSOUREH REZAPOURIANGHAHFAROKHI





TALLINN UNIVERSITY OF TECHNOLOGY  
School of Engineering  
Department of Mechanical and Industrial Engineering

This dissertation was accepted for the defence of the degree on 19 February 2024

**Supervisor:** Professor Irina Hussainova,  
Department of Mechanical and Industrial Engineering  
Tallinn University of Technology  
Tallinn, Estonia

**Opponents:** Professor Michael Gasik,  
Aalto University Foundation  
Helsinki, Finland

Professor Oscar Samuel Novais Carvalho,  
Department of Mechanical Engineering  
University of Minho  
Campus de Azurém, 4800-058 Guimarães, Portugal

**Defence of the thesis:** 21 March 2024, Tallinn

**Declaration:**

*Hereby I declare that this doctoral thesis, my original investigation and achievement, submitted for the doctoral degree at Tallinn University of Technology, has not been submitted for any academic degree elsewhere.*

Mansoureh Rezapourianghahfarokhi

---

signature

Copyright: Mansoureh Rezapourianghahfarokhi, 2024

ISSN 2585-6898 (publication)

ISBN 978-9916-80-113-0 (publication)

ISSN 2585-6901 (PDF)

ISBN 978-9916-80-114-7 (PDF)

DOI <https://doi.org/10.23658/taltech.9/2024>

Printed by EVG Print

Rezapourianghahfarokhi, M. (2024). *Biomimicry and Novel Structures: Advancing the Design Paradigm of Bone Implants* [TalTech Press]. <https://doi.org/10.23658/taltech.9/2024>

TALLINNA TEHNIKAÜLIKOOL  
DOKTORITÖÖ  
9/2024

# **Biomimikri ja uudsed struktuurid: luuimplantaatide disainiparadigma edendamine**

MANSOUREH REZAPOURIANGHAHFAROKHI





# Contents

List of publications .....	7
Author's contributions to the publications .....	8
Abbreviations.....	9
Introduction .....	10
1 Review of the literature .....	12
1.1 Bone architecture and models .....	12
1.2 The choice of material .....	13
1.3 The importance of scaffold/implant design in BTE .....	14
1.3.1 Architectural features .....	16
1.3.2 Mechanical compliance .....	17
1.4 Objectives of the study .....	18
2 Materials and methods.....	20
2.1 Scaffold design .....	20
2.1.1 Taguchi-based design of Ti6Al4V TPMS structures .....	20
2.1.2 Haversian bone mimicking Ti6Al4V porous structure .....	21
2.1.3 Split-P Ti6Al4V TPMS cellular lattice structure .....	22
2.1.4 Voronoi-based HA scaffold .....	23
2.2 Lattice structure fabrication by SLM .....	24
2.2.1 Taguchi-based design of Ti6Al4V TPMS structures .....	24
2.2.2 Split-P Ti6Al4V TPMS cellular lattice structure .....	24
2.3 Characterization of the designed scaffolds/implants .....	25
2.3.1 Taguchi-based design of Ti6Al4V TPMS structures .....	25
2.3.2 Haversian bone mimicking Ti6Al4V porous structure .....	26
2.3.3 Split-P Ti6Al4V TPMS cellular lattice structure .....	26
2.3.4 Voronoi-based HA scaffold .....	26
3 Results and discussion.....	27
3.1 Taguchi-based design of Ti6Al4V TPMS structures .....	27
3.1.1 Taguchi analysis results .....	27
3.2 Haversian bone mimicking Ti6Al4V porous structure .....	28
3.2.1 Morphology effects on Geometrical features .....	28
3.2.1.1 Cortical bone component: .....	28
3.2.1.2 Trabecular bone component: .....	29
3.2.2 Morphology effects on mechanical performance.....	30
3.2.2.1 Cortical bone component's mechanical properties: .....	30
3.2.2.2 Mechanical properties of whole bone implant: .....	32
3.3 Split-P lattices and their structural advantages .....	33
3.3.1 Geometrical analysis of fabricated lattices .....	34
3.3.2 Manufacturability of Split-P TPMS.....	36
3.3.3 Surface morphology of fabricated lattices .....	37
3.3.4 Morphology effects on the mechanical performance - Experimental results .....	38
3.3.5 Morphology effects on the mechanical performance - Numerical results .....	42

3.3.5.1	Unit cell analysis:.....	42
3.3.5.2	Lattice structure analysis:.....	43
3.3.6	Morphology effects on the energy absorption capacity.....	46
3.3.7	Anisotropy comparison of Split-P lattices .....	47
3.4	Voronoi-based HA scaffold.....	48
3.4.1	Morphology effects on architectural features .....	48
3.4.2	Morphology effects on mechanical performance.....	50
3.5	Human bone and TPMS/Voronoi-based lattices .....	52
4	Conclusions .....	53
5	Future work .....	56
	References .....	57
	Acknowledgements .....	67
	Abstract.....	68
	Kokkuvõte .....	70
	Appendix .....	73
Paper I.....		73
Paper II .....		83
Paper III .....		99
Paper IV .....		123
	Curriculum Vitae .....	136
	Elulookirjeldus.....	137

## List of publications

The present PhD thesis is based on the following publications that are referred to in the text in Roman numbers.

- I **Rezapourian, M.**, Kamboj, N., & Hussainova, I. (2021). Numerical study on the effect of geometry on mechanical behavior of triply periodic minimal surfaces. In IOP Conference Series: Materials Science and Engineering, 1140, 012038.
- II **Rezapourian, M.**, Kamboj, N., Jasiuk, I., & Hussainova, I. (2022). Biomimetic design of implants for long bone critical-sized defects. Journal of the Mechanical Behavior of Biomedical Materials, 134, 105370.
- III **Rezapourian, M.**, Jasiuk, I., Saarna, M., & Hussainova, I. (2023). Selective laser melted Ti6Al4V split-P TPMS lattices for bone tissue engineering. International Journal of Mechanical Sciences, 251, 108353.
- IV **Rezapourian, M.**, & Hussainova, I. (2023). Optimal mechanical properties of Hydroxyapatite gradient Voronoi porous scaffolds for bone applications — A numerical study. Journal of the Mechanical Behavior of Biomedical Materials, 148, 106232.

## **Author's contributions to the publications**

- I First author. Writing – original manuscript, Formal analysis, Investigation, Methodology, Software, Visualization, Writing – original manuscript.
- II First author. Writing – original manuscript, Formal analysis, Investigation, Methodology, Software, Visualization.
- III First author. Writing – original manuscript, Formal analysis, Investigation, Methodology, Software, Visualization.
- IV First & corresponding author. Writing – original manuscript, Formal analysis, Investigation, Methodology, Software, Visualization.

## Abbreviations

AM	Additive manufacturing
BC	Boundary condition
BISO	Bilinear isotropic hardening
BTE	Bone tissue engineering
CAD	Computer aided design
CM	Cell morphology
FEA	Finite element analysis
FE	Finite element
HA	Hydroxyapatite
IVL	Irregular Voronoi-based lattice
MISO	Multi linear isotropic hardening
PS	Point space
PC	Constant PS
PG	Gradient PS
RD	Relative density
SA	Surface area
SA/VR	Surface area-to-volume ratio
SEM	Scanning electron microscope
SLM	Selective laser melting
ST	Strut thickness
TC	Constant ST
TG	Gradient ST
TPMS	Triply periodic minimal surface
V	Volume



## Introduction

The field of engineering artificial tissue substitutes is at the forefront of innovative medical research, offering the promise of regenerating damaged bone. In this context, bone tissue engineering (BTE) holds a distinctive position as it strives to address the formidable challenges posed by critical-sized bone defects, fractures, and bone disorders. The engineered structures of bone scaffolds and/or implants should serve as temporary or permanent templates for new bone formation and/or damaged bone replacements. While numerous factors contribute to these scaffolds/implants' success, some are pivotal determinants such as morphology, porosity, distributions, and the number of pores.

Surgical scaffolds and implants provide remarkable advantages in restoring and augmenting bodily tissues in orthopedic surgery. Scaffolds serve as temporary three-dimensional structures designed to guide tissue growth and regeneration. They provide mechanical support, encourage cell adhesion and proliferation, and ultimately degrade as new tissue forms, leaving behind a fully integrated, functional replacement. Conversely, implants are permanent or long-term fixtures, often fabricated from biocompatible materials like metals or polymers. They are used to replace, support, or enhance the function of biological structures. The advantages of scaffolds and implants lie in their ability to restore or augment bodily tissues, mitigate pain and dysfunction, and improve patients' overall quality of life. These biomedical marvels enable the reconstruction of damaged bone, joints, and organs, facilitate tissue regeneration, and offer solutions for various medical conditions, from traumatic injuries to degenerative diseases. Their versatility, biocompatibility, and capacity to promote healing make scaffolds and implants indispensable tools in modern medicine, ushering in new possibilities for patient recovery and well-being.

The selection of such factors within the design of bone scaffolds represents a critical facet of this multidisciplinary field. This concept embraces the principle that the shape and structure of individual cells within the scaffold wield profound influence over its performance and, consequently, the outcome of tissue regeneration. The mimicry of natural bone microenvironments through tailored morphology allows guiding cellular responses, from initial adhesion and proliferation to the intricate processes of differentiation and tissue remodeling. As such, this doctoral thesis explores the significance of lattice morphology in bone scaffold design, revealing the intricate interplay between structural morphology, mechanical performance, and geometrical attributes, a crucial aspect of successful bone regeneration.

In the context of bone application, TPMS has remarkable structural advantages. Several noteworthy benefits can be derived from these surfaces due to their intricate, precisely ordered structural morphology. The unique geometric features of these surfaces, including their SA and SA/VR, facilitate enhanced bone formation by encouraging cellular adhesion and tissue growth. Furthermore, the inherent complexity and diverse inclinations of TPMS structures stimulate intricate interactions with cells and biological molecules, enhancing the scaffold's bioactivity. The Gaussian curvature of TPMS promotes a diverse range of local curvatures, supporting cell attachment and migration across the scaffold. Together, these structural advantages of TPMS play a pivotal role in fostering an environment conducive to bone regeneration, making them a particularly promising choice for load-bearing implants and bone tissue engineering applications.

Voronoi tessellation lattice scaffolds offer a promising approach for bone tissue engineering applications, providing several key benefits that enhance morphology and biological performance. These lattice structures are characterized by their intricate network of irregular unit cells, with each unit cell uniquely shaped and interconnected, closely mirroring the complex interconnectivity of natural bone. This geometric diversity allows for

tailoring design parameters to optimize mechanical properties and cell infiltration. Additionally, the irregular Voronoi-based lattice scaffold's gradual variations in design parameters influence mechanical strength, stiffness, and overall performance, making them highly adaptable for specific load-bearing requirements. Furthermore, their biomimetic nature facilitates enhanced cell attachment, proliferation, and vascularization, which is vital for tissue integration and regeneration. With their unique morphological and biological advantages, the irregular Voronoi tessellation lattice scaffolds represent a promising solution for advancing bone tissue engineering and regenerative medicine.

A key component of bone substitution designs is the selection of scaffold and implant morphology, which provides new avenues for BTE to extend the frontiers of orthopedic surgery and enhance the quality of life for patients facing critical bone defects. In the following chapters, this thesis will explore the intricate correlation between different biomaterials, scaffold/implant design, and mechanical behavior, offering ideas for addressing critical bone defects with other applications.

The overall objective of this doctoral thesis is to advance the field of bio-medical applications by exploring innovative approaches to the design, fabrication, and optimization of bone implants/scaffolds. The research aims to address the specific goals in the context of:

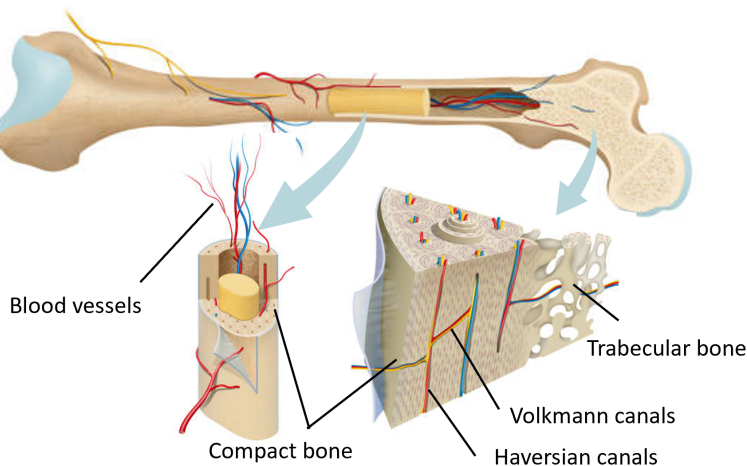
- Designing different lattice morphology like triply periodic minimal surfaces (TPMS), and Voronoi-based structures.
- Using both ceramic and metal biomaterials such as Ti6Al4V and Hydroxyapatite (HA) to analyze numerically/manufacture the designed lattices.
- Integrating finite element analysis (FEA) with statistical methods and selective laser melting (SLM) to predict the mechanical performance of the designed scaffolds/implants.

# 1 Review of the literature

## 1.1 Bone architecture and models

Biomedical research and regenerative medicine have converged on BTE - an innovative field in which adequate bone replacements are being developed [1]. Innovative approaches are being developed for repairing and regenerating damaged or lost bone tissue acquired from trauma, congenital defects, cancer resections, and age-related conditions like osteoporosis [2]. Due to the risks of donor site morbidity and immune rejection associated with traditional treatments, such as autografts and allografts, the demand for safe and effective bone substitutes has escalated [3]. To overcome these challenges, BTE circumvents these issues by integrating biomaterials, cells, growth factors, and scaffold designs to fabricate bone substitutes that restore injured bone tissue [4].

A human skeleton is made up of hard and rigid bones that are capable of regeneration and self-repair [5]. 60% of bone is composed of inorganic components (HA), 10% water, and 30% organic components (proteins) [6]. Inorganic minerals mainly regulate bone stiffness and compressive strength whereas organic proteins are responsible for bone flexibility and toughness [7]. However, diseases, sex, and age can affect bone composition. Bone's structure is hierarchical, porous, interconnected, anisotropic, and nonhomogeneous [8]. Depending on its porosity, bone can be divided into two types: cortical or compact bone, which has a porosity of 5-30% includes longitudinal haversian canals and transverse Volkmann canals passing through the center of osteons, and trabecular bone with highly interconnected pores containing several types of cells and blood vessels with the porosity of 30-90% [9, 10]. Human bone morphology depicted in Fig. 1.



*Figure 1: Illustration of human bone structure showing cortical and trabecular bone vascularized by blood vessels.*

In micro-level damages, the body goes into instant healing mode immediately. In contrast, in the case of the critical-sized bone defect ( $> 10mm$ ), the healing process fails and remains a clinical problem [11, 12]. Traditionally, bone loss has been replaced with autologous implants, allogeneic banked bone, or xenogeneic bone. These methods, however,

produce limited structural and functional recovery, depending on the availability of donor tissues, infection at the donor site, and immune rejection. To address these issues in the treatment of critical-sized bone defects, bone substitutes can be used to accelerate the healing process.

The term "bone substitute" broadly refers to materials that are used to treat bone defects as a replacement for autologous (from the same individual) or allogeneic (from a different individual of the same species) bone. Bone substitutes can include synthetic materials (organic or inorganic), and biologically organic materials that treat bone defects instead of autologous or allogeneous bone [13]. For this purpose, implants and scaffolds are being developed in BTE to support osteogenesis, vascularization, and tissue replacement and encourage bone regeneration[14]. A scaffold is not a permanent substitute for bone since it resorbs over time in contrast to bone implants that remain in the body permanently to provide long-term structural support [15]. Therefore, more focus should be placed on developing scaffolds with mechanical properties and architectural features similar to the host bone.

## 1.2 The choice of material

The choice of biomaterial in BTE is a critical decision, as it profoundly influences the application, the success and longevity of bone substitutes, and patient's long-term well-being [16]. The ideal material must possess a delicate balance of biocompatibility, mechanical strength, and osteoconductivity to effectively support bone regeneration [17]. Biocompatibility guarantees non-toxicity and no immune response, allowing seamless integration with the host tissue [18]. Mechanical strength enables the implant to withstand the forces imposed during daily activities. To minimize the effects of stress shielding and ensure sufficient toughness to withstand fatigue fracture caused by cyclic loading, the material should have a modulus of elasticity similar to bone's. Osteoconductivity also encourages bone-forming cells to recruit and deposit new bone [19]. Additionally, biodegradability is a key characteristic of bone replacement instead of the material used on the defect site, which material degrades at the same rate as new bone formation leading to a gradual transfer of the load to the regenerating bone [20]. Therefore, selecting of the suitable material is a pivotal decision in BTE, as it directly impacts patient outcomes, implant longevity, and life quality.

Among the materials that have gained prominence in this field, metal and ceramic materials stand out for their advantages, which make them suitable for specific bone replacement applications [21, 14]. Metals like Ti6Al4V are highly regarded for their outstanding biocompatibility and mechanical strength, making them ideal for orthopedic applications. Its corrosion resistance and ability to integrate with surrounding bone tissue have made it a preferred material for hip and knee replacements, spinal implants, and dental implants[22, 23]. Their high strength and durability make them well-suited for dealing with the mechanical stresses in these areas. As a result of their high strength and durability, they are ideal for these areas, where mechanical stresses are common. [14, 23].As a bio-ceramic, HA closely resembles natural bone in its mineral composition, enhancing osseointegration and bone growth, making it ideal for applications requiring bone-like properties. HA is often used in bone cement, femoral plugs in total hip replacement, and coatings for orthopedic implants due to its exceptional bioactivity and resemblance to natural bone minerals [24, 21]. Its biocompatibility and osteoconductivity also make it ideal for dental implants, craniofacial reconstructions, and spinal fusion procedures[21].

Clinical applications of bioceramics are limited to non-load-bearing sites [25]. Figure 2 shows metals' different applications, especially Ti6Al4V and ceramics specifically HA in the human body.

Depending on the specific clinical context, the mechanical demands of the implant site, and the desired biological response, selecting metals and ceramics enables healthcare professionals to tailor the choice to the patient's needs. The versatility of these biomaterials underscores their significance in BTE and scaffold design, offering tailored solutions for optimal patient outcomes.

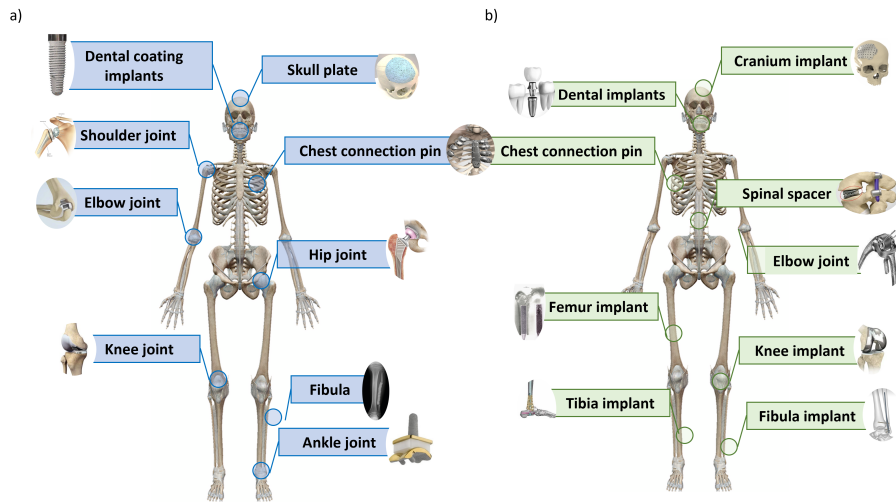


Figure 2: Application of a) ceramic (HA) and b) metallic (Ti6Al4V) bone substitutions in the human body [26, 27, 28, 29, 30, 31, 32].

### 1.3 The importance of scaffold/implant design in BTE

The design of lattice structures relies heavily on biomimicry. The employed lattice structures should mimic the network of human bone in either cortical or trabecular bone, or a combination of the two depending on its application in the body [33]. Scaffold/implant design parameters include the combination of struts and void spaces, porosity, pore size, interconnectivity, mechanical properties, and the amount of surface area for nutrient diffusion, cell attachment, and the ingrowth of new bone tissue. These parameters should be carefully considered when designing lattice scaffolds to perform balanced physical and biological properties [34, 35]. A scaffold/implant can be tailored to suit the specific requirements of the implant site such as facilitating optimal bone regeneration, integration, and cell migration, as well as optimizing mechanical performance by customizing the lattice's size, shape, and density/porosity [36]. Therefore, the morphology or shape of the scaffold significantly influences the scaffold's effectiveness and its regeneration ability [37]. This control over morphology within the scaffold can be instrumental in achieving optimal integration, vascularization, and mechanical stability as well as the optimum therapeutic results, enhancement of bone healing, and pain relief, thereby emphasizing the critical role of designing scaffolds for successful clinical applications. Therefore, research efforts are devoted to finding the most optimum structural morphology.

Responding to this, several studies explored how topology affects mechanical and biological response. Cellular structures with mathematically defined architectures, such as TPMS, have recently attracted attention [38, 39, 40, 41, 42, 43]. Complex geometry of TPMS that locally minimize surface area for a given boundary, is achievable by repeating the unit cell in three perpendicular directions periodically [44]. Their novel topological features, enable them to be used in many engineering disciplines like tissue engineering [45, 43]. By thickening the minimal surface, sheet-based TPMS cellular structures will be created while solidifying the volumes enclosed by the minimal surfaces, resulting in skeletal-based TPMS structures [43].

Numerous studies also have been conducted on strut-based cell topologies [39, 46, 47, 48, 49, 50, 51]. Among strut-based lattices, newly developing randomized structures (irregular structures) gained attention in orthopedic applications due to their unique morphology and intimating to the bone structure [52]. Bionics and mechanical properties of Voronoi are the most similar designs for cancellous bone [53]. However, it is still plagued with the common problem of cross-structure, leading to stress concentration on the intersection of the struts [54] which can simply be solved by flattening the connection areas in the design process. The internal Voronoi structure can be homogeneous and heterogeneous [55], and their irregularity may enhance some mechanical properties, including anisotropic stiffness against certain forces [56]. Aside from these excellent properties of irregular Voronoi-based lattices (IVL), the Voronoi structure also allows for better cell adhesion and migration, which leads to better bone implantation [57]. Compared to some common regular beam lattices, it is found that Voronoi Scaffolds are more effective in lighter weight and stress reductions than beam lattices which opens new applications in BTE and even in additive manufacturing (AM) [58]. Figure 3 shows the classification of lattices in bone substitution designs.

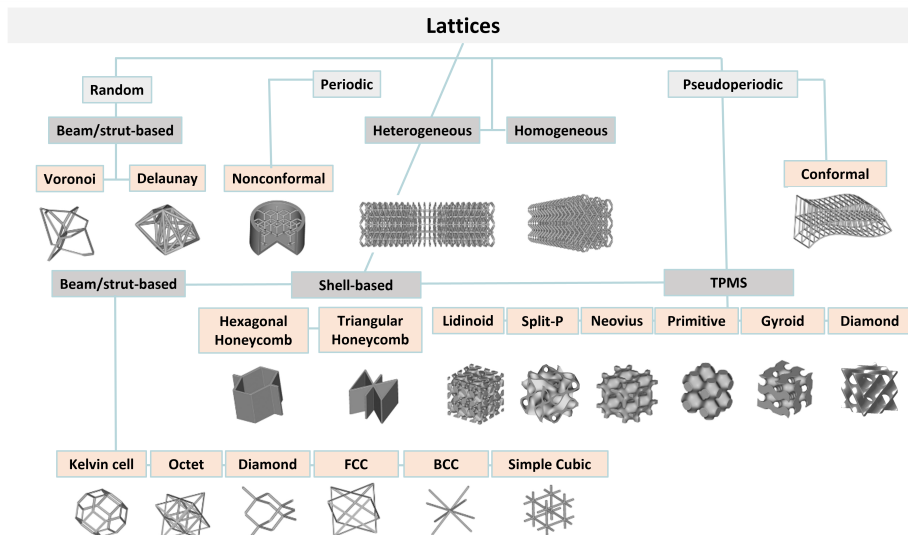


Figure 3: BTE lattice structure classification [59].

Accordingly, the selection of the lattice morphology is fundamental to the bone replacement design due to their unique geometric and mechanical properties, which align with the requirements for effective bone implants and scaffolds. Therefore, algorithm-based structures such as TPMS and Voronoi-based lattice structures due to their advan-

tages are both considered in this thesis. There are several reasons why TPMS structures are commonly selected, such as structural mimicry of natural bone, optimized mechanical properties with tailoring the implant to match the mechanical requirements of the surrounding bone, uniform distribution of stress due to periodic nature of TPMS structures, and customization of porosity and permeability to promote a favorable environment for cell growth and tissue regeneration [60]. The selection of Voronoi-based structures is also influenced by several factors, including: mimicking natural bone architecture especially trabecular bone, tailored porosity which is essential for vascularization within the implants/scaffolds, enhanced mechanical properties due to customization of the specific design parameters, and adaptability to different materials including ceramics and metals causing the versatility of Voronoi structures in bone tissue engineering [61].

### 1.3.1 Architectural features

Architectural features such as interconnectivity, pore size, surface area (SA), and surface area-to-volume ratio (SA/VR) of scaffolds/implants in bone substitutions play pivotal roles in the success of BTE [62]. These parameters collectively influence the scaffold's ability to support cell attachment, proliferation, and differentiation. An optimal pore size allows for nutrient and oxygen diffusion while facilitating the ingrowth of new bone tissue and more protein absorption [63, 64]. A larger surface area promotes more extensive cell-scaffold interactions, aiding in cell adhesion and important signaling processes for bone regeneration. Additionally, a high SA/VR enhances the scaffold's bioactivity by providing more sites for biomolecule adsorption and cellular response [65]. In the case of biodegradable biomaterials, larger surfaces usually result in faster biodegradation [62]. Therefore, turning carefully of these factors ensures that the scaffold provides an environment conducive to bone cell activity, ultimately leading to improved osseointegration and the successful restoration of bone function.

TPMS lattice structures are good candidates for tissue growth due to providing high SA/VR [66]. Periodic repetition of interconnected pores in TPMS can optimize bone regeneration very effectively, besides being mechanically strong enough [67] to withstand mechanical forces, provide stable support for bone regeneration, and integrate effectively into the existing skeletal structure. They also have the capability to mimic the biological characteristics of natural bone in order to integrate well with surrounding tissues [68] promote oxygen diffusion, ion exchange, and nutrient transport [69]. Due to this combination of mechanical and morphological properties, TPMS structure-based scaffolds have attracted significant attention in regenerative medicine for their ability to provide optimal growth environments for bone cells [70].

In the case of irregular lattice structures such as Voronoi tessellation scaffolds, the importance of pore size variety cannot be overstated in the realm of tissue engineering and bone substitutions. Voronoi tessellations create a network of interconnected polygons, resulting in a diverse range of pore sizes and shapes within a single scaffold. Larger pores facilitate nutrient and oxygen diffusion, supporting cell viability, while smaller ones encourage cell adhesion and proliferation [63] and formation of blood vessels [71]. The variety in pore sizes accommodates various stages of tissue regeneration, from initial cell colonization to mature tissue formation [71]. By providing this adaptable microenvironment, Voronoi tessellation scaffolds promote comprehensive tissue integration, enhancing the effectiveness of BTE strategies.

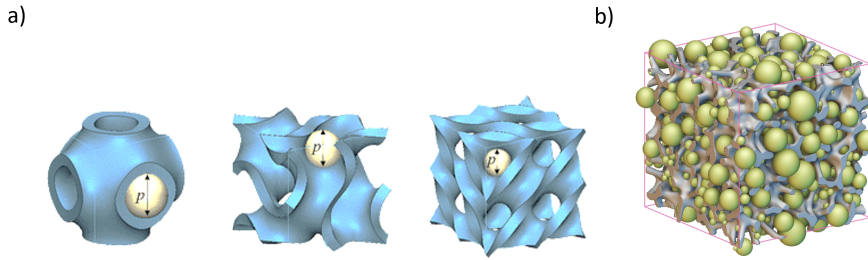


Figure 4: A comparison of a) TPMS and b) Voronoi-based lattice structures pores and their differences.

### 1.3.2 Mechanical compliance

There is an importance to studying the mechanical properties of trabecular/cortical bone. In general, trabecular bone provides strength and transfers away the external loads from the joint to the cortical bone [72]. In vertebral bodies, the main load-bearing part of the bone is the trabecular bone which has the main role of transferring load from the joint to the cortical part [73]. Providing the necessary support and facilitating bone regeneration requires scaffolds that conform to the mechanical properties of natural bone (cortical or trabecular). In determining the location of an implant/scaffold, compressive strength and elastic modulus are vital variables. As a result of a stiffness mismatch between bone substitutions and the host bone, stress shielding is a problematic phenomenon that inhibits the healing of fractures [74]. This problem can be avoided by designing implants/scaffolds with an appropriate harmony between elastic modulus and compressive strength of design lattice with human bone depending on the fracture site.

The utilization of numerical methods in predicting the mechanical properties of bone implants and scaffolds holds paramount importance in the field of BTE [75, 76, 77, 78]. By employing numerical simulations, researchers and engineers can optimize the design of implants and scaffolds, ensuring they meet the stringent mechanical requirements for bone replacements [79, 80]. These predictions offer valuable insights into stress distributions, deformation patterns, and potential failure points, helping to refine the design for enhanced performance and longevity. Furthermore, numerical methods allow for the rapid evaluation of numerous design iterations, saving time and resources compared to experimental testing alone. Ultimately, the application of numerical methods not only accelerates the development of safer and more efficient bone implants and scaffolds but also contributes significantly to the overall success and reliability of BTE applications.

Advanced additive manufacturing technologies and more specifically, selective laser melting (SLM), offer profound advantages in the fabrication of intricate and customized lattice morphologies for bone replacements. Within the field of bone tissue engineering and orthopedics, SLM's capacity to fabricate intricate lattice designs is of particular significance [81]. This novel approach holds immense promise for fabricating these lattice structures, where traditional implant solutions fall short. By leveraging SLM, researchers can advance the development of patient-specific implants/scaffolds that align with the unique requirements of individual patients, advancing orthopedic surgery and bone tissue engineering [82, 83]

Integrating numerical methods, either separately or in conjunction with SLM, in predicting the mechanical properties of bone implants and scaffolds is paramount in advanc-



ing the field of BTE [84, 85]. Numerical simulations, particularly FEA, enable researchers to model and evaluate the structural behavior of complex, patient-specific implants and scaffolds. When combined with SLM, a state-of-the-art additive manufacturing technique, these simulations allow for the precise customization of implant designs to achieve desired mechanical properties. The ability to predict and optimize the structural performance of implants prior to fabrication not only ensures their biomechanical compatibility but also reduces material waste and production costs.

## 1.4 Objectives of the study

Recent advancements in AM have shown potential in enabling the fabrication of intricate cellular structures including porous architectures, which can successfully serve as implants and/or scaffolds required by personalized medicine. Therefore, the role of design is one of the most profound as it helps to tackle complex challenges in BTE and to generate effective solutions for bone substitutions.

The overall objective of this study is the design of bioinspired bone implants considering metal and ceramics material, and the evaluation of the most suitable and printable architectures using FEA, statistical methods and SLM approaches. The aims of this study include analysis of the mechanical behavior of implants/scaffolds, optimization of their design for better mechanical and morphological performance, and evaluation of the potential of SLM in producing complex-structured implants with customized geometries. The specific objectives of this work are as follows:

- (i) Design of the anatomically matched hybrid implants composed of both cortical and trabecular bones with mechanical parameters compatible with the characteristics of human bone.
- (ii) Design, optimization, and printing of TPMS lattices for bone tissue engineering.
- (iii) Experimental and numerical evaluation of Spilt-P TPMS lattices produced by SLM.
- (iv) Design and numerically optimization of mechanical properties of irregular gradient Voronoi-based scaffolds for bone applications.

The following research questions are addressed in this work:

1. How does the design of bone implants affect their mechanical performance?
2. How can the Taguchi method be utilized to explore new insights into the interaction of geometric factors, including structure type, number of unit cells, and wall thickness.
3. What is the optimal design of bone implants for required and biomimicking mechanical properties?
4. How is the printability of the designed architectures?
5. What design parameters are the most influential on the mechanical properties of the implants?
6. What kind of design can be applied for biomimetic load-bearing implants to treat long bone critical-sized defects in different regions of the human body?

To achieve the goals, Taguchi method was employed to optimize the mechanical properties of metallic TPMS cellular structures with analyzing the effect of geometric characteristics like TPMS type, wall thickness, and number of unit cells for enhanced performance in bone-related applications. Furthermore, this study investigates the creation of a Haversian bone-mimicking strategy for cortical bone, optimizing the arrangement of Haversian and Volkmann canals within hollow cylinders to mirror the mechanical properties of human cortical bone has been worked out. Subsequently, the selected optimal structure has been merged with the trabecular bone component represented by TPMS-based lattices (Diamond, Primitive, Split-P, and Gyroid) in order to fabricate a pioneering biomimetic implant design that seamlessly amalgamates cortical and trabecular bone qualities. In addition, this research has been focused on SLM-fabricated Ti6Al4V Split-P TPMS structures, which unveil the potential of SLM to manufacture Split-P architectures. From quasi-static mechanical behavior to stress-strain attributes and plateau stress responses, this dimension systematically has examined the mechanical properties of these innovative lattice structures. Moreover, FEM has offered a deeper insight into the elastoplastic behavior of the Split-P structures, while unit cell homogenization elucidated the equivalent stiffness tensor. Irregular Voronoi tessellation scaffolds, with a particular focus on those designed by HA, has been studied. These irregular Voronoi-based lattice (IVL) structures are designed to closely mimic the interconnectivity of natural human trabecular bone. The research scrutinizes the influence of design parameters, including strut thickness and point space, on mechanical properties (stiffness and strength) and geometrical features (pore size, pores distribution, pore numbers, SA, and SA/VR). Four distinct IVL scaffold types were examined, each characterized by its unique attributes. The research emphasizes the significance of irregularity and morphology in governing geometrical features and mechanical performance, illuminating novel avenues for bone substitution therapies.

The significance and contribution of this research are highlighted by a novel bone-mimicking implant design with cortical and trabecular bone components for reconstruction of critical-sized defects in a long bone. For the first time, the design of Split-P lattices, SLM manufacturability of biocompatible Ti6Al4V alloy, and the evaluation of their mechanical efficiency have been performed. Moreover, the effect of design parameters on implants durability have been demonstrated based on numerical studies. An improvement in the suitability of Voronoi lattices has been recorded by considering gradient point space and strut thickness in the lattices. The findings of this study may lead to the development of more efficient and reliable bone implants with reduced failure rates, which can ultimately improve the quality of life for patients in need of bone replacement or repair. Moreover, this research contributes to the growing body of knowledge on the applications of FEA and SLM in biomedical engineering, paving the way for the further advancements in the field.

According to Table 1, the following goals and objectives were formed:

*Table 1: Correlation between the objectives, implants/scaffold's designs, and solutions proposed in publications (Pub.).*

Objectives	Pub. I	Pub. II	Pub. III	Pub. IV
1		✓		
2	✓	✓	✓	✓
3			✓	
4				✓

## 2 Materials and methods

### 2.1 Scaffold design

#### 2.1.1 Taguchi-based design of Ti6Al4V TPMS structures

This study investigated the mechanical properties of metallic cellular structures inspired by TPMS. Taguchi method was employed to design experiments, incorporating three factors and three levels for each factor. The research focused on three distinct TPMS structures, namely IWP, Neovius, and the Primitive. Two additional factors, unit cell's number in each  $X$ ,  $Y$ , and  $Z$  direction (with values of 2, 3, and 4) and the thickness of 0.3, 0.4, and 0.5, were considered. The initial surface of TPMS was generated using MATLAB software, followed by the thickening and creation of 3D models using SolidWorks. The study utilizes a cube as a bulk sample with a constant length of 25 mm in  $X$ ,  $Y$ , and  $Z$  directions, defined by a multiple of unit cell size and the number of unit cells in each direction as illustrated in Fig.5. Taguchi's orthogonal array L9 is used to estimate the influence of factors on mechanical properties, determining which factors are more significant. Total of 9 tests as presented in Table 2. It should be noted that the name of final lattice structure, Pri030-3, refers to the Primitive lattice with a thickness of 0.30 mm and 3 unit cells in each direction. Other typologies are named similarly.

Table 2: Factor influence matrix according to Taguchi L9

Topologies	Type of TPMS	Wall thickness (mm)	Cell numbers ( $L/l$ )
IWP050-2	I-WP	0.50	2
IWP040-3	I-WP	0.40	3
IWP030-4	I-WP	0.30	4
Neo050-3	Neovius	0.50	2
Neo040-4	Neovius	0.40	3
Neo030-2	Neovius	0.30	4
Pri050-4	Primitive	0.50	2
Pri040-2	Primitive	0.40	3
Pri030-3	Primitive	0.30	4

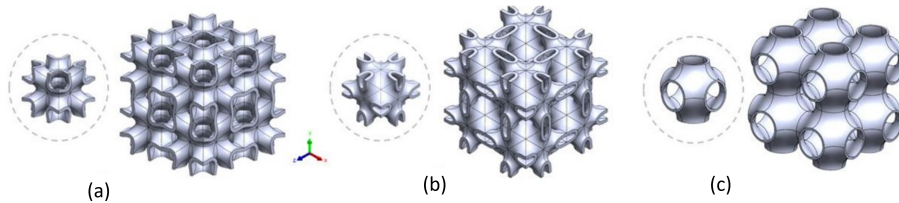


Figure 5: TPMS lattice structures, (a) I-WP, (b) Neovius, and (c) Primitive. - (adopted from publication I).

The Taguchi method presents several advantages in experimental design and optimization. One notable advantage is its efficiency in conducting experiments with a relatively

small number of trials compared to full factorial designs, resulting in significant time and cost savings. Additionally, the method excels in identifying influential factors and their interactions, contributing to a more focused understanding of the system under study. The emphasis on robust design makes it particularly effective in minimizing the impact of variations and external factors, leading to increased reliability and stability in the designed system. However, the Taguchi method is not without its limitations. Its assumption of linear relationships between factors and responses may not accurately capture the complexities of some real-world systems that exhibit nonlinear behavior. The method's reliance on orthogonal arrays and the assumption of factor independence may also be restrictive in situations where factors are interrelated. Despite the limitations, Taguchi method continues to be a valuable and effective tool for experimental design and optimization in diverse fields. As a result, in this study, Taguchi method was applied in order to determine the effect of design parameters on the mechanical performance of generated lattice structures.

### 2.1.2 Haversian bone mimicking Ti6Al4V porous structure

In the design of this part, a comprehensive approach was employed to investigate the intricate design of bone mimicry implants. The study encompassed both cortical and trabecular bone structures, with a particular focus on their geometrical characteristics and mechanical properties. For the cortical component, a diverse array of structures was created using CAD software SolidWorks (Dassault Systems SolidWorks Corporation, Waltham, Massachusetts, USA), varying in terms of Haversian and Volkmann canal arrangements, cross-sectional shapes, sizes, numbers, and orientation of canals within a hollow cylinder configuration as shown in Table 3.

Table 3: Design parameters of various combinations of Haversian and Volkmann canals resulting 9 different topologies; (Num.: Number, Dia.:Diameter (mm), Ver.:Vertical, Hor.:Horizontal)

Designs	Num./Dia. of Haversian canals	Cross section of Haversian canals	Num./Dia. of Volkmann canals	Cross section of Volkmann canals	Sahpe of Haverasian and Volkmann canals
D1	16/0.6	Circular	5/0.8	Circular	Ver./Hor.
D2	8/0.6	Circular	4/0.7	Circular	Ver./Hor.
D3	20/0.6	Circular	4/0.4	Circular	Ver./Hor.
D4	20/0.6	Circular	5/0.65	Circular	Ver./Hor.
D5	20/0.6	Circular	5/0.65	Circular	Helix/Helix
D6	20/0.6	Circular	5/0.65	Circular	Helix/Hor.
D7	20/0.6	Circular	5/0.65	Circular	Ver./Helix
D8	20/0.6	Circular	5/0.55, 1.4	Elliptical	Ver./Hor.
D9	20/0.6	Circular	5/0.55, 1.4	Elliptical	Ver./Helix

An inner diameter of 8 mm, an outer diameter of 10 mm, and a height of 11 mm were considered for the design of the hollow cylinder. The number of Haversian canals was considered as 8, 16, and 20 with a constant diameter of 0.6 mm with a circular cross-section. Similarly, Volkmann canals were designed with 4 and 5 in number in both circular and elliptical cross-sections. The diameter of circular Haversian canals ranges from 0.4-0.65 mm

and for the elliptical cross-sections type 0.55 and 1.44 *mm* denoting the minor semi-axis and major semi-axis, respectively. In terms of the orientation of each canal horizontal and helical were considered for the Haversian canals, and vertical and helical, were chosen for the Volkmann canals. The results of the combination of these factors were 9 topologies for cortical part structure as shown in Fig. 6.

In parallel, the trabecular component was developed using four distinct TPMS lattice structures – Gyroid, Diamond, Split-P, and Primitive using nTopology software (3.13.4, nTopology, New York, NY, USA). Each of these structures was merged with the optimized cortical designs. To ensure uniformity, all trabecular structures were set at a 15% relative density (RD) and 85% porosity. The ultimate goal of this methodology was to identify how implant architectures affect mechanical and morphological properties of implants to enhance the potential for bone tissue regeneration and structural support. Fig. 6 illustrates the process design of Haversian bone mimicking implant:

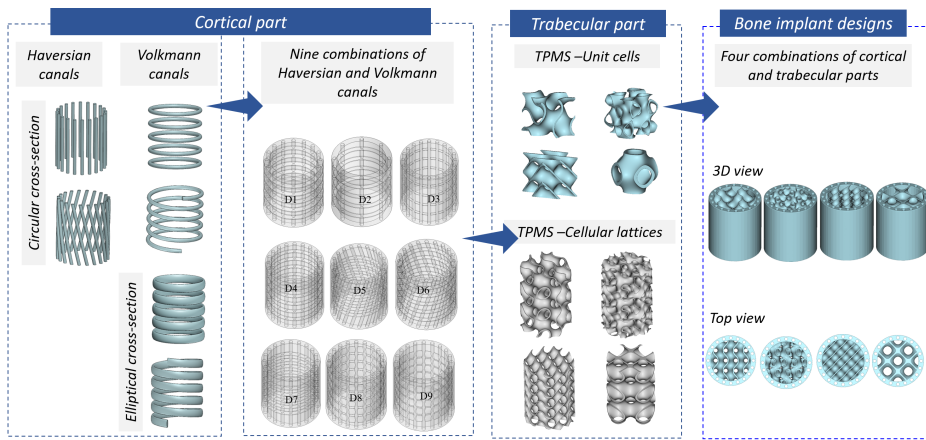


Figure 6: The design process of Haversian bone-mimicking lattice structure.

This approach, combining the principles of biomimicry and computational analysis, facilitated the comprehensive exploration of innovative designs for load-bearing bone implants, crucial to addressing critical-sized bone defects.

### 2.1.3 Split-P Ti6Al4V TPMS cellular lattice structure

This part, the design of lattice-based implants, focuses on the utilization of TPMS, particularly the Split-P structure. The design process began by selecting two distinct cell sizes, measuring 12.5 and 14 *mm*, to occupy a defined design space of  $25 \times 25 \times 25 \text{ mm}^3$ . Iso-values of 0 and 1 were strategically employed to manipulate the structural morphology, resulting in the creation of five unique cellular lattices. With an isovalue of 0, variations in the sheet thickness of the Split-P TPMS, ranging from 0.25 to 0.6 *mm* and maintaining a constant unit cell size of 12.5 *mm* were led to generate a spectrum of porosity levels spanning from 75% to 90%, ultimately achieving target RD of 10.47%, 16.74%, and 25.19%. In order to further diversify the design, a specific target RD of 21% was targeted, leading to the development of two additional cellular lattices. One was configured with an isovalue of 0 and a unit cell size of 14 *mm*, while the other featured an isovalue of 1 with a unit cell size of 12.5 *mm*. nTopology software package (3.35.2, nTopology, New York, NY, USA) was used to create computer-aided design files (CAD) of the Split-P lattices. As a result of

this design approach, laid the foundation for the creation of innovative and tailored lattice implants, offering a broad range of porosities and RDs to cater to diverse orthopedic and bone tissue engineering applications. Figure 7 depicts the designs and changeable parameters (Isovalue, thickness, and unit cell size) to create different morphology of Split-P lattice structures. It should be noted that SP05U140 refers to a Split-P morphology with 0.50 *mm* thickness and a unit cell size of 140 *mm*. Other morphologies are also named in this manner in the following.

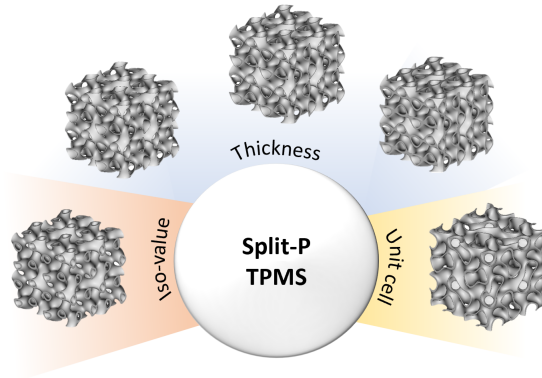


Figure 7: Changeable design parameters in generation of Split-P lattice structures.

#### 2.1.4 Voronoi-based HA scaffold

In this section, an innovative approach is employed to develop scaffolds for bone tissue engineering, specifically utilizing irregular Voronoi tessellation as a structural foundation. The design, known as IVL, was generated with features gradually changing in strut thickness (ST) and seed point spacing (PS), closely mirroring the intricate interconnectivity found in human bone morphology. This tailored transition within the scaffold was meticulously designed to provide an influence on both mechanical and biological performance, thereby enhancing its potential for bone regeneration. This section goes into great detail about how the design parameters can have a significant impact., specifically the ST and PS, within the HA Voronoi-based lattice structure. The focus of this study is on assessing critical factors, including stiffness, strength, pore size, pore distribution, pore numbers, SA, and SA/VR. To comprehensively explore the design space, four distinct IVL scaffold types were meticulously engineered: PC-TC (Constant PS-Constant ST), PC-TG (Constant PS-Gradient ST), PG-TC (Gradient PS-Constant ST), and PG-TG (Gradient PS-Gradient ST). Applying this novel design methodology sets the stage for the creation of tailored scaffolds with the potential to revolutionize bone tissue engineering, offering a diverse array of structural variations to address a spectrum of orthopedic and regenerative medicine.

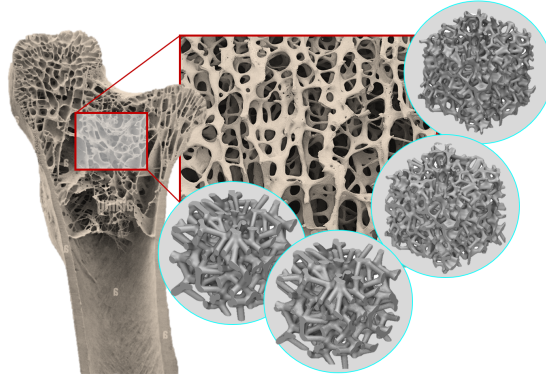


Figure 8: Interconnectivity of human bone and the designed IVL structures.

## 2.2 Lattice structure fabrication by SLM

### 2.2.1 Taguchi-based design of Ti6Al4V TPMS structures

The Realizer SLM50 metal printer was utilized to print Ti6Al4V Primitive TPMS lattice with particle sizes ranging from 20 to 63  $\mu\text{m}$ . The fabrication process employed with the print parameters defined in Table 4 based on the optimization process. The calculated laser energy density is determined to be  $31.11 \text{ J/mm}^3$ .

Table 4: 3D-printed parameters used for SLM-ed Ti6Al4V-based TPMS

Parameter	Value
Laser power (W)	84
Scanning speed ( $\text{mm/s}$ )	750
Hatch distance ( $\text{mm}$ )	120
Layer thickness ( $\text{mm}$ )	30
Rotation between the consecutive layer( $\text{degree}$ )	60

### 2.2.2 Split-P Ti6Al4V TPMS cellular lattice structure

In the fabrication phase of Split-P lattice structures and solid tensile specimens, the SLM process was used employing a gas-atomized Ti6Al4V powder characterized by rounded particles falling within a size range spanning from 15 to 37  $\mu\text{m}$ . The execution of this intricate process adhered to established processing parameters summarized in Table 5.

High-purity argon gas was carefully used throughout the manufacturing procedure to prevent oxidation, preserving the integrity of the material. Following the completion of the manufacturing process, the fabricated samples were wire cut from the substrate, followed by ultrasonic cleaning with pure alcohol. Fig 9 shows a schematic representation of SLM process.

This methodology underpins the fabrication of intricate lattice structures, contributing to developing biomaterials with potential applications in bone tissue engineering and load-bearing implants.

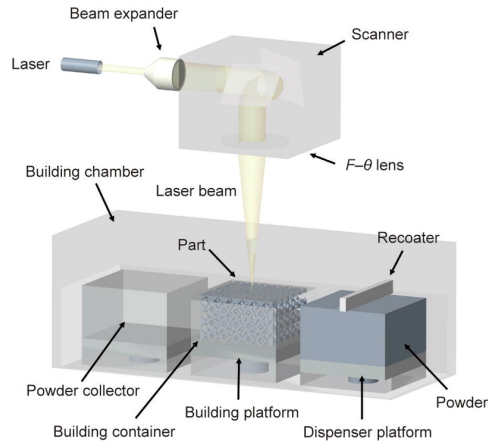


Figure 9: Schematic representation of the SLM chamber, adapted from [86].

Table 5: 3D-printed parameters used for SLM-ed Ti6Al4V Split-P cellular lattices [87]

Parameter	Value
Laser power (W)	275
Scanning speed ( $mm/s$ )	1100
Hatch distance ( $mm$ )	110
Layer thickness ( $mm$ )	30
Rotation between the consecutive layer( $degree$ )	57

## 2.3 Characterization of the designed scaffolds/implants

### 2.3.1 Taguchi-based design of Ti6Al4V TPMS structures

The Taguchi method utilizes the signal-to-noise ratio (SNR) to establish the relationship between calculated data and error. In statistical analysis, the main effect factor represents the impact of varying levels of each factor on outcomes when they are in contrast. Consistency between the trends observed in SNR and main effect analyses ensures accuracy of the obtained and designed data. The 'larger is better' criterion was selected to maximize the modulus of elasticity and compressive strength.

A non-linear FEA was conducted to validate the experimental compression test results for Ti6Al4V SLM printed Pri030-2, featuring 91% porosity. The results for elastic modulus and maximum stress reveal a minimal deviation of 3% and 1.9%, respectively, between the numerical and experimental findings. Scanning electron microscope (SEM) analysis was conducted on lattice using Hitachi TM1000. This analysis specifically focuses on the top surface of the printed structure, aiming to assess any dimensional differences between the designed model and the actual 3D-printed structure. The lattice structure, as produced, closely adheres to the CAD model. However, residual particles were observed adhering to the fabricated structures. The presence of these residual particles could potentially contribute to thickness variations in the structure. More detail has been provided in Publication. II.



### 2.3.2 Haversian bone mimicking Ti6Al4V porous structure

To study the compressive behavior of the designed implants, the non-linear elastic-plastic FE analysis was conducted using Bilinear Isotropic Hardening (BISO). ANSYS R2 19.4 software was used to predict the behavior of the implants under compressive load. Two cylindrical plates were placed on the top and bottom of the structures as rigid bodies. The bottom plate was subjected to the fixed displacement boundary conditions (BC) in all directions while the top plate was allowed to move in the z-direction the fully constrained movements in the X- and Y-directions.

### 2.3.3 Split-P Ti6Al4V TPMS cellular lattice structure

SEM analysis (SEM, HR-SEM Zeiss Merlin) was used to morphologically examine the manufacturability in the case of SLM-fabricated Split-P TPMS lattice structure.

Geometrical parameters of fabricated Ti6Al4V Split-P lattices such as RD were assessed by Archimedes method and dry weighing was used to calculate the weight.

Quasi-static compression tests were conducted experimentally and numerically. An experimental compression test was performed at the strain rate of  $1\text{ mm/min}$  up to the densification region at the ambient temperature by an Instron 8802 machine equipped with a  $250\text{ KN}$  load cell.

FEM compression test was performed using ANSYS software by applying an elastoplastic material model with multi-linear isotropic hardening (MISO) using both shell and solid elements depending on the lattice morphology. Lattices were placed between two plates and the top plate was subjected to a velocity of  $2\text{ m/s}$  while keeping the kinetic energy below 2% of the total internal energy.

To study the relationship between RD of the periodic cellular structures and their mechanical properties, the Gibson-Ashby model was employed, and the relationship between modulus of elasticity and yield strength of the structures was calculated. The energy absorption of the lattice structures was investigated carefully to represent the material's resistance to load without severe failure, which is an important property in the design of orthopedic structures.

Finally to accurately estimate the effective elastic properties of lattice structures, a periodic homogenization method was performed for the Split-P unit cells using the nTopology software, and a lattice anisotropy comparison was performed.

### 2.3.4 Voronoi-based HA scaffold

To study the effect of the uniform and gradient on the design parameters such as PS and ST on the mechanical properties of IVL structures, linear static structural analysis was employed, and maximum stress criteria were applied. ABAQUS (6.19) software incorporated with a UMAT code was used to assess the compressive behavior and investigate two important parameters including elastic modulus ( $E$ ) and compressive strength ( $\sigma_c$ ). Two rigid plates were placed on the top and the bottom of all scaffolds. Apart from the loading direction, the top plate was fixed in all directions, while the bottom plate was subjected to the fixed displacement in all directions, and finally, a load of  $1\text{ KN}$  was applied at the reference point of the top plate in the Y-direction. Mechanical properties of a  $4\text{ GPa}$  elastic modulus, an  $8\text{ MPa}$  breaking strength, and a 0.27 Poisson's ratio was considered for HA used in FEA. More detail about material was provided in Publication IV.

### 3 Results and discussion

#### 3.1 Taguchi-based design of Ti6Al4V TPMS structures

##### 3.1.1 Taguchi analysis results

Figure 10 presents the main effect and SNR for both elasticity and compressive strength. The alignment of trends in these figures confirms the results' correctness. Table 6 and 7 outline the ranking of three factors for elastic modulus and compressive strength respectively. Mean of SN ratio is in maximum value for type of structure followed by L/I and wall thickness. Accordingly, the type of structure was identified as the most influential factor. Notably, Neovius structure emerges as the most influential for maximizing both elastic modulus and compressive strength. This is due to increased numbers of unit cells and wall thickness contributing to reduced porosity and increase the densification, resulting in higher structural weight and mechanical properties.

Table 6: SNR and mean values for elastic modulus

Response Table for Signal to Noise Ratios				Response Table for Means			
Level	Lattice type	wall thickness	(L /I)	Level	Lattice type	wall thickness	L /I
1	10.69	11.27	3.34	1	3.45	4.06	1.81
2	13.58	7.86	8.52	2	5.50	3.94	3.77
3	0.06	5.20	12.47	3	1.27	2.23	4.653
Delta	13.52	9.12	8.14	Delta	4.22	1.83	2.83
Rank	1	3	2	Rank	1	3	2

Table 7: SNR and mean values for compressive strength

Response Table for Signal to Noise Ratios				Response Table for Means			
Level	Lattice type	wall thickness	(L /I)	Level	Lattice type	wall thickness	L /I
1	32.27	33.20	25.90	1	41.38	48.03	22.23
2	33.72	30.17	31.04	2	55.17	42.94	43.32
3	24.99	27.62	34.04	3	21.26	26.84	52.26
Delta	8.73	5.58	8.14	Delta	33.91	21.19	30.03
Rank	1	3	2	Rank	1	3	2

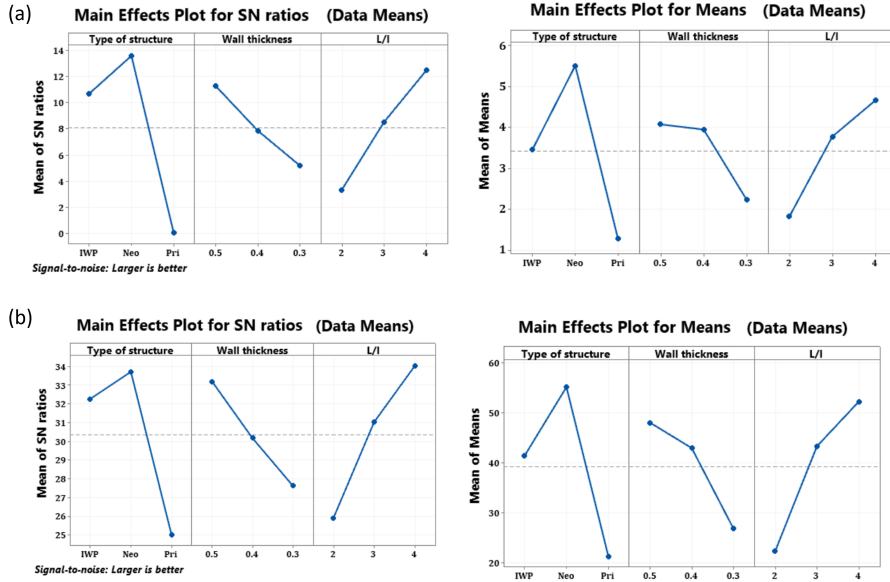


Figure 10: SNR and mean values for (a):elastic modulus and (b): compressive strength - (**adopted from publication I**).

## 3.2 Haversian bone mimicking Ti6Al4V porous structure

### 3.2.1 Morphology effects on Geometrical features

**3.2.1.1 Cortical bone component:** Nine combinations of Haversian and Volkmann canals were considered when designing the cortical part. The combinations are shown in Fig. 11 and the corresponding geometric features of each combination are provided in the table 8.

Table 8: Surface area, Volume, RD and porosity of various combinations of Haversian and Volkmann canals

Designs	SA ( $mm^2$ )	V ( $mm^3$ )	RD	Porosity
D1	696.11	120.82	66.39	33.61
D2	419.11	68.41	79.83	20.17
D3	674.71	105.73	77.25	22.75
D4	714.69	109.11	70.10	29.90
D5	722.37	109.11	70.11	29.89
D6	721.44	109.11	70.10	29.90
D7	715.61	109.11	70.10	29.90
D8	881.49	149.26	62.79	37.21
D9	881.13	147.69	62.75	37.26

Table 8 provides details about the different designs of Haversian and Volkmann canals. As it is clear, the combination of canals significantly affect all parameters. Figure 11 visually

presents the volume, SA, and various combinations generated by intersecting canals. The minimum SA, V, and porosity can be seen in D2 with the lowest number of canals while the maximum value of these parameters was recorded by designs D8 and D9, It should be noted that the information regarding the design parameters is available in Section 2.1.2 and Table 3.

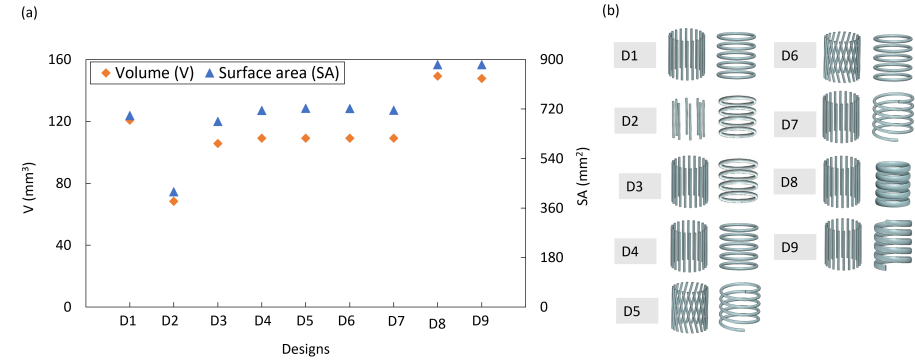


Figure 11: Geometrical features of Haversian and Volkmann canals designed in cortical component; (a) SA and V provided by the various combinations of canals; (b) different combinations of Haversian and Volkmann canals - **(unpublished images)**.

**3.2.1.2 Trabecular bone component:** Four selected morphology of TPMS were chosen to combine with cortical component as shown in Fig. 12. Geometrical feature of each morphology like SA and SA/VR are presented in Table 9.

Table 9: Geometrical features on different TPMP morphologies

TPMS	SA (mm <sup>2</sup> )	SA/VR (1/mm)
Gyroid	888.17	10.66
Split-P	1462.71	17.56
Diamond	1087.66	13.06
primitive	681.71	8.19

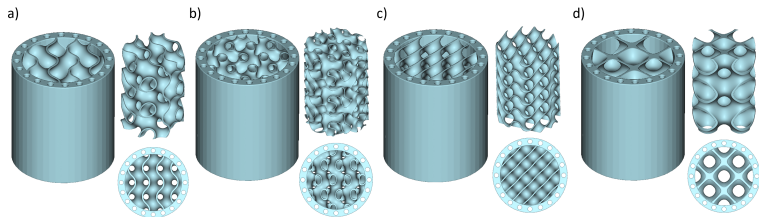


Figure 12: Four TPMS morphology selected for trabecular part and their combination with cortical part creating whole bone implants - **(adopted from publication II)**.

According to Table 9, Primitive lattice structure provided the minimum values for both parameters and the maximum were recorded for Split-P design followed by Diamond and Gyroid.

### 3.2.2 Morphology effects on mechanical performance

**3.2.2.1 Cortical bone component's mechanical properties:** FE analysis was conducted to explore the relationship between the elastic modulus, strength, and porosity of cortical bone in various designs. The goal was to identify the optimal design for the mechanical properties of cortical bone by taking into account different factors like the number, diameter, shape, and orientation of vertical (Haversian) and horizontal (Volkman) canals. The details about FEA analysis, validation, and mesh convergence study are provided in publication II. Table 10 presents FEA results for nine geometrical designs, highlighting the impact of porosity and cross-section shape on the elastic modulus and yield strengths.

Table 10: Mechanical properties of cortical bone component obtained from FEA

Designs	E (GPa)	Yield stress (MPa)
D1	13.33	198.20
D2	20.27	184.00
D3	26.38	109.20
D4	19.55	125.60
D5	19.43	125.60
D6	19.46	125.60
D7	19.74	125.60
D8	19.86	144.40
D9	20.18	144.40

Figure 11, Table 8, and Table 10 provide evidence that altering the shape of Volkman and Haversian canals, and different combinations of them, can substantially affect porosity and influence mechanical properties. The comparison of two groups of D1-D3, D2-D4, D2-D3, and D1-D4 showed that changing Haversian and Volkman canals and the diameter of Volkman canals leads to noticeable changes in both mechanical properties.

When D1 and D3 are compared, it becomes apparent that increasing the number of Haversian canals, decreasing the number of Volkman canals, and changing diameter, can reduce porosity by as much as 23%. This leads to an increase in the elastic modulus reaching 26.38 GPa and representing about 50% growth. These two models highlight that the number and diameter of Volkman canals exert a more pronounced influence on the final elastic modulus showing that Volkman canals have a more significant effect than Haversian canals. In the group D2-D4 decreasing Haversian canals and increasing Volkman canals lead to changes in mechanical properties. In the D2-D3 group, changes in mechanical properties are caused by increasing Haversian canals and decreasing Volkman canal diameters, and in the group D1-D4, mechanical properties change as Haversian canals increase and Volkman canal diameters decrease. As a result, the most influential parameters leading to a change in mechanical properties are changing the Haversian canals and decreasing the diameter of the Volkman canals. Comparison between two groups of D1-D3 and D2-D4 revealed that decreasing/increasing Volkman canals also affect mechanical properties.

Consequently, the optimal configuration to consider elastic modulus in the range of

human cortical bone for subsequent steps involves 20 Haversian canals and 5 Volkmann canals. The Haversian canals were considered circular cross-sections with diameters of 0.6 mm, while Volkmann canals come in two varieties: circular cross-sections with a 0.65 mm diameter and elliptical cross-sections with minor and major semi-axes measuring 0.55 mm and 1.4 mm, respectively. The analysis was conducted under the assumption of RD of about 70% for the following designs (D4, D5, D6, and D7) to investigate the influence of the Volkmann and Haversian canal's shape on the mechanical properties.

The lowest elastic modulus, at 19.43 GPa, was observed when both Haversian and Volkmann canals exhibited a helical orientation. The highest elastic modulus, at 19.74 GPa, was found in models with Haversian canals oriented vertically and Volkmann canals of the helical type. All four structures exhibited the same yield strength of 125.6 MPa, but the elastic modulus varied across the structural designs. Figure 13 illustrates the trend of increasing porosity and elastic modulus in the seven suitable models within the range of cortical bone elasticity.

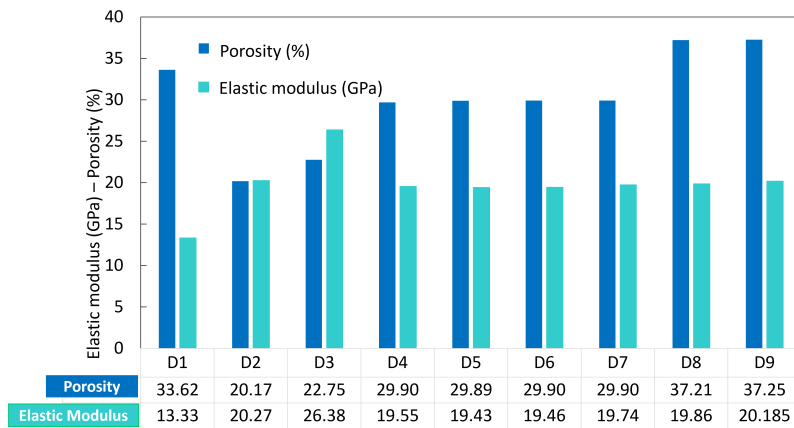


Figure 13: Porosity vs elastic modulus of various cortical component designs - (*adopted from publication II*).

All the geometries are shown with their stress distribution and plastic strain in Fig 14. A change from a circular to an elliptical cross-section has a notable impact on stress concentration. Stress concentration is significantly reduced when the ellipse is flattened along the y-axis, parallel to the direction of the applied load. This transition from a circular to an elliptical cross-section results in lower stress concentrations compared to the circular counterpart, thus delaying failure around the pores [88]. In the case of two models, D4 and D8, changing the cross-section of Volkmann canals from circular to elliptical led to a 1.5% increase in the modulus of elasticity and a significant 24.59% rise in porosity. This outcome underscores that selecting an elliptical cross-section in the helical orientation results in a structure that is both lighter and stiffer, as noted by Schultz in 2019. It's important to note that the orientation of the elliptical cross-section was considered with the direction of the applied force for all the mentioned designs.

A similar pattern was observed in D7 and D9, where vertical Haversian canals and helical Volkmann canals with circular and elliptical cross-sections were employed. In these

two models, after the cross-section change, porosity increased from 30% to 37%, and the elastic modulus rose from 19.74 *GPa* to 20.18 *GPa*, which represents the highest elastic modulus value among all nine structures and closely approximates the maximum elasticity of human cortical bone (20.7 *GPa*). Based on the computational results for the nine designs, the D9 implant was deemed the most suitable choice for integration with the trabecular part, aiming to mimic bone architecture and investigate the impact of trabecular morphology on controlling stress distribution, plasticity, stiffness, and strength.

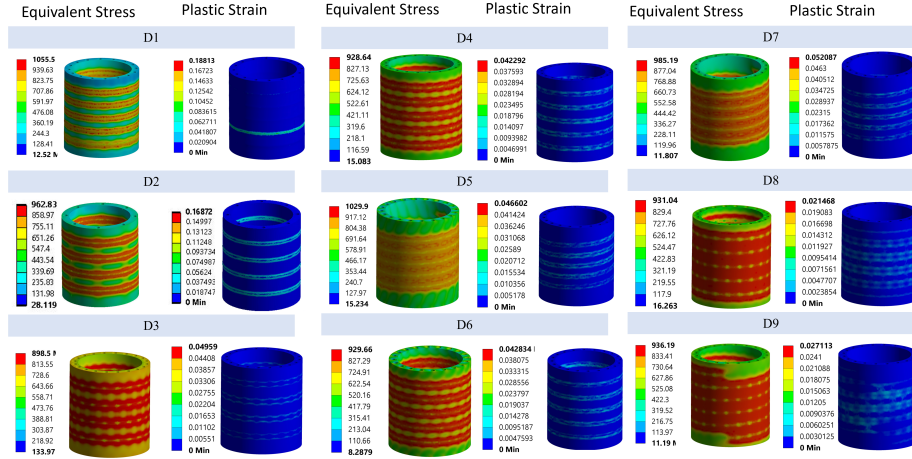


Figure 14: vonMises stress and plastic strain of nine designs of cortical component - (adopted from publication II).

Finally, D9 was chosen as the best design for the cortical component due to its ideal combination of stiffness, strength, and optimal pore size, SA, and volume that can provide for vascularization and bone growth. Accordingly, in Strategy II, D9 will be integrated with four different minimal surface implants to examine the overall mechanical performance of the entire bone structure and assess how the interior architecture influences stress and strain distribution.

**3.2.2.2 Mechanical properties of whole bone implant:** The numerical results derived from compressive strength, depicted in Fig. 15. The findings reveal that the Diamond implant exhibits the highest elastic modulus and yield strength when compared to the other three structural types. Conversely, the Primitive implant displays the lowest elastic modulus and yield strength. The stress-strain curves obtained from the FEA for all configurations are depicted in Fig. 16. Fig. 15 shows the elastic-plastic behavior of four different cortical component designs when trabecular parts are added. All the configurations exhibit plastic deformation. Upon an initial examination of the vonMises stress contour, it becomes evident that the interior design featuring Split P has a substantial stress reduction effect on both the outer and inner layers of the cortical component when compared to the other three implant types.

The highest stress value, reaching 1132 *MPa*, is primarily concentrated in the boundary regions. Notably, the stress in the outer and inner layers of the cortical part remains below the yield point, and it is evenly distributed throughout the entire structure, signifying a desirable load transfer. Diamond design exhibits a relatively high-stress level of 1040 *MPa*, similarly concentrated in the boundary region. In contrast, Gyroid and Primitive structures

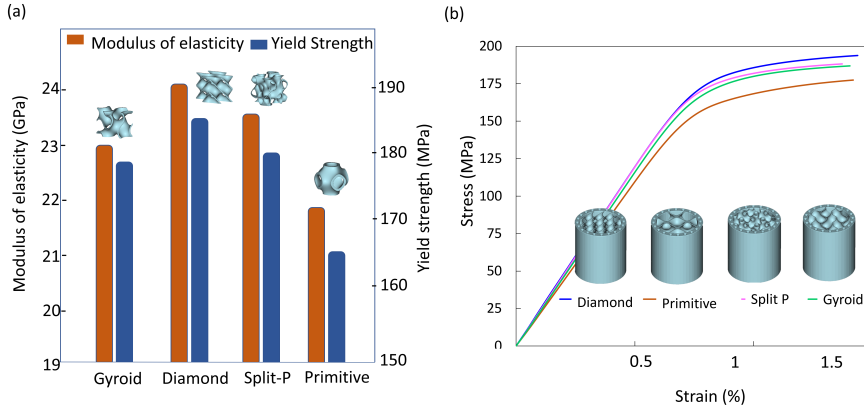


Figure 15: FEA results; (a) elastic modulus and yield strength of four implant designs, (b) stress-strain curve of corresponding implant designs - (adopted from publication II).

show lower stress values of 977 and 947 MPa, respectively, but they still exhibit areas of stress concentration, particularly in the outer layer of the cortical component and the trabecular part. Primitive architecture displays more pronounced concentration. For all designs, regions near the boundary conditions exhibit areas with high-stress levels. Stress transitions appear smoother in the Diamond and Split-P designs, with the Gyroid showing some stress concentration, and the Primitive structure displaying more regions of high stress.

The smoother stress transition across the entire model corresponds to the desired load transfer and can enhance load-bearing capacity. Among the four designs, the Diamond and Split P designs demonstrate superior efficiency, higher stiffness, and strength, followed by Gyroid. Primitive design displays the least uniformity in stress distribution. The structure with Gyroid interior design, stress concentration is observed in certain areas of the outer layer of the cortical part and the layers within the trabecular part. In the Primitive design, most stress concentration occurs in the neck and the connection region of unit cells. This phenomenon don not observe in the other designs. Within the TPMS structures, stress transfer tends to be smoother than in strut-based lattice structures due to the absence of sharp edges. In all structures, certain areas do not contribute significantly in load-bearing, and these regions are more pronounced in the Split-P, Diamond, and Gyroid designs than in Primitive one. High-stress areas are usually more susceptible to crack initiation or debonding. Split-P and Diamond designs exhibits better properties in terms of fracture or yield, while the Primitive design shows lower efficiency.

### 3.3 Split-P lattices and their structural advantages

Split-P is one of the TPMS structures. This lattice structure was found as a structure with maximum energy absorption capacity and higher mechanical strength [89], maintaining a high strength to flexibility ratio [90]. Optimized Split-P lattices are also found to be effective in providing the greatest cell growth and can be one of the best candidates for bone scaffolding among other types of TPMS due to its pore size, high SA/VR, and high local curvature [66]. In terms of SA and SA/VR, Split-P lattice provides the largest amount



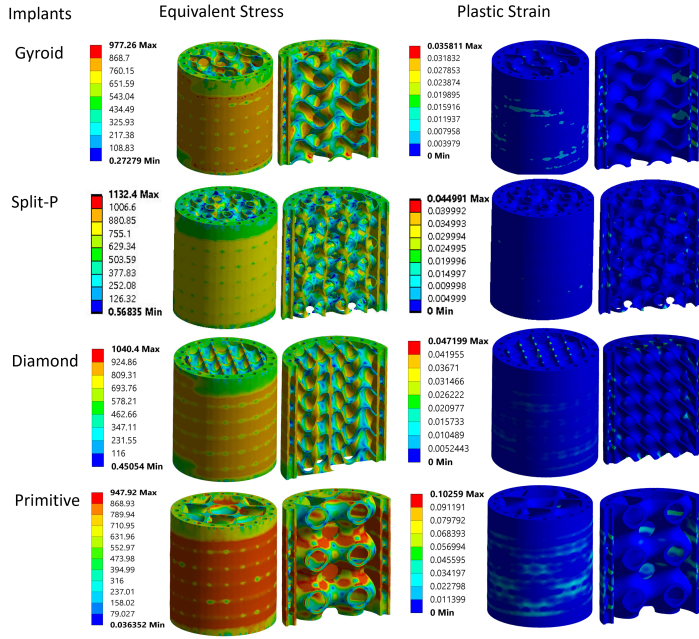


Figure 16: von Mises stress and plastic strain distribution in the four whole implant designs - (adopted from publication II).

among other TPMS with the same CAD parameters like design space of 25 mm in  $X$ ,  $Y$ , and  $Z$  directions, the unit cell size of 12.5 mm, and an isovalue of 0 resulting in the same RD of 20% for all lattice. Figure 17 shows a comparison between these two parameters for four types of TPMS.

An extensive SA encourages cell attachment and growth, while a larger pore size enhances the implant's permeability, influencing the ingrowth of bone. Hence, the SA and pore size of implants constitute vital biological factors [91]. A reduced porosity hampers bone development, whereas higher porosity promotes it. The optimal pore size for fostering new bone formation falls within the range of 100–300  $\mu\text{m}$  [92]. In comparison to other TPMS, Split-P lattices, as indicated in Fig. 17, exhibit notably higher SA and exhibit a wide range of pore sizes and shapes, exemplified in Fig. 18, offering different cross-sectional views of the SP05U140 lattice structure.

Adjusting the pore size can be achieved by scaling the unit cell size and thickness, allowing it to fall within the desired range for promoting bone growth. Consequently, the fine-tuning of structural parameters, such as unit cell size and isovalue, plays a pivotal role in managing SA while preserving mechanical integrity.

### 3.3.1 Geometrical analysis of fabricated lattices

Detailed specifications regarding the geometrical aspects of the manufactured samples and CAD models can be found in Table 11.

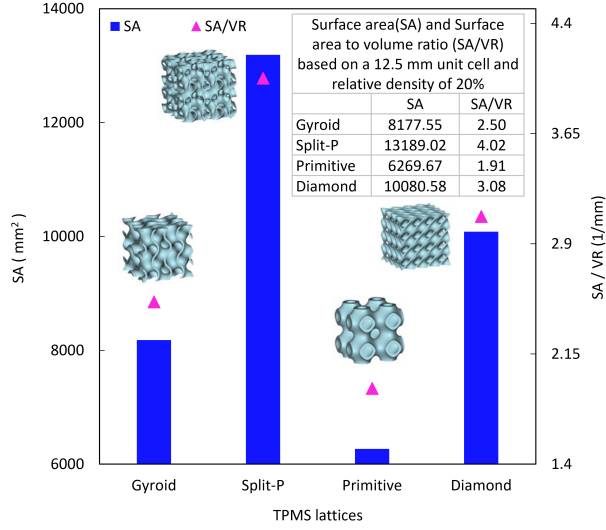


Figure 17: Comparison of SA and SA/VR of four types of TPMS with constant design spaces of 25 mm in X, Y, Z directions, unit cell sizes of 12.5 mm, and in the same RD of 20% - (unpublished image).

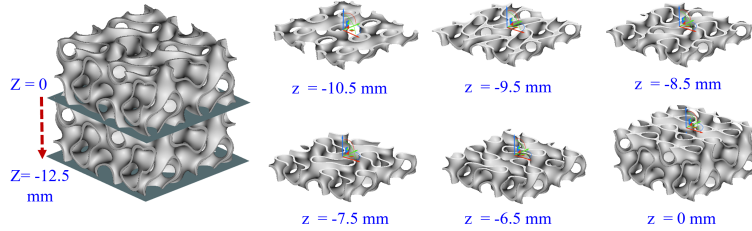


Figure 18: Diverse pore shapes and sizes along the Z-axis observed at various cross-sectional views of the Split-P lattice with the specific SP05U140 morphology developed in this study-(adopted from publication III).

Table 11: Comparison of the geometrical parameters such as weight and RD of the fabricated Split-P lattices with CAD models.

Design	Weight (gr)			RD (%)			SA (mm <sup>2</sup> )	SA/VR (1/mm)	Porosity (%)
	Actual	CAD	Relative error(%)	Actual	CAD	Relative error(%)	CAD	CAD	CAD
SP025U125	9.72 ± 0.00	6.91	25.90	14.13	10.48	34.89	12823.17	7.83	89.52
SP04U125	13.99 ± 0.01	11.04	26.72	20.33	16.74	21.44	13115.03	5.01	83.26
SP06U125	18.02 ± 0.04	16.61	8.53	26.00	25.19	3.22	13144.44	3.34	74.81
SP06U125Iso1	16.42 ± 0.02	13.84	18.64	23.86	21.00	13.67	11548.69	3.52	79.00
SP05U140	16.55 ± 0.10	13.16	20.48	23.00	21.00	9.25	12018.47	3.85	79.00

The present investigation highlights variations in RD between the Split-P lattice structures as built and their corresponding CAD models. As-built Split-P lattices were weighed using a dry weighing method and their solid density was measured using an Archimedes

method. Table 11 compares the geometrical parameters such as weight and RD between the fabricated Split-P lattices and CAD models. The observed variations are possibly due to the presence of un-melted powder particles that have adhered to the lattice surfaces, leading to an increase in surface roughness. It's worth noting that the Split-P lattice, as depicted in Fig. 17, possesses the most extensive SA among other TPMS like Gyroid, Diamond, and Primitive TPMS structures. This enlarged SA intensifies the interactions between the unconsolidated powder particles and the solidifying base materials [93]. Consequently, in Split-P structures, partially molten metal powder particles clinging to the specimen's surface may influence the RD measurements, as reported in a prior study [91]. Blockage-free samples affirm the SLM process's competence in fabricating Split-P TPMS lattices. With considering three lattices with the same morphology and different RD (SPo6U125, SPo4U125, and SPo25U125) from Table11, the relationship between the intended and observed RD can be established as illustrated in Fig. 19.

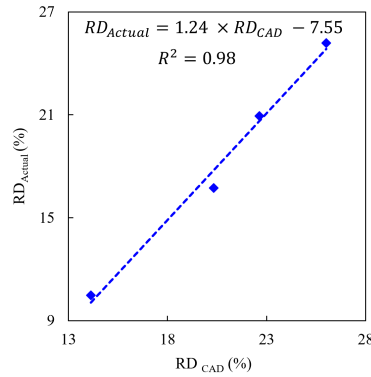


Figure 19: CAD to actual (fabricated) RD correlation of Split-P lattices at an isovalue of 0 - (**adopted from publication III**).

Empirical findings demonstrate that there is a strong alignment between the actual RD values and the CAD designs, with a high coefficient of determination ( $R^2$ ) of 0.98. This correlation can thus serve as a valuable guideline for designing Split-P lattice structures.

### 3.3.2 Manufacturability of Split-P TPMS

Split-P structures inherently incorporate overhanging sections, which can potentially result in issues such as layer collapse, dross formation, and printing challenges. Therefore, it may be necessary to employ support structures to ensure successful printing and reduce disparities in shape between the manufactured samples and the CAD models [94]. With providing support structures the printability of Split-P TPMS lattice can be guaranteed as Fig. 20 illustrates.

As can be seen, large dimensions of the unit cell, minimizing wall thickness, and in the specific porosity of the lattice, there's an elevated concern about unsupported regions in the air, potentially leading to a failed 3D printing process. Hence, it is essential to incorporate suitable support structures into the lattice design. another approach to address this issue is by increasing the lattice's thickness reaching the desired RD, which effectively bridges the suspended sections, allowing the Split-P lattice to become self-supporting. Nevertheless, the SLM-ed Ti6Al4V structures in this study exhibited a discrepancy in RD with CAD models ranging from 9% to 34% higher than their corresponding CAD models.

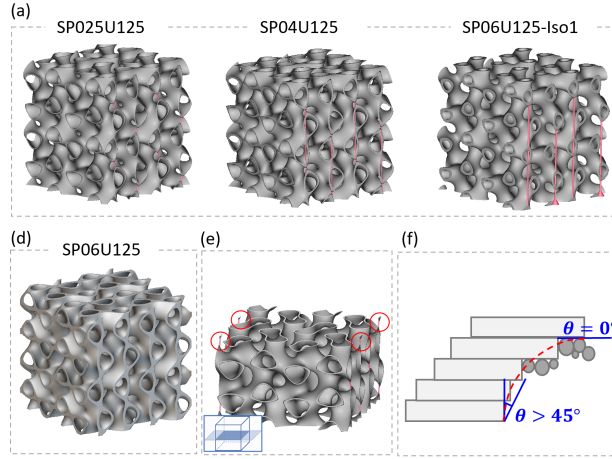


Figure 20: The CAD models of the Split-P lattices and the specific areas requiring additional support to prevent deformation during the additive manufacturing (AM) processes are depicted in (a) SP025U125, (b) SP04U125, (c) SP06U125-Iso1, and (d) SP06U125. (e) a sectional view of the Split-P lattice structure, highlighting regions that do not necessitate self-support. (f) illustration of the overhang area giving rise the possibility of distortion and structural collapse. - (adopted from publication III).

### 3.3.3 Surface morphology of fabricated lattices

The 3D-printed SP04U125 Split-P lattice, produced using SLM, was examined in terms of its surface morphology illustrated in Fig. 21. Multiple locations were chosen to capture images of both the upper and lower surfaces, each designated by distinct colors. These images reveal robust interconnectivity within the manufactured porous lattice. The precision of pore and strut dimensions in the as-built sample is showcased in the sections colored cyan and orange. In comparison to other TPMS or strut-based structures, Split-P provides the largest SA, as indicated in Fig. 17. Moreover, certain areas, marked in green, exhibit partially melted or unmelted powder particles adhering to the surfaces. Publication II provides more details about the other colors.

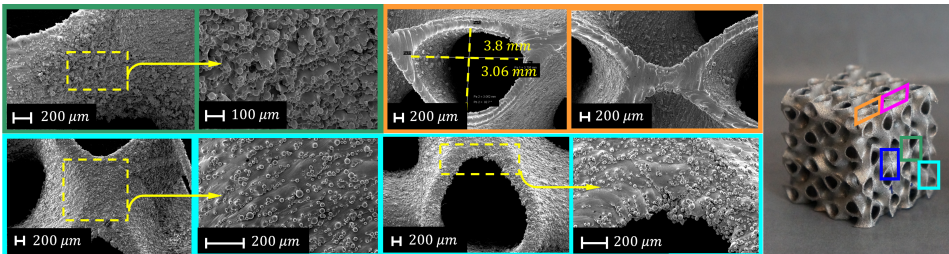


Figure 21: Surface features of SLM-ed Ti6Al4V SP04U125 lattice captured by SEM, representing distinct regions by various colors; Green: the lower surface on the lattice side, Orange: the dimensions of the pores and struts on the top surface, Cyan: lateral surface displaying dross formation and the staircase effect- (adopted from publication III).

### 3.3.4 Morphology effects on the mechanical performance - Experimental results

It is noteworthy that the response characteristics of Split-P lattice structures appear to be consistent with those observed in a majority of other lattice configurations, commonly categorized into four deformation zones as illustrated in Fig. 22 with specifying regions in distinct colors. In the first zone (Region I), there's an initial nonlinear phase at low strain, mainly resulting from the initial misalignment between the lattice and compressive plates. Region II marks the onset of a linear elastic phase, where the slope signifies the material's elastic modulus. This is followed by a post-yield hardening phase, showcasing nonlinear behavior, leading to the attainment of maximum stress ( $\sigma_{l,U}$ ). Region III portrays the plateau stage, characterized by multiple instances of layer collapse and failure. Finally, in Region IV, the densification phase commences, where the compressive response rapidly increases due to the unit cell surfaces coming into contact and the full collapse of unit cells. Fluctuations in stress become noticeable within the plateau region, owing to the collapse of layers and localized densification.

For Split-P lattices with the same RD of 21% and different cell morphology (CM) such as SP05U140 and SP06U125Iso1, marked disparities are visible in the stress-strain profiles of the two lattices after reaching their ultimate strength, underscoring the significant influence of CM on their compressive behavior. In the plateau phase of each lattice, fluctuations occur due to layer collapse and localized densification. Both lattice types exhibit hardening behavior during the plateau phase, followed by rapid increases in stress-strain curves as they approach the end of the plateau stage. For SP05U140, this transition occurs at a compressive strain of approximately 80%, while for SP06U125Iso1, it takes place at around 70%. Figure 22 shows the result of the experimental compression test for all lattice structures under compression test at a strain rate of  $1 \text{ mm/min}$ .

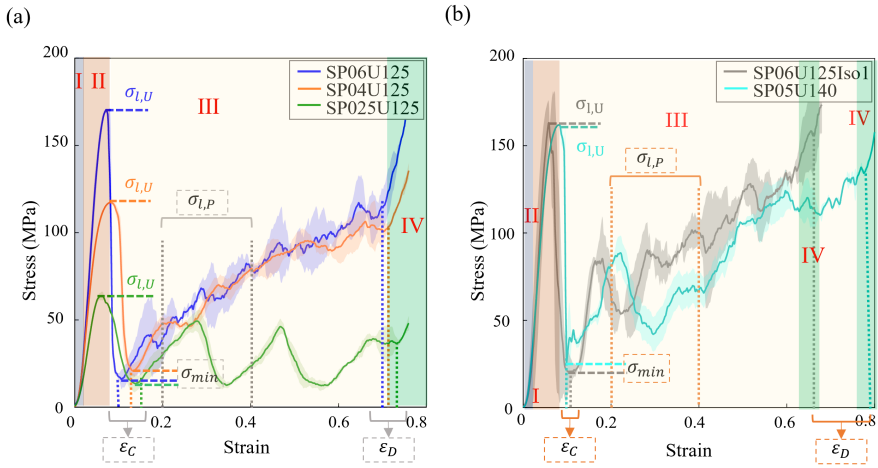


Figure 22: The experimental stress-strain curves of all lattice structures under quasi-static compression at  $1 \text{ mm/min}$  - (adopted from publication III).

In the case of the same lattice configuration with different RD (SP06U125, SP04U125, and SP025U125), the deformation responses in experimental tests from 0% to 50% illustrated the initiation of failure at the uppermost layers of the SP06U125 and SP04U125 lattices, whereas, for SP025U125, failure commences in the lower layers. During the initial elastic stage, the specimens undergo uniform deformation. As the compressive load

increases, the stress-strain curves ascend until they reach their peak strength, typically around 10% strain. Subsequently, cracks begin to emerge, giving way to the formation of shear bands, and these continue to propagate until eventual failure. In the cases of SP06U125 and SP04U125, shear band failure is conspicuous, extending from the upper right corner to the middle of the lower left side, and this failure mode becomes more pronounced with higher RD. SP025U125, on the other hand, exhibits a layer-by-layer failure pattern, starting with the last layer. After the last layer's failure, subsequent layers gradually make contact. Notably, SP025U125 does not demonstrate a strain-hardening effect throughout the deformation process. The initial collapse of each lattice structure occurs within the strain range of 10% to 13%.

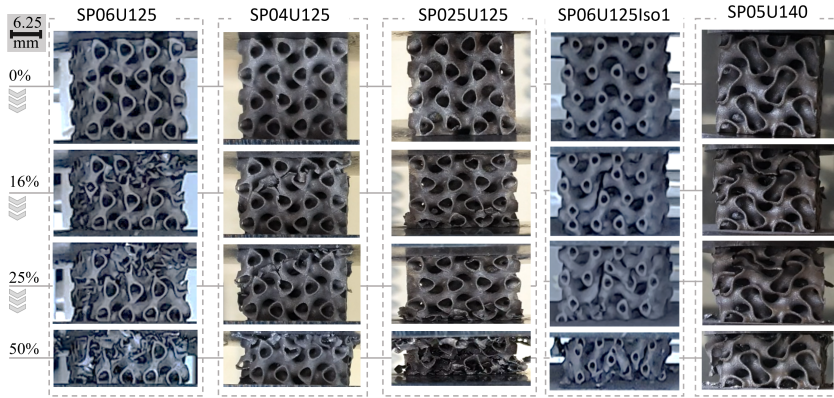


Figure 23: Illustration of failure modes of SLM-ed Ti6Al4V Split-P lattice structure under compression test up to 50% strain at a strain rate of 1 mm/min - (adopted from publication III).

Distinct deformation patterns can be observed from the experimental tests for all samples in Fig. 23. The first failure instances corresponded to the initial layer collapses. Each lattice exhibits different failure behaviors: SP06U125, SP04U125 shows shear failure and layer by layer failure is observed for SP025U125 and SP05U140 starting from lowermost and uppermost layers respectively. And finally, SP06U125Iso1 demonstrates complete shear failure, occurring at an angle of 45 degrees to the load direction. This behavior is linked to the observable interconnected pores and connection points within the lattice structure. These connection sites exhibit high levels of normal and shear stress concentration, thus increasing the likelihood of failure.

Table 12, listed all mechanical properties of tested Split-P lattices such as the modulus of elasticity ( $E$ ), yield strength ( $\sigma_{l,Y}$ ), ultimate strength ( $\sigma_{l,U}$ ), the first lowest stress value after the first plastic failure ( $\sigma_{min}$ ), the load-bearing capacity ( $K$ ), collapse strain ( $\epsilon_C$ ), and densification strain ( $\epsilon_D$ ) under compression tests.

Table 12: Parameters of 3D-printed Split-P cellular lattice by SLM

Lattices	$E$ (GPa)	$\sigma_{l,Y}$ (MPa)	$\sigma_{l,U}$ (MPa)	$\sigma_{l,P}$ (MPa)	$\sigma_{min}$ (MPa)	$K$ (%)	$\epsilon_C$ (%)	$\epsilon_D$ (%)
SP06U125	3.48±0.14	152.74±0.01	170.47±0.67	30.16±2.4	15.14±4.9	0.08±0.02	11.22±0.99	70.19±0.65
SP04U125	2.50±0.12	83.19±1.26	117.32±0.48	59.93±1.50	20.65±3.76	0.17±0.03	13.29±0.38	70.70±0.96
SP025U125	1.55±0.18	57.95±3.60	93.93±2.26	61.32±8.84	13.25±0.96	0.16±0.00	13.87±0.05	68.03±2.15
SP05U140	3.48±0.07	116.02±2.05	137.15±0.79	63.21±0.21	12.81±8.05	0.09±0.05	10.44±1.15	62.38±1.87
SP06U125Iso1	2.63±0.00	100.88±5.03	129.59±0.19	50.31±7.55	5.6±0.14	0.04±0.00	9.76±0.16	77.91±0.67

As a result, Porous scaffolds exhibit distinct responses to compressive loads, and their



behavior depends on various morphological factors, including porosity and the shapes of their pores [95]. The stress-strain reactions of cellular lattices experience a pronounced decline following the initial peak strength, attributed to the collapse of wall elements and the fracture of load-bearing struts. This behavior is typically associated with a brittle failure of struts in Ti6Al4V lattices manufactured through SLM [96]. The substantial drop in stress is observable for all lattice structures upon reaching the ultimate strength, an occurrence influenced by the RD. These initial sharp reductions take place at approximately 7%, 10%, and 6% compressive strains for SP06U125, SP04U125, and SP025U125, respectively.

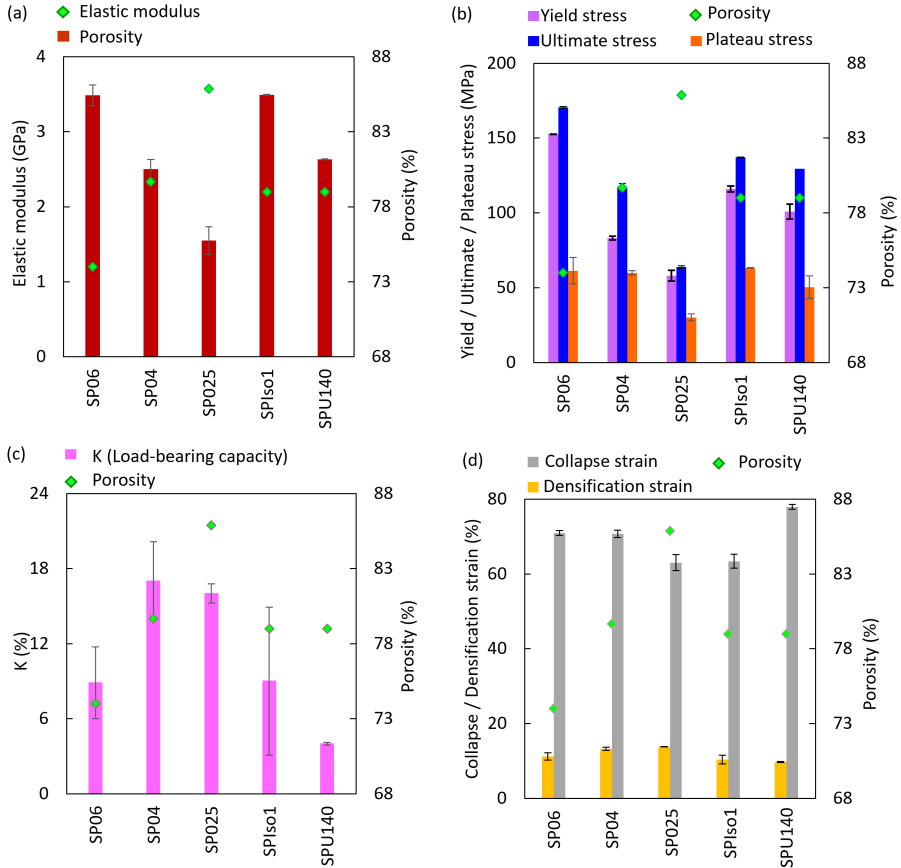


Figure 24: Evaluating the mechanical characteristics of Split-P lattices relative to porosity; including SP06 (SP06U125), SP04 (SP04U125), SP025 (SP025U125), SP1so1 (SP06U125Iso1), and SP140 (SP05U145), considering aspects such as (a) Elastic modulus, (b) Yield, ultimate, and plateau stress, (c) Load-bearing capacity ( $K$ ), and (d) Collapse and densification strain. - (adopted from publication III).

The load-bearing capacity (referred as  $K$ ) of lattice structures is significantly influenced by their morphology and RD [97]. It hinges on the first recorded minimum stress value following the initial plastic failure and the ultimate stress. Among the lattice configurations, SP06U125 exhibited the minimum load-bearing capacity. In contrast, SP025U125 and SP04U125 showcased the highest load-bearing capacities, surpassing that of SP06U125 by nearly 50%. The compressive behavior of Split-P lattices suggests that lattices with lower porosity can mimic the properties of a solid block, resulting in heightened shear

stresses and a reduced load-bearing capacity, according to findings in [97]. Consequently, the lattice's RD can significantly influence its load-bearing performance. Table 12 reveals the considerable impact of CM on mechanical properties. Despite having a lower RD than SP06U125, SP06U125Iso1 displays a higher elastic modulus and strain collapse, with nearly identical load-bearing capacity. SP05U140 and SP04U125 exhibit nearly identical elastic moduli, despite a 13% RD difference, with SP04U125 exhibiting lower RD. SP06U125Iso1 surpasses SP04U125 in terms of yield strength, ultimate strength, and load-bearing capacity. Among the five lattices, SP025U125 and SP06U125 showcase the lowest and highest elastic moduli, yield strengths, and ultimate strengths. The load-bearing capacity is at its peak for SP04U125 and is the lowest for SP05U140.

Within the plateau region, all lattice structures display stress values below the ultimate strength, signifying that the majority of energy is dissipated during the initial failure. However, comparing the stress-strain profiles of different lattices reveals that the plateau region exhibits strain hardening, featuring an undulating growth of stress attributable to the densification stage. The layer-by-layer failure mode, observed in lattices with lower RD, introduces noticeable stress fluctuations during the plateau phase. These fluctuations are primarily caused by individual layer failures and the buckling of local unit cells. For SP06U125 and SP04U125, the plateau region exhibits some strain hardening, with stress displaying undulating growth up to the densification stage. Conversely, SP025U125 demonstrates substantial fluctuations, marked by four distinct stress fluctuations. The deformation behavior of SP025U125 highlights layer-by-layer collapse. However, all specimens reach densification at the end of the plateau stage, resulting in an upward trend in stress-strain profiles and reaching their initial peaks. As the lattice structure becomes denser by the end of the plateau, the stress-strain behavior displays a rising trend. A denser lattice structure exhibits a sharp increase in the elastic region, indicative of a high elastic modulus, substantial yield strength, and an extensive plateau region.

It can be concluded that unit cell morphology, thickness, and thus, RD exert a strong influence on failure mechanisms, with denser structures displaying reduced fluctuations in stress-strain profiles and a more uniform response, behaving akin to compact materials. Consequently, the lattice's architectural design determines the failure mechanisms it undergoes [98]. Low RD leads to layer-by-layer failure, while high RD structures exhibit shear band formation, as reported in [99]. Additionally, it was observed that Split-P TPMS lattices exhibit both stretching and shearing in certain areas due to their intricate shapes, and the designed RD also affects the failure behavior. Figure 24 illustrated a comparison of mechanical properties of Split-P lattice structures versus porosity.

As it is obvious in Fig 24, SP025U125 displays the lower mechanical characteristics, encompassing the elastic modulus, yield stress, ultimate stress, and plateau stress while surprisingly, its load-bearing capacity ranks among the highest. Altering unit cell size and isovalue induces substantial shifts in mechanical properties [96]. A comparison between SP06U125 and SP06U125Iso1 reveals that a mere 5% increase in porosity for SP06U125Iso1 yields an identical elastic modulus but results in diminished yield stress and ultimate stress. Both lattices exhibit almost identical plateau stress values.

Moving to SP04U125 and SP05U140, these two possess nearly the same elastic modulus, although the porosity of SP04U125 exceeds that of SP05U140 by 4%. However, the yield stress and ultimate stress of SP05U140 surpass those of SP04U125. As a result, SP05U140 features the lowest plateau stress value, whereas SP04U125 demonstrates the highest load-bearing capacity within the entire spectrum of Split-P lattices. On the contrary, SP05U140 exhibits the lowest load-bearing capacity. The maximum collapse strains are evident in SP025U125, which can also be attributed to its exceptional load-bearing ca-



capacity. In summary, unit cell morphology possesses a significant influence over mechanical properties.

At last, from the results obtained from the mechanical tests of three fabricated lattice structures of SPO6U125, SPO4U125, and SPO25U125. The Gibson-Ashby model applied to the tested samples illustrating the relationship between RD and the predicted mechanical properties such as modulus of elasticity and yield strength of the structures in Fig. 25. The relative modulus of elasticity and relative yield strength exhibit a positive correlation with the actual RD of the Split-P lattices. The Gibson-Ashby model's characteristic parameters and their corresponding correlation coefficient  $R^2$  are as follows:  $C_1 = 0.04$ ,  $n_1 = 1.32$ ,  $R^2 = 0.99$  for the modulus of elasticity, and  $C_2 = 0.91$ ,  $n_2 = 1.54$ ,  $R^2 = 0.99$  for yield strength. Notably, both the modulus of elasticity and the strength of these structures experience exponential growth as RD increases. The robust fitting coefficients, represented by the high  $R^2$  values, underscore the precision and accuracy of this adaptation. Consequently, it is possible to directly anticipate the real mechanical characteristics of 3D printed Ti6Al4V Split-P TPMS lattices based on their structural parameters ( $C, n$ ). For Split-P lattices, when the modulus is represented as a function of RD, the stretching deformation behavior becomes increasingly conspicuous as the curve approaches a linear trend [100]. For lattices with identical RD, those featuring stretching-dominated deformation modes demonstrate elevated elastic modulus and strength, rendering them particularly attractive for applications requiring lightweight structures, such as orthopedic implants [101].

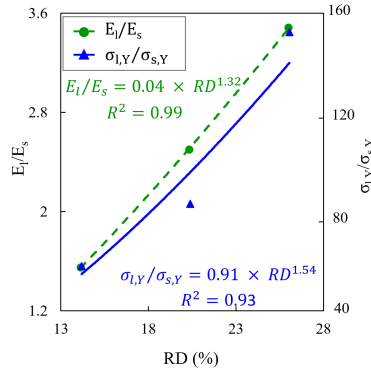


Figure 25: The Gibson Ashby model fitted as a function of the relative elastic modulus and the relative yield strength of SLM-ed SPO6U125, SPO4U125, and SPO25U125 lattices - (adopted from publication III).

### 3.3.5 Morphology effects on the mechanical performance - Numerical results

**3.3.5.1 Unit cell analysis:** In all Split-P unit cells, effective load-bearing capacity and stress transfer were found due to uniform stress distribution across their surfaces. However, in the case of SPO5U125Iso1, stress levels increase at the strut connection points aligned with the load direction, highlighting the potential effectiveness of solid network Split-P lattices in bearing loads. Unit cells with varying RD and morphologies exhibit yield behavior at different levels of strain. The contour map of equivalent plastic strain, depicted in Figure 26, reveals regions with a heightened potential for failure. SPO5U125Iso demonstrates the most localized plastic deformation at the strut connection sites. For SPO25U125, areas of substantial plastic deformation are observed in the uppermost and

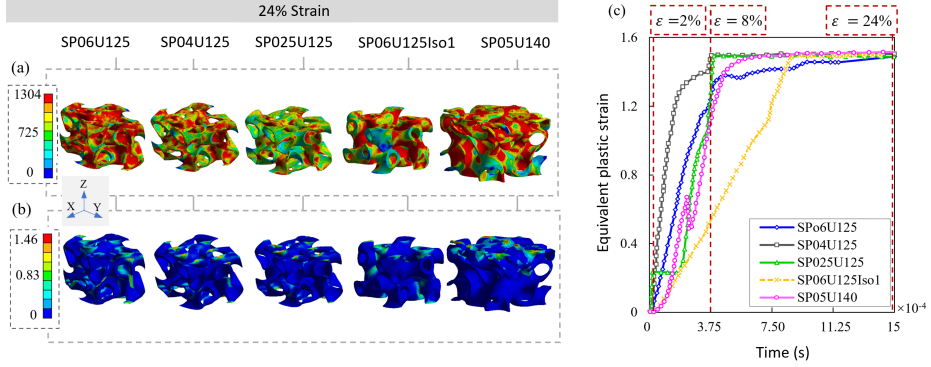


Figure 26: Illustration of numerical simulation of a) von Mises stress and b) equivalent plastic strain, c) demonstration of equivalent plastic strain versus time of the unit cells of proposed Split-P lattices under compression test at a strain of 24%. -(adopted from publication III).

lowermost layers. At a strain of 2%, the connection regions of SP06U125, SP04U125, and SP025U125 exhibit signs of plasticity, while no significant plastic deformation is evident in the middle layers. Similarly, SP05U140 displays plastic deformation commencing in the uppermost layers.

As evident from the strain-time curves depicted in Fig. 26, all lattices exhibit a progressive increase in plastic behavior up to a strain of 2%. At this 2% strain point, a distinctive failure mode is observed in SP025U125, signifying that the first layer (the bottom layer) reaches its yield point. Subsequently, plastic strain uniformly spreads within the unit cell, encompassing the second layer. For all lattices, there is a continuous rise in plastic strain within the range of 2% to 8%, with the exception of SP05U140. In the case of SP05U140, there is a noticeable dip in the curve, indicating the failure of the first layer (the top layer). Among all the lattices, SP05U125Iso displays the shallowest slope at an 8% strain, implying that it requires a longer duration to reach the yield point. Notably, SP04U125 attains a high level of plastic strain at approximately 3.75e-4 seconds, closely followed by SP025U125. Meanwhile, SP06U125 reaches a high level of plasticity around 15e-4 seconds, and SP05U140 and SP06U125Iso1 exhibit their maximum plasticity at approximately 6e-4 and 8e-4 seconds, respectively.

**3.3.5.2 Lattice structure analysis:** Figure 27 and 28 present the outcomes of numerical simulations for Split-P TPMS lattice structures representing VonMises stress distributions and equivalent plastic strains at overall strains of 0%, 16%, and 20% are showcased. The distributions of vonMises stress display significant stress concentrations in the layers and connection sites, contingent on the lattice type. The ultimate stress is more prominently concentrated in the upper and lower layers of SP025U125 and SP04U125. In SP06U125, the upper layers exhibit higher stress levels than the lower layers, ultimately leading to the primary failure. Within SP05U140, regions of stress concentration in both the top and bottom layers are unmistakably visible, with additional stress concentration observed in the middle layers as shown in Fig. 28.

For SP06U125Iso1, heightened stress levels are detected in the middle of connection struts. As the strain increases during compression, more stress concentrates within the lattice, ultimately resulting in fractures. The fracture may propagate between layers as the stress concentration region shifts from one layer to the next. In terms of equivalent plastic

strain distributions, as shown in Figures 13 and 14, the majority of plastic deformations occur in the uppermost layers, contributing to the initial collapse of SP06U125, SP04U125, and the lower layers in SP025U125.

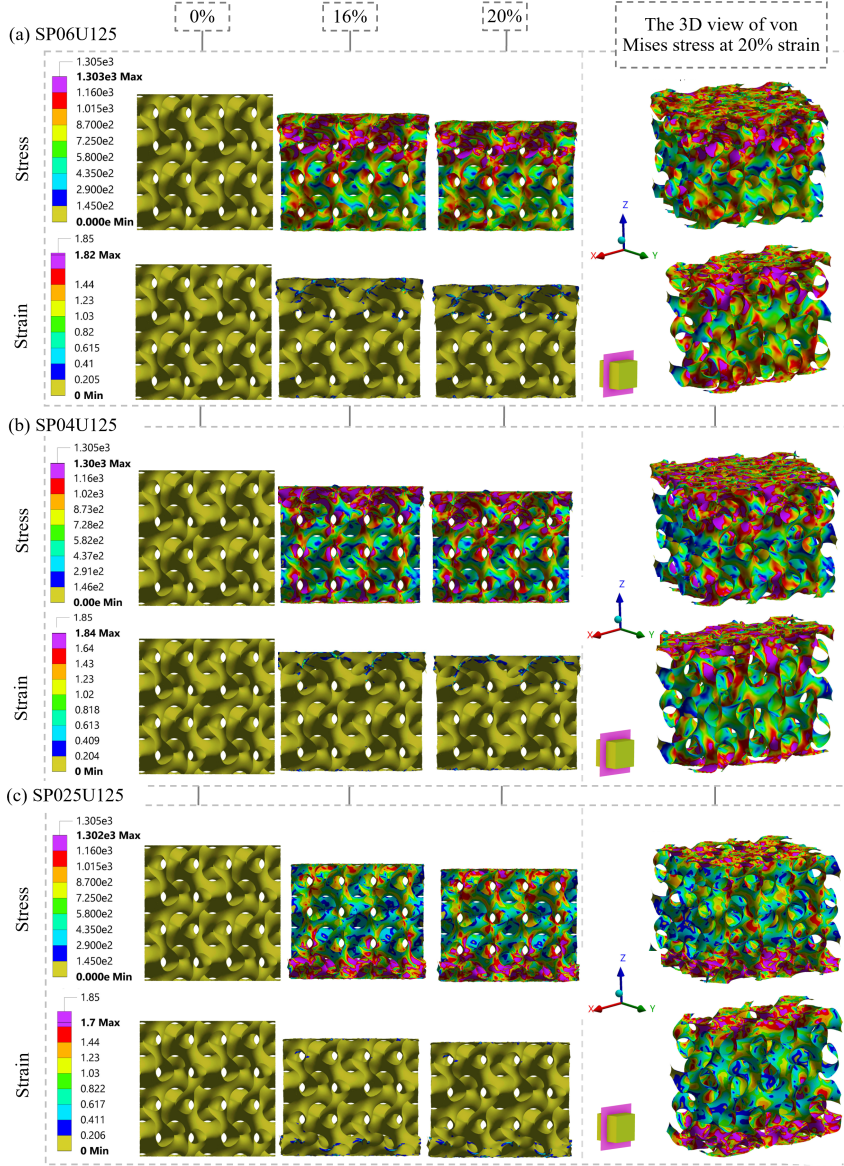


Figure 27: Distributed equivalent stress and plastic strain of Split-P lattices for strain levels of 0%, 16%, and 20%, and depictions of vonMises stress distributions at 20% strain; (a) SP06U125, (b) SP04U125, (c) SP025U125 *-(adopted from publication III)*.

Nonetheless, several indications of plasticity are also observed in the middle layers of SP05U140 lattices. For SP025U125, the bottom layer reaches plasticity first, followed by a uniform increase in plastic strain within the lattices, extending to the second layer.

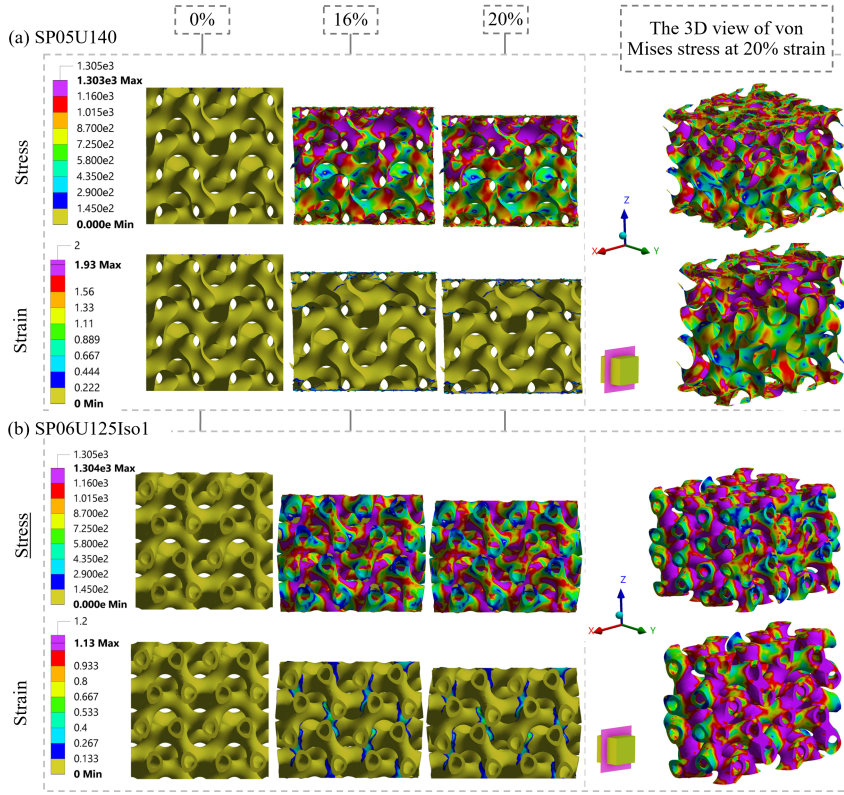


Figure 28: Distributed equivalent stress and plastic strain of Split-P lattices in strain levels of 0%, 16%, and 20%, and depictions of vonMises stress distributions at 20% strain; (a) SP05U140, and (b) SP06U125Iso1 -(adopted from publication III).

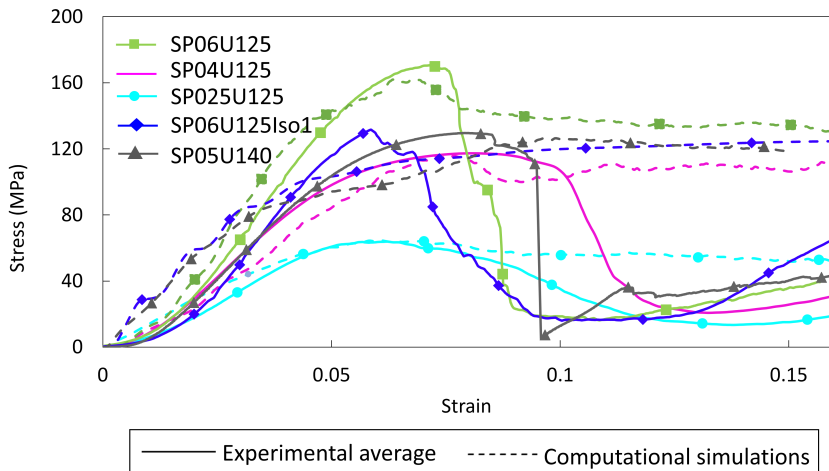


Figure 29: Illustration of the numerical and experimental stress-strain behaviors of all Split-P lattice structures at 16% strain. -(adopted from publication III).

In the case of SP06U125Iso1, most strut joints exhibit localized deformation, heightening the potential for collapse. Shell elements were employed for numerical simulations in all lattices except SP06U125Iso1. The use of shell elements in numerical simulations offers time-saving advantages, primarily due to a reduced number of elements [102]. The reliability of the FE method in predicting mechanical properties, specifically the elastic modulus and yield strength, was evaluated through the relative error between numerical simulations and experimental results, as depicted in Fig. 29.

### 3.3.6 Morphology effects on the energy absorption capacity

Figure 30 displays a comparison of energy absorption concerning RD and compressive strain for various Split-P lattice configurations. Notably, the SP06U125 lattice shows the highest value at  $61.41 \pm 2.52 \text{ MJ/m}^3$ , while SP025U12 records the lowest one at  $22.82 \pm 0.86 \text{ MJ/m}^3$ . In Fig. 30, it is evident that SP06U125 exhibits roughly 2.7 times the energy absorption capacity compared to SP025U125. This underscores the pronounced impact of RD on the lattices' energy absorption capacities. A comparison between SP05U140 and SP06U125Iso1 demonstrates that, with comparable RD values, SP05U140 displays a higher energy absorption ( $57.35 \pm 2.52 \text{ MJ/m}^3$ ), nearly matching that of SP04U125 ( $58.22 \pm 0.69 \text{ MJ/m}^3$ ), which has an RD of approximately 26%. This suggests that the unit CM significantly influences the energy absorption potential. Interestingly, SP05U140 exhibits nearly equivalent energy absorption to SP06U125Iso1, despite its lower density. In Fig. 30, the energy absorption curves for all Split-P lattices are depicted versus strain. These curves display a consistent and linear growth pattern, except for SP025U125, which shows fluctuations attributable to layer collapse.

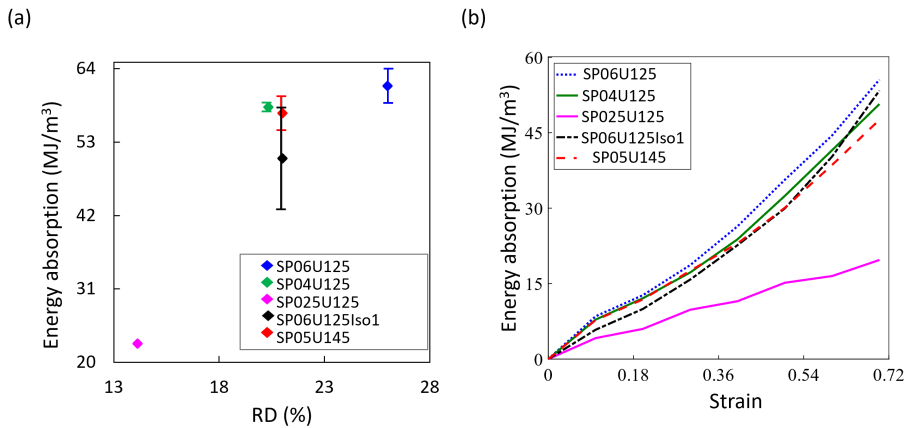


Figure 30: Split-P lattices' energy absorption in response to compression load in different RD and strains; (a) Total energy absorption at various RD; (b) Strain-dependent energy absorption - (**adopted from publication III**).

Energy absorption capacity is a crucial characteristic in the design of orthopedic structures [66]. Several parameters, including RD, pore size, unit cell size, and unit cell type, influence this property. Among all of these factors, RD showed a significant role [20]. An effective lattice structure for energy absorption should be capable of enduring substantial deformations under relatively constant stress, thereby preventing the lattice from being



subjected to excessive strain [67]. This endurance ensures the structure's long-term resilience and its ability to withstand impact loads [68]. As demonstrated in the comparative mechanical responses shown in Fig. 22 illustrates a gradual increase in energy absorption capacity with rising RD. The primary factors influencing a lattice structure's energy absorption characteristics are its plateau stress and densification strain; higher and more prolonged plateau stress enhances energy absorption [69].

In the current study, it was observed that SP06U125, SP04U125, and SP06U125Iso1 exhibited high energy absorption, attributed to their substantial densification strain and plateau stress. Consequently, these lattices exhibit potential for applications requiring energy absorption. Energy absorption capacity of the lattice structures falls within a range of 22.82 to 61.41  $MJ/m^3$ .

### 3.3.7 Anisotropy comparison of Split-P lattices

In various applications, it is crucial to grasp the anisotropic nature of a structure and pinpoint its most rigid and flexible orientations. Particularly in structural uses like load-bearing implants, this anisotropy significantly influences the lattice's performance in diverse orientations [103].

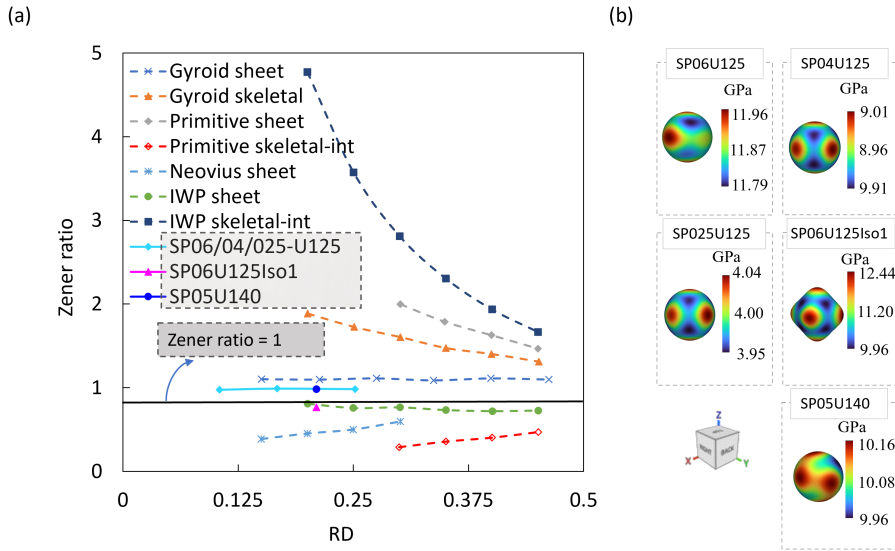


Figure 31: (a) Comparison of Zener anisotropy index of Split-P lattices with TPMS unit cells with different RDs, (b) Split-P 3-dimensional elastic modulus surface - (adopted from publication III).

Therefore, achieving a precise assessment of the effective elastic properties is of paramount importance. The Zener ratio ( $Z$ ) describes isotropic material behavior and  $Z = 1$  indicates an isotropic material behavior [104, 105]. 3D elastic modulus surface is visually illustrated in Fig. 31 and represents the degree of anisotropy. Notably, SP06U125Iso1 exhibits the most pronounced anisotropy, evident in its conspicuous protrusion in X, Y, and Z directions. Conversely, the remaining Split-P lattice configurations display nearly isotropic moduli. The illustration in Fig. 31 Zener ratio of SP06U125, SP04U125, SP025U125, and SP05U140 lattices exhibited corresponding Zener ratios at 0.97, 0.99, and 0.98 respectively, suggesting a uniformity in their

elastic characteristics. However, the Zener ratio for SPO6U125Iso1 is notably lower at 0.75, indicating a degree of anisotropy in the lattice's mechanical properties. Among all, the SPO4U125 lattice stands out with the highest Zener ratio, indicating a remarkable degree of isotropy, closely approaching unity.

### 3.4 Voronoi-based HA scaffold

#### 3.4.1 Morphology effects on architectural features

SA and SA/VR represent pivotal geometric characteristics, particularly in the context of applications such as bone replacements, where they exert significant influence over both the scaffold's biological and mechanical performance [106]. These two factors directly impact various essential aspects, including growth factors, nutrient exchange, and the interactions among cells and the scaffold. Additionally, the SA/VR plays a key role in enhancing fluid permeability [65]. A higher SA/VR indicates more favorable conditions for cell growth and attachment, as well as enhancing collisions between oxygen molecules and cells, leading to better transportation within the scaffold and improving delivery to cells [69]. A gradient mode's impact on SA and SA/VR for IVL scaffolds cannot be ignored in their design. The highest percentage enhancements compared to the PC-TC lattice were observed in the PG-TG lattice for both SA and SA/VR about 38.49% and 40.00% followed by PG-TC with the values of 36.28% and 36.40% respectively. The minimum percentage enhancements recorded for PC-TG lattice. Figure 32 shows the values of SA and SA/VR and the percentage improvements for four designed HA IVL scaffolds.

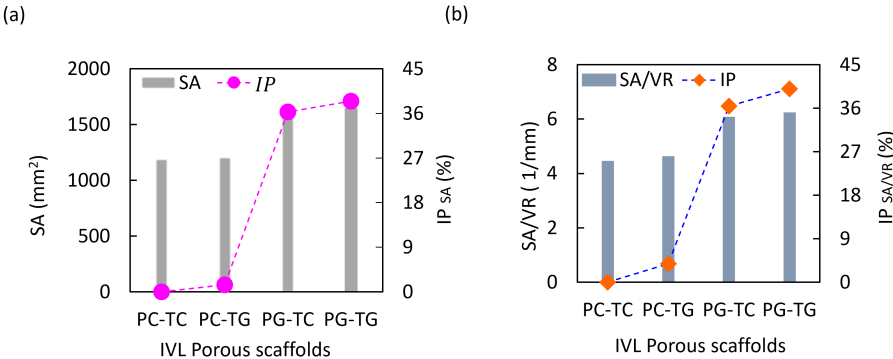


Figure 32: Graphical representation of a)SA and b)SA/VR of four designed IVL scaffolds and their percentage improvements in comparison with TC-PC lattice scaffold - (Adopted from publication IV).

The results showed that in lattices with constant PS, transitioning from a constant ST to a gradient mode (GT) yields relatively modest increases in SA and SA/VR. Conversely, when switching from a constant PS to the gradient mode, scaffolds with constant ST exhibit substantially greater enhancements of a remarkable increase in SA and a boost in SA/VR. Furthermore, with gradient ST, these enhancements escalate. The results, as depicted in 32, clearly indicated that the scaffold featuring both gradient PS and ST experiences the most significant improvements in SA and SA/VR, while the scaffold with constant PS and gradient ST registers the smallest enhancements. An exploration into the effect of

irregularity on the pore size, shape, and distribution, studies show that the largest pore size promoted an increased in vitro cell proliferation and in the trabecular part of bone based on an IVL structure design, pore size would be in the range of 458.80 - 989.10  $\mu\text{m}$  is desirable [107] and also ideal pore size for simulating cell proliferation and differentiation lying within the span of 20-1200  $\mu\text{m}$  was reported in [57, 108].

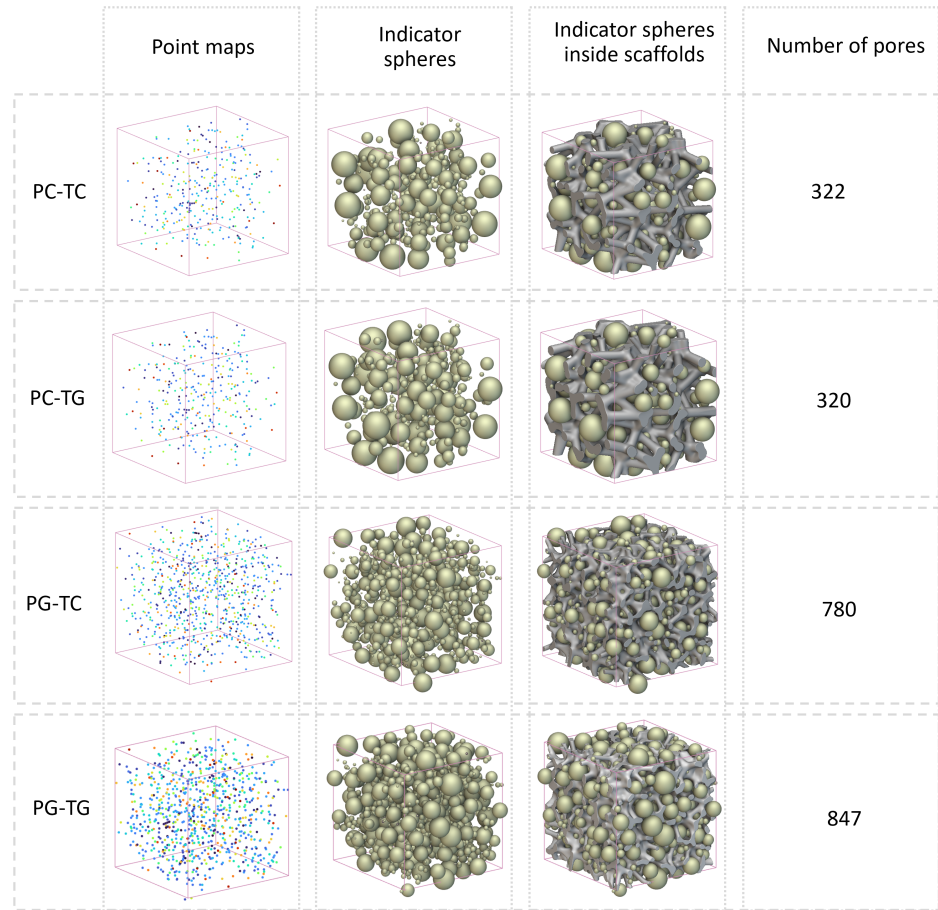


Figure 33: Assembly of point maps and indicator spheres, as well as the number of pores within four designed IVL scaffolds- **(adopted from publication IV)**.

Consequently, it is imperative that pore size distributions encompass a variety of ranges. As illustrated in Fig. 33, the scaffolds in this study exhibit a diverse range of sizes, numbers, and distributions, rendering them suitable for bone replacement applications. Figure 34 revealed the range of pore size within each scaffold. The PG-TG scaffold boasts the highest pore count at 847, characterized by gradient PS and ST, closely followed by the PG-TC scaffold with 780 pores. In contrast, the PC-TG lattice exhibits the lowest pore count at 320, with the PC-TC lattice not far behind at 322 pores. Interestingly, both Fig. 33 and Fig. 34 reveal that the incorporation of a gradient approach in IVL structure design results in an augmentation of the number of pores, particularly those falling within the desirable size range akin to human bone. It becomes evident that applying a gradient approach to both PS and ST contributes to an increased prevalence of pores within the desired size range,



consequently enhancing both SA and SA/VR, critical factors for promoting bone growth and cell adhesion.

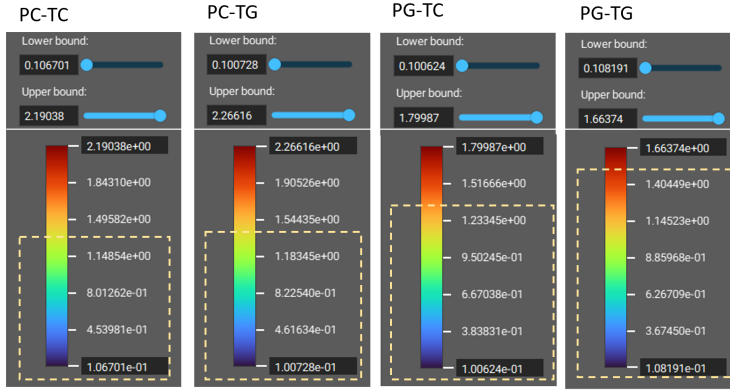


Figure 34: An illustration showing the two lower and upper bands of pore size in IVL scaffolds; Dimensions in (mm) - (adopted from publication IV).

### 3.4.2 Morphology effects on mechanical performance

HA Voronoi scaffolds showed consistent von Mises stress distribution across connection sites with no indication of regional stress concentrations. Notably, the PC-TC and PC-TG scaffolds displayed extensive stress distribution throughout a significant portion of their structures, while the PG-TC and PG-TG scaffolds exhibited less intense and more stable distributions of stress. These results underscore the substantial influence of geometric factors on the load distribution within Voronoi porous scaffolds. Among all VTL structures, the PC-TC and PC-TG scaffolds pose a higher risk of failure due to the presence of elevated stress concentrations at the connection sites. Figure 35 illustrates von Mises stress distributions of VTL structures. When considering the impact of irregularity on stress distribution, it becomes evident that the PG-TC lattice displays a smaller region experiencing stress, followed by PG-TG. In contrast, PC-TC and PC-TG exhibited less favorable performance, as they experienced a higher concentration of stress in their struts and curves. As compared to other Voronoi porous scaffolds, PC-TC displayed the least displacement along the load direction, while the highest displacement was observed in PC-TG, followed by PG-TC and PG-TG. The displacement of VTL structures is depicted in Fig. 35.

Mechanical characteristics of the designed porous scaffold, including the elastic modulus and maximum compressive strength showed in Fig. 36 and can be summarized as follows: PG-TC displayed the highest stiffness and strength, reaching 271.23 MPa and 1.61 MPa, respectively, positioning it as the top performer in terms of mechanical properties. Subsequently, PG-TG exhibited the second-highest stiffness at 241.02 MPa, followed by PC-TC, which recorded a stiffness value of 238.58 MPa. While PC-TG recorded a stiffness value of 212.24 MPa with a higher strength value of 1.41 MPa in comparison with PC-TC and PG-TG. The strength of PG-TG is slightly lower with a value of 1.07 MPa while PC-TC is much lower at the value of 0.60 MPa. Lastly, the PC-TC lattice exhibited the lowest values for both stiffness and strength with a value of 238 MPa.

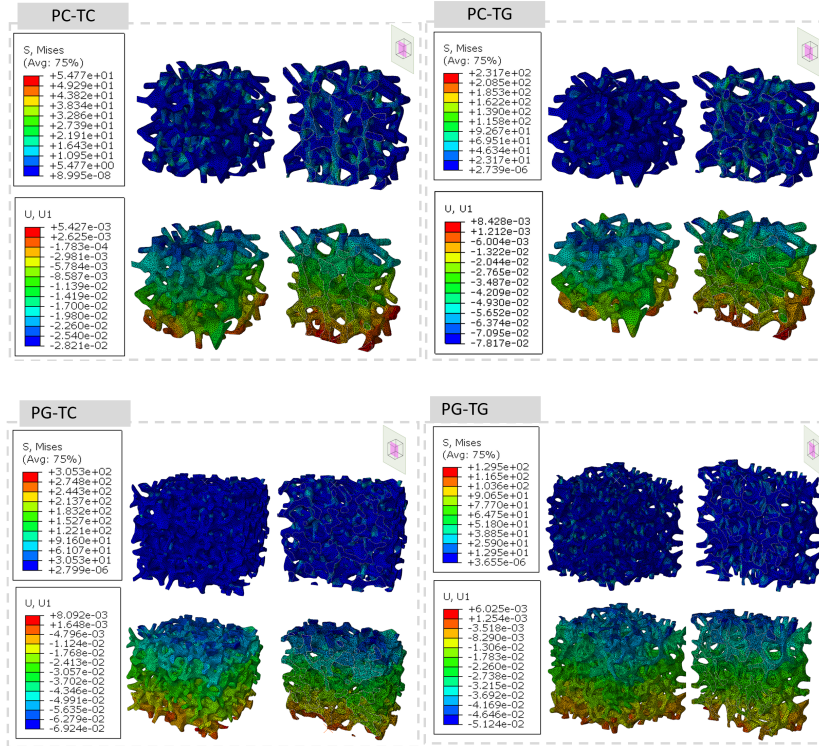


Figure 35: von Mises stress distributions and displacement of HA VTL scaffolds under compression test - (adopted from publication IV).

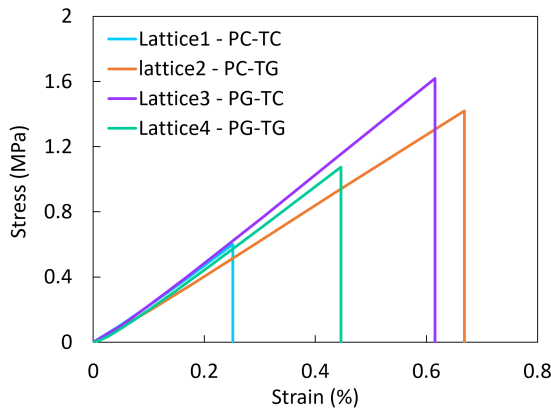


Figure 36: Stress-Strain curve for Voronoi lattices under compression test - (adopted from publication IV).

### 3.5 Human bone and TPMS/Voronoi-based lattices

Human cancellous and cortical bone exhibits an elastic modulus ranging from 0.1 to 4.5 *GPa* and 3 to 20 *GPa*, respectively, along with yield strengths within the ranges of 2 to 17 *MPa* and 33 to 193 *MPa* [64]. The elastic modulus of the human skull falls between 2 and 6 *GPa* [109, 110]. In other literature, the elastic modulus of cancellous bone was reported in the range of 0.4 to 4.5 *GPa*, and the yield strength of the spine, tibia, and proximal femur was reported in the range of 0.56 to 55.3 *MPa* [111].

As compared to human bones, TPMS designed lattices using Taguchi optimization method showed good agreement with elastic modulus and compressive strength with high porosity level which is important factor in bone substitutions. A Neovius lattice structure with 0.40 *mm* wall thickness and 4 unit cells in each direction showed the highest values of compressive strength and elastic modulus, while Primitive TPMS with 0.40 *mm* wall thickness and 2 unit cells in each direction recorded the lowest values.

Between nine hybrid topologies, D1 to D9 designed with Volkmann and Haversian canals, the results suggested that D9 out of nine designs shows mechanical properties (elastic modulus and yield strength of 20.18 *GPa* and 144.40 *MPa*, respectively) in the range of human bone while providing the maximum porosity of 37.25% with considering elliptical cross-section and helical orientation for Volkmann canals and retaining circular cross-section for Haversian in the vertical direction. Related surface area also increased up to 881.1 *mm*<sup>2</sup> in the cortical component. when it comes to the hybrid design including cortical and trabecular parts, Diamond had the highest stiffness and yield strength at 23.81 *GPa* and 185.85 *MPa* followed by Split-P lattice with a stiffness value of 23.67 *GPa* and 180.85 *MPa* of yield strength respectively. Gyroid ranked third with 22.99 *GPa* of elastic modulus and 179.45 *MPa* yield strength followed by Primitive with the lowest stiffness and yield strength at 21.84 *GPa* 166.44 *MPa*. All lattices showed the potential for bone replacement while Split-P and Diamond were reported as the best lattice structures. these hybrid-designed lattices can be used in the proximal diaphysis region to treat long bone critical-size defects.

The 3D-printed Ti6Al4V Split-P lattices display elastic modulus raging from 1.55 to 3.48 *GPa*, which is lower than the values for human cortical bone. However, they exhibit yield strengths around 57 to 152 *MPa*, comparable to those of cortical bone. Notably, among all the Split-P lattices, SP025u125 boasts an elastic modulus and yield stress within the range and surpassing those of cancellous bone, while the remaining lattices are better suited for applications involving cortical bone and the cortical segment of skull bone. Consequently, the SLM Ti6Al4V Split-P lattices prove to be apt structures for load-bearing purposes, given their combination of high yield strength and low elastic modulus, minimizing stress shielding concerns [112].

In the case of Voronoi lattice structures, all the scaffolds showed mechanical properties in the range of human bone. The elastic modulus was reported from 2.12 to 2.71 *GPa* and maximum strength also ranged from 0.60 to 1.61 *MPa*. All lattices showed the possibility of application in bone substitution while among them PG-TC scaffold with gradient PS and constant ST showed the best performance in terms of strength and stiffness. These types of lattices can be used in the cancellous bone of the spine, tibia, and proximal femur.

## 4 Conclusions

This doctoral thesis has provided a multifaceted exploration of cutting-edge advancements in the realm of biomimetic load-bearing implants/scaffolds and lattice structures for bone engineering applications with a specific focus on mechanical properties and geometrical attributes.

In this work, the design of bioinspired bone implants considering metal and ceramics material, and evaluation of the most suitable and printable architectures using FEA and SLM approaches have been performed. Furthermore, analysis of the mechanical behavior of the implants/scaffolds, optimization of its design for better performance, and evaluation of the potential of SLM in producing complex-structured implants with customized geometries have demonstrated a promising potential for the application of the designed structures, which can be introduced into the industrial process of personalized medicine in the field of bone regeneration, substitution, and treatment.

Based on the outcomes of the work, the following conclusions can be drawn:

1. The application of the Taguchi method has proven in the optimization of metallic cellular structures inspired by TPMS for bone-related applications.
2. The innovative design of anatomically tailored and personalized implants consisting of cortical bone mimicking Haversian and Volkmann canals combined with trabecular-bone-simulating parts has been developed.
3. A novel approach to design of biomimetic load-bearing implants by introducing two complementary strategies has been presented. The integration of these strategies has resulted in the creation of a hybrid implant with remarkable mechanical properties closely resembling those of natural bone. The outcomes have highlighted the significance of not only material selection but also the internal architecture of the implant, demonstrating potential for the treatment of long bone critical-sized defects.
4. For the first time, design and printing by SLM of Ti6Al4V Split-P TPMS structures has been performed. Among other TPMS, Split-P lattices with the largest SA and SA/VR can also achieve mechanical properties close to those of trabecular and cortical bones, making them suitable for load-bearing bone implants.
5. The size of unit cells and the walls' thickness significantly affect the manufacturability of Split-P structures. The large unit cell and small wall thickness, together with the specific porosity, have increased the risk of failure of 3D printing process. By increasing the thickness of the lattice' walls, it is possible to connect the zone suspended in the air and make the Split-P lattice a self-supporting structure.
6. Gibson-Ashby model has indicated stretching-dominated deformation mechanisms of failure in Split-P TPMS. The study of the effect of CM and RD on mechanical properties of lattices has shown that these two parameters significantly influence the mechanical response of the structures. The von Mises stress and equivalent plastic strain distributions has demonstrated that Split-P lattices designed with dissimilar RD and CM possess different stress and plastic strain concentrations. For the solid-based lattice, the greatest von Mises stress was concentrated around the connection sites. In other Split-P lattices, the stress concentration mostly appears around the top and/or bottom layers. The study on the homogenization of the unit cells has revealed a dependence between the Zener ratio and the cell morphology.

7. A comprehensive study on the effect of design parameters, including ST and seed PS, on HA-based Voronoi-based lattice for BTE based on static structural FEA and maximum stress criteria has been performed. The outcomes of this study provide valuable insights into the potential for enhancing the scaffolds' mechanical properties and geometrical characteristics. Results demonstrated that the morphology and irregularity of the Voronoi-based scaffolds can directly affect the architectural features, such as pore sizes, their distribution, and amounts, as well as SA, and SA/VR, and mechanical characteristics such as modulus of elasticity and maximum compressive strength.
8. The gradient PS was found to be more effective than the gradually altering ST in improving mechanical performance and structural stability. However, the most significant improvements were achieved when both PS and ST were subjected to gradient changes. The PS and ST play a key role in optimization of geometry, resulting in better bone regeneration.
9. The study of porosity level and pore distribution within the scaffolds has revealed that constructs, such as the Gradient PS-Gradient ST lattice, provided the largest number of pores and a variety pore sizes and their distributions. These results highlighted the capacity to customize scaffold porosity to mimic the interconnected nature of natural bone.
10. In terms of mechanical properties, changing from constant PS to gradient PS reduced the modulus of elasticity, noticeably improving MCS. The PG-TC structure offered an excellent performance considering both geometrical and mechanical properties. This demonstrated the importance of introducing gradients to accomplish better geometrical and mechanical characteristics.

The results of the research work are presented in four publications:

The first study proved successfully the application of Taguchi method in the design metallic TPMS cellular structures for bone-related applications . Through systematic experimentation, statistical analysis and FEA, influential factors like TPMS type, number of cells, and wall thickness were identified, impacting both elastic modulus and compressive strength. Taguchi strategy enhances TPMS lattice development, providing valuable insights into geometric factors' interplay for precise control of structural parameters. This contributes to improved mechanical performance in biomedical applications, advancing TPMS structure design in biomedical engineering.

The second paper presented a novel approach to design of hybrid biomimetic load-bearing implants by introducing two complementary strategies, one mimicking the structural characteristics of cortical bone and the other one representing a trabecular bone. The integration of these strategies resulted in a hybrid implant with remarkable mechanical properties closely resembling those of natural bone. This research work addresses the research question of 1, 2, 4, and 5.

In the third research paper, the focus shifted to the use of Ti6Al4V Split-P TPMS structures manufactured through SLM. This study investigated the mechanical characteristics of these structures, taking into account different RD and CM. The findings highlighted the versatility and potential of these structures, revealing their capacity to achieve mechanical properties comparable to those of cortical and trabecular bone. This research opens new possibilities for the development of load-bearing bone implants with enhanced mechanical performance. Research questions 1, 2, 3, 4, and 5 are addressed in this study.

The forth research paper introduced IVL structures for tissue engineering applications. By varying ST and PS, the IVL structures were designed to closely mimic the natural interconnectivity of human bone. This investigation explored how design parameters influence both the geometrical and mechanical properties of the lattice structures. The results demonstrated that through the strategic manipulation of design parameters, it is possible to enhance both the mechanical and biological performance of these scaffolds, thus offering potential solutions for bone regeneration therapies. In this study research questions 1, 2, 4, and 5 are addressed.

**Scientific novelty and practical importance:** The novelty of this work lies in their pioneering contributions to the field of load-bearing implants/scaffolds and lattice structures for tissue engineering. In the first paper, Taguchi method is applied to the design lattice structure in order to determine the most consequential design parameters for the mechanical properties such as elastic modulus and yield strength. The second study introduces a hybrid implant design that combines the biomimicry of both cortical and trabecular bone structures, representing a significant departure from traditional implant designs. This innovative approach underscores the importance of the internal architecture of load-bearing implants and has the potential to improve the treatment of long bone critical-sized defects. In the third paper, the utilization of Ti6Al4V Split-P TPMS structures produced by SLM introduces an entirely new level of mechanical properties, offering a range of mechanical properties that closely approximate those of natural bone, marking a substantial step forward in the development of load-bearing implants. The fourth paper introduces irregular Voronoi-based lattice structures with varying ST and PS, offering a unique and biologically inspired approach to tissue engineering. The manipulation of design parameters in this manner presents a novel method for achieving enhanced mechanical and biological performance, positioning these lattices as innovative solutions for bone regeneration. Collectively, these papers contribute fresh perspectives and novel methodologies to the field, offering promising directions for improving the design of load-bearing implants and bone tissue engineering. Through the examination of three distinct research papers, this research has significantly contributed to the understanding of the design, manufacturing, and mechanical characterization of load-bearing implants, showcasing their potential for critical-sized defect treatment and bone substitution therapies.

## 5 Future work

The future directions propose remarkable opportunities to advance the field of biomimetic load-bearing implants and lattice structures for tissue engineering.

- Exploring the biocompatibility and bone integration of designed lattice structures represents a critical step toward clinical application, ensuring the safety and effectiveness of these implants.
- The investigation of functionally graded TPMS, with a specific focus on Split-P lattices, provides an opportunity to enhance the mechanical performance of these structures.
- The integration of artificial intelligence (AI) in lattice design and optimization is a forward-looking approach that promises to revolutionize the design process, allowing for tailored structures with superior mechanical properties.
- The exploration of multi-morphology TPMS and their combination effects on mechanical properties, (aided by AI or without it), offers a deeper understanding of the potential of these structures.
- Incorporating failure criteria for numerical analysis will provide insights into the structural robustness of these lattices.
- Investigating permeability with fluid dynamics brings a new dimension to the research, considering their interaction with bodily fluids.
- The development of functionally graded material lattice structures, combining Ti6Al4V and hydroxyapatite, offers a new approach for advanced implant designs. These future works collectively promise to expand the horizons of load-bearing implants and contribute significantly to the field of tissue engineering. performance of the designed scaffolds/implants.

## References

- [1] François Berthiaume, Timothy J Maguire, and Martin L Yarmush. Tissue engineering and regenerative medicine: history, progress, and challenges. *Annual review of chemical and biomolecular engineering*, 2:403–430, 2011.
- [2] C Kiernan, C Knuth, and E Farrell. Chapter 6-enchondral ossification: Recapitulating bone development for bone defect repair, içinde: Mj stoddart, am craft, g. pattappa, ofwbt-db and mte gardner, 2018.
- [3] Maria Pia Ferraz. Bone grafts in dental medicine: An overview of autografts, allografts and synthetic materials. *Materials*, 16(11):4117, 2023.
- [4] Jingqi Qi, Tianqi Yu, Bangyan Hu, Hongwei Wu, and Hongwei Ouyang. Current biomaterial-based bone tissue engineering and translational medicine. *International journal of molecular sciences*, 22(19):10233, 2021.
- [5] Mojtaba Ansari. Bone tissue regeneration: biology, strategies and interface studies. *Progress in biomaterials*, 8(4):223–237, 2019.
- [6] Xu Feng. Chemical and biochemical basis of cell-bone matrix interaction in health and disease. *Current chemical biology*, 3(2):189–196, 2009.
- [7] Yunhua Luo, Oghenerioborue Amromanoh, et al. Bone organic-inorganic phase ratio is a fundamental determinant of bone material quality. *Applied Bionics and Biomechanics*, 2021, 2021.
- [8] Steve Weiner, Wolfie Traub, and H Daniel Wagner. Lamellar bone: structure–function relations. *Journal of structural biology*, 126(3):241–255, 1999.
- [9] Sebastien JP Callens, Duncan C Tourolle né Betts, Ralph Müller, and Amir A Zadpoor. The local and global geometry of trabecular bone. *Acta Biomaterialia*, 130:343–361, 2021.
- [10] LM McNamara. 2.10 bone as a material. 2017.
- [11] David Holmes. Non-union bone fracture: a quicker fix. *Nature*, 550(7677):S193–S193, 2017.
- [12] Antalya Ho-Shui-Ling, Johanna Bolander, Laurence E Rustom, Amy Wagoner Johnson, Frank P Luyten, and Catherine Picart. Bone regeneration strategies: Engineered scaffolds, bioactive molecules and stem cells current stage and future perspectives. *Biomaterials*, 180:143–162, 2018.
- [13] Wolfgang Schlickewei and Carsten Schlickewei. The use of bone substitutes in the treatment of bone defects—the clinical view and history. In *Macromolecular symposia*, volume 253, pages 10–23. Wiley Online Library, 2007.
- [14] Olha Bazaka, Katia Bazaka, P Kingshott, RJ Crawford, and EP Ivanova. Metallic implants for biomedical applications. 2021.
- [15] Fergal J O'brien. Biomaterials & scaffolds for tissue engineering. *Materials today*, 14(3):88–95, 2011.



- [16] Gabriel Fernandez de Grado, Laetitia Keller, Ysia Idoux-Gillet, Quentin Wagner, Anne-Marie Musset, Nadia Benkirane-Jessel, Fabien Bornert, and Damien Offner. Bone substitutes: a review of their characteristics, clinical use, and perspectives for large bone defects management. *Journal of tissue engineering*, 9:2041731418776819, 2018.
- [17] Håvard Jostein Haugen, Ståle Petter Lyngstadaas, Filippo Rossi, and Giuseppe Perale. Bone grafts: which is the ideal biomaterial? *Journal of clinical periodontology*, 46:92–102, 2019.
- [18] David F Williams. On the mechanisms of biocompatibility. *Biomaterials*, 29(20):2941–2953, 2008.
- [19] Peter V Giannoudis, Haralambos Dinopoulos, and Eleftherios Tsiridis. Bone substitutes: an update. *Injury*, 36(3):S20–S27, 2005.
- [20] Sharookh P Vatchha, Amit Kohli, Sanjay Kumar Tripathi, Saurav Narayan Nanda, Prasant Pradhan, and Shaikh Muzammil Shiraz. Biodegradable implants in orthopaedics. *Annals of International Medical and Dental Research*, 1(1):3–8, 2015.
- [21] Lorenzo Vaiani, Antonio Boccaccio, Antonio Emmanuele Uva, Gianfranco Palumbo, Antonio Piccininni, Pasquale Guglielmi, Stefania Cantore, Luigi Santacroce, Ioannis Alexandros Charitos, and Andrea Ballini. Ceramic materials for biomedical applications: An overview on properties and fabrication processes. *Journal of Functional Biomaterials*, 14(3):146, 2023.
- [22] Yuhua Li, Chao Yang, Haidong Zhao, Shengguan Qu, Xiaoqiang Li, and Yuanyuan Li. New developments of ti-based alloys for biomedical applications. *Materials*, 7(3):1709–1800, 2014.
- [23] G Santos. The importance of metallic materials as biomaterials. *Adv Tissue Eng Regen Med Open Access*, 3(1):300–302, 2017.
- [24] H Oonishi. Orthopaedic applications of hydroxyapatite. *Biomaterials*, 12(2):171–178, 1991.
- [25] Racquel Z LeGeros, Guy Daculsi, and John P LeGeros. Bioactive bioceramics. *Musculoskeletal tissue regeneration: biological materials and methods*, pages 153–181, 2008.
- [26] Koji Demiya, Toshiyuki Kunisada, Eiji Nakata, Joe Hasei, Toshifumi Ozaki, et al. Regeneration of the fibula with unidirectional porous hydroxyapatite. *Case Reports in Orthopedics*, 2019, 2019.
- [27] M Rizwan, Wan Jeffrey Basirun, Bushroa Abd Razak, and Rodianah Alias. Bioinspired ceramics for bone tissue applications. In *Ceramic Science and Engineering*, pages 111–143. Elsevier, 2022.
- [28] K. Ishikawa, S. Matsuya, Y. Miyamoto, and K. Kawate. 9.05 - bioceramics. In I. Milne, R.O. Ritchie, and B. Karihaloo, editors, *Comprehensive Structural Integrity*, pages 169–214. Pergamon, Oxford, 2003.
- [29] Kiran Suresh Naik. Chapter 25 - advanced bioceramics. In Surya Nandan Meena and Milind Mohan Naik, editors, *Advances in Biological Science Research*, pages 411–417. Academic Press, 2019.

- [30] Deepika Shekhawat, Amit Singh, MK Banerjee, Tej Singh, and Amar Patnaik. Bio-ceramic composites for orthopaedic applications: A comprehensive review of mechanical, biological, and microstructural properties. *Ceramics International*, 47(3):3013–3030, 2021.
- [31] L Bai, C Gong, X Chen, Y Sun, J Zhang, L Cai, S Zhu, and SQ Xie. Additive manufacturing of customized metallic orthopedic implants: Materials, structures, and surface modifications, metals (basel). 9 (2019).
- [32] Meena Pant, Pritam Pidge, Harish Kumar, Leeladhar Nagdeve, and Girija Moona. Additive manufacturing: The significant role in biomedical and aerospace applications. 2021.
- [33] Reza Noroozi, Farzad Tatar, Ali Zolfagharian, Roberto Brighenti, Mohammad Amin Shamekhi, Abbas Rastgoo, Amin Hadi, and Mahdi Bodaghi. Additively manufactured multi-morphology bone-like porous scaffolds: experiments and micro-computed tomography-based finite element modeling approaches. *International Journal of Bioprinting*, 8(3), 2022.
- [34] Kyobum Kim, Andrew Yeatts, David Dean, and John P Fisher. Stereolithographic bone scaffold design parameters: osteogenic differentiation and signal expression. *Tissue Engineering Part B: Reviews*, 16(5):523–539, 2010.
- [35] Soheila Mohammadzadehmoghadam, Yu Dong, and Ian Jeffery Davies. Modeling electrospun nanofibers: An overview from theoretical, empirical, and numerical approaches. *International Journal of Polymeric Materials and Polymeric Biomaterials*, 65(17):901–915, 2016.
- [36] Naghmeh Abbasi, Stephen Hamlet, Robert M Love, and Nam-Trung Nguyen. Porous scaffolds for bone regeneration. *Journal of science: advanced materials and devices*, 5(1):1–9, 2020.
- [37] FSL Bobbert and AA Zadpoor. Effects of bone substitute architecture and surface properties on cell response, angiogenesis, and structure of new bone. *Journal of Materials Chemistry B*, 5(31):6175–6192, 2017.
- [38] Shivank A Tyagi and M Manjaiah. Additive manufacturing of titanium-based lattice structures for medical applications—a review. *Bioprinting*, page e00267, 2023.
- [39] Oraib Al-Ketan, Reza Rowshan, and Rashid K Abu Al-Rub. Topology-mechanical property relationship of 3d printed strut, skeletal, and sheet based periodic metallic cellular materials. *Additive Manufacturing*, 19:167–183, 2018.
- [40] Hussain Gharehbaghi, Amin Farrokhabadi, and Zahra Noroozi. Introducing a new hybrid surface strut-based lattice structure with enhanced energy absorption capacity. *Mechanics of Advanced Materials and Structures*, pages 1–10, 2023.
- [41] Diab W Abueidha, Ahmed S Dalaq, Rashid K Abu Al-Rub, and Hammad A Younes. Finite element predictions of effective multifunctional properties of interpenetrating phase composites with novel triply periodic solid shell architected reinforcements. *International Journal of Mechanical Sciences*, 92:80–89, 2015.

- [42] Diab W Abueidda, Mete Bakir, Rashid K Abu Al-Rub, Jörgen S Bergström, Nahil A Sobh, and Iwona Jasiuk. Mechanical properties of 3d printed polymeric cellular materials with triply periodic minimal surface architectures. *Materials & Design*, 122:255–267, 2017.
- [43] Sebastian C Kapfer, Stephen T Hyde, Klaus Mecke, Christoph H Arns, and Gerd E Schröder-Turk. Minimal surface scaffold designs for tissue engineering. *Biomaterials*, 32(29):6875–6882, 2011.
- [44] Minhao Shen, Wei Qin, Bohang Xing, Weiming Zhao, Shuyue Gao, Ying Sun, Ting Jiao, and Zhe Zhao. Mechanical properties of 3d printed ceramic cellular materials with triply periodic minimal surface architectures. *Journal of the European Ceramic Society*, 41(2):1481–1489, 2021.
- [45] Srinivasan Rajagopalan and Richard A Robb. Schwarz meets schwann: design and fabrication of biomorphic and durataxic tissue engineering scaffolds. *Medical image analysis*, 10(5):693–712, 2006.
- [46] Ifeanyichukwu Echeta, Ben Dutton, Richard K Leach, and Samanta Piano. Finite element modelling of defects in additively manufactured strut-based lattice structures. *Additive Manufacturing*, 47:102301, 2021.
- [47] MR Kamranfard, H Darijani, H Rokhghireh, and S Khademzadeh. Analysis and optimization of strut-based lattice structures by simplified finite element method. *Acta Mechanica*, 234(4):1381–1408, 2023.
- [48] Shivangi Sarabhai, Nikita Letov, Mitch Kibsey, Fabian Sanchez, and Yaoyao Fiona Zhao. Understanding the flow and thermal characteristics of non-stochastic strut-based and surface-based lattice structures. *Materials & Design*, 227:111787, 2023.
- [49] J Kadkhodapour, H Montazerian, A Ch Darabi, AP Anaraki, SM Ahmadi, AA Zadpoor, and S Schmauder. Failure mechanisms of additively manufactured porous biomaterials: Effects of porosity and type of unit cell. *Journal of the mechanical behavior of biomedical materials*, 50:180–191, 2015.
- [50] Mohammad Zahid Khan, Jitendra Bhaskar, and Anand Kumar. Design and analysis of strut-based lattice structure cranial implant. *Journal of Mechanical Engineering and Sciences*, pages 9307–9314, 2023.
- [51] Sajad Arabnejad, R Burnett Johnston, Jenny Ann Pura, Baljinder Singh, Michael Tanzer, and Damiano Pasini. High-strength porous biomaterials for bone replacement: A strategy to assess the interplay between cell morphology, mechanical properties, bone ingrowth and manufacturing constraints. *Acta biomaterialia*, 30:345–356, 2016.
- [52] Hao Chen, Qing Han, Chenyu Wang, Yang Liu, Bingpeng Chen, and Jincheng Wang. Porous scaffold design for additive manufacturing in orthopedics: a review. *Frontiers in Bioengineering and Biotechnology*, 8:609, 2020.
- [53] Yue Du, Huixin Liang, Deqiao Xie, Ning Mao, Jianfeng Zhao, Zongjun Tian, Changjiang Wang, and Lida Shen. Design and statistical analysis of irregular porous scaffolds for orthopedic reconstruction based on voronoi tessellation and fabricated via selective laser melting (slm). *Materials chemistry and physics*, 239:121968, 2020.

- [54] Georgios Maliaris and Elias Sarafis. Mechanical behavior of 3d printed stochastic lattice structures. *Solid State Phenomena*, 258:225–228, 2017.
- [55] Ulas Yaman, Nabeel Butt, Elisha Sacks, and Christoph Hoffmann. Slice coherence in a query-based architecture for 3d heterogeneous printing. *Computer-Aided Design*, 75:27–38, 2016.
- [56] Pu Zhang, Jikai Liu, and Albert C To. Role of anisotropic properties on topology optimization of additive manufactured load bearing structures. *Scripta Materialia*, 135:148–152, 2017.
- [57] Huixin Liang, Youwen Yang, Deqiao Xie, Lan Li, Ning Mao, Changjiang Wang, Zongjun Tian, Qing Jiang, and Lida Shen. Trabecular-like ti-6al-4v scaffolds for orthopedic: fabrication by selective laser melting and in vitro biocompatibility. *Journal of Materials Science & Technology*, 35(7):1284–1297, 2019.
- [58] Attila Piros and Laura Trautmann. Creating interior support structures with lightweight voronoi scaffold. *International Journal on Interactive Design and Manufacturing (IJDeM)*, 17(1):93–101, 2023.
- [59] Eujin Pei, Israt Kabir, Tomislav Breški, Damir Godec, and Axel Nordin. A review of geometric dimensioning and tolerancing (gd&t) of additive manufacturing and powder bed fusion lattices. *Progress in Additive Manufacturing*, 7(6):1297–1305, 2022.
- [60] Lei Yang, Yang Li, Siqi Wu, Peng Chen, Hongzhi Wu, Jin Su, Haoze Wang, Jie Liu, Chunze Yan, and Yusheng Shi. Tailorable and predictable mechanical responses of additive manufactured tpms lattices with graded structures. *Materials Science and Engineering: A*, 843:143109, 2022.
- [61] Guanjun Wang, Lida Shen, Jianfeng Zhao, Huixin Liang, Deqiao Xie, Zongjun Tian, and Changjiang Wang. Design and compressive behavior of controllable irregular porous scaffolds: Based on voronoi-tessellation and for additive manufacturing. *ACS biomaterials science & engineering*, 4(2):719–727, 2018.
- [62] Shuai Wei, Jian-Xiong Ma, Lai Xu, Xiao-Song Gu, and Xin-Long Ma. Biodegradable materials for bone defect repair. *Military medical research*, 7(1):1–25, 2020.
- [63] Ciara M Murphy and Fergal J O’Brien. Understanding the effect of mean pore size on cell activity in collagen-glycosaminoglycan scaffolds. *Cell adhesion & migration*, 4(3):377–381, 2010.
- [64] Ke Zhang, Yubo Fan, Nicholas Dunne, and Xiaoming Li. Effect of microporosity on scaffolds for bone tissue engineering. *Regenerative biomaterials*, 5(2):115–124, 2018.
- [65] Thanh Danh Nguyen, Olufemi E Kadri, Vassilios I Sikavitsas, and Roman S Voronov. Scaffolds with a high surface area-to-volume ratio and cultured under fast flow perfusion result in optimal o2 delivery to the cells in artificial bone tissues. *Applied Sciences*, 9(11):2381, 2019.
- [66] EF Lehder, IA Ashcroft, RD Wildman, LA Ruiz-Cantu, and I Maskery. A multiscale optimisation method for bone growth scaffolds based on triply periodic minimal surfaces. *Biomechanics and modeling in mechanobiology*, 20:2085–2096, 2021.

- [67] Xiaofeng Guo, Xiaoyang Zheng, Yang Yang, Xinyu Yang, and Yong Yi. Mechanical behavior of tpms-based scaffolds: a comparison between minimal surfaces and their lattice structures. *SN Applied Sciences*, 1(10):1145, 2019.
- [68] M Fantini, M Curto, and Francesca De Crescenzo. Tpms for interactive modelling of trabecular scaffolds for bone tissue engineering. In *Advances on Mechanics, Design Engineering and Manufacturing: Proceedings of the International Joint Conference on Mechanics, Design Engineering & Advanced Manufacturing (JCM 2016)*, 14-16 September, 2016, Catania, Italy, pages 425–435. Springer, 2017.
- [69] Sanjairaj Vijayavenkataraman, Lei Zhang, Shuo Zhang, Jerry Ying Hsi Fuh, and Wen Feng Lu. Triply periodic minimal surfaces sheet scaffolds for tissue engineering applications: An optimization approach toward biomimetic scaffold design. *ACS Applied Bio Materials*, 1(2):259–269, 2018.
- [70] Zhifei Dong and Xin Zhao. Application of tpms structure in bone regeneration. *Engineered Regeneration*, 2:154–162, 2021.
- [71] Naoya Taniguchi, Shunsuke Fujibayashi, Mitsuru Takemoto, Kiyoyuki Sasaki, Bungo Otsuki, Takashi Nakamura, Tomiharu Matsushita, Tadashi Kokubo, and Shuichi Matsuda. Effect of pore size on bone ingrowth into porous titanium implants fabricated by additive manufacturing: An in vivo experiment. *Materials Science and Engineering: C*, 59:690–701, 2016.
- [72] Tracy L Kivell. A review of trabecular bone functional adaptation: what have we learned from trabecular analyses in extant hominoids and what can we apply to fossils? *Journal of Anatomy*, 228(4):569–594, 2016.
- [73] Ramin Oftadeh, Miguel Perez-Viloria, Juan C Villa-Camacho, Ashkan Vaziri, and Ara Nazarian. Biomechanics and mechanobiology of trabecular bone: a review. *Journal of biomechanical engineering*, 137(1):010802, 2015.
- [74] Omer Subasi, Bedri Karaismailoglu, Soheil Ashkani-Esfahani, and Ismail Lazoglu. Investigation of lattice infill parameters for additively manufactured bone fracture plates to reduce stress shielding. *Computers in Biology and Medicine*, 161:107062, 2023.
- [75] Bin Zhang, Liwei Guo, Hongyi Chen, Yiannis Ventikos, Roger J Narayan, and Jie Huang. Finite element evaluations of the mechanical properties of polycaprolactone/hydroxyapatite scaffolds by direct ink writing: Effects of pore geometry. *Journal of the Mechanical Behavior of Biomedical Materials*, 104:103665, 2020.
- [76] Davar Ali and Sadri Sen. Finite element analysis of mechanical behavior, permeability and fluid induced wall shear stress of high porosity scaffolds with gyroid and lattice-based architectures. *Journal of the mechanical behavior of biomedical materials*, 75:262–270, 2017.
- [77] Akesh Babu Kakarla, Ing Kong, Satya Guha Nukala, and Win Kong. Mechanical behaviour evaluation of porous scaffold for tissue-engineering applications using finite element analysis. *Journal of Composites Science*, 6(2):46, 2022.
- [78] Ranjan Bora, Mukul Shukla, and Anuj Kumar. Finite element analysis based design of biomimetic functionally graded ti-6al-4v alloy scaffolds for human cortical bone applications. *Materials Today: Proceedings*, 2023.

- [79] MR Karamooz Ravari, M Kadkhodaei, M Badrossamay, and R Rezaei. Numerical investigation on mechanical properties of cellular lattice structures fabricated by fused deposition modeling. *International Journal of Mechanical Sciences*, 88:154–161, 2014.
- [80] Zhichao Luo, Qian Tang, Qixiang Feng, Shuai Ma, Jun Song, Rossitza Setchi, Fuyu Guo, and Yuanhang Zhang. Finite element analysis of the mechanical properties of sheet-and skeleton-gyroid ti6al4v structures produced by laser powder bed fusion. *Thin-Walled Structures*, 192:111098, 2023.
- [81] Liang Hao, David Rayment, Chunze Yan, Ahmed Hussein, and Philippe Young. Design and additive manufacturing of cellular lattice structures. In *The International Conference on Advanced Research in Virtual and Rapid Prototyping (VRAP)*. Taylor & Francis Group, Leiria, pages 249–254, 2011.
- [82] Swee Leong Sing, Florencia Edith Wiria, and Wai Yee Yeong. Selective laser melting of lattice structures: A statistical approach to manufacturability and mechanical behavior. *Robotics and Computer-Integrated Manufacturing*, 49:170–180, 2018.
- [83] Horatiu Rotaru, Ralf Schumacher, Seong-Gon Kim, and Cristian Dinu. Selective laser melted titanium implants: a new technique for the reconstruction of extensive zygomatic complex defects. *Maxillofacial plastic and reconstructive surgery*, 37:1–6, 2015.
- [84] Shaun Eshraghi and Suman Das. Micromechanical finite-element modeling and experimental characterization of the compressive mechanical properties of polycaprolactone–hydroxyapatite composite scaffolds prepared by selective laser sintering for bone tissue engineering. *Acta biomaterialia*, 8(8):3138–3143, 2012.
- [85] Bowen Xu, Kee-Won Lee, Wenjie Li, Michael J Yaszemski, Lichun Lu, Yabin Yang, and Shanfeng Wang. A comparative study on cylindrical and spherical models in fabrication of bone tissue engineering scaffolds: Finite element simulation and experiments. *Materials & Design*, 211:110150, 2021.
- [86] Balasubramanian Nagarajan, Zhiheng Hu, Xu Song, Wei Zhai, and Jun Wei. Development of micro selective laser melting: The state of the art and future perspectives. *Engineering*, 5(4):702–720, 2019.
- [87] Xiaojie Fan, Qian Tang, Qixiang Feng, Shuai Ma, Jun Song, Mengxia Jin, Fuyu Guo, and Peng Jin. Design, mechanical properties and energy absorption capability of graded-thickness triply periodic minimal surface structures fabricated by selective laser melting. *International Journal of Mechanical Sciences*, 204:106586, 2021.
- [88] Timothy Davis, D Healy, A Bubeck, and Richard Walker. Stress concentrations around voids in three dimensions: The roots of failure. *Journal of Structural Geology*, 102:193–207, 2017.
- [89] R Miralbes, D Ranz, FJ Pascual, D Zouzias, and M Maza. Characterization of additively manufactured triply periodic minimal surface structures under compressive loading. *Mechanics of Advanced Materials and Structures*, 29(13):1841–1855, 2022.
- [90] Mubasher Ali, Resy Kumala Sari, Uzair Sajjad, Muhammad Sultan, and Hafiz Muhammad Ali. Effect of annealing on microstructures and mechanical properties of pa-12 lattice structures proceeded by multi jet fusion technology. *Additive Manufacturing*, 47:102285, 2021.

- [91] Zhiqiang Liu, He Gong, Jiazi Gao, and Lu Liu. Topological design, mechanical responses and mass transport characteristics of high strength-high permeability tpms-based scaffolds. *International Journal of Mechanical Sciences*, 217:107023, 2022.
- [92] Vassilis Karageorgiou and David Kaplan. Porosity of 3d biomaterial scaffolds and osteogenesis. *Biomaterials*, 26(27):5474–5491, 2005.
- [93] Hailun Zhou, Miao Zhao, Zhibo Ma, David Z Zhang, and Guang Fu. Sheet and network based functionally graded lattice structures manufactured by selective laser melting: Design, mechanical properties, and simulation. *International Journal of Mechanical Sciences*, 175:105480, 2020.
- [94] Amal Charles, Ahmed Elkaseer, Umberto Paggi, Lore Thijs, Veit Hagenmeyer, and Steffen Scholz. Down-facing surfaces in laser powder bed fusion of ti6al4v: Effect of dross formation on dimensional accuracy and surface texture. *Additive Manufacturing*, 46:102148, 2021.
- [95] Jiawei Feng, Jianzhong Fu, Xinhua Yao, and Yong He. Triply periodic minimal surface (tpms) porous structures: From multi-scale design, precise additive manufacturing to multidisciplinary applications. *International Journal of Extreme Manufacturing*, 4(2):022001, 2022.
- [96] J Kadhodapour, H Montazerian, A Ch Darabi, A Zargarian, and S Schmauder. The relationships between deformation mechanisms and mechanical properties of additively manufactured porous biomaterials. *Journal of the mechanical behavior of biomedical materials*, 70:28–42, 2017.
- [97] Miao Zhao, Fei Liu, Guang Fu, David Z Zhang, Tao Zhang, and Hailun Zhou. Improved mechanical properties and energy absorption of bcc lattice structures with triply periodic minimal surfaces fabricated by slm. *Materials*, 11(12):2411, 2018.
- [98] Anton Du Plessis, Nima Razavi, Matteo Benedetti, Simone Murchio, Martin Leary, Marcus Watson, Dhruv Bhate, and Filippo Berto. Properties and applications of additively manufactured metallic cellular materials: A review. *Progress in Materials Science*, 125:100918, 2022.
- [99] Markel Alaña, Antonio Cutolo, Sergio Ruiz de Galarreta, and Brecht Van Hooreweder. Influence of relative density on quasi-static and fatigue failure of lattice structures in ti6al4v produced by laser powder bed fusion. *Scientific Reports*, 11(1):19314, 2021.
- [100] So-Yeon Park, Kyu-Sik Kim, Bandar AlMangour, Dariusz Grzesiak, and Kee-Ahn Lee. Effect of unit cell topology on the tensile loading responses of additive manufactured cocrmo triply periodic minimal surface sheet lattices. *Materials & Design*, 206:109778, 2021.
- [101] Oraib Al-Ketan and Rashid K Abu Al-Rub. Multifunctional mechanical metamaterials based on triply periodic minimal surface lattices. *Advanced Engineering Materials*, 21(10):1900524, 2019.
- [102] Nejc Novak, Oraib Al-Ketan, Matej Borovinšek, Lovre Krstulović-Opara, Reza Rowshan, Matej Vesenjak, and Zoran Ren. Development of novel hybrid tpms cellular lattices and their mechanical characterisation. *journal of materials research and technology*, 15:1318–1329, 2021.

- [103] Sultan Al Hassanieh, Ahmed Alhantoobi, Kamran A Khan, and Muhammad A Khan. Mechanical properties and energy absorption characteristics of additively manufactured lightweight novel re-entrant plate-based lattice structures. *Polymers*, 13(22):3882, 2021.
- [104] Zeyao Chen, Yi Min Xie, Xian Wu, Zhe Wang, Qing Li, and Shiwei Zhou. On hybrid cellular materials based on triply periodic minimal surfaces with extreme mechanical properties. *Materials & design*, 183:108109, 2019.
- [105] Shanqing Xu, Jianhu Shen, Shiwei Zhou, Xiaodong Huang, and Yi Min Xie. Design of lattice structures with controlled anisotropy. *Materials & Design*, 93:443–447, 2016.
- [106] Dong-Jin Yoo. Advanced porous scaffold design using multi-void triply periodic minimal surface models with high surface area to volume ratios. *International journal of precision engineering and manufacturing*, 15:1657–1666, 2014.
- [107] Jialiang Li, Dong Guo, Jie Li, Xinyu Wei, Zhongwei Sun, Baohui Yang, Teng Lu, Pengrong Ouyang, Weiwei Liu, Xijing He, et al. Irregular pore size of degradable bio-ceramic voronoi scaffolds prepared by stereolithography: Osteogenesis and computational fluid dynamics analysis. *Materials & Design*, 224:111414, 2022.
- [108] J Elizabeth Biemond, René Aquarius, Nico Verdonshot, and Pieter Buma. Frictional and bone ingrowth properties of engineered surface topographies produced by electron beam technology. *Archives of orthopaedic and trauma surgery*, 131:711–718, 2011.
- [109] Junfang Zhang, Yifan Shen, Yuanxi Sun, Jianxing Yang, Yu Gong, Ke Wang, Zhiqing Zhang, Xiaohong Chen, and Long Bai. Design and mechanical testing of porous lattice structure with independent adjustment of pore size and porosity for bone implant. *Journal of Materials Research and Technology*, 18:3240–3255, 2022.
- [110] Jamila Rahmoun, Audrey Auperrin, Rémi Delille, Hakim Naceur, and Pascal Drazetic. Characterization and micromechanical modeling of the human cranial bone elastic properties. *Mechanics Research Communications*, 60:7–14, 2014.
- [111] Jin-Ho Kang, Kumaresan Sakthiabirami, Kyoung-Jun Jang, Jae-Gon Jang, Gye-Jeong Oh, Chan Park, John G Fisher, and Sang-Won Park. Mechanical and biological evaluation of lattice structured hydroxyapatite scaffolds produced via stereolithography additive manufacturing. *Materials & Design*, 214:110372, 2022.
- [112] Daniel A Shimko, Valerie Franz Shimko, Edward A Sander, Kyle F Dickson, and Eric A Nauman. Effect of porosity on the fluid flow characteristics and mechanical properties of tantalum scaffolds. *Journal of Biomedical Materials Research Part B: Applied Biomaterials: An Official Journal of The Society for Biomaterials, The Japanese Society for Biomaterials, and The Australian Society for Biomaterials and the Korean Society for Biomaterials*, 73(2):315–324, 2005.





## Acknowledgements

I wish to express my deepest gratitude to my beloved husband, Mohsen, whose unconditional support and presence have been the bedrock of my doctoral journey. Throughout the challenges of this academic pursuit, you have been my constant source of strength and encouragement. You listened patiently to my complaints, celebrated my successes, and stood by me as we embarked on this educational adventure as a united family. Your love, understanding, and sacrifices have been the cornerstones of my success, and I could not have accomplished this without you. Thank you for being the unwavering pillar of support and love that you are.

I would like to extend my heartfelt gratitude to my supervisor, [Prof. Irina Hussainova], for her exceptional support and profound understanding throughout my doctoral journey. Her guidance has been instrumental in shaping this thesis and my growth as a researcher. She demonstrated an exceptional level of support, patience, and understanding, making this challenging process significantly more achievable. I greatly appreciate her commitment to my success. Thank you for being an extraordinary mentor and for believing in my capabilities.

I would like to express my sincere gratitude to my colleagues whose contributions and camaraderie have enriched my doctoral journey. They always remind me of happy moments, tea-drinking conversations, and continuous long talks. The shared experiences with you all have not only broadened my perspective but also made this academic pursuit a more fulfilling and enjoyable endeavor. Thank you for being an integral part of this journey.

I would like to thank everyone from the Department of Mechanical and Industrial Engineering at Tallinn University of Technology, especially Ruth Kolbas for always being kind, helpful, and supportive.

Finally, I finish with my family, my mom and dad, for always giving me love and support in my whole life.

This current research was supported by the Estonian Research Council, Estonia, under Grant PRG643, and M-ERA.Net project “BiLaTex” MNHA23020.”

MANSOUREH REZAPOURIAN  
NOV. 2023  
TALLINN

## Abstract

### **Biomimicry and novel structures: Advancing the design paradigm of bone implants**

This doctoral thesis embarks on a multifaceted exploration of innovative strategies in bone tissue engineering, with the overarching objective of refining the design and manufacturing of load-bearing bone implants and scaffolds. The research is organized in four interrelated dimensions:

- **Dimension I: Taguchi-based optimization of Ti6Al4V TPMS structures** The purpose of the first research is to optimize the mechanical properties of metallic TPMS cellular structures using the Taguchi method. SLM was used to generate the lattices and finite element analysis employed to evaluate the mechanical properties of metal-based Neovius, Schoen I-WP, and Schwarz Primitive structures. Geometric factors such as wall thickness, number of unit cells, and type of TPMS were considered to create the design of experiments to investigate the impact of geometric characteristics on the mechanical responses, including elastic modulus and compressive strength. According to the findings, Neovius demonstrates superior elastic modulus and compressive strength compared to other structures. This shows that the TPMS type is the first potential factor that strongly affects both elastic modulus and compressive strength. The number of cells and wall thickness emerge as the second and third significant factors directly affecting structural response.
- **Dimension II: Biomimetic Load-Bearing Implants** The second research delves into the creation of biomimetic load-bearing implants tailored to address critical-sized defects in the proximal diaphysis of long bones. Drawing inspiration from the intricate structure of natural bone, this dimension employs a dual-pronged approach. Firstly, a Haversian bone-mimicking strategy is devised for cortical bone, aimed at replicating the mechanical properties of human cortical bone. This involves the generation of various hollow cylinder topologies, and strategically arranging Haversian and Volkmann canals. Subsequently, an optimal structure is selected from this array and merged with the trabecular bone part, represented by triply periodic minimal surface (TPMS)-based lattices (Diamond, Primitive, Split-P, and Gyroid). The outcome is a groundbreaking biomimetic implant design, harmonizing the qualities of both cortical and trabecular bone, poised to address long bone critical-sized defects effectively.
- **Dimension III: Novel Ti6Al4V Split-P TPMS Structures** The third dimension consists of Ti6Al4V Split-P TPMS structures produced through selective laser melting (SLM). Unveiling the potential of this novel manufacturing technique, the research dissects the mechanical responses of these structures, from quasi-static mechanical behavior to stress-strain attributes and plateau stress responses. Finite element analysis provides further insight into the elasto-plastic behavior of the Split-P structures, while unit cell homogenization elucidates the equivalent stiffness tensor. Findings reveal a range of mechanical properties, including elastic modulus, yield strength, and ultimate strength, showcasing the versatility of Ti6Al4V Split-P lattices for load-bearing applications in bone implants.
- **Dimension IV: Irregular HA Voronoi Tessellation Scaffolds for Bone Regeneration** The fourth study explores the potential of irregular Voronoi tessellation scaffolds, with a particular focus on those constructed from Hydroxyapatite (HA). Designed to mimic

the interconnectivity of natural human bone, these irregular Voronoi-based lattice (IVL) structures offer a tailored transition that significantly impacts both mechanical and biological performance. Investigating design parameters such as strut thickness and point space, this research scrutinizes the influence on mechanical properties (stiffness and strength) and geometrical features (pore size, distribution, numbers, surface area, and surface area-to-volume ratio). Four distinct IVL scaffold types are examined, each with its unique attributes. The study underscores the importance of irregularity and morphology in dictating geometrical features and mechanical performance, opening new avenues for bone substitution therapies.

In summary, this doctoral thesis constitutes a comprehensive journey through the realms of biomimetic load-bearing implants, novel Ti6Al4V Split-P TPMS structures, and irregular Voronoi tessellation scaffolds. The culmination of these dimensions offers a promising convergence of innovation in bone tissue engineering, poised to redefine the landscape of bone implant and scaffold design, ultimately enhancing the prospects for critical bone defect treatments and bone regeneration therapies.

## Kokkuvõte

### Biomimikri ja uudsed struktuurid: luuimplantaatide disaini-paradigma edendamine

See doktoritöö alustab luukoetehnoloogia valdkonna uuenduslike strateegiate mitmekülgset uurimist, mille üldeesmärk on täiustada kandvate luuimplantaatide ja -tellingute disaini ja tootmist. Uuring areneb läbi kolme omavahel seotud mõõtme:

- mõõde I: Taguchi-põhine Ti6Al4V TPMS-struktuuride optimeerimine Esimese uurimistöö eesmärgiks on Taguchi meetodi abil optimeerida metalliliste TPMS-i rakustruktuuride mehaanilisi omadusi. SLM-i kasutati võre ja lõplike elementide analüüsi loomiseks, mida kasutati metallipõhiste Neovius, Schoen I-WP ja Schwarz Primitive struktuuride mehaaniliste omaduste hindamiseks. Katsete kavandamisel võeti arvesse geomeetrilisi tegureid, nagu seina paksus, ühikurakkude arv ja TPMS-i tüüp, et uurida geomeetriliste omaduste mõju mehaanilistele reaktsioonidele, sealhulgas elastsusmoodulile ja survetugevusele. Taguchi meetodit rakendatakse süstemaatiliselt nende mõjude uurimiseks ning elastsusmooduli ja survetugevuse optimeerimiseks. Tulemuste kohaselt on Neoviusel teiste struktuuridega võrreldes parem elastsusmoodul ja survetugevus. See näitab, et TPMS tüüp on esimene potentsiaalne tegur, mis mõjutab tugevalt nii elastsusmoodulit kui ka survetugevust. Rakkude arv ja seina paksus on teine ja kolmas oluline struktuurset reaktsiooni otseselt mõjutav tegur.
- mõõde II: biomimeetilised koormust kandvad implantaadid Teises uuringus käsitletakse biomimeetiliste kandvate implantaatide loomist, mis on kohandatud pikkade luude proksimaalse diafüüsi kriitilise suurusega defektide kõrvaldamiseks. Loodusliku luu keerukast struktuurist inspiratsiooni ammutades kasutab see mõõde kahe-suunalist lähenemist. Esiteks on ajukoore luu jaoks välja töötatud Haversi luu jäljendamise strateegia, mille eesmärk on replitseerida inimese kortikaalse luu mehaanilisi omadusi. See hõlmab erinevate õõnessilindrite topoloogiatega genereerimist ning Haversi ja Volkmanni kanalite strateegilist korrastamist. Seejärel valitakse sellest massiivist välja optimaalne struktuur ja liidetakse trabekulaarse luuosaga, mida esindavad kolmekordselt perioodilised minimaalse pinna (TPMS) põhised võred (teemant, primitiivne, split-P ja gyroid). Tulemuseks on murranguline biomimeetiline implantaadi disain, mis ühtlustab nii kortikaalse kui ka trabekulaarse luu omadusi ja on valmis tõhusalt lahendama pika luu kriitilise suurusega defekte.
- mõõde III: uudsed Ti6Al4V Split-P TPMS-struktuurid Kolmas mõõde koosneb Ti6Al4V Split-P TPMS struktuuridest, mis on toodetud selektiivse lasersulatamise (SLM) abil. Avaldades selle uude tootmistehnika potentsiaali, lahkavad uuringud nende struktuuride mehaanilisi reaktsioone kvaasistaatilisest mehaanilisest käitumisest kuni pinge-deformatsiooni atribuutide ja platoo stressireaktsioonideni. Lõplike elementide analüüs annab täiendava ülevaate Split-P struktuuride elastoplastilisest käitumisest, samas kui ühikurakkude homogeniseerimine selgitab välja samaväärse jäikuse tensori. Leiud näitavad mitmesuguseid mehaanilisi omadusi, sealhulgas elastsusmoodulit, volavuspiiri ja lõplikku tugevust, mis näitavad Ti6Al4V Split-P võre mitmekülgset kandvate rakenduste jaoks luuimplantaatides.
- mõõde IV: ebaregulaarsed Voronoi tessellatsioonikarkassid luude regenereerimiseks Neljandas uuringus uuritakse ebaregulaarsete Voronoi tessellatsioonikarkasside potentsiaali, pöörates erilist tähelepanu hüdroksüapatiidist (HA) valmista-

tud karkassidele. Need ebaregulaarsed Voronoi-põhised võre (IVL) struktuurid, mis on loodud imiteerima inimese loomuliku luu vastastikust seotust, pakuvad kohandatud üleminekut, mis mõjutab oluliselt nii mehaanilist kui ka bioloogilist jõudlust. Uurides projekteerimisparameetreid, nagu tugiposti paksus ja punktide ruum, uurib see uurimistöö mõju mehaanilistele omadustele (jäikus ja tugevus) ja geomeetrilistele omadustele (pooride suurus, jaotus, arvud, pindala ja pinna-mahu suhe). Uuritakse nelja erinevat IVL-i karkassitüüpi, millest igaühel on oma ainulaadsed omadused. Uuring rõhutab ebakorrapärasuse ja morfoloogia tähtsust geomeetriliste omaduste ja mehaanilise jõudluse dikteerimisel, avades uusi võimalusi luu asendusravi jaoks.

Kokkuvõttes kujutab käesolev doktoritöö endast terviklikku teekonda läbi biomeetiliste kandvate implantaatide, uudsete Ti6Al4V Split-P TPMS struktuuride ja ebakorrapärase Voronoi tessellatsioonikarkasside valdkondade. Nende mõõtmete kulminatsioon pakub paljutöötavat luukoetehnoloogia innovatsiooni lähenemist, mis on valmis luuimplantaatide ja karkasside kujundamise maastiku uuesti määratlemiseks, suurendades lõppkokkuvõttes kriitiliste luudefektide ravi ja luu regenereerimise teraapiate väljavaateid.



## **Appendix**

### **Paper I**

Rezapourian, M., Kamboj, N., & Hussainova, I. (2021). Numerical study on the effect of geometry on mechanical behavior of triply periodic minimal surfaces. In IOP Conference Series: Materials Science and Engineering, 1140, 012038.





PAPER • OPEN ACCESS

## Numerical study on the effect of geometry on mechanical behavior of triply periodic minimal surfaces

To cite this article: Mansoureh Rezapourian *et al* 2021 *IOP Conf. Ser.: Mater. Sci. Eng.* **1140** 012038

View the [article online](#) for updates and enhancements.

### You may also like

- [Surface curvature in triply-periodic minimal surface architectures as a distinct design parameter in preparing advanced tissue engineering scaffolds](#)

Sébastien B G Blanquer, Maïke Werner, Markus Hannula *et al.*

- [3D printing polyurethane acrylate\(PUA\) based elastomer and its mechanical behavior](#)

Huan Li, Lei Liang, Wenxiang Zeng *et al.*

- [3D printed flexible wearable sensors based on triply periodic minimal surface structures for biomonitoring applications](#)

Mohammad Ebrahim Imanian, Mostafa Kardan-Halvaei, Fatemeh Nasrollahi *et al.*



245th ECS Meeting • May 26-30, 2024 • San Francisco, CA

Present your work at the leading electrochemistry & solid-state science conference.

Network with academic, government, and industry influencers!

Submit abstracts by December 1, 2023

Learn more & submit!



# Numerical study on the effect of geometry on mechanical behavior of triply periodic minimal surfaces

Mansoureh Rezapourian<sup>1</sup>, Nikhil Kamboj<sup>1</sup>, Irina Hussainova<sup>1</sup>

<sup>1</sup> Mechanical and Industrial Engineering Department, Tallinn University of Technology, Tallinn, Estonia

Email: [Mareza@taltech.ee](mailto:Mareza@taltech.ee)

**Abstract.** Metallic cellular structures with triply periodic minimal surfaces (TPMS) is a great approach to enhance multifunctionality for several engineering disciplines. In the present study, we aimed to generate metal-based Neovious, Schoen I-WP and Schwarz Primitive structures, leveraging on TPMS based design methods. Neovious, Schoen I-WP and Schwarz Primitive structures are mathematically formulated. Geometric factors like wall thickness, number of cells and the length of unit cell can affect the mechanical response namely elastic modulus and compressive strength. Herein, Neovious, I-WP and Primitive based materials are fabricated through Selective Laser Melting (SLM) to evaluate the difference between the aforementioned geometrical factors both experimentally and through simulations. The Taguchi method was implemented to explore the effect of geometric factors on structural response. These results were further extended to the structures to optimize the elastic modulus and compressive strength.

## 1. Introduction

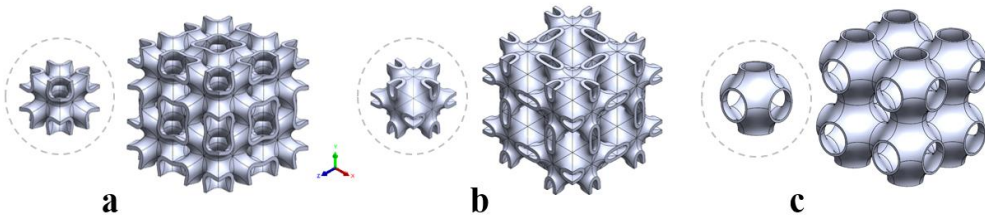
High performance of cellular structures related to excellent energy absorption, lightweight, high strength-weight ratio and excellent thermal, acoustic, mechanical and electrical properties are gaining increasing interest in their specific design. Cellular materials have a wide range of applications in biomedicine, energy absorption and aerospace [1,2]. Recently, many researches have been focused on controllable topology and design of shell-based structures of minimal surfaces which are known as Triply Periodic Minimal Surfaces (TPMS) [2-7]. Triply periodic demonstrates a repeated structure in 3D which is devoid of any self-intersections. TPMS are specified as surfaces with a zero mean curvature at each point on the surface [8]. Nowadays, the fabrication of complex architectures has been perceived due to development of Additive Manufacturing (AM) approaches. Conventional ways to produce cellular materials have many limitations about using material and simplicity in design which can be addressed by application of AM technologies to mitigate the challenges. Selective laser melting (SLM) as a kind of AM process has a great potential to fabricate complex structures [9]. Traditional structures such as a strut-based lattice fabricated by SLM with a lack of continuous transition on their surface and sharp edges demonstrated a poor manufacturability in the AM process [10,11]. It is notable that the absence of nodes and other stress concentration regions in TPMS make them valuable structures with improved strength and toughness [12-15]. The absence of joints and struts in TPMS lattice structure (in



comparison with strut-based architectures) is a considerable benefit in terms of processability [16]. SLM as an AM method is known an appropriate technique to printing metallic structures. Variety of metal powders, such as Ti6Al4V, 316 L stainless steel, Fe–Mn and Zn can be produced with design in TPMS lattice architecture with the help of SLM techniques [17, 18].

The geometric parameters such as wall thickness, sample size, number of surface periods, and the associated iso-value can affect the mechanical response of gyroid structure fabricated of Ti6Al4V by SLM [19]. To quantify the influence of mentioned geometric factors on structural response, OFAT (One Factor at a Time) and Taguchi methods were used and it was shown that an increase in the number of cells and wall thickness strongly effect the elastic modulus and compressive strength whilst a decrease in the sample size and iso-value can lead to improved mechanical response.

This research focuses on finding optimum design and studying the effect of wall thickness and number of cells on a structural response of Neovius (Neo), Schoen I-WP (IWP) and Schwarz Primitive (Pri) structures by implementing Taguchi method. To identify the effect of mentioned factors on mechanical properties, numerical and experimental procedures are required. Validity has been verified by the experimental data of compression test performed on the SLM printed structures of Ti-6Al-4V.



**Figure 1.** TPMS unit cells and designed specimens of a) IWP, b) Neovius and c) Primitive

## 2. Material and method

### 2.1. Modeling and computer-aided design of cellular lattice

In x-y-z spatial coordinates, the TPMS can be approximated using implicit methods and introduced by a level-set function  $\varphi = c$ , which is defined for Neovius (Neo), Schoen I-WP (IWP) and Schwarz Primitive(P) surfaces, respectively in equation (1) [20]:

$$\begin{aligned}\varphi_{Neo} &= 3(\cos kx + \cos kz + \cos ky) + 4kx \cos kz \cos ky = c \\ \varphi_{IWP} &= 2(\cos(kx) \cos(ky) + \cos(ky) \cos(kz) + \cos(kz) \cos(Kx)) - (\cos 2kx + \cos 2ky + \cos 2kz) = c \\ \varphi_P &= \cos kx + \cos ky + \cos kz = c\end{aligned}\quad (1)$$

Where  $k = 2\pi q/l$ .  $q$  defines the number of cells in each direction, and  $l$  is the length of the unit cell. The value of  $c$  controls the shape of surfaces and is known as iso-value parameter. In this research, the value of  $c$  is assumed to be zero. MATLAB software was used to generate the initial surface of TPMS and SolidWorks followed by a CAD software which was used to thicken and create 3D models of TPMS. Labeling of structures has been shown in figure 1. For example, the label of “Neo050 – 2” describes the Neovius structure with wall thickness of 0.5 mm and 2 repeated cells at each edge. Designed models are shown in figure 1.

### 2.2. Material, Machine, and Methods

The Ti6Al4V powder of particle size 20 – 63  $\mu\text{m}$  was printed by Realizer SLM50 metal printer. The associated laser parameters were applied for fabrication with laser power of 84 W, layer thickness of 30  $\mu\text{m}$ , hatch distance of 120  $\mu\text{m}$ , at a scanning speed of 750 mm/s, rotate hatch at 60 degree and 35 degree with y axis was selected to print structure. According to these parameters, the calculated laser energy density is 31.11 J/mm<sup>3</sup>.

### 2.3. Uniaxial compression test and finite element analysis

Pri030-2 specimen with the length size of 16.67 mm in x, y and z direction was chosen for experimental study, which was performed by a servo-hydraulic model 8500 universal testing machine (Instron Ltd., UK). A computational finite element (FE) analysis was performed to evaluate mechanical performance with experimental compression test (figure 3). For static compression at a room temperature, a strain rate of 0.1 mm/s was applied with compressive load and displacement recorded at each 0.1 s intervals during testing. It is notable that in all simulations from now on, the coefficient of the friction was defined as 0.1 to prevent sliding during applied load. The ANSYS 2019 software was used to simulate compression tests.

### 2.4. Taguchi method

To investigate the effect of individual geometric factors on mechanical properties, statistical Taguchi method was implemented to improve the quality of the outcomes. According to full factorial approach, with three significant factors considering three level of each TPMS surface, the designed experiments could reach up to 81 which henceforth is very time-consuming. Therefore, in order to decrease the number of tests without any loss in accuracy, it is recommended to implement Taguchi approach. In total 9 test were designed, which were assigned to three factors such as type of structures; surface wall thickness and number of cells ( $L/l$ ). For designing, a cube, as a bulk sample with constant length 25 mm in x, y and z direction was assumed. Bulk size can be defined by multiple of cell size to the number of cells on each direction. It is noted that with changing cell number, cell size can be altered. This study represents the importance of above-mentioned factors on mechanical properties with Taguchi method. All designed topologies and calculated modulus of elasticity with maximum compressive strength at 4% strain was based on Taguchi orthogonal L9 matrix henceforth represented in Table 1.

**Table 1.** Taguchi L9 Matrix for study of factor influence

Taguchi L9 Matrix		Factors		Results		Porosity (%)
Topology	Structures	Thickness (mm)	Number of cells ( $L/l$ )	Elastic Modulus (GPa)	Max. Stress (MPa)	
IWP050-2	I-WP	0.5	2	2.804	34.336	85.87
IWP040-3	I-WP	0.4	3	3.730	45.718	82.93
IWP030-4	I-WP	0.3	4	3.839	44.084	83.09
Neo050-3	Neovius	0.5	3	6.839	70.121	79.12
Neo040-4	Neovius	0.4	4	7.561	73.060	77.71
Neo030-2	Neovius	0.3	2	2.109	22.318	91.50
Pri050-4	Primitive	0.5	4	2.557	39.633	81.33
Pri040-2	Primitive	0.4	2	0.536	10.030	92.50
Pri030-3	Primitive	0.3	3	0.744	14.108	91.56

## 3. Results

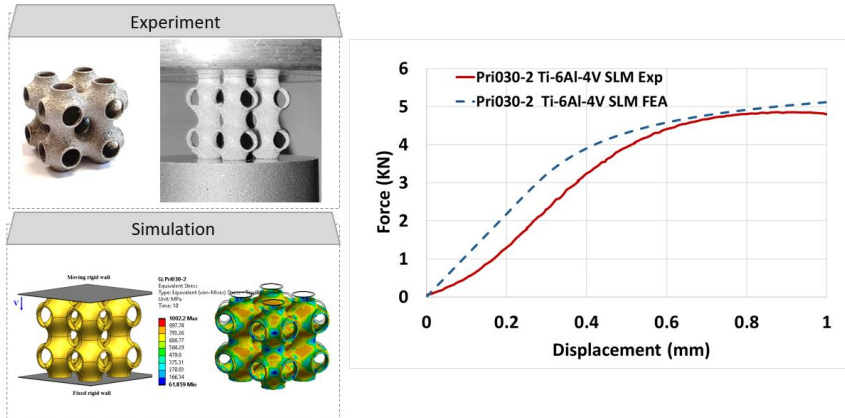
### 3.1. Evaluation compression test result

FE model was performed to validate the result with experiment compression test of Ti6Al4V SLM printed Pri030-2 with 91% porosity and figure 2 represent force-displacement result of both FE analysis and experimental data. The outcomes of elastic modulus and maximum stress indicate 3% and 1.9% deviation in the result of the numerical and experiment which is acceptable and shows strong agreement with the physically obtained result.

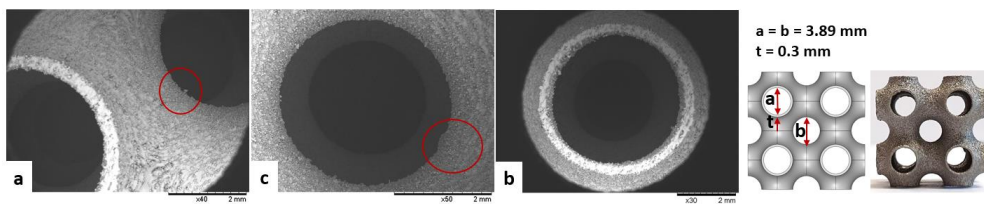
### 3.2. SEM Analysis

The fabricated lattice sample Pri030-2 with its SEM analysis figure 3 which is done for top surface of printed structure to investigate dimensional variations between the designed and 3D-printed structures. The as-fabricated lattice structure clearly followed the CAD model. Residual particles were found

attached to the fabricated structures as shown figure 3(a-c). Residual particles can cause the thickness variations.



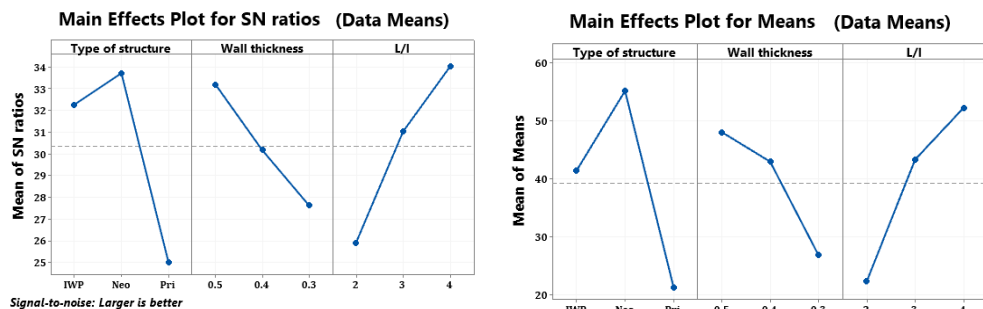
**Figure 2.** Compression test of Pri030-2 at 6% strain at  $t=10$  s in experiment and simulation, contour of equivalent (Von-Mises) stress with undeformed wireframe, force-displacement curve



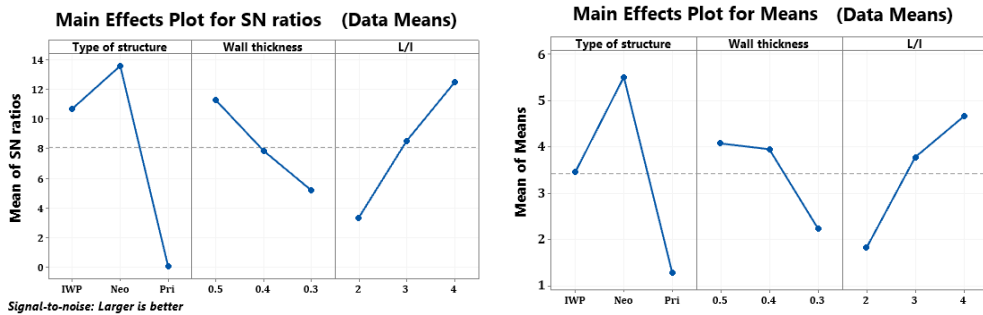
**Figure 3.** SEM image of top surface of printed Pri030-2

### 3.3. Taguchi Method

Based on Taguchi method, a signal to noise ratio (SNR) defines the ratio of calculated data to the error. The accuracy of measured value and calculated data for each test were determined by SNR. In statistical analysis, main effect is the influence of different levels of each factor on outcomes when they are contrary. If SNR and main effect shows the same trend, the obtained data and designed data are correct.



**Figure 4.** SNR and mean values for compressive stress



**Figure 5.** SNR and mean values for elastic modulus

The criteria ‘large is better’ was chosen to maximize the modulus of elasticity and compressive strength. Figure 4 and figure 5 illustrate the main effect and SNR for both modulus of elasticity and compressive strength. As mentioned above, they have the same trend indicating the results to be correct. Table 2 shows the ranking of three factors for compressive strength based on ‘large is better’ criteria. First of all, the average response for all parameters is determined. Then the delta (the difference between minimum and maximum average) is calculated. Finally, all factors are categorized from largest to smallest. The result for the means reveals the type of structure as the best type for maximizing compressive strength with the first rank. The factor number of cells (L/I) and wall thickness are identified as the second and third effective factors.

**Table 2.** SNR and mean values for compressive strength, ‘Larger is better’

Response Table for Signal to Noise Ratios				Response Table for Means			
Level	Type of structure	Wall thickness	L/I	Level	Type of structure	Wall thickness	L/I
1	32.27	33.20	25.90	1	41.38	48.03	22.23
2	33.72	30.17	31.04	2	55.17	42.94	43.32
3	24.99	27.62	34.04	3	21.26	26.84	52.26
Delta	8.73	5.58	8.14	Delta	33.91	21.19	30.03
Rank	1	3	2	Rank	1	3	2

Table 3 shows the ranking of three factors for elastic modulus based on ‘large is better’ method. Similar to compressive strength according to the means result, the type of structures is the first effective factor to maximize elastic modulus, with number of cell (L/I) is in the second ranking. Based on the main effects, the wall thickness of 0.5 and 0.4 mm shows that there is no significant difference for maximizing elastic modulus. Also, the ranking of the SNR represents the same result for all the three factors.

**Table 3.** SNR and mean values for elastic modulus, ‘Larger is better’

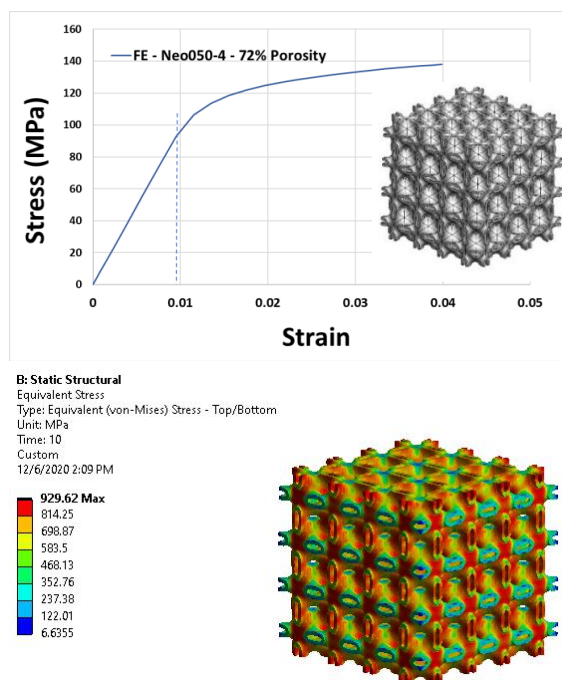
Response Table for Signal to Noise Ratios				Response Table for Means			
Level	Type of structure	Wall thickness	L/I	Level	Type of structure	Wall thickness	L/I
1	10.6929	11.2709	3.3448	1	3.458	4.067	1.817
2	13.5856	7.8666	8.5252	2	5.504	3.943	3.771
3	0.0626	5.2035	12.4711	3	1.279	2.231	4.653
Delta	13.5229	6.0674	9.1263	Delta	4.224	1.836	2.836
Rank	1	3	2	Rank	1	3	2

These results revealed that the Neovious structure has the most influential effect on maximizing both elastic modulus and compressive strength. Increasing number of cells and wall thickness can decrease

the volume fraction which means less densification with less porosity that results heavier structure and higher elastic modulus and compressive strength.

#### 4. Case study

Regarding the Taguchi results, among different levels of selected factors, the optimum values were chosen. As result represents, the most influential effect on mechanical behavior is related to the type of structure, maximum cell number and wall thickness. A custom designed Neo050-4 with defined parameter length of 25 mm, with Neovius structure, wall thickness of 0.5 mm and 4 unit cells in each direction and porosity of 72% was developed using Ti6Al4V material. The outcome represents a simulated yield stress of 93.01 MPa and ultimate strength of 140 MPa and elastic modulus of 9.7555 GPa.



**Figure. 6** Mechanical response of Neo050-4 – FE analysis

#### 5. Conclusions

This study has demonstrated the effect of geometric parameters on mechanical response of Neovius (Neo), Schoen I-WP (IWP) and Schwarz Primitive (P) complex structures based on a statistical approach. Triply Periodic Minimal Surfaces (TPMS) were produced from Ti6Al4V alloy using SLM. A numerical model has been defined to validate with experimental data which shows a close agreement. Based on the results, Neovius (Neo) has shown to outperform other structures in terms of strength and stiffness, which can lead to significant effect on elastic modulus and compressive strength. The number of cells and wall thickness are the second and third important factors which can affect structural response directly. A candidate structure of Neovius structure with wall thickness of 0.5 mm and cell number of 4 with the porosity of 72% was developed to validate the result and FE analysis of structural response indicated high elastic modulus and compressive yield strength respectively (9.75 GPa) and (93.01 MPa).

#### 6. Acknowledgements.

This work was supported by the Estonian Research Council grant PRG643 (I. Hussainova).



## 7. References

- [1] L I Gibson M F Ashby 1997 Cellular solids: structure and properties. New York: Cambridge university press
- [2] M Helou, S Kara 2018, Design, Analysis and manufacturing of lattice structures: An overview *Int. J. Comput. Integr. Manuf.* **31** 243–261
- [3] I Maskery, L Sturm, A O Aremu, A Panesar, C B Williams, C J Tuck, R D Wildman, I A Ashcroft, R J M Hague 2018 Insights into the mechanical properties of several triply periodic minimal surface lattice structures made by polymer additive manufacturing, *Polymer* **152** 62–71
- [4] O Al-ketan, R Rezgui, R Rowshan, H Du, N X Fang 2018 Micro architected stretching-dominated mechanical metamaterials with minimal surface, *Topologies* **20** 1–15
- [5] I Maskery, N T Aboulkhair, A O Aremu, C J Tuck, I A Ashcroft 2017 Compressive failure modes and energy absorption in additively manufactured double gyroid lattices *Addit. Manuf.* **16** 24–9
- [6] L Bai, C Gong, X Chen, Y Sun, J Zhang, L Cai, S Zhu, S Q Xie 2019 Additive manufacturing of customized metallic orthopedic implants: Materials, structures, and surface modifications *Metals (Basel)* **9** 1004
- [7] A Ataei, Y Li, M Brandt, C Wen 2018 Ultrahigh-strength titanium gyroid scaffolds manufactured by selective laser melting (SLM) for bone implant applications *Acta Mater.* **158** 354–68
- [8] L Han, S Che 2018 An Overview of Materials with Triply Periodic Minimal Surfaces and Related Geometry: From Biological Structures to Self-Assembled Systems *Adv. Mater.* **30** 1705708
- [9] A Nazir, K M Abate, A Kumar, J Jeng-Ywan 2019 A state-of-the-art review on types, design, optimization, and additive manufacturing of cellular structures *Int J Adv Manuf. Technol* **104** 3489–3510
- [10] M Mazur, M Leary, S Sun, M Vcelka, D Shidid, M Brandt 2016 Deformation and failure behavior of Ti–6Al–4V lattice structures manufactured by selective laser melting (SLM) *Int J Adv Manuf. Technol* **84** 1391–411
- [11] L Liu, T Minasyan, N Kamboj, S Aydinyan, I Hussainova, 2020 Bio-inspired TiB<sub>2</sub>-TiB-TiN lattices by selective laser melting *Mater. Lett.* **277** 128337
- [12] M-T Hsieh, B Endo, Y Zhang, J Bauer, L Valdevit. 2019 The mechanical response of cellular materials with spinodal topologies *J. Mech. Phys. Solids* **125** 401–19
- [13] R Schwaiger, L R Meza, X Li 2019 The extreme mechanics of micro- and Nano-architected materials *MRS Bull.* **44** 758–65
- [14] S C Han, J W Lee, K Kang, 2015 A new type of low-density material: Shellular *Adv. Mater.* **27** 5506–11
- [15] A E Garcia, C S Wang, R N Sanderson, K M McDevitt, Y Zhang, L Valdevit, D R Mumm, A Mohraz, R Ragan 2019 Scalable synthesis of gyroid-inspired freestanding three-dimensional graphene architectures *Nanoscale Adv.* **350** 1508–13
- [16] K A Kamran, and K R Abu Al-Rub 2017 Time dependent response of architected Neovius foams *Int. J. Mech. Sci.* **126** 106–19
- [17] C Y Yap, C K Chua, Z L Dong, Z H Liu, D Q Zhang, L E Loh, and S L Sing, 2015 Review of selective laser melting: materials and applications *Appl. Phys. Rev.* **2** 041101
- [18] M Antonov, R Ivanov, Y Holovenko, D Goljandin, R Rahmaniahranjani, L Kollo, I Hussainova, 2019 3D printing of plain and gradient cermet with efficient use of raw materials *Key Eng. Mater.* **799** 239–245
- [19] E Yang, L Leary, B Lozanovski, D Downing, M Mazur, A Sarker, A Khorasani, A Jones, T Maconachie, S Bateman, M Easton, M Qian, P Choong and M Brandt 2019 Effect of geometry on the mechanical properties of Ti-6Al-4V Gyroid structures fabricated via SLM: A numerical study *Mater. Des.* **184** 0264–1275
- [20] M T Hsieh and L Valdevit 2020 Minisurf – A minimal surface generator for finite element modeling and additive manufacturing *Software Impacts* **6** 100026.

**Paper II**

Rezapourian, M., Kamboj, N., Jasiuk, I., & Hussainova, I. (2022). Biomimetic design of implants for long bone critical-sized defects. *Journal of the Mechanical Behavior of Biomedical Materials*, 134, 105370.





## Biomimetic design of implants for long bone critical-sized defects

Mansoureh Rezapourian<sup>a</sup>, Nikhil Kamboj<sup>a,b</sup>, Iwona Jasiuk<sup>c</sup>, Irina Hussainova<sup>a,\*</sup>

<sup>a</sup> Department of Mechanical and Industrial Engineering, Tallinn University of Technology, Tallinn, Estonia

<sup>b</sup> Turku Clinical Biomaterials Center-TCBC, Department of Biomaterials Science, Faculty of Medicine, Institute of Dentistry, University of Turku, FI-20014, Turku, Finland

<sup>c</sup> Department of Mechanical Science and Engineering, University of Illinois at Urbana-Champaign, Urbana, IL, 61801, USA

### ARTICLE INFO

#### Keywords:

Bone  
Haversian canal  
Porous implant  
Finite element analysis  
Triply periodic minimal surfaces  
Mechanical properties

### ABSTRACT

This computational study addresses new biomimetic load-bearing implants designed to treat long bone critical-sized defects in a proximal diaphysis region. The design encompasses two strategies: a Haversian bone-mimicking approach for cortical bone and lattices based on triply periodic minimal surfaces (TPMS) for trabecular bone. Compression tests are modeled computationally via a non-linear finite element analysis with Ti6Al4V alloy as a base material. Nine topologies resembling cortical bone are generated as hollow cylinders with different channel arrangements simulating Haversian (longitudinal) and Volkmann (transverse) canals to achieve properties like those of a human cortical bone (Strategy I). Then, the selected optimal structure from Strategy I is merged with the trabecular bone part represented by four types of TPMS-based lattices (Diamond, Primitive, Split-P, and Gyroid) with the same relative density to imitate the whole bone structure. The Strategy I resulted in finding a hollow cylinder including Haversian and Volkmann canals, optimized in canals number, shape, and orientation to achieve mechanical behavior close to human cortical bone. The surface area and volume created by such canals have the maximum values among all studied combinations of transverse and longitudinal channels. Strategy II reveals the effect of interior design on the load-bearing capacity of the whole component. Between four types of selected TPMS, Diamond-based lattice and Split-P have more uniform stress distribution, resulting in a superior load-bearing efficiency than Gyroid and Primitive-based design showing less uniformity. This work offers a new design of the bone-mimicking implant, with cortical and trabecular bone components, to repair long bone critical-sized defects.

### 1. Introduction

Over the past decades, the use of implants and scaffolds has rapidly grown, driven by an aging population. Lightweight structures possessing suitable strength and stiffness have been widely used for load-bearing applications, including clinical solutions in orthopedics and bone tissue engineering (BTE). Implants and scaffolds are being developed to support osteogenesis and vascularization and replace damaged tissues in critical-sized bone defects (Bazaka et al., 2021).

With the rapid development of Additive Manufacturing (AM) techniques to implement complex designs found in nature in the final product, it has become possible to produce patterns optimized for a particular function and with specific architecture across multiple length scales (Wang et al., 2016; Bose et al., 2013). Biomimicry (or bio-inspiration) guides the design of new smart materials and complex-shaped structures such as bone. Bone possesses dense exterior

(cortical bone) and sparse interior (trabecular bone) architectures with porosity and composition changing over a person's life (Liu et al., 2016; Sabet et al., 2016). The exterior constructs have to match the complicated geometry of a defect site. The scaffolds or implants have to support networks of interconnected pores and facilitate the ingrowth of blood vessels to provide the tissue with oxygen and other nutrients (Wang, 2004). The cortical (compact) bone's porosity is 5–30%, with Haversian canals running longitudinally through the center of osteons and transversely oriented Volkmann canals. The spongy trabecular (cancellous) bone possesses 30–95% porosity (Callens et al., 2021; McNamara, 2017). The implant's pore size and porosity play a critical role in bone re-growth and vascularization. Optimized porosity enhances the cellular response of the scaffolds and implants (Bilgiç et al., 2020; Cardinali et al., 2020; Aversa et al., 2020; Borciani et al., 2020; Karageorgiou and Kaplan, 2005; Weatherholt et al., 2012). Generally, the pore sizes >300  $\mu$  m enhance the osseointegration process and the formation of

\* Corresponding author.

E-mail address: [irina.hussainova@taltech.ee](mailto:irina.hussainova@taltech.ee) (I. Hussainova).

<https://doi.org/10.1016/j.jmbbm.2022.105370>

Received 23 February 2022; Received in revised form 9 May 2022; Accepted 10 July 2022

Available online 14 July 2022

1751-6161/© 2022 Elsevier Ltd. All rights reserved.

vascularization capillaries (Otsuki et al., 2006; Kayacan et al., 2017).

Ideally, the bone implants and scaffolds should have comparable properties to the bone to alleviate stress shielding. When elastic moduli of implants are higher than the surrounding tissue, the bone does not carry a sufficient portion of the load and resorbs, leading to implant loosening (Callens et al., 2021; Kaur and Singh, 2019; Li et al., 2021; Zhang et al., 2020a). The modulus of elasticity of a human cortical bone is 18.6–20.7 GPa, and of trabecular bone is 0.02–2.0 GPa (Wang et al., 2016; Rho et al., 1993; Hunt et al., 1998; Goldstein, 1987). The compressive strengths of cortical and trabecular bone are 100–230 MPa and 2–12 MPa, respectively (Bilgiç et al., 2020; Morgan et al., 2018).

Titanium and its alloys are widely accepted biomaterials of well-proven biocompatibility combined with high strength, good fracture toughness, and corrosion resistance (Sarraf et al., 2021; Ma et al., 2020; Al Hashimi et al., 2022). However, a relatively high modulus of elasticity and strength of these materials, exceeding the characteristic properties of bone, may result in a predominant distribution of the stresses through the implant and lead to a poor osteointegration, which is known as the stress shielding phenomenon (Bobbett et al., 2017). Therefore, improving biomechanical integration through topology/architecture optimization of the scaffold is one of the challenges for the BTE. Finite element analysis allows studying the stress fields and relationships between the structural design and mechanical properties (Sabet et al., 2021).

The topological characteristics of human trabecular bone display high similarity to the triply periodic minimal surface (TPMS) architectures, which can be described as periodic infinite frameworks with a zero mean-curvature at any point along three independent axes (Maskery et al., 2018; Zhang et al., 2018; Myakinin et al., 2021; Al-Ketan and Abu Al-Rub, 2019; Kapfer et al., 2011). The geometric characteristics of TPMS porous structures, such as smooth surfaces without sharp edges or corners, distinguish them from other porous architectures and make them attractive candidates for bone replacement due to their biomimicry and the tunable porosity-to-strength ratio (Barber et al., 2021; Lehder et al., 2021; Abueidda et al., 2017).

TPMS can be categorized into network-based and sheet-based structures (Kapfer et al., 2011). The network-based TPMS structure is divided into two subspaces, one filled and another left empty. The sheet-based TPMS structure is created by thickening a minimal surface. The high surface area to volume ratio and better mechanical properties of sheet-based TPMS are the advantages of sheet-based systems over network-based ones (Al-Ketan and Abu Al-Rub, 2019; Kapfer et al., 2011). In this paper, we utilize the sheet-based TPMS structures.

The significant advantage of TPMS sheet-like constructs over strut-like structures is a high surface area combined with a more uniform stress distribution under loading (Kamboj et al., 2021; Afshar et al., 2018). Also, TPMS can adequately mimic the interconnected trabecular bone architecture. Tailoring the parameters of the TPMS structures, unit cell shape, and porosity distribution can be controlled to match the mechanical properties of the natural human bone (Ataee et al., 2018; Cai et al., 2019; Castro et al., 2019; Wang et al., 2019; Vijayavenkataraman et al., 2018). TPMS representing a trabecular part of the bone with a cortical-like shell can facilitate bone formation in the implant's core and reinforce the implant's load-bearing capacity (Charbonnier et al., 2020; Xiong et al., 2020; Vance et al., 2018; Langton et al., 2012).

This work studies the compressive behavior of anatomically matched bioinspired implants composed of cortical bone mimicking canals (Haversian and Volkmann) and trabecular parts with the internal TPMS porous structures. Finite element analysis was used to reveal the behavior of the designed architectures reaching the stiffness comparable to bone's stiffness. In the first Strategy (Strategy I), a hollow cylinder including Haversian and Volkmann-like canals of nine different morphologies was considered as a cortical bone part to find the optimal design allowing to mimic the mechanical properties of a human cortical bone. In the second Strategy (Strategy II), four types of sheet-based TPMS structures were generated as a trabecular part of the bone. The

optimal design obtained from Strategy I was then merged with the structures in Strategy II to create the model of the whole bone component. Herein, the bone-mimicking implant's design optimization addresses the long bone critical-sized defects that define the defects with lengths greater than 1–2 cm. Naturally, critical-sized defects cannot be healed without intervention and surgical stabilization (Kamboj et al., 2021; Neffe et al., 2014; Schemitsch, 2017; Nauth et al., 2018). Fig. 1 shows the schematic representation of the designed porous implant considering Haversian and Volkmann canals.

## 2. Materials and methods

### 2.1. Strategy I – design of the cortical bone mimicking implant

This section presents the design of the implant mimicking cortical bone. Nine topologies representing different arrangements of Haversian and Volkmann canals were considered to imitate the anatomy of a cortical bone. The CAD software SolidWorks (Dassault Systems SolidWorks Corporation, Waltham, Massachusetts, USA) was used to create the architectures of the compact part, and ANSYS R2 19.4 software was used to predict the structural behavior to achieve the optimal design with the stiffness and strength in the range of a healthy human cortical bone. Several factors such as the shape of the cross-section, size, the number of canals, and the orientation of canals along the hollow cylinder were studied computationally under a static compression test loading. The target properties were those of the healthy human cortical bone, which has an elastic modulus of 18.6–20.7 GPa. In the design, a hollow cylinder with the outer and inner diameters of 10 mm and 8 mm and a height of 11 mm was considered for a compact part. The outer and inner diameters were chosen based on tibiae from postmenopausal donors (Schmidutz et al., 2021; Zhang et al., 2020b). The outcome of this section is the optimal design, including the Volkmann and Haversian canals, that meets the mechanical properties of the cortical bone while maximizing them.

To explore the relationship between the geometrical characteristics such as size, shape, orientation, and the number of Haversian and Volkmann canals and mechanical properties such as the stiffness and yield strength, different implant structural designs with various architecture porosities were created. For this purpose, 8, 16, and 20 Haversian canals with constant diameter of 0.6 mm were selected, and 4 and 5 Volkmann canals were created with the three different diameter sizes of 0.65, 0.7, and 0.8 mm. Pore size and interconnectivity of the pores play a critical role in designing implants or scaffolds for the regeneration of bone tissue. In general, a pore size >600  $\mu\text{m}$  is an anticipated size for vascularization and bone formation. Generally, pore sizes less than 250 result in reduced infiltration of cells and vascular capillaries (Peng et al., 2019; Wu et al., 2021). The geometrical characteristics of nine models (D1–D9) are listed in Table 1. Fig. 2 indicates the shapes of Haversian and Volkmann canals (a–f) and four samples out of nine final topologies (g–j) to display the connectivity of the canals (perpendicularly) passing through the hollow cylinder (considered as the compact part of bone in this study). Fig. 3 represents the wireframe view of all nine topologies in a combination of two types of canals. The details of the amount of the surface area and the volume provided by the combinations of Volkmann and Haversian are presented in Table 2 for the designs of D4–D9.

To study the effect of the canals' cross-sections on the mechanical properties and porosity, circular and elliptical cross-sections were selected for Volkmann canals. In contrast, all the Haversian canals were designed to have a circular cross-section only. For the elliptical cross-section, the sizes of 0.55 mm and 1.4 mm denote the minor semi-axis and major semi-axis, respectively, with the major axes being in the longitudinal direction of the cylinder. Helical and vertical patterns were considered for Haversian canals, and helical and horizontal types were chosen to design Volkmann canals. In the helical design for the Volkmann canals, 5 mm and 1.46 represent the pitch size and the amount of revolution. In designing the helical Haversian channels, these two

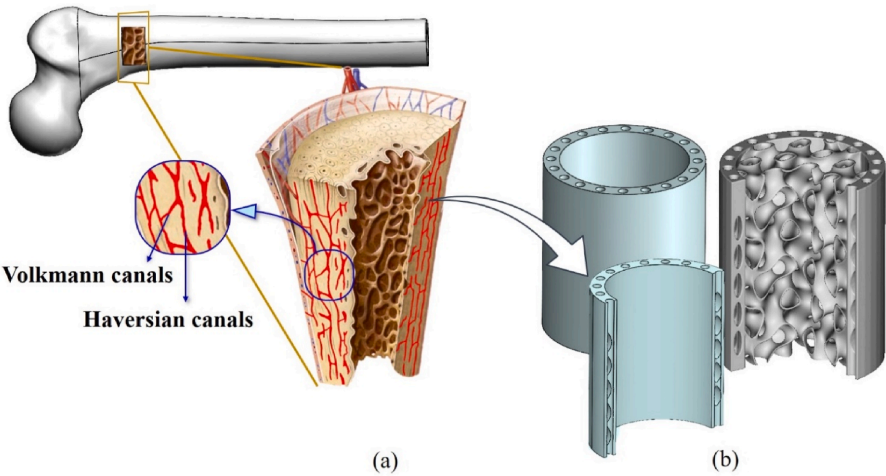


Fig. 1. Schematic representation of a) Cortical bone component of the implant including Haversian and Volkmann canals with the inspiration of natural bone (Modified image from (Basicmedical Key Fastest Basicmedical Insight, 2022)) and b) Cortical component merged with trabecular part to create a whole bone architecture.

**Table 1**  
Geometrical properties of a hollow cylinder as a cortical component (H (Haversian canals), V (Volkmann canals), RD (Relative Density), d (Diameter of Haversian canals and Volkmann canals), Num (Number of Haversian canals and Volkmann canals), Ver. (Vertical), Hor. (Horizontal), CS (Cross-section), c (Circle) and e (Ellipse)).

Design	Volume	RD	Porosity	Num/d of H	CS of H	Num/d of V	CS of V	Shape of H/V.
D1	206.47	0.66	0.34	16/0.6	c	5/0.8	c	Ver./Hor.
D2	248.3	0.79	0.21	8/0.6	c	4/0.7	c	Ver./Hor.
D3	240.26	0.77	0.23	20/0.6	c	4/0.4	c	Ver./Hor.
D4	218.03	0.70	0.30	20/0.6	c	5/0.65	c	Ver./Hor.
D5	218.05	0.70	0.30	20/0.6	c	5/0.65	c	Helix/Helix
D6	218.04	0.70	0.30	20/0.6	c	5/0.65	c	Helix/Hor.
D7	218.02	0.70	0.30	20/0.6	c	5/0.65	c	Ver./Helix
D8	195.29	0.63	0.37	20/0.6	c	5/0.55,1.4	e	Ver./Hor.
D9	195.18	0.63	0.37	20/0.6	c	5/0.55,1.4	e	Ver./Helix

parameters were 110 mm and 0.1, respectively.

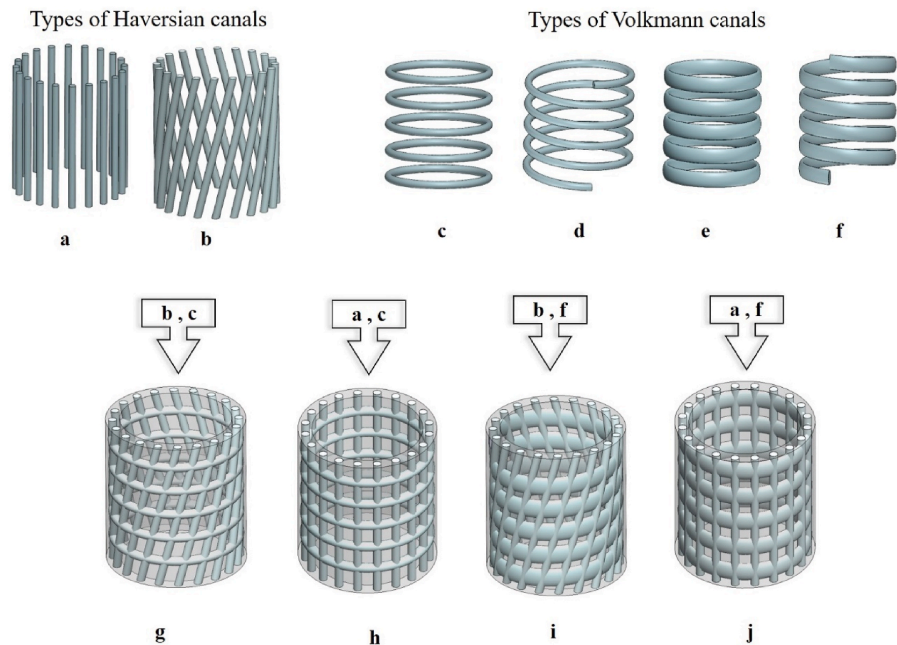
2.1.1. Strategy II – Whole bone model incorporating the cortical and trabecular bone

The inner part of the bone, a trabecular bone, affects the whole bone's properties. To design a trabecular part, four types of the lattice structure of TPMS were generated and merged with the resulting designs of Strategy I. Boolean union tools were used to join the cortical component with the trabecular part to create a whole bone and to replicate the topology of human bone. Gyroid, Diamond, Split P, and Primitive TPMS structures were utilized to architect the trabecular part. All designs of the trabecular bone-mimicking parts were assigned to have 15% relative density (RD) and 85% porosity. The design objective was to find the architectures giving the maximum yield strength and stiffness. A compressive test was performed computationally using ANSYS R2 19.4 software to predict the mechanical response. The average stress was computed by dividing the resultant force of the bottom plate by the whole cross-sectional area of a cylinder with a 10

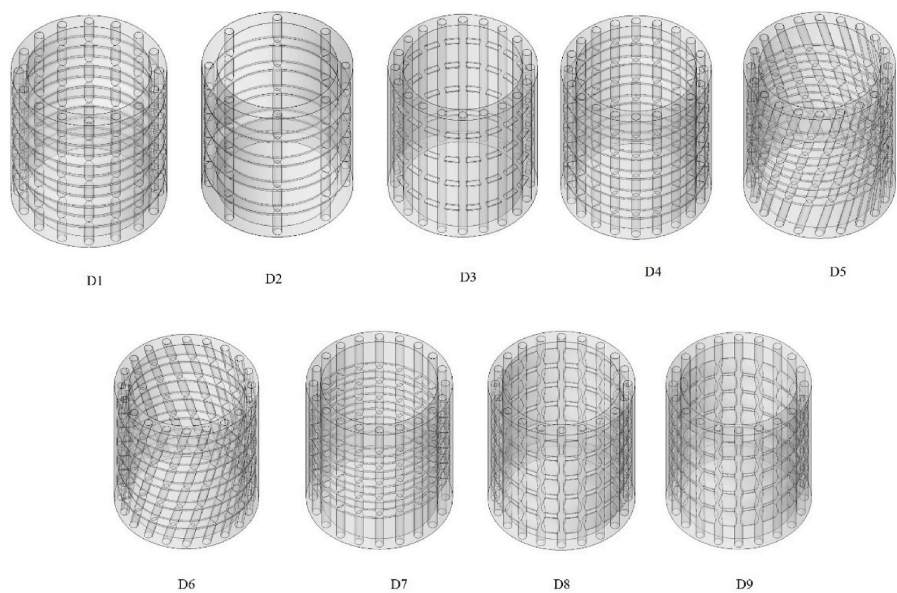
mm diameter. The Gyroid, Diamond, and Primitive are popular types in the minimal surface category. The Split P structure stands out due to the large surface area factor and the high surface-area-to-volume ratio compared to others, and a high curvature to enhance cell growth. These four types of structures were selected due to their robust mechanical properties (compressive response and toughness) and biomedical applications (Zhang et al., 2022; Yang et al., 2019; Miralbes et al., 2020; Bai et al., 2020). Fig. 4 illustrates the unit cells of the chosen architectures. In the three-dimensional coordinate system, TPMS can be defined using implicit methods and introduced by the function of  $\varphi = r$ , which is defined for Gyroid, Split P, Diamond, and Primitive surfaces, respectively, in equations (1)–(4) (Lehder et al., 2021; Kim et al., 2015). Fig. 4 shows the unit cells and the influence of changing  $r$  on the geometrical designs.

$$\varphi_{Gyroid} = \sin(X)\cos(Y) + \sin(Y)\cos(Z) + \cos(X)(Z) = r \tag{1}$$

$$\varphi_{Split\ P} = 1.1(\sin(2X)\sin(Z)\cos(Y) + \sin(2Y)\sin(X)\cos(Z) + \sin(2Z)\sin(Y)\cos(X)) - 0.2(\cos(2X)\cos(2Y) - \cos(2Y)\cos(2Z) + \cos(2Z)\cos(2X)) - 0.4(\cos(X) + \cos(Y) + \cos(Z)) = r \tag{2}$$











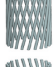

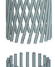



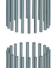



**Fig. 2.** Types of Haversian and Volkmann canals in the hollow cylinder mimicking the cortical bone structure. a) Vertical Haversian canals, b) Helical Haversian canals, c) Horizontal Volkmann canals with a circular cross-section, d) Helical Volkmann canals with a circular cross-section, e) Horizontal Volkmann canals with an elliptical cross-section, f) Helical Volkmann canals with an elliptical cross-section, g-h) Four samples out of nine final topologies to display connectivity of Haversian and Volkmann canals passing through the compact part (Hollow cylinder).

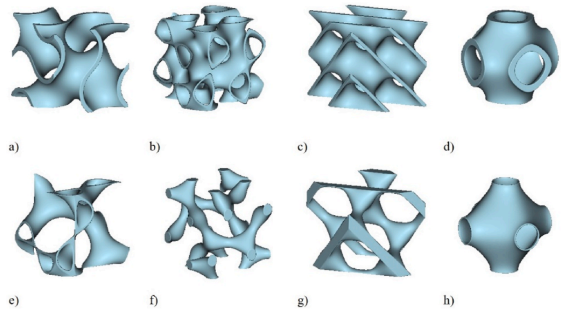


**Fig. 3.** Resulting Haversian bone mimicking implant designs with different numbers of Haversian and Volkmann canals, with different diameters, cross-sections, shapes, orientations, and interconnected porosity for the cortical component.



**Table 2**  
The detail of the amount of the volume and the surface area can be provided in the combination of different types of Haversian and Volkmann canals.

Corresponding design	Type of Haversian Canals	Types of Volkmann canals	Surface area (mm <sup>2</sup> )	Volume (mm <sup>3</sup> )
D1			696.11	120.82
D2			419.11	68.41
D3			674.71	105.73
D4			714.69	109.11
D5			722.37	109.11
D6			721.44	109.11
D7			715.61	109.11
D8			881.49	149.26
D9			881.13	147.69



**Fig. 4.** Topology of TPMS architectures and the effect of iso-value on the geometry a) Gyroid, b) Split P, c) Diamond, and d) Primitive at  $r = 0$ ; e) Gyroid and f) Split P, g) Diamond, and h) Primitive at  $r = 0.7$ .

$$\begin{aligned} \varphi_{Diamond} &= \sin(X)\sin(Y)\sin(Z) + \sin(X)\cos(Y)\cos(Z) + \cos(X)\sin(Y)\cos(Z) \\ &\quad + \cos(X)\cos(Y)\sin(Z) \\ &= r \end{aligned} \tag{3}$$

$$\varphi_{Primitive} = \cos(X) + \cos(Y) + \cos(Z) = r \tag{4}$$

$r$  is an iso-value parameter, which can control the geometry variation. With the change in iso-value  $r$  from 0 to 0.7, the topology of TPMS and associated geometrical properties are changed. An increase in the iso-value reduces the surface area (SA), and, as a result, the surface area-

**Table 3**  
Overview of morphological properties of each TPMS lattice (without cortical part).

	Thickness (mm)	SA (mm <sup>2</sup> )	SA/VR
Gyroid	0.31	888.17	10.66
Split P	0.23	1462.71	17.56
Diamond	0.26	1087.66	13.06
Primitive	0.18	681.71	8.19

to-volume ratio (VR) can reach the minimum value. In bone tissue engineering, the SA and SA-to-VR can be crucial in cell growth and mass transport (Vijayavenkataraman et al., 2018; Kamboj et al., 2020) and can be considered the critical structural characteristics. This study discusses four types of TPMS structures with the iso-value of zero, which can produce the highest level of SA.

The implants were generated by commercial software nTop Platform (3.13.4, nTopology, New York, NY, USA). The scaffolds have 4 mm unit sizes in the x, y, and z-directions, and the developed porous implants have asymmetric topology in the z-direction. The relative density (RD) of all the structures was calculated automatically by the software and using the block “Mass Properties from Body.” The computed value of RD for all topologies is 15%, and the corresponding porosity is 85%. The value of surface area (SA) and surface area to volume ratio (SA/VR) were also calculated automatically using the software. Table 3 illustrates the geometrical characteristics, and Fig. 5 shows the implants separately and the merged ones with the compact part with the top view of the whole bone implant.

The implant designs from Strategy II were merged with the optimal design obtained in Strategy I. The structures were meshed with the high-quality tetrahedral meshes in nTopology software using the “Robust Tetrahedral mesh” block and then imported to ANSYS software as an input format for finite element analysis discussed in the next section.

2.2. Simulation

To study the non-linear elastic-plastic efficiency of the whole bone using FEM, Bilinear Isotropic Hardening (BISO), more specifically the elastic-perfectly plastic model, was the constitutive law employed for all the implants in this study. Ti6Al4V was used as a material, with mechanical properties listed in Table 4. ANSYS R2 19.4 software was used to predict the behavior of the implants under compressive load. Two cylindrical plates with a diameter of 6 mm and a thickness of 0.2 mm were placed on the top and bottom of the structures as rigid bodies. Fig. 6a shows the implant under compressive load with the specified boundary conditions. The base plate was subjected to the fixed displacement boundary conditions (BC), and the top plate was allowed to move in the z-direction while the movement in the x- and y-directions was fully constrained. Fig. 6b and c shows a fine mesh for the cortical part (D9) and whole implant, including the cortical and trabecular part, with the interior design of Gyroid separately, respectively. Such fine mesh was considered for all the structures in this study, as discussed below.

The FE models were meshed with quadratic tetrahedral mesh elements, and mesh sensitivity analysis was performed to ensure accuracy. The optimal mesh size was selected to minimize the computational time without affecting accuracy. For this purpose, four mesh sizes, 0.2, 0.15, 0.12, and 0.1 mm, were tested. Many elements lead to high computational time in the 0.1 mm mesh size case. The 0.2 mm mesh size resulted in a higher computed elastic modulus with fewer elements. Fig. 7 shows the result of the mesh sensitivity study for the whole porous implant (with compact and trabecular parts) with the internal topology of Primitive as a sample to show the convergence of elastic modulus. As it can be seen, there is no significant difference in the elastic modulus in the three sizes of 0.15, 0.12, and 0.1 mm. Therefore, a mesh size of 0.15 mm was used for all the structures to run the FE analysis. The number of



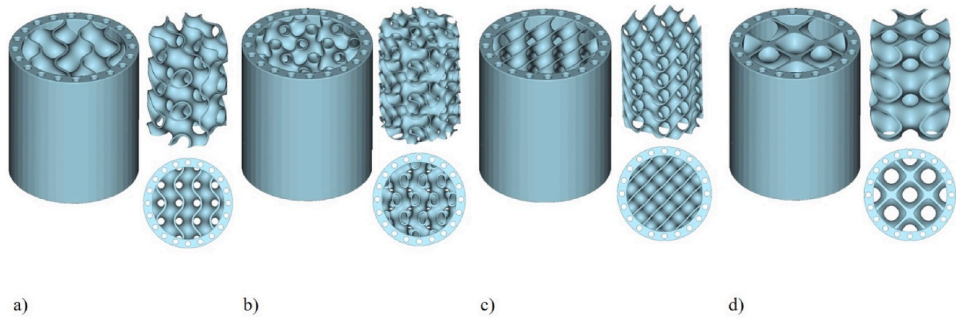


Fig. 5. Four types of generated implants and merged with the compact part and their top view, a) Gyroid, b) Split P, c) Diamond, and d) Primitive.

**Table 4**  
Mechanical properties of Ti6Al4V used in finite element analysis (Arjunan et al., 2020).

Material properties	Value
Elastic modulus	104.80 (GPa)
Yield strength	860.0 (MPa)
Poisson's ratio	0.30
Density	4428.78 (kg/m <sup>3</sup> )

finite element nodes and elements for four mesh element sizes is listed in Table 5 for the Primitive TPMS structure with the maximum and minimum element size and solution time and the final elastic modulus value for each mesh size. The same approach was used for the compact bone parts.

Table 6 shows the nodal and elemental distribution of the converged FE model of four topologies of TPMS merged with the compact part at the target size of 0.15 mm element size. In Table 6, the “Gyroid” means the combination of cortical components with the Gyroid design used for the trabecular part. The global elemental matrix was solved using an AMD Ryzen 9 3900X- 12 Core Processor 3.79 GHz with 64 GB RAM.

In the FE analysis, the displacement of 0.1 mm was applied to the compact parts, and the displacement of 0.15 mm was applied to the merged compact and trabecular structures on the top plate in the z-direction to reach the plastic state. The displacement was applied in 30 sub-steps. Large deformation theory was used to achieve the final result.

The base material’s behavior was modeled as elastic-perfectly plastic with the tangent modulus of zero in the plastic region to explore the elastic modulus and yield strength, which were the mechanical properties of interest.

3. Results and discussion

3.1. Strategy I - Elastic-plastic behavior of a cortical component

The finite element analysis was carried out on the different designs to find the relationship between the cortical bone’s elastic modulus, strength, and porosity. To reach the optimum design for the mechanical properties of the cortical bone, vertical (Haversian) and horizontal (Volkmann) canals of different numbers, diameters, shapes, and orientations were considered. To validate the FE result compression test was carried out on the model of the SC1. An associated scaffold design is detailed elsewhere (Arjunan et al., 2020). The fixed support was placed on a bottom plate, and −10% displacement was applied in the z-direction on the top plate. The displacement was constrained in x- and y-directions to avoid sliding during the compression tests. Bilinear isotropic hardening was considered for a material model, as mentioned in Table 4. For this purpose, the elastic modulus (*E*) and yield stress ( $\sigma_y$ ) were computed, and the results were compared. The results, represented in Table 7, showed good agreement.

The optimum design was selected using the nine simulations of the compression test. The force-displacement data obtained from finite

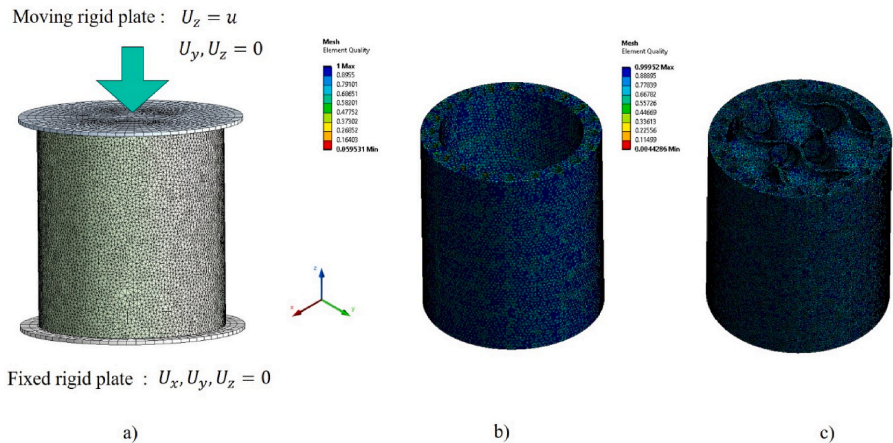


Fig. 6. a) Boundary conditions on the implant used in FE analysis, and fine mesh used in the numerical model a) mesh of D7 (cortical component) and c) mesh of the whole implant with gyroid topology.

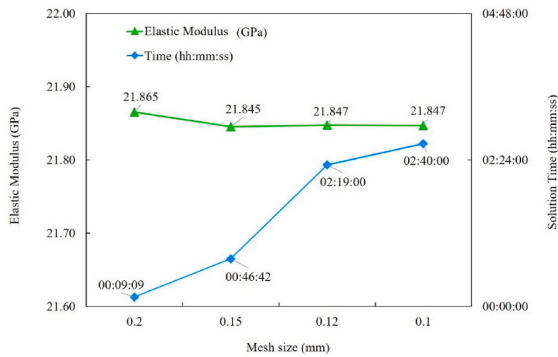


Fig. 7. Sensitivity of the Elastic modulus to mesh element size and the model solving time as a function of the element size for the whole implant with the Primitive interior design.

Table 5

Detail of converged Elastic modulus for one topology of Primitive TPMS merged with the compact part with the solution time, element, and node numbers with the detail of the minimum and the maximum length of the elements used in the FE simulation.

Mesh element size (mm)	Solution Time (hh: mm: ss)	Elastic modulus (GPa)	Element numbers	Nodes Numbers	Min length (mm)	Max length (mm)
0.2	00:09:09	21.865	383271	640931	1.024e-03	0.21
0.15	00:46:42	21.845	810045	1295002	8.09e-03	0.16
0.12	02:19:00	21.847	1628064	2507836	2.73e-03	0.13
0.1	02:40:00	21.847	2811127	4225753	5.53e-04	0.11

Table 6

Nodal and elemental data with the detail of minimum and maximum element length with the final implant’s solution time, including four topologies of TPMS, merged with the compact part used in the FE simulation.

Implant design	Total elements	Total nodes	Min length (mm)	Max length (mm)	solution time (hh:mm:ss)
Gyroid	868277	1391623	9.83E-04	0.16	1:13:00
Diamond	819890	1348193	2.01E-03	0.16	0:46:24
Split P	837835	1409273	9.05E-04	0.16	1:09:00
Primitive	810045	1295002	8.09E-03	0.16	0:46:42

element analysis were used to obtain the stress-strain curves. The stress was computed by dividing the resultant force by the whole circular cross-sectional area of the cylinder. The elastic modulus was computed as the slope of the initial straight-line region of the stress-strain curve. The implants’ yield strength was obtained using the 0.2 percent offset

Table 7

Validation of the compression test with the literature.

Model	Parameter	Validation	Arjunan et al. (2020)	% Difference	Corresponding implant
SC1 (Arjunan et al., 2020)	Elastic modulus (GPa)	7.00	6.81	2.71%	
	Yield stress (MPa)	126.20	125.86	0.26%	

rule, following the ASTM standard ASTM E 8-01 (Designation: E8, 1520). Table 8 shows the finite element analysis results for the various geometrical design of canals and illustrates the effect of porosity and shape of the cross-section on the elastic moduli and strengths for each structural design.

Fig. 8 graphically displays the elastic modulus of the designed architectures and the range of elastic modulus of a human cortical bone.

Depending on the patient’s age and health conditions, it is essential to prepare bone-mimetic implants with a tailored strength (Clark et al., 2017). The cortical bone can significantly affect the strength of the long bone, and the porosity is an essential factor affecting bone quality (Cho et al., 2017). Consequently, an implant’s compression strength or porosity can be modulated. Canals play a crucial role (Zhang et al., 2020b; Zimmermann and Ritchie, 2015) as they decrease the cross-sectional area, leading to a lower resulting stress and lower stiffness of the implant. The porosity and orientation of vascular canals are strongly related to bone fracture risk and can affect the mechanical properties of bone (Uniyal et al., 2021).

Table 8 and Fig. 8 demonstrate that the shape of the Volkmann canals

Table 8

The outcome result of the designs of hollow cylinders as a cortical bone with the mechanical properties extracted from finite element analysis.

Structures	RD	Porosity	E (GPa)	Yield stress (MPa)
D1	66.39	33.61	13.33	198.20
D2	79.83	20.17	20.27	184.00
D3	77.25	22.75	26.38	109.20
D4	70.10	29.90	19.55	125.60
D5	70.11	29.89	19.43	125.60
D6	70.10	29.90	19.46	125.60
D7	70.10	29.90	19.74	125.60
D8	62.79	37.21	19.86	144.40
D9	62.75	37.26	20.18	144.40

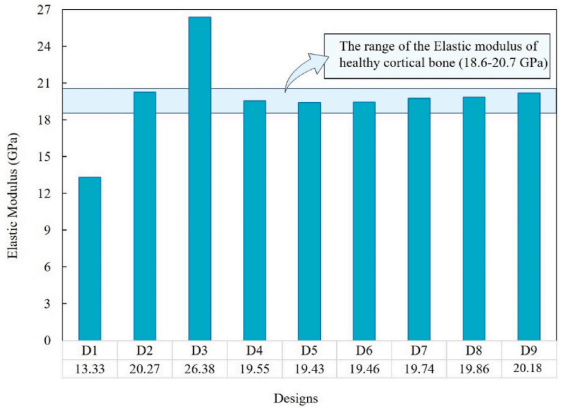


Fig. 8. Elastic modulus of the designed structures of a compact bone superimposed with the range of Elastic modulus of natural human bone.

and changing the cross-section to elliptical can significantly increase the porosity and affect elastic modulus. Analyzing D1 and D3 reveals that with increasing the number of Haversian canals and decreasing the number of Volkmann canals and considering corresponding diameter change sizes, the porosity can decrease up to 23%. The elastic modulus increases above the cortical bone range and reaches 26.38 GPa, which shows a 50% growth. Observation of these two models shows that the number and diameter of the Volkmann canals have more influence on the final elastic modulus and the effect of Volkmann canals is more significant than that of the Haversian canals. Analysis of these two models shows that the amount of porosity and the diameter of Volkmann canals strongly affect the stiffness. As a result, the optimal number of channels for the following steps was considered as 20 Haversian canals and 5 Volkmann canals. Haversian canals were all circular in cross-sections with diameters of 0.6 mm. In contrast, Volkmann canals were chosen with two types of circular cross-sections with a diameter of 0.65 mm and elliptical cross-sections with minor semi-axis and major semi-axis lengths of 0.55 mm and 1.4 mm, respectively. The effect of the shape of Volkmann canals and Haversian canals was studied, assuming the same relative density of 70% (D4, D5, D6, and D7). The minimum elastic modulus of 19.43 GPa was recorded for the helical orientation of both Haversian and Volkmann canals. The maximum elastic modulus of 19.74 GPa was found for the vertical direction of Haversian canals and the helical type of Volkmann canals. The yield strengths of these four structures had the same value of 125.6 MPa, while the elastic modulus differed for each structural design. Fig. 9 illustrates the trend of increasing porosity and increasing elastic modulus for the seven suitable models in the range of cortical bone elasticity. Table 2 shows different Haversian and Volkmann canals designs (D4-D9). D9, among all topologies, has the maximum surface area and volume created by the interconnected canals, which can help increase vascularization. Fig. 10 represents the volume and surface area created by intersecting canals, an important geometric feature for vascularization.

Change in the cross-section from a circular to an elliptical affects stress concentration. Stress concentration significantly decreases when the ellipse is flattened in the y-axis parallel to a load direction. Compared to a circular cross-section, the elliptical cross-section leads to lower stress concentrations, which delays the failure around the pores (Davis et al., 2017). In two models, D4 and D8, changing the cross-section of Volkmann canals from circular to the elliptical type led to an increase of 1.5% in modulus of elasticity and 24.59% in porosity. This result signifies that selecting an elliptical cross-section in the helical orientation results in a lighter and stiffer structure (Schultz, 2019). The cross-sectional shape of the ellipse was considered with respect to the direction of the applied force for all of the above-mentioned designs.

The same result was reported for D7 and D9 with the vertical Haversian canals and helical Volkmann canals with circular and elliptical cross-sections. In these two models, after changing the cross-section, the porosity increased from 30% to 37%, and the elastic modulus increased

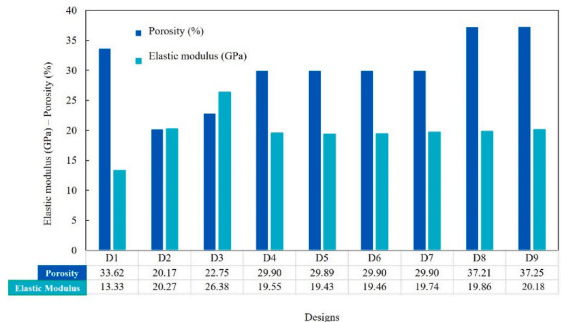


Fig. 9. Porosity and elastic modulus of different implant designs.

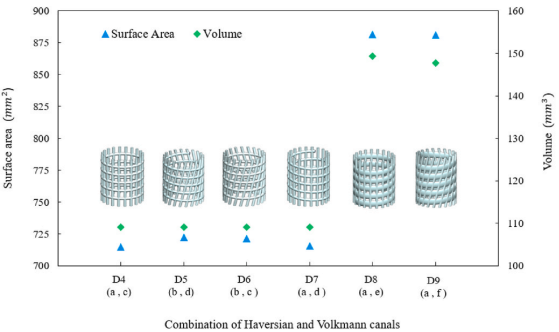


Fig. 10. The volume and surface area of the different types of intersecting Haversian and Volkmann canals in the cortical component.

from 19.74 GPa to 20.18 GPa, which is the highest value of the elastic modulus of all the nine structures and is close to the maximum elasticity of human cortical bone (20.7 GPa). Based on the computational results for nine designs, the D9 implant was selected as a more appropriate design to merge with the trabecular part to mimic the bone architecture and explore the effect of trabecular morphology on controlling the stress distribution, plasticity, stiffness, and strength.

Fig. 11 shows the stress distribution and plastic strain for all the geometries. The elastic moduli of D1 and D3 exceed the range of cortical bone mechanical properties, but the rest of the models are in the range. High-stress zones and plastic deformation can be seen on all the designs' inner and outer surfaces. A comparison of D4 and D7 shows that the change of the Volkmann canals from a horizontal shape to a helix shape can reduce the high-stress zone and the plastic region. Among three designs of D4, D6, and D7 with the same porosity of 29.90%, D7 with helix design for Volkmann canals and vertical Haversian canals shows more efficiency in mechanical response. The stress distribution is more uniform, leading to better load-bearing capacity. Therefore, it can be shown that the combination of vertical Haversian canals and helical Volkmann canals can lead to better structural efficiency. A comparison of D8 and D9, in which Haversian and Volkmann canals have the same orientation, shows that plastic strain for both structures has the same value of 0.02 and von Mises stress has the value of 931.04 and 936.19 MPa, respectively, but changing the Volkmann canal cross-section to elliptical in D9 can reduce the high-stress zone and plastic deformation as well. Comparison of elastic modulus between D4 and D8 and D7 and D9, respectively (with the horizontal and helical design of Volkmann canals) shows the effect of the shape of Volkmann canals on load-bearing capacity. Note that the plastic strain in structure D9 is 83% lower than in D2. No stress concentration can be observed on the boundary region for all nine samples.

Finally, D9 was selected as the optimum design for a cortical part for stiffness, strength, and optimal pore size to facilitate vascularization and bone growth. In Strategy II, D9 will be merged with four types of minimal surface implants to investigate the mechanical behavior of whole bone architecture and the effect of interior architecture on the stress and strain distributions.

3.2. Strategy II - Elastic-plastic behavior of the whole bone implant

A compressive test was carried out to elucidate the mechanical properties of the whole bone, which includes the compact part merged with the trabecular part. Numerical predictions are shown in Fig. 12 and Fig. 13, and the effective elastic modulus (E) and yield strength ( $\sigma_y$ ) are summarized in Table 8. All the structures reach a plastic region. As previously mentioned, the modulus of elasticity was derived from the slope of the stress-strain curve, and yield strength was determined by finding the intersection of the stress-strain curve with a line parallel to

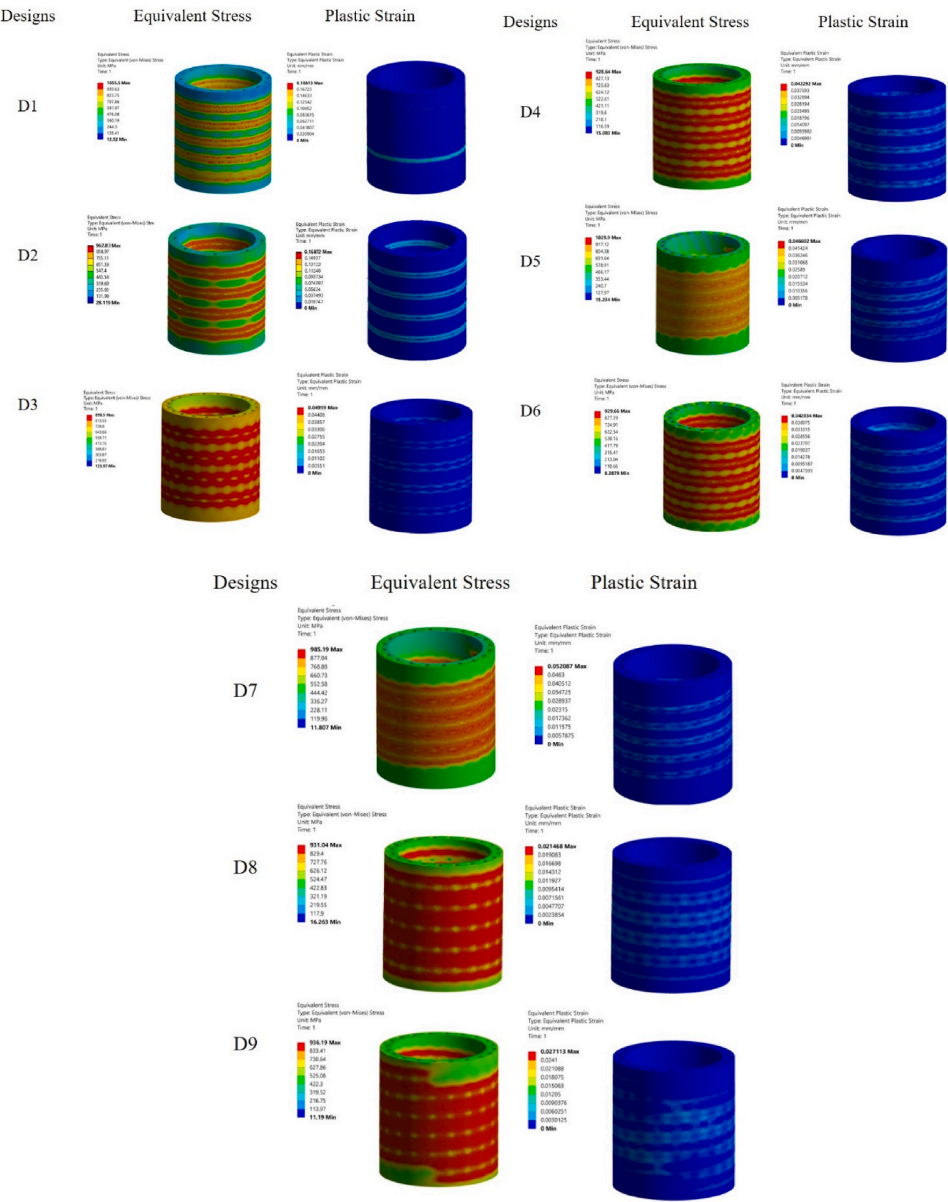


Fig. 11. Von Mises stress distribution and plastic strain obtained in numerical simulation under 0.1 mm displacement of the cortical component.

the initial slope at 0.2% strain. Again, the stress was computed by dividing the resultant force by the cross-sectional area of the cylinder ( $\pi$  times outer diameter squared).

The results from Fig. 12 indicate that the Diamond implant shows the highest elastic modulus and yield strength among the four types of structures. In contrast, the Primitive implant has the lowest elastic modulus and yield strength. Fig. 13 presents the stress-strain curves obtained from the finite element analysis for all the structures. The mechanical properties of the four architectures are summarized in Table 9.

Fig. 14 indicates the elastic-plastic behavior of the four designs of

whole bone structures after adding trabecular parts in the cortical component under the uniaxial compression test. At the first look at the contour of Von Mises stress, it can well describe that between four implants, the interior design with Split P could significantly reduce the stress in the outer and even on the inner layer of the cortical part. The highest stress value of 1132 MPa can be observed in the boundary regions. The outer and inner layers of the cortical part are under the yield point, and stress is distributed uniformly throughout the whole structure, which is the sign of desired load transfer. The Diamond design had a high-stress value of 1040 MPa which also can be observed in the boundary region. Gyroid and Primitive structures show the minimum



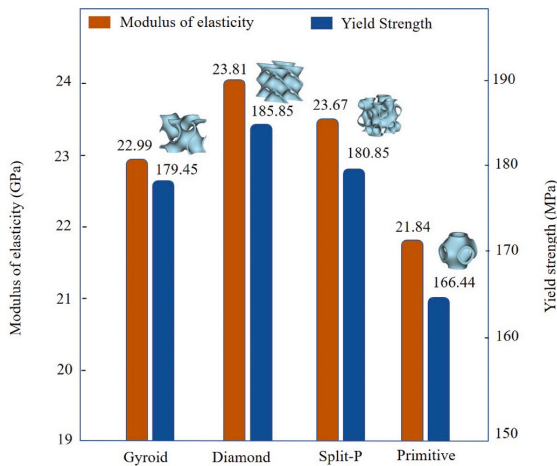


Fig. 12. Comparison of elastic modulus and yield strength for four trabecular architectures merged with the optimum compact part (D9) under compression test using FE analysis and their corresponding unit cells.

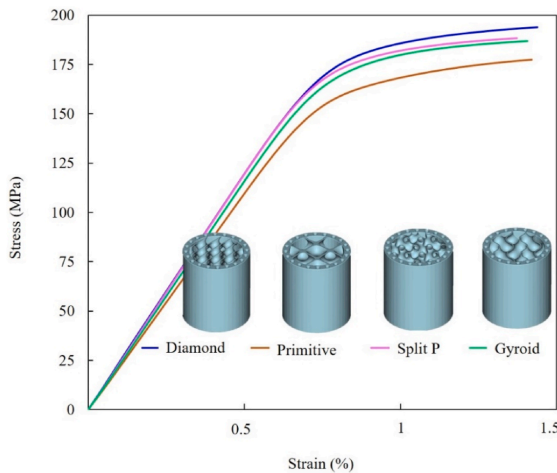


Fig. 13. Stress-Strain diagram extracted from finite element analysis for four trabecular architectures merged with the compact part.

Table 9  
Stiffness and strength value of four types of TPMS implant.

Implants	Elastic modulus (GPa)	Yield strength (MPa)
Gyroid	22.99	179.45
Split P	23.67	180.85
Primitive	21.84	166.44
Diamond	23.81	185.85

value of 977 and 947 MPa, respectively. Still, more areas had stress concentration on the outer layer of cortical component and trabecular, especially in Primitive architecture. For all designs, areas near the boundary condition show highly stressed spots. Stress transitions are smoother in Diamond and Split P designs. Gyroid has some stress concentration while Primitive structure shows the more regions of high stress. Because smooth transition of stress throughout the whole models

corresponds to the desired load transfer and can lead to enhancing the load-bearing capability, among the four designs, Diamond and Split P show better efficiency, higher stiffness and strength, followed by Gyroid and finally Primitive, which has the least uniformity in stress distribution. For the structure with the interior design of Gyroid, the outer layer of the cortical part and the layers in the trabecular part exhibit stress concentration in some spots. In the Primitive design, most stress concentration happened in the neck and the connection region of unit cells, while this phenomenon was not observed in others. In TPMS structures, stress transferring can be smoother than in strut base type of lattices due to the absence of sharp edges. In all structures, some areas do not participate in load-bearing. They are more visible in Split P, Diamond, and Gyroid than Primitive. High-stress regions usually can be prone to crack initiation or debonding. Split P and Diamond demonstrate better properties in terms of fracture or yield, while Primitive shows low efficiency.

The equivalent plastic strain distribution is represented in Fig. 14 as well. Adding a trabecular part to the cortical component can highly affect plastic strain distribution. In the areas in which Von Mises reaches the yield strength of the material, plastic strain can be seen in those regions. The plastic strain region for all of the designs in cortical parts can be seen more in the inner layer of Haversian canals. In the Primitive structure, these plastic regions are localized in regions near the thin neck region at the connection of unit cells. These regions are prone to undergo plasticity first. Some plastic regions can be observed on the outer boundaries of the Diamond structure, but the trabecular part does not experience plasticity. Similar results were also observed in Split P. The outer layer of the cortical part in the Gyroid structure shows plastic deformation regions. The Primitive had the highest value of plastic strain of 0.1.

4. Conclusions

This research study has demonstrated the designs of anatomically matched implants composed of cortical bone mimicking Haversian and Volkmann canals combined with the trabecular-bone-mimicking parts with the uniform internal TPMS structures. A numerical simulation was performed to predict the compressive behavior of the implants under uniaxial compression load.

Strategy I, representing the study of the cortical bone behavior, allowed choosing the optimal structure to ensure an appropriate stiffness and strength in the range of cortical bone. Nine topologies (D1-D9) were analyzed with Volkmann and Haversian canals of different numbers, shapes, diameters, and cross-sections. The results suggest that D9 had the best mechanical properties out of nine designs with elastic modulus and yield strength of 20.18 GPa and 144.40 MPa, respectively, and increased porosity up to 37.25% with elliptical cross-section and helical orientation for Volkmann canals and retaining circular cross-section for Haversian in the vertical direction. Related surface area also increased up to 881.1 mm<sup>3</sup> in the cortical component. Increasing porosity typically results in a decrease in the mechanical properties of the implants. At the same time, Strategy I shows that as porosity increases and the surface area increase, mechanical properties also increase. Such a combination is desired for implants. The result shows that changing the cross-section of Volkmann canals from circular to elliptical cross-section with respect to the load direction can strongly affect the mechanical properties.

Strategy II analyzed the mechanical behavior of the implant based on the interior design (trabecular part). Their mechanical properties have been deduced from the corresponding compressive stress-strain responses. Four types of TPMS were considered, Gyroid, Diamond, Split P, and Primitive, to merge with the resulting topology from Strategy I. In terms of the effect of interior design on the stress distribution of the cortical part (D9), it is evident that adding the trabecular part to the cortical component can significantly reduce the high-stress region in the cortical component and result in a more uniform stress distribution.

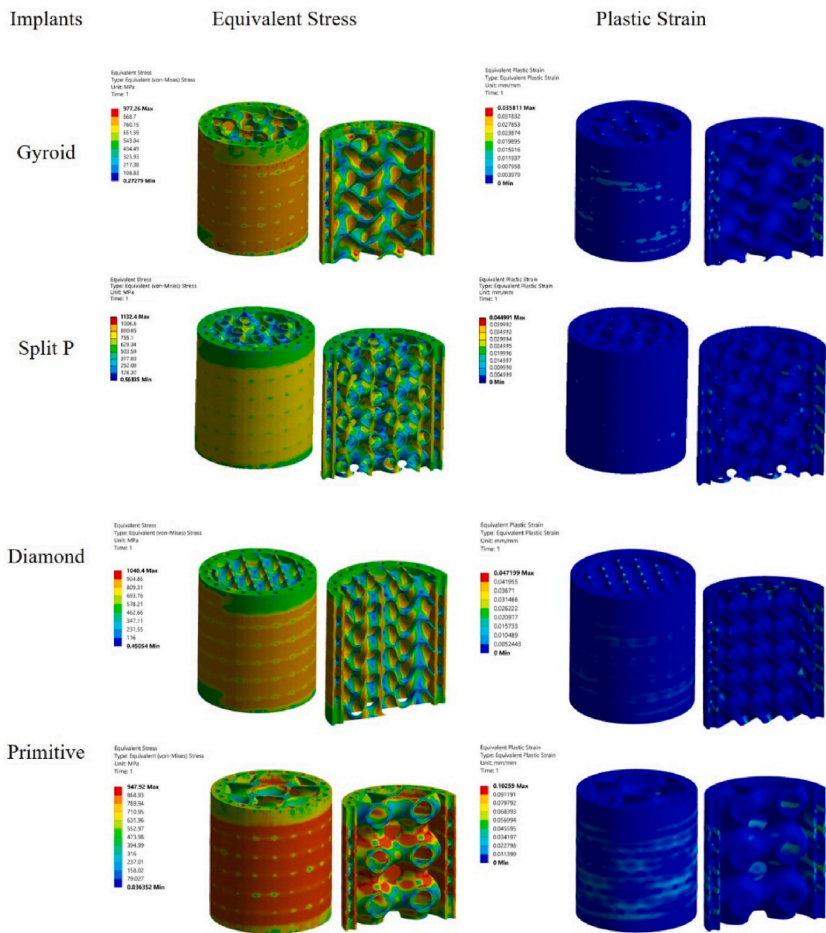


Fig. 14. Equivalent stress and equivalent plastic strain distribution in the four TPMS types of implants merged with the compact part.

Numerical simulation of structural behavior indicated that yield stress of the Diamond architecture was higher than others with the value of 185.85 MPa, and Primitive design shows the lowest at 166.44 MPa. Yield stress value of Split P and Gyroid was found as 180.85 and 179.45 MPa, respectively. According to the obtained results, Primitive architecture showed the highest plastic deformation among the four structures, while Split P and Diamond showed the lowest. In Split P architecture, the plastic deformation is confined to the inner layer of the cortical part, while in terms of Diamond architecture, it also can be seen in scattered spots in the boundary condition regions (both top and bottom surfaces of the implant). Diamond was the stiffest topology with 23.81 GPa, while Primitive had the lowest modulus with 21.84 GPa. Split P followed Diamond by showing higher structural efficiency with 23.67 GPa elastic modulus while Gyroid came in third with 22.99 GPa. Without considering the cortical component, the highly complex sheet-based Split P architecture showed a surface area that could reach more than twice the values obtained for Primitive and Gyroid-based and exhibited 25.64% surface area more than Diamond-based structures.

The current study presents the possible strategies that can be used for creating bone mimicking implants with Haversian and Volkmann-like canals. This work points out the role of geometry in controlling the mechanical response of different topologies using the finite element method.

CRediT authorship contribution statement

**Mansoureh Rezapourian:** Writing – original draft, Visualization, Software, Methodology, Investigation, Formal analysis. **Nikhil Kamboj:** Methodology, Investigation. **Iwona Jasiuk:** Writing – review & editing, Validation, Methodology, Formal analysis, Data curation, Conceptualization. **Irina Hussainova:** Writing – review & editing, Validation, Supervision, Resources, Project administration, Funding acquisition, Formal analysis, Data curation, Conceptualization.

Declaration of competing interest

The authors declare that they have no known competing financial interests or personal relationships that could have appeared to influence the work reported in this paper.

Acknowledgments

This work has been supported by the Estonian Research Council, Estonia, under Grant PRG643 (I. Hussainova). The authors would like to acknowledge Peter Newman from the ANSYS community for helping us carry out the FEA for this study.

## References

- Abueidda, D.W., Bakir, M., Abu Al-Rub, R.K., Bergström, J.S., Sobh, N.A., Jasiuk, I., 2017. Mechanical properties of 3D printed polymeric cellular materials with triply periodic minimal surface architectures. *Mater. Des.* 122, 255–267. <https://doi.org/10.1016/j.matdes.2017.03.018>.
- Afshar, M., Pourkamali Anaraki, A., Montazerian, H., 2018. Compressive characteristics of radially graded porosity scaffolds architected with minimal surfaces. *Mater. Sci. Eng. C* 92, 254–267. <https://doi.org/10.1016/j.msec.2018.06.051>.
- Al Hashimi, N.S., Soman, S.S., Govindharaj, M., Vijayavenkataraman, S., 2022. 3D printing of complex architected metamaterial structures by simple material extrusion for bone tissue engineering. *Mater. Today Commun.* 31, 103382 <https://doi.org/10.1016/j.mtcomm.2022.103382>.
- Al-Ketan, O., Abu Al-Rub, R.K., 2019. Multifunctional mechanical metamaterials based on triply periodic minimal surface lattices. *Adv. Eng. Mater.* 21, 1900524 <https://doi.org/10.1002/adem.201900524>.
- Arjunan, A., Demetriou, M., Baroutaji, A., Wang, C., 2020. Mechanical performance of highly permeable laser melted Ti6Al4V bone scaffolds. *J. Mech. Behav. Biomed. Mater.* 102, 103517 <https://doi.org/10.1016/j.jmbbm.2019.103517>.
- Ataee, A., Li, Y., Brandt, M., Wen, C., 2018. Ultrahigh-strength titanium gyroid scaffolds manufactured by selective laser melting (SLM) for bone implant applications. *Acta Mater.* 158, 354–368. <https://doi.org/10.1016/j.actamat.2018.08.005>.
- Aversa, R., Petrescu, R.V.V., Apicella, A., Petrescu, F.I.T., 2020. Trabecular prostheses. *Indepen. J. Manag. Prod.* 11, 1223. <https://doi.org/10.14807/ijmp.v11i4.989>.
- Bai, L., Gong, C., Chen, X., Sun, Y., Xin, L., Pu, H., Peng, Y., Luo, J., 2020. Mechanical properties and energy absorption capabilities of functionally graded lattice structures: experiments and simulations. *Int. J. Mech. Sci.* 182, 105735 <https://doi.org/10.1016/j.ijsmecsci.2020.105735>.
- Barber, H., Kelly, C.N., Nelson, K., Gall, K., 2021. Compressive anisotropy of sheet and strut based porous Ti-6Al-4V scaffolds. *J. Mech. Behav. Biomed. Mater.* 115, 104243 <https://doi.org/10.1016/j.jmbbm.2020.104243>.
- Basicmedical Key Fastest Basicmedical Insight Engine, (n.d.). <https://basicmedicalkey.com/> (accessed February 8, 2022).
- Bazaka, O., Bazaka, K., Kingshort, P., Crawford, R.J., Ivanova, E.P., 2021. Chapter 1. Metallic Implants for Biomedical Applications 3, 1–98. <https://doi.org/10.1039/9781788019828-00001>.
- Bilgiç, E., Boyacıoğlu, Ö., Gizer, M., Korkusuz, P., Korkusuz, F., 2020. Architecture of bone tissue and its adaptation to pathological conditions. *Comp. Kinesiol. Hum. Body* 71–90. <https://doi.org/10.1016/B978-0-12-812162-7.00006-0>.
- Bobbert, F.S.L., Liettaert, K., Eftekhari, A.A., Pournan, B., Ahmadi, S.M., Weinans, H., Zadpoor, A.A., 2017. Additively manufactured metallic porous biomaterials based on minimal surfaces: a unique combination of topological, mechanical, and mass transport properties. *Acta Biomater.* 53, 572–584. <https://doi.org/10.1016/j.actbio.2017.02.024>.
- Borciani, G., Montalbano, G., Baldini, N., Cerqueni, G., Vitale-Brovarone, C., Ciapetti, G., 2020. Co-culture systems of osteoblasts and osteoclasts: simulating in vitro bone remodeling in regenerative approaches. *Acta Biomater.* 108, 22–45. <https://doi.org/10.1016/j.actbio.2020.03.043>.
- Bose, S., Vahabzadeh, S., Bandyopadhyay, A., 2013. Bone tissue engineering using 3D printing. *Mater. Today* 16, 496–504. <https://doi.org/10.1016/j.mattod.2013.11.017>.
- Cai, Z., Liu, Z., Hu, X., Kuang, H., Zhai, J., 2019. The effect of porosity on the mechanical properties of 3D-printed triply periodic minimal surface (TPMS) bio-scaffold. *Bio-Design Manuf.* 2, 242–255. <https://doi.org/10.1007/s42242-019-00054-7> FIGURES/14.
- Callens, S.J.P., Tournelle né Betts, D.C., Müller, R., Zadpoor, A.A., 2021. The local and global geometry of trabecular bone. *Acta Biomater.* 130, 343–361. <https://doi.org/10.1016/j.actbio.2021.06.013>.
- Cardinali, M.A., Govoni, M., Dallari, D., Caponi, S., Fioretto, D., Morresi, A., 2020. Mechano-chemistry of human femoral diaphysis revealed by correlative Brillouin–Raman microspectroscopy. *Sci. Reports* 2020 101 10, 1–11. <https://doi.org/10.1038/s41598-020-74330-3>.
- Castro, A.P.G., Pires, T., Santos, J.E., Gouveia, B.P., Fernandes, P.R., 2019. Permeability versus design in TPMS scaffolds. *Materials* 12, 1313. <https://doi.org/10.3390/MA12081313>, 2019.
- Charbonnier, B., Manassero, M., Bourguignon, M., Decambron, A., El-Hafci, H., Morin, C., Leon, D., Bensidoum, M., Corsia, S., Petite, H., Marchat, D., Potier, E., 2020. Custom-made macroporous bioceramic implants based on triply-periodic minimal surfaces for bone defects in load-bearing sites. *Acta Biomater.* 109, 254–266. <https://doi.org/10.1016/j.actbio.2020.03.016>.
- Cho, D.C., Brennan, H.J., Johnson, R.W., Poulton, J.L., Gooi, J.H., Tonkin, B.A., McGregor, N.E., Walker, E.C., Handelsman, D.J., Martin, T.J., Sims, N.A., 2017. Bone corticalization requires local SOCS3 activity and is promoted by androgen action via interleukin-6. *Nat. Commun.* 8 <https://doi.org/10.1038/s41467-017-00920-X>.
- Clark, D., Nakamura, M., Miclau, T., Marcucio, R., 2017. Effects of aging on fracture healing. *Curr. Osteoporos. Rep.* 15, 601–608. <https://doi.org/10.1007/s11914-017-0413-9>.
- Davis, T., Healy, D., Bubeck, A., Walker, R., 2017. Stress concentrations around voids in three dimensions: the roots of failure. *J. Struct. Geol.* 102, 193–207. <https://doi.org/10.1016/j.jsg.2017.07.013>.
- Designation: E8/E8M – 13a Standard Test Methods for Tension Testing of Metallic Materials 1, (n.d.). <https://doi.org/10.1520/E0008/E0008M-13A>.
- Goldstein, S.A., 1987. The mechanical properties of trabecular bone: dependence on anatomic location and function. *J. Biomech.* 20, 1055–1061. [https://doi.org/10.1016/0021-9290\(87\)90023-6](https://doi.org/10.1016/0021-9290(87)90023-6).
- Hunt, K.D., Dean O’Loughlin, V., Fitting, D.W., Adler, L., 1998. Ultrasonic determination of the elastic modulus of human cortical bone. *Med. Biol. Eng. Comput.* 36, 51–56. <https://doi.org/10.1007/BF02522857>, 1998 361.
- Kamboj, N., Kazantseva, J., Rahmani, R., Rodríguez, M.A., Hussainova, I., 2020. Selective laser sintered bio-inspired silicon-wollastonite scaffolds for bone tissue engineering. *Mater. Sci. Eng. C* 116, 111223. <https://doi.org/10.1016/j.msec.2020.111223>.
- Kamboj, N., Ressler, A., Hussainova, I., 2021. Bioactive ceramic scaffolds for bone tissue engineering by powder bed selective laser processing: a review. *Materials* 14, 5338. <https://doi.org/10.3390/MA14185338>.
- Kapfer, S.C., Hyde, S.T., Mecke, K., Arns, C.H., Schröder-Turk, G.E., 2011. Minimal surface scaffold designs for tissue engineering. *Biomaterials* 32, 6875–6882. <https://doi.org/10.1016/j.biomaterials.2011.06.012>.
- Karageorgiou, V., Kaplan, D., 2005. Porosity of 3D biomaterial scaffolds and osteogenesis. *Biomaterials* 26, 5474–5491. <https://doi.org/10.1016/J.BIOMATERIALS.2005.02.002>.
- Kaur, M., Singh, K., 2019. Review on titanium and titanium based alloys as biomaterials for orthopaedic applications. *Mater. Sci. Eng. C* 102, 844–862. <https://doi.org/10.1016/J.MSEC.2019.04.064>.
- Kayacan, M.C., Baykal, Y.B., Karaaslan, T., Özsoy, K., Alaca, İ., Duman, B., Delikanlı, Y. E., 2017. Monitoring the osseointegration process in porous Ti6Al4V implants produced by additive manufacturing: an experimental study in sheep. <https://doi.org/10.5301/JABFM.5000385>, 16,68-75.
- Kim, J.N., Lee, J.Y., Shin, K.J., Gil, Y.C., Koh, K.S., Song, W.C., 2015. Haversian system of compact bone and comparison between endosteal and periosteal sides using three-dimensional reconstruction in rat. *Anat. Cell Biol.* 48, 258–261. <https://doi.org/10.5115/ACB.2015.48.4.258>.
- Langton, D.J., Sidaginamale, R., Lord, J.K., Nargol, A.V.F., Joyce, T.J., J K Lord, P., Student, T J Joyce, 2012. Taper junction failure in large-diameter metal-on-metal bearings. <https://doi.org/10.1302/2046-3758.14.2000047>. <https://doi.org/10.1302/2046-3758.14.2000047>.
- Lehder, E.F., Ashcroft, I.A., Wildman, R.D., Ruiz-Cantu, L.A., Maskery, I., 2021. A multiscale optimisation method for bone growth scaffolds based on triply periodic minimal surfaces. *Biomech. Model. Mechanobiol.* 20, 2085–2096. <https://doi.org/10.1007/s10237-021-01496-8>.
- Li, Y., Shi, J., Jahr, H., Zhou, J., Zadpoor, A.A., Wang, L., 2021. Improving the mechanical properties of additively manufactured micro-architected biodegradable metals. *J. Occup. Med.* 73, 4188–4198. <https://doi.org/10.1007/s11837-021-04949-8>.
- Liu, Y., Luo, D., Wang, T., 2016. Hierarchical structures of bone and bioinspired bone tissue engineering. *Small* 12, 4611–4632. <https://doi.org/10.1002/SMLL.201600626>.
- Ma, S., Song, K., Lan, J., Ma, L., 2020. Biological and mechanical property analysis for designed heterogeneous porous scaffolds based on the refined TPMS. *J. Mech. Behav. Biomed. Mater.* 107, 103727 <https://doi.org/10.1016/j.jmbbm.2020.103727>.
- Maskery, I., Aremu, A.O., Parry, L., Wildman, R.D., Tuck, C.J., Ashcroft, I.A., 2018. Effective design and simulation of surface-based lattice structures featuring volume fraction and cell type grading. *Mater. Des.* 155, 220–232. <https://doi.org/10.1016/j.matdes.2018.05.058>.
- McNamara, L.M., 2017. 2.10 Bone as a material. *Compr. Biomater.* II 202–227. <https://doi.org/10.1016/B978-0-12-803581-8.10127-4>.
- Miralbes, R., Ranz, D., Pascual, F.J., Zouzias, D., Maza, M., 2020. Characterization of additively manufactured triply periodic minimal surface structures under compressive loading. <https://doi.org/10.1080/15376494.2020.1842948>. <https://doi.org/10.1080/15376494.2020.1842948>.
- Morgan, E.F., Unnikrisnan, G.U., Hussein, A.I., 2018. Bone mechanical properties in healthy and diseased states. <https://doi.org/10.1146/Annurev-Bioeng-062117-121139>. <https://doi.org/10.1146/Annurev-Bioeng-062117-121139>, 20, 119–143.
- Myakinin, A., Turlybekuly, A., Pogrebnyak, A., Mirek, A., Bechelany, M., Liubchak, I., Oleshko, O., Husak, Y., Kornienko, V., Leśniak-Ziółkowska, K., Dogadkin, D., Banasiuk, R., Moskalenko, R., Pogorielov, M., Simka, W., 2021. In vitro evaluation of electrochemically bioactivated Ti6Al4V 3D porous scaffolds. *Mater. Sci. Eng. C* 121, 111870. <https://doi.org/10.1016/J.MSEC.2021.111870>.
- Nauth, A., Schemitsch, E., Norris, B., Nollin, Z., Watson, J.T., 2018. Critical-size bone defects: is there a consensus for diagnosis and treatment? *J. Orthop. Trauma* 32 (Suppl. 1), S7–S11. <https://doi.org/10.1097/BOT.0000000000001115>.
- Neffe, A.T., Julich-Gruner, K.K., Lendlein, A., 2014. Combinations of biopolymers and synthetic polymers for bone regeneration. *Biomater. Bone Regen. Nov. Tech. Appl.* 87–110. <https://doi.org/10.1533/978085798104.1.87>.
- Otsuki, B., Takemoto, M., Fujibayashi, S., Neo, M., Kokubo, T., Nakamura, T., 2006. Pore throat size and connectivity determine bone and tissue ingrowth into porous implants: three-dimensional micro-CT based structural analyses of porous bioactive titanium implants. *Biomaterials* 27, 5892–5900. <https://doi.org/10.1016/J.BIOMATERIALS.2006.08.013>.
- Peng, X.Y., Hu, M., Liao, F., Yang, F., Ke, Q.F., Guo, Y.P., Zhu, Z.H., 2019. La-Doped mesoporous calcium silicate/chitosan scaffolds for bone tissue engineering. *Biomater. Sci.* 7, 1565–1573. <https://doi.org/10.1039/C8BM01498A>.
- Rho, J.Y., Ashman, R.B., Turner, C.H., 1993. Young’s modulus of trabecular and cortical bone material: ultrasonic and microtensile measurements. *J. Biomech.* 26, 111–119. [https://doi.org/10.1016/0021-9290\(93\)90042-D](https://doi.org/10.1016/0021-9290(93)90042-D).
- Sabet, F.A., Najafi, A.R., Hamed, E., Jasiuk, I., 2016. Modelling of bone fracture and strength at different length scales: a review. *Interface Focus* 6. <https://doi.org/10.1098/RSFS.2015.0055>.
- Sabet, F.A., Koric, S., Idkaidek, A., Jasiuk, I., 2021. High-Performance computing comparison of implicit and explicit nonlinear finite element simulations of

- trabecular bone. *Comput. Methods Progr. Biomed.* 200, 105870 <https://doi.org/10.1016/J.CMPB.2020.105870>.
- Sarrafi, M., Rezvani Ghomi, E., Alipour, S., Ramakrishna, S., Liana Sukiman, N., 2021. A state-of-the-art review of the fabrication and characteristics of titanium and its alloys for biomedical applications. *Bio-Design Manuf.* 1, 1–25. <https://doi.org/10.1007/S42242-021-00170-3>, 2021.
- Schemitsch, E.H., 2017. Size matters: defining critical in bone defect size! *J. Orthop. Trauma* 31, S20–S22. <https://doi.org/10.1097/BOT.0000000000000978>.
- Schmidutz, F., Milz, S., Schiuma, D., Richards, R.G., Windolf, M., Sprecher, C.M., 2021. Cortical parameters predict bone strength at the tibial diaphysis, but are underestimated by HR-pQCT and  $\mu$ CT compared to histomorphometry. *J. Anat.* 238, 669–678. <https://doi.org/10.1111/JOA.13337>.
- Schultz, R.A., 2019. Elastic rock rheology and stress concentration. *Geol. Fract. Mech.* 27–74. <https://doi.org/10.1017/9781316996737.002>.
- Uniyal, P., Sihota, P., Tikoo, K., Kumar, N., 2021. Anatomical variation in intracortical canal network microarchitecture and its influence on bone fracture risk. *J. Mech. Behav. Biomed. Mater.* 123, 104770 <https://doi.org/10.1016/J.JMBBM.2021.104770>.
- Vance, A., Bari, K., Arjunan, A., 2018. Compressive performance of an arbitrary stiffness matched anatomical Ti64 implant manufactured using Direct Metal Laser Sintering. *Mater. Des.* 160, 1281–1294. <https://doi.org/10.1016/J.MATDES.2018.11.005>.
- Vijayavenkataraman, S., Zhang, L., Zhang, S., Fuh, J.Y.H., Lu, W.F., 2018. Triply periodic minimal surfaces sheet scaffolds for tissue engineering applications: an optimization approach toward biomimetic scaffold design. *ACS Appl. Bio Mater.* 1, 259–269. <https://doi.org/10.1021/ACSABM.8B00052>.
- Wang, M., 2004. *Biomaterials for Implants and Scaffolds*.
- Wang, X., Xu, S., Zhou, S., Xu, W., Leary, M., Choong, P., Qian, M., Brandt, M., Xie, Y.M., 2016. Topological design and additive manufacturing of porous metals for bone scaffolds and orthopaedic implants: a review. *Biomaterials* 83, 127–141. <https://doi.org/10.1016/J.BIOMATERIALS.2016.01.012>.
- Wang, Z., Huang, C., Wang, J., Wang, P., Bi, S., Abbas, C.A., 2019. Design and simulation of flow field for bone tissue engineering scaffold based on triply periodic minimal surface. *Chinese J. Mech. Eng. (English Ed.* 32, 1–10. <https://doi.org/10.1186/S10033-019-0329-7/FIGURES/23>.
- Weatherholt, A.M., Fuchs, R.K., Warden, S.J., 2012. Specialized connective tissue: bone, the structural framework of the upper extremity. *J. Hand Ther.* 25, 123–132. <https://doi.org/10.1016/J.JHT.2011.08.003>.
- Wu, R., Li, Y., Shen, M., Yang, X., Zhang, L., Ke, X., Yang, G., Gao, C., Gou, Z., Xu, S., 2021. Bone tissue regeneration: the role of finely tuned pore architecture of bioactive scaffolds before clinical translation. *Bioact. Mater.* 6, 1242–1254. <https://doi.org/10.1016/J.BIOACTMAT.2020.11.003>.
- Xiong, Y.Z., Gao, R.N., Zhang, H., Dong, L.L., Li, J.T., Li, X., 2020. Rationally designed functionally graded porous Ti6Al4V scaffolds with high strength and toughness built via selective laser melting for load-bearing orthopedic applications. *J. Mech. Behav. Biomed. Mater.* 104, 103673 <https://doi.org/10.1016/j.jmbbm.2020.103673>.
- Yang, E., Leary, M., Lozanovski, B., Downing, D., Mazur, M., Sarker, A., Khorasani, A.M., Jones, A., Maconachie, T., Bateman, S., Easton, M., Qian, M., Choong, P., Brandt, M., 2019. Effect of geometry on the mechanical properties of Ti-6Al-4V Gyroid structures fabricated via SLM: a numerical study. *Mater. Des.* 184, 108165 <https://doi.org/10.1016/j.matdes.2019.108165>.
- Zhang, L., Feih, S., Daynes, S., Chang, S., Wang, M.Y., Wei, J., Lu, W.F., 2018. Energy absorption characteristics of metallic triply periodic minimal surface sheet structures under compressive loading. *Addit. Manuf.* 23, 505–515. <https://doi.org/10.1016/j.addma.2018.08.007>.
- Zhang, M., Lin, R., Wang, X., Xue, J., Deng, C., Feng, C., Zhuang, H., Ma, J., Qin, C., Wan, L., Chang, J., Wu, C., 2020a. 3D printing of Haversian bone-mimicking scaffolds for multicellular delivery in bone regeneration. *Sci. Adv.* 6 <https://doi.org/10.1126/sciadv.aaz6725>.
- Zhang, M., Lin, R., Wang, X., Xue, J., Deng, C., Feng, C., Zhuang, H., Ma, J., Qin, C., Wan, L., Chang, J., Wu, C., 2020b. 3D printing of Haversian bone-mimicking scaffolds for multicellular delivery in bone regeneration. *Sci. Adv.* 6 [https://doi.org/10.1126/SCIADV.AAZ6725/SUPPL\\_FILE/AAZ6725.SM.PDF](https://doi.org/10.1126/SCIADV.AAZ6725/SUPPL_FILE/AAZ6725.SM.PDF).
- Zhang, C., Zheng, H., Yang, L., Li, Y., Jin, J., Cao, W., Yan, C., Shi, Y., 2022. Mechanical responses of sheet-based gyroid-type triply periodic minimal surface lattice structures fabricated using selective laser melting. *Mater. Des.* 214, 110407 <https://doi.org/10.1016/J.MATDES.2022.110407>.
- Zimmermann, E.A., Ritchie, R.O., 2015. Bone as a structural material. *Adv. Healthc. Mater.* 4, 1287–1304. <https://doi.org/10.1002/ADHM.201500070>.





### **Paper III**

Rezapourian, M., Jasiuk, I., Saarna, M., & Hussainova, I. (2023). Selective laser melted Ti6Al4V split-P TPMS lattices for bone tissue engineering. *International Journal of Mechanical Sciences*, 251, 108353.





Contents lists available at ScienceDirect

## International Journal of Mechanical Sciences

journal homepage: [www.elsevier.com/locate/ijmecsci](http://www.elsevier.com/locate/ijmecsci)

# Selective laser melted Ti6Al4V split-P TPMS lattices for bone tissue engineering

Mansoureh Rezapourian<sup>a</sup>, Iwona Jasiuk<sup>b</sup>, Mart Saarna<sup>a</sup>, Irina Hussainova<sup>a,\*</sup>

<sup>a</sup> Department of Mechanical and Industrial Engineering, Tallinn University of Technology, Tallinn, Estonia

<sup>b</sup> Department of Mechanical Science and Engineering and The Carle Illinois College of Medicine, University of Illinois at Urbana-Champaign, Urbana, IL 61801, United States of America

## ARTICLE INFO

### Keywords:

Homogenization  
Split-p triply periodic minimal surface  
Finite element analysis  
Mechanical properties  
Load-bearing  
Bone implants

## ABSTRACT

This study investigates Ti6Al4V Split-P triply periodic minimal surface (TPMS) structures produced by selective laser melting for the first time. The designs include two different cell morphologies (CM) with five different relative densities (RD). Scanning electron microscopy is utilized to assess the manufacturability and accuracy of the 3D printed Split-P lattice structures. The quasi-static mechanical responses are then studied to identify the failure mechanisms of each lattice type. Afterward, the stress-strain behavior and plateau stress responses are explored to evaluate the load-bearing capacity and energy absorption of five Split-P lattices. Furthermore, finite element analysis is performed to gain insight into the elasto-plastic behavior of the Split-P structures, and unit cell homogenization is employed to determine the equivalent stiffness tensor. The results demonstrate that the elastic modulus, yield strength, and ultimate strength of the 3D printed Split-P lattices range from 1.50 to 3.50 GPa, 57.95 to 152.74 MPa, and 93 to 170 MPa, respectively. Depending on RD and CM, load-bearing capacity range from 0.04 to 0.17. The energy absorption capacity and plateau stress of lattices vary from 22 to 61 MJ/m<sup>3</sup> and 30 to 63 MPa, respectively. Gibson-Ashby power law represents the elastic modulus and yield stress of the Split-P lattices as a function of RD and reveals a stretch-dominated deformation behavior. Unit cell homogenization on Split-P structures with zero isovalue shows isotropy in mechanical properties and anisotropy for lattices with non-zero isovalue. Ti6Al4V Split-P lattices with the highest surface area and surface area-to-volume ratio, among other TPMS, can achieve mechanical properties close to those of trabecular and cortical bones, making them suitable for bone implants in load-bearing applications.

## 1. Introduction

Repairing bone defects traditionally involves autografts, allografts, and xenografts [1]. However, long-term outcomes may be compromised by severe risks associated with these treatments, including infection, potential morbidity at the donor site, and unpredictable functional outcomes [2]. To overcome the inherent limitations of autograft and allograft, bone-graft substitutes were developed as an alternative strategy, and biomaterials have also been used for bone tissue repair as a bone substitution [3]. Bone graft substitutes can be classified as synthetic, inorganic, or bio-organic [3,4]. Specially designed scaffolds produced by biomaterials can support three-dimensional (3D) tissue growth, maintain physical integrity, and promote bone ingrowth at the defect site [5]. A scaffold can facilitate the formation of uniform bone tissue by providing a guiding template. In general, scaffolds do not

replace bone permanently as they resorb over time [4,6]. In contrast, bone implants remain permanently in the body to provide long-term structural support [3,4,6,7]. In tissue engineering (TE), the suitability of a bone construct is determined by four factors: biocompatibility, biodegradability, mechanical properties, and architecture [4,8]. Bone substitutes with relatively large surface area (SA) and surface area-to-volume ratio (SA/VR) with significant interconnectivity of pores promote osteoblast activity [9,10]. Therefore, pore size, pore shape, and porosity correlate with bone ingrowth [11–14].

Human trabecular bone is a highly porous tissue with intricately interconnected plates and struts. Such complex architecture can be represented by lattices based on triply periodic minimal surfaces (TPMS). Fig. 1 shows a schematic representation of the Split-P TPMS lattice that resembles the morphology of trabecular bone.

TPMS-based lattices can provide the elastic modulus in the range of

\* Corresponding author.

E-mail address: [irina.hussainova@taltech.ee](mailto:irina.hussainova@taltech.ee) (I. Hussainova).

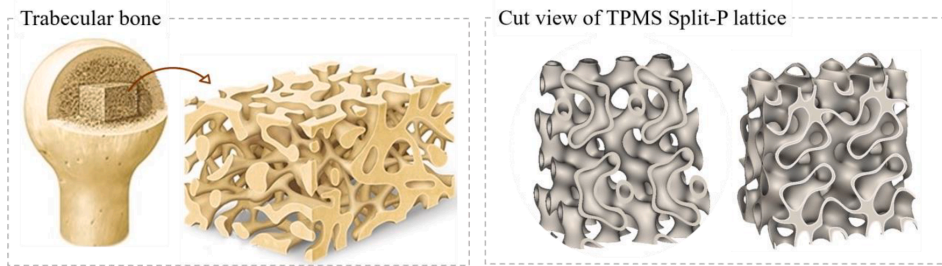


Fig. 1. Schematic representation of the porous cellular structure of trabecular bone and sectional view of TPMS Split-P lattice resembling the morphology of trabecular bone.

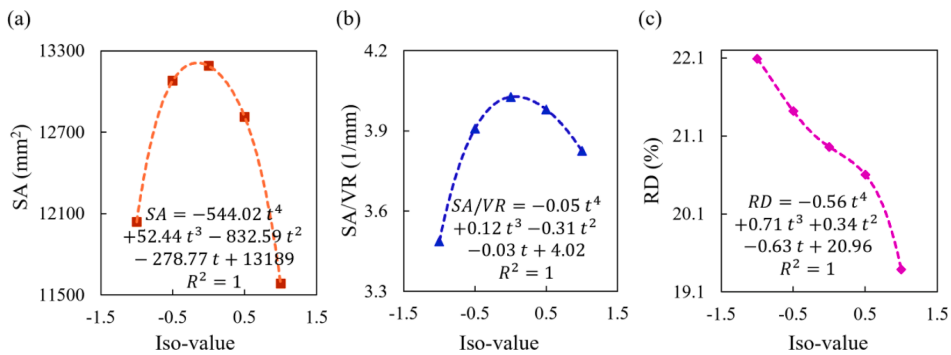


Fig. 2. Nonlinear fitted relationship to determine SA, SA/VR, and RD as a function of the iso-value; (a) Fitting of SA, (b) SA/VR, and (c) RD as a function of iso-value.

human trabecular and cortical bones and achieve the required compressive strength, energy absorption, and fatigue resistance, which are not easily obtained with strut-based structures [15–17]. Recently, TPMS structures have been explored as bone scaffolds and implants due to their smooth surfaces, high interconnectivity porous architectures, and mathematically controllable geometry [18–21].

TPMS-based architectures have minimal surfaces with zero mean curvature at any point. Examples include Gyroid, Diamond, Neovius, Primitive, and Split-P [22–24]. Numerous studies have been conducted on the mechanical behavior of Gyroid, Diamond, and Primitive TPMS in orthopedic applications [20,25–27]. In contrast, less is known about the mechanical response of Split-P structures. Mubasher et al. [28] studied the mechanical behavior of seven different polymeric lattices and found that Split-P ranked third in energy absorption capacity. Miralbes et al. [29] investigated six different polymeric TPMS lattices under a quasi-static compression test; their results showed the remarkable energy absorption capacity of the Split-P lattice. Lehder et al. [30] presented a method to optimize the geometry of six TPMS-based lattices, including Split-P, made of nylon, to maximize cell growth rate while maintaining an elastic modulus equivalent to human bone. They found that the Split-P morphology is a strong candidate for bone scaffolds after the Lillioid architecture, which has the highest cell growth rate due to its high pore size, large SA/VR, and high local curvature. Recently, extensive experiments and numerical simulations have been performed to investigate the mechanical behavior of cellular structures to achieve high strength and stability [31–33]. However, there is still limited information on the suitability of Split-P TPMS for bone substitutions.

Advances in additive manufacturing (AM) have enabled the fabrication of cellular solids with complex shapes, including porous materials and lattice structures [34,35]. Selective laser melting (SLM), one of the 3D printing technologies, is of high interest as it enables the customization of complex structures [36,37] and offers advantages over

traditional manufacturing methods, such as time savings, lower material consumption, and fabrication of complex shapes [38]. SLM allows freedom in modulating the geometric specifications of complex metallic structures in orthopedic and other engineering applications.

SLM has demonstrated the ability to utilize various types of metal powders. One of the preferred metal materials for medical applications is titanium and its alloys [39,40]. Ti6Al4V is widely used for bone implants due to its good biocompatibility, predictable mechanical performance, and high corrosion resistance [41,42]. However, its elastic modulus ranges from 110 to 120 GPa [38], which is significantly larger than that of compact cortical bone (3–20 GPa) and porous trabecular bone (0.1–4.5 GPa) [43,44]. Such a high mismatch in the mechanical properties of a titanium alloy and human bone may result in stress shielding, leading to bone resorption.

This paper focuses on the experimental and numerical evaluation of Ti6Al4V Split-P TPMS lattices additively manufactured by SLM. The fabricated lattices have large SA/VR and high curvatures, characteristics that promote bone growth. Quasi-static uniaxial compression tests were used to investigate the mechanical behavior of the lattices. A quasi-static finite element analysis (FEA) was applied to simulate the elastic-plastic deformation behavior of the as-built lattices. To our knowledge, this is the first study investigating the mechanical behavior of 3D printed biocompatible Ti6Al4V alloy Split-P lattices using SLM.

The contents of the paper are as follows. Section 2 presents all methodology steps, including design parameters and printing procedures, followed by mechanical testing and numerical simulation procedures. Section 3 describes the structural response of the lattices, including the Gibson-Ashby relation and the energy absorption capacity. Homogenization of the unit cells is then performed to determine equivalent elastic moduli. Section 4 discusses the research findings, suggests possible areas of future work, and states the limitations of this study. Afterward, a comparison is made between the properties of

Table 1

SA and SA/VR of four types of TPMS with a design space of 25 mm in X, Y, and Z directions, a unit cell size of 12.5 mm, and iso-value of 0, in the same RD of 20%.

TPMS lattices	SA (mm <sup>2</sup> )	SA/VR (1/mm)
Split-P	13,189.02	4.02
Diamond	10,080.58	3.08
Gyroid	8177.55	2.50
Primitive	6269.67	1.91

human bone (trabecular and cortical parts) and fabricated lattices. Finally, conclusions are drawn in Section 5.

2. Materials and methods

This section discusses the designs, followed by the preparation process. After describing the mechanical testing procedure, a finite element analysis is presented, followed by the investigation of the anisotropy of the Split-P unit cells using numerical periodic homogenization.

2.1. Design of split-p structures

Mathematical form of the Split-P TPMS lattice is given in Appendix A, Eq. (A.1) [45]. The level set equation of the Split-P TPMS structure can be generated using the Cartesian coordinate system (X, Y, Z) at the specified iso-value *t*, which controls the RD, surface area, and surface area-to-volume ratio of the resulting lattices. The iso-value plays an important role in controlling the morphology and associated geometric properties of Split-P lattices. Geometric parameters SA and SA/VR, as well as RD, which is the ratio of the volume of the lattice structure to the volume of the solid cube, are all dependent on *t*. The changes in the local geometry due to varying iso-value (*t*) are shown in Appendix A, Fig. A.1. In this study, the nTopology software package (3.35.2, nTopology, New York, NY, USA) was used to create computer-aided design files (CAD) of the Split-P lattices. The values of SA and SA/VR were calculated using the corresponding blocks ("surface area from the body" and "surface area to volume ratio") for all designed lattices. Fig. 2 represents a nonlinear fitted relationship to determine RD, SA, and SA/VR as a function of the iso-value. The design space in this study is a cube with a side length of 25 mm.

SA and SA/VR of four types of TPMS, namely Split-P, Gyroid, Diamond, and Primitive, are compared in Table 1. To provide the same RD of 20% for all lattices, two unit cells (12.5 mm) of each type of TPMS were used to fill a design space of 25 mm in X, Y, and Z directions. Iso-value was set to 0 and the thickness was changed to achieve the final RD. The results were obtained by nTopology software using the blocks mentioned above.

To design target lattices, we selected two different cell sizes of 12.5 and 14 mm to fill the design space of 25 × 25 × 25 mm<sup>3</sup>, and iso-values of 0 and 1 were used to alter the structural morphology and create five different cellular lattices. With an iso-value of 0, by varying the sheet thickness of the Split-P TPMS as 0.25, 0.4, and 0.6 mm and maintaining the same unit cell size of 12.5 mm, different porosity levels between 75% and 90% were developed to achieve the target relative densities of 10.47%, 16.74%, and 25.19%. With the target RD of 21%, two cellular lattices were modeled with the following geometric considerations: iso-value 0 with a unit cell size of 14 mm and iso-value 1 with a unit cell size of 12.5 mm. The expected porosity was chosen according to the

porosity estimated for a human trabecular bone (> 70%) [46]. The CAD designs of Split-P lattices and the solid tensile specimen are presented in Appendix A, Fig. A.2, and the geometrical parameters of the lattices are listed in Table 2. SolidWorks software was used for designing the tensile specimens with a round cross-section according to the ASTM E8-E8M standard [47].

2.2. Materials and fabrication

Split-P lattices and solid tensile specimens were fabricated by the SLM process (SLM solution 280, SLM Solutions Group AG, Germany) using a gas-atomized Ti6Al4V powder consisting of rounded particles with a size distribution between 15 and 37 μm and the composition given in Table 3.

The processing parameters were taken from previous work [20] with a laser power of 275 W, a scanning speed of 1100 mm/s, a layer thickness of 30 μm, a hatch spacing of 110 μm, and a rotation of 57 between the consecutive layers. High-purity argon gas was used throughout the manufacturing process to avoid oxidation. The fabricated samples were then wire cut from the substrate and ultrasonically cleaned with pure alcohol. As-built lattice structures and powder particles were morphologically examined using a high-resolution scanning electron microscope (HR-SEM Zeiss Merlin), as shown in Fig. 3.

The designed Split-P architectures naturally have overhang areas, which may lead to layer collapse, cross formation, and printing issues. Thus, support may be required to ensure successful prints and minimize geometric deviations between the fabricated samples and CAD models [48]. Various Split-P lattice structures and areas that need supports are shown in Appendix B, Fig. B.1. The solid density of the 3D printed tensile specimens (*ρ<sub>solid</sub>*) was measured using an Archimedes method, and the weight of the as-built Split-P lattices was calculated using a dry weighing method. Finally, the solid volume fraction of lattices were calculated using  $V = \frac{W_{as-built}}{\rho_{solid} l_x l_y l_z}$  where *l<sub>x</sub>*, *l<sub>y</sub>* and *l<sub>z</sub>* are the average length sizes of the fabricated Split-P lattices. *W<sub>as-built</sub>* is the average weight of 3D printed specimens after supports removal and ultrasonic cleaning.

2.3. Mechanical tests

Uniaxial quasi-static tensile and compression tests were performed at a strain rate of 1 mm/min in the direction parallel to the 3D printing direction to investigate the mechanical properties of the as-built specimens. The tests were performed according to ISO 13,314–2011 using an Instron 8802 machine equipped with a 250 KN load cell [49]. The deformation behavior was recorded using a cell phone camera. Experimental results contained noisy data. Thus, a moving average filter (MAF) [39] was implemented using MATLAB software to eliminate the noise without affecting the main results. This method was applied to the tensile and compression tests.

The mechanical properties of the bulk material, including the elastic modulus (*E<sub>s</sub>*) and 0.2% offset yield strength (*σ<sub>s,γ</sub>*), where the subscript *s*

Table 3  
Chemical composition of Ti6Al4V powder.

Sample (wt%)	Ti	N	C	H	Fe	O	Al	V
Actual	Bal.	≤ 0.03	≤ 0.08	≤ 0.012	≤ 0.25	≤ 0.13	5.5 – 6.5	3.5 – 4.5

Table 2

Nominal thickness and RD of designed Split-P lattices in CAD design.

Structure label	Iso-value = 0 SP025U125	SP04U125	SP06U125	SP05U140	Iso-value = 1 SP06U125Iso1
RD (%)	10.47	16.74	25.19	21.00	21.00
Thickness (mm)	0.25	0.4	0.6	0.5	0.6

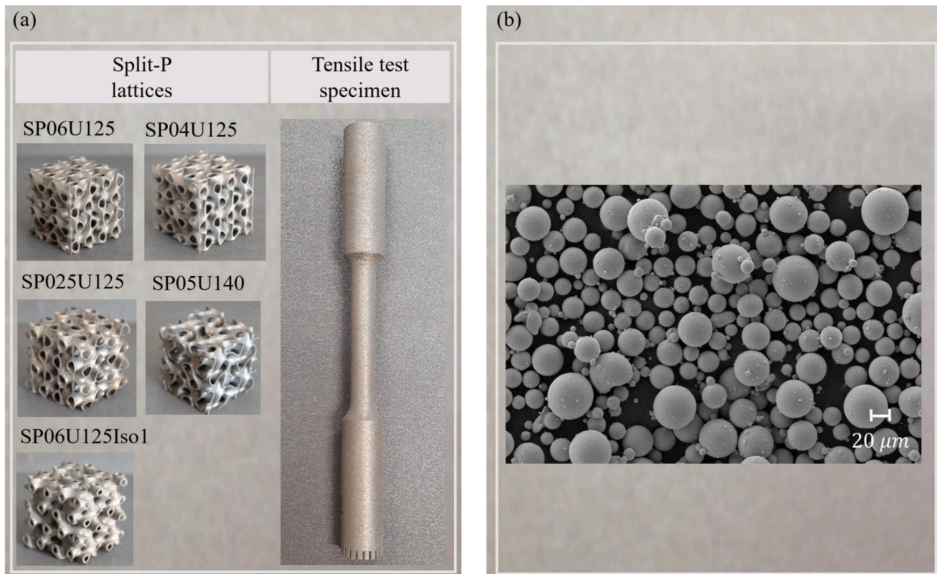


Fig. 3. SLM-fabricated Ti6Al4V alloy samples and a scanning electron microscope of Ti6Al4V powder used in 3D printed of Split-P lattice structures and tensile test specimens: (a) As-built Split-P lattices: SP06U125, SP04U125, SP025U125, SP05U140, SP06U125-Iso1, and tensile test specimen, (b) SEM image of Ti6Al4V powder used in 3D printing process.

stands for solid material, were obtained from the tensile stress-strain curve. The mechanical properties of each lattice, including the elastic modulus ( $E_l$ ), 0.2% offset yield strength ( $\sigma_{l,Y}$ ), ultimate strength ( $\sigma_{l,U}$ ), and the first minimum strength after failure ( $\sigma_{min}$ ), were calculated from the compressive stress-strain curve. The plateau stress ( $\sigma_{l,P}$ ) of as-built lattices is defined as the average of the stresses between 20%–40% compressive strain of each lattice [49]. Collapse strain ( $\epsilon_c$ ) is defined as a strain related to the first collapse after the first failure, and the densification strain ( $\epsilon_D$ ) is a strain at which the corresponding stress reaches the ultimate strength at the end of the compression test. The values are reported in Tables 5 and 6.

The Gibson-Ashby model [50] was employed to study the relationship between the relative density of periodic cellular structures and their mechanical properties using the equations:  $E_l/E_s = C_1(\rho)^n$  and  $\sigma_{l,Y}/\sigma_{s,Y} = C_2(\rho)^m$ , where  $\rho$  represents the relative density of the as-built lattices and constants  $C_1$ ,  $C_2$ ,  $n$ , and  $m$  are fitting constants related to the structural configuration and mode of deformation [51]. Finally, the energy absorption of the lattice structures was calculated by  $W = \int_0^{\epsilon} \sigma(\epsilon) d\epsilon$ ; [J/m<sup>3</sup>] [49], where  $W$  represents the energy absorption per unit volume defined as the area between the stress-strain curve,  $\epsilon$  is the engineering strain, and  $\sigma(\epsilon)$  is the corresponding engineering stress. We also compute the load-bearing capacity ( $K$ ) of the lattices, defined as  $\sigma_{min}/\sigma_U$ , where  $\sigma_{min}$  represents the first minimum value of stress after the initial plastic failure and  $\sigma_U$  is the ultimate stress defined as the highest stress in the engineering stress-strain curve.

#### 2.4. Finite element model

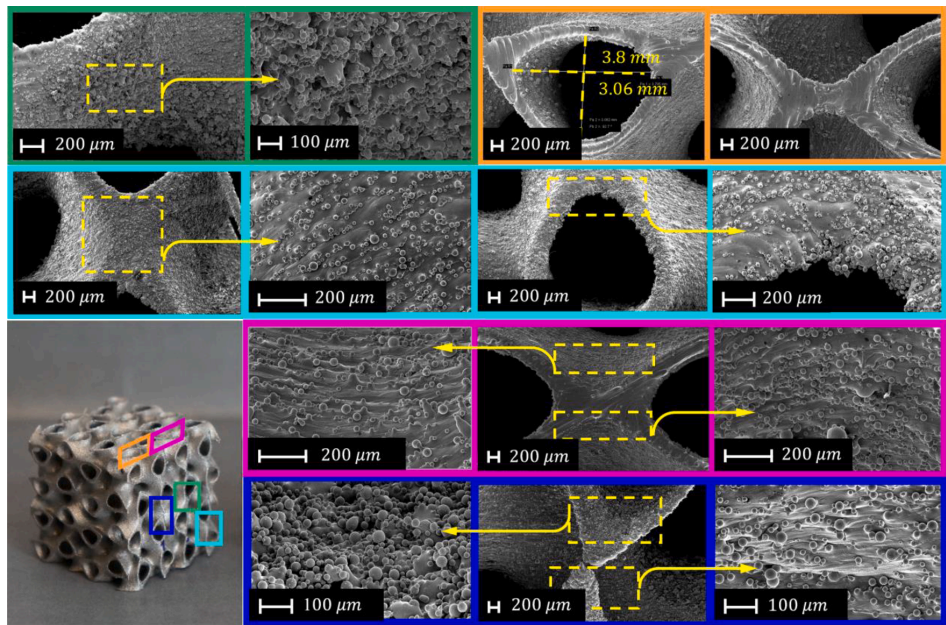
The finite element (FE) analysis of the unit cells and the Split-P lattice structures was performed using ANSYS software to capture the compressive response of TPMS structures. An elastoplastic material model with multi-linear isotropic hardening was used with shell and solid elements [32,52]. Linear tetrahedral mesh files were created with nTopology software and were then imported into ANSYS software for

the FE analysis. We applied loading by placing two plates with linear brick elements on the top and bottom of each TPMS lattice. The top plate was subjected to a velocity of 2 m/s while keeping the kinetic energy below 2% of the total internal energy. The bottom plate was defined as fully fixed in all degrees of freedom. The side surfaces were traction free. The material of the plates was assumed to have a modulus of elasticity of 210 GPa, a density of  $7.85 \times 10^{-6}$  kg/mm<sup>3</sup>, and a Poisson's ratio of 0.3. A friction coefficient of 0.1 was assumed for the frictional contact between the lattices and two plates, while a frictionless self-contact was chosen for Split-P lattice surfaces. Finite element analyses of the unit cells and lattice structures were performed under the same conditions as those mentioned above. Mesh sensitivity analyses were done for the unit cells using solid elements, three mesh sizes, and a mass scale factor. The finite element results for the selected solid mesh size were compared with the surface mesh results. Note that shell elements cannot be used when the RD is greater than 50% since they produce unrealistic geometry due to the thickening of the walls [32]. In this study, all relative densities are under 50%. Therefore, shell elements can also be used for FE analysis as well as solid elements.

#### 2.5. Numerical periodic homogenization

In many applications, it is critical to understand the structure's anisotropy and identify its stiffest and softest directions. In structural applications, such as load-bearing implants, anisotropy affects the performance of the lattice in different directions [53]. Therefore, to accurately estimate the effective elastic properties of lattice structures, a periodic homogenization method was performed for the Split-P unit cells using the nTopology software and the "Homogenized Unit Cell" block. The material was assumed to be linearly elastic. The modulus of elasticity was obtained from the experimental tensile test, and a Poisson's ratio of 0.3 was applied. Finally, the three-dimensional elastic moduli surface was plotted as a function of direction using the mesh size selected from the mesh sensitivity study. For most general anisotropic linear elastic materials, there are 21 independent elastic constants in the fourth-order stiffness tensor  $C$  in Hooke's law  $\{\sigma\} = [C]\{\epsilon\}$ . The Split-P





**Fig. 4.** SEM images of surface morphology at different orientations and locations of Ti6Al4V SP04U125 lattice fabricated by SLM, indicated by different colors for each region. Colors: Green (downward surface on the side of the lattice), Orange (pore and strut size of the top of the lattice), Cyan (side surface of the lattice showing dross formation and staircase phenomenon), Purple (top surface; oblique and curved surfaces with observed staircase effect), and Blue (upward and downward surfaces on the side with partially melted metal powder adhering to the surface).

**Table 4**  
Geometrical parameters of fabricated Ti6Al4V Split-P lattices and CAD model.

Design	Weight (gr) Actual	CAD	Relative error (%)	RD (%) Actual	CAD	Relative error (%)	SA (mm <sup>2</sup> ) CAD	SA/VR (1/mm) CAD	Porosity (%) CAD
SP025U125	9.72 ± 00	6.91	25.90	14.13	10.48	34.89	12823.17	7.83	89.52
SP04U125	13.99 ± 0.01	11.04	26.72	20.33	16.74	21.44	13115.03	5.01	83.26
SP06U125	18.02 ± 0.04	16.61	8.53	26.00	25.19	3.22	13144.44	3.34	74.81
SP06U125Iso1	16.42 ± 0.02	13.84	18.64	23.86	21.00	13.67	11548.69	3.52	79.00
SP05U140	16.55 ± 0.1	13.16	20.48	23.00	21.00	9.25	12018.47	3.85	79.00

lattices have cubic symmetry, meaning that the stiffness tensor has three independent components  $C_{11} = C_{22} = C_{33}, C_{44} = C_{55} = C_{66}, C_{12} = C_{23} = C_{13}$ , using a contracted notation, with the remaining constants equal zero [54], as shown in Eq. (3).

$$C = \begin{bmatrix} C_{11} & C_{12} & C_{12} & 0 & 0 & 0 \\ C_{12} & C_{11} & C_{12} & 0 & 0 & 0 \\ C_{12} & C_{12} & C_{11} & 0 & 0 & 0 \\ 0 & 0 & 0 & C_{44} & 0 & 0 \\ 0 & 0 & 0 & 0 & C_{44} & 0 \\ 0 & 0 & 0 & 0 & 0 & C_{44} \end{bmatrix} \quad (3)$$

The Zener ratio is defined as  $Z = 2C_{44}/(C_{11} - C_{12})$ , and  $Z = 1$  indicates an isotropic material behavior [55,56].

3. Results

The first part of this section focuses on manufacturing imperfections and experimental surface morphology. After presenting the effect of the manufacturing process on the RD of the produced Split-P lattices, the structural response under the quasi-static compression test will be presented along with the Gibson-Ashby model. In the following sections, the effect of cell morphology on the mechanical response will be shown and all fabricated lattices will be evaluated for energy absorption

capacity. Afterward, a comparison will be made between the numerical and experimental results. Finally, to compare lattice anisotropy, the homogenization of unit cells will be described.

3.1. Structural analysis

Fig. 4 shows the 3D-printed SP04U125 Split-P lattice fabricated by SLM and its surface morphology. Several locations were selected to capture images of the upward and downward surfaces and marked by different colors. Images show good interconnectivity within the fabricated porous lattice. The accuracy of the pore and strut size of the as-built sample is displayed in the cyan and orange area. Compared to other TPMS or strut-based structures, Split-P has the largest surface area (as shown in Table 1). Semi-melted or unmolten powder particles are attached to the surfaces, as seen in the blue and green regions. According to SEM images, the staircase effect is prominent on the structure's surface. This phenomenon is more evident on oblique and curved surfaces, such as the TPMS structure with various curvatures and large inclination angles. This staircase effect can clearly be seen in the purple and blue areas.

The measured density of 4.404 (gr/cm<sup>3</sup>) for the 3D printed tensile specimens shows the highest RD of 99.59%, demonstrating a high degree of densification. The geometric parameters of the fabricated sam-



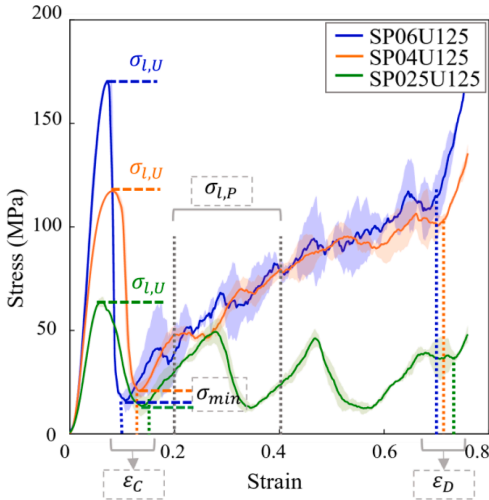


Fig. 5. Experimental stress-strain curves of SP06U125, SP04U125, and SP025U125 lattice structures subjected to a quasi-static compression test at a strain rate of 1 mm/min.

ples and CAD designs are listed in Table 4. All the CAD designs of the lattices have lengths of 25 mm in Y, and Z directions.

### 3.2. Mechanical properties

This section presents the experimental tensile and compression test results of SLM-fabricated structures. Afterward, the Gibson-Ashby model is used to predict the designed lattice structure properties, including the elastic modulus, yield stress.

#### 3.2.1. Mechanical tests

Engineering stress-strain curves of tensile specimens are shown in Appendix C, Fig. C.1. All data, such as modulus of elasticity, yield strength, and ultimate strength, were averaged and then used in finite element analysis.

In the case of Split-P lattice structures, three specimens of each lattice configuration were tested under the quasi-static compression test. The stress-strain curves of each group of Ti6Al4v Split-P lattice are shown in Appendix C, Fig. C.2, and the average experimental stress-strain curves are shown in Fig. 5. The behavior of all Split-P lattices represents the typical behavior of most lattice structures which is generally categorized into four deformation zones. Region I shows an initial nonlinear region at a low strain, attributed to the misalignments between the lattices and compressive plates. Region II starts with the linear elastic regime, where the slope represents the elastic modulus. Next, follows the nonlinear regime demonstrating post-yield hardening. The stress-strain curve rises until it reaches the maximum stress ( $\sigma_{L,U}$ ). Region III displays the plateau stage with multiple collapses and failures. Finally, Region IV is the densification stage in which the compressive response increases sharply due to the self-contacting of the unit cell surfaces and full collapse of the cells. Due to the layers collapse and local densification of the collapsed layers, noticeable stress fluctuations are observed in the plateau zone.

Table 5 lists the corresponding mechanical properties, including the modulus of elasticity, yield strength, ultimate strength, the first lowest stress value after the first plastic failure, the load-bearing capacity, collapse strain ( $\epsilon_C$ ), and densification strain ( $\epsilon_D$ ). The mechanical performance, such as modulus of elasticity, yield strength, and peak compressive strength, is improved with an increase in RD, as the lower porosity leads to a rise in plateau stress, load-bearing capacity, and collapse and densification strains. The SP06U125 series, with a porosity of 89.52%, has the highest calculated elastic modulus of  $3.48 \pm 0.14$  GPa and the SP025U125 series has the lowest elastic modulus of  $1.55 \pm 0.18$  GPa.

The deformation behavior of SP06U125, SP04U125, and SP025U125 during compression testing is shown in Fig. 6 at strain levels ranging from 0 to 50%, indicating that failure begins in the highest layers of the lattices SP06U125 and SP04U125 and in lower layers for SP025U125.

The specimens deform uniformly during the initial elastic stage. As the compressive load increases, the stress-strain curves rise until reaching the maximum strength (at around 10% strain) shown in Fig. 5. Then, the cracks initiate, followed by shear band(s) formation, and continue propagating until the failure point. Shear band failure is visible in SP06U125 and SP04U125 from the upper right corner to the middle of the lower left side. High RD makes the shear band failure mode more apparent for these two lattices. The layer-by-layer failure mode, starting with the last layer, is demonstrated by SP025U125. After the last layer failure, the subsequent layers slowly come into contact. However, the SP025U125 does not show a strain-hardening effect during the deformation process. The initial collapse of each lattice is observed at a strain between 10% and 13% (Fig. 5).

#### 3.2.2. Gibson-Ashby model

The Gibson-Ashby model of the tested samples is plotted in Fig. 7 as a function of RD to predict the fitting function between the RD and mechanical properties. The relative modulus of elasticity and the relative yield strength are positively correlated with the actual RD of the Split-P lattices. The characteristic parameters of Gibson-Ashby fitting model and their correlation coefficient  $R^2$  are  $C_1 = 0.04$ ,  $n_1 = 1.32$ ,  $R^2 = 0.99$  for modulus of elasticity and  $C_2 = 0.91$ ,  $n_2 = 1.54$ ,  $R^2 = 0.99$  for yield strength. The modulus of elasticity and strength of the structures increase exponentially with the RD, and high fitting coefficients  $R^2$  indicate a high level of precision in adaptation.

### 3.3. Effect of cell morphology on the mechanical behavior of split-p lattices

Fig. 8 shows the stress-strain curves of SP06U125Iso1 and SP05U145 with the same RD of 21% and different CM. Four regions can be seen in the stress-strain curve of two lattices (as discussed in Section 3.2.1). An initial nonlinearity (I) is followed by a linear elastic stage (II) extending to the first peak. Then, after a sharp drop, a plateau stage (III) occurs, which continues until the densification stage (IV). Marked differences can be seen in stress-strain curves of two lattices with the same RD after reaching ultimate strength, demonstrating the influence of CM on the compressive behavior. In the plateau zone of each lattice, fluctuations caused by layer collapse and local densification are visible. Both lattice types show a hardening behavior in the plateau region and densification at the end of the plateau stage, where the stress-strain curves increase sharply. The stress rises to the initial peak values at the compressive strain of around 80% for SP05U140 and about 70% for SP06U125Iso1.

Table 5  
Mechanical properties of SP06U125, SP04U125, and SP025U125 lattices with different RD (unit cell = 12.50 mm, isoalue = 0).

	$E_f$ (GPa)	$\sigma_{LY}$ (MPa)	$\sigma_{LU}$ (MPa)	$\sigma_{LP}$ (MPa)	$\sigma_{min}$ (MPa)	K	$\epsilon_C$ (%)	$\epsilon_D$ (%)
SP06U125	$3.48 \pm 0.14$	$152.74 \pm 0.01$	$170.47 \pm 0.67$	$30.16 \pm 2.41$	$15.14 \pm 4.9$	$0.08 \pm 0.02$	$11.22 \pm 0.99$	$70.19 \pm 0.65$
SP04U125	$2.50 \pm 0.12$	$83.19 \pm 1.26$	$117.32 \pm 0.48$	$59.93 \pm 1.50$	$20.65 \pm 3.76$	$0.17 \pm 0.03$	$13.29 \pm 0.38$	$70.70 \pm 0.96$
SP025U125	$1.55 \pm 0.18$	$57.95 \pm 3.60$	$93.93 \pm 2.26$	$61.32 \pm 8.84$	$13.25 \pm 0.96$	$0.16 \pm 0.00$	$13.87 \pm 0.05$	$68.03 \pm 2.15$

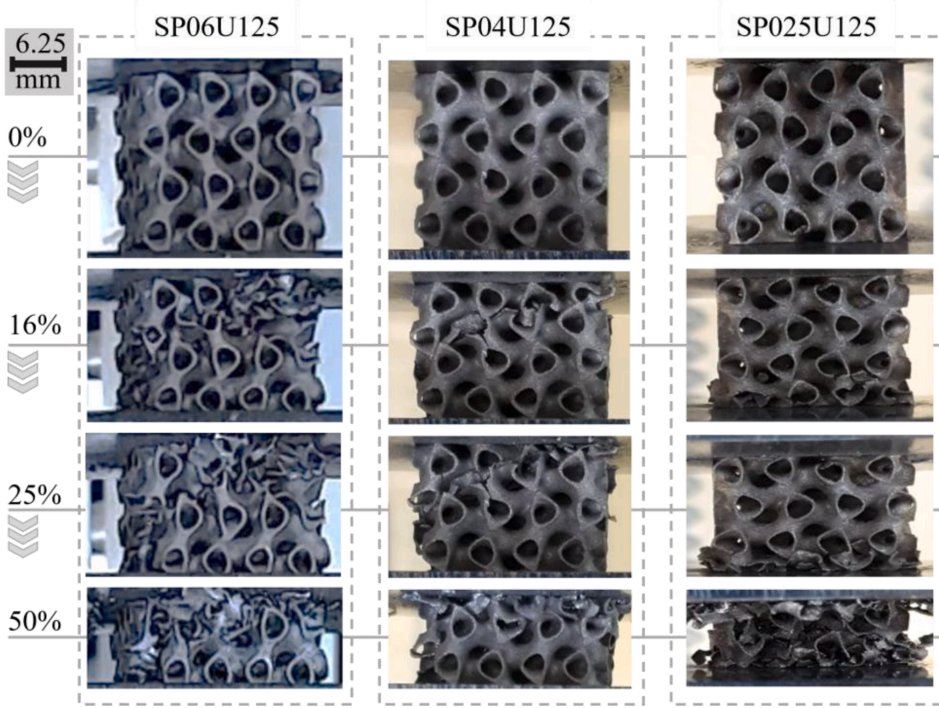


Fig. 6. Failure modes of SP06U125, SP04U125, SP025U125 lattices under compression test up to 50% strain at a strain rate of 1 mm/min.

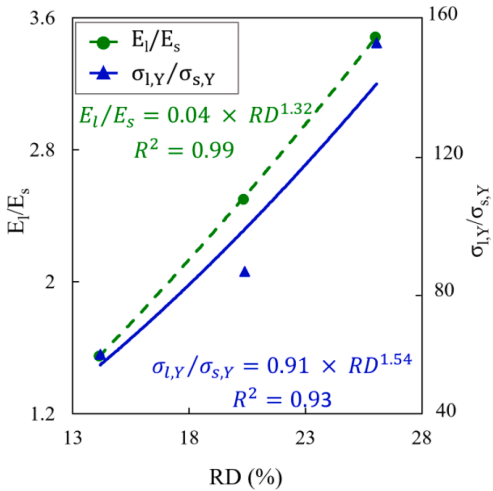


Fig. 7. Fitting of Gibson Ashby model as a function for relative elastic modulus and relative yield strength of SP06U125, SP04U125, and SP025U125 as a function of RD.

The appearance of deformed SP06U125Iso1 and SP05U140 after the uniaxial compression test is shown in Fig. 9, indicating their different deformation modes. According to Figs. 8 and 9, failure initiated at around 10% strain for both lattices, and according to Fig. 8, the first failure occurred with the first collapse of the layers. Two different failure behaviors are observed for each lattice. SP06U125Iso1 shows complete

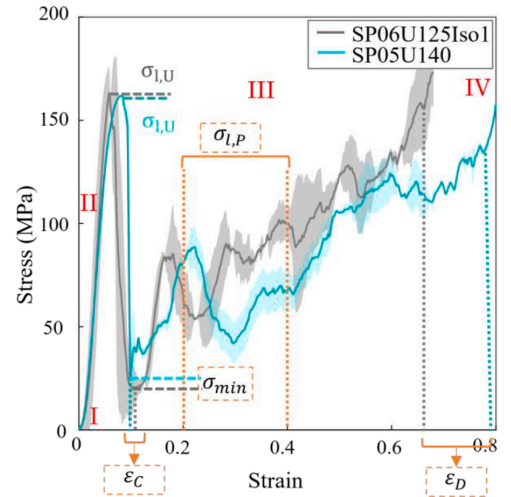


Fig. 8. Experimental stress-strain curves of SP025U125 and SP05U140 subjected to a quasi-static compression test at strain rate of 1 mm/min.

shear failure behavior at 45° to the load direction, which can be related to the visible interconnected pores and connection sites in the lattices. High localization of normal and shear stress occurs within the connection sites increasing the possibility of failure. SP05U140 shows failure starting at the top layers and then continuing to next layers.

The mechanical properties of the two lattice structures are listed in Table 6. A noticeable difference is found in their mechanical properties.

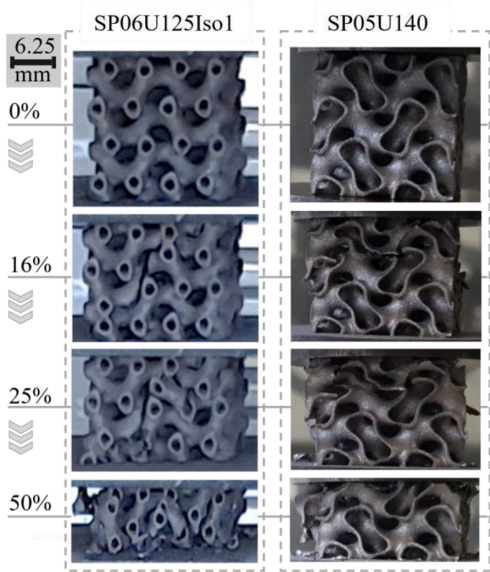


Fig. 9. Failure modes of SP06U125Iso1 and SP05U140 lattices under compression test up to 50% strain at a strain rate of 1 mm/min.

At the same RD, SP06U125Iso1 has better mechanical properties in terms of elastic modulus, yield strength, ultimate strength, plateau strength, and load-bearing capacity than SP05U140. It is evident that Split-P with a solid network morphology exhibits better mechanical performance than a sheet-base Split-P lattice.

Table 6  
Experimental mean value result of the mechanical properties of specimens SP06U125Iso1 and SP05U145.

Lattice	$E_t$ (GPa)	$\sigma_{LY}$ (MPa)	$\sigma_{LU}$ (MPa)	$\sigma_{LP}$ (MPa)	$\sigma_{min}$ (MPa)	K	$\epsilon_c$ (%)	$\epsilon_D$ (%)
SP06U125Iso1	3.48 ± 0.07	116.02 ± 2.05	137.15 ± 0.79	63.21 ± 0.21	12.81 ± 8.05	0.09 ± 0.05	10.44 ± 1.15	62.38 ± 1.87
SP05U140	2.63 ± 0.007	100.88 ± 5.03	129.59 ± 0.19	50.31 ± 7.55	5.6 ± 0.14	0.04 ± 0.00	9.76 ± 0.16	77.91 ± 0.67

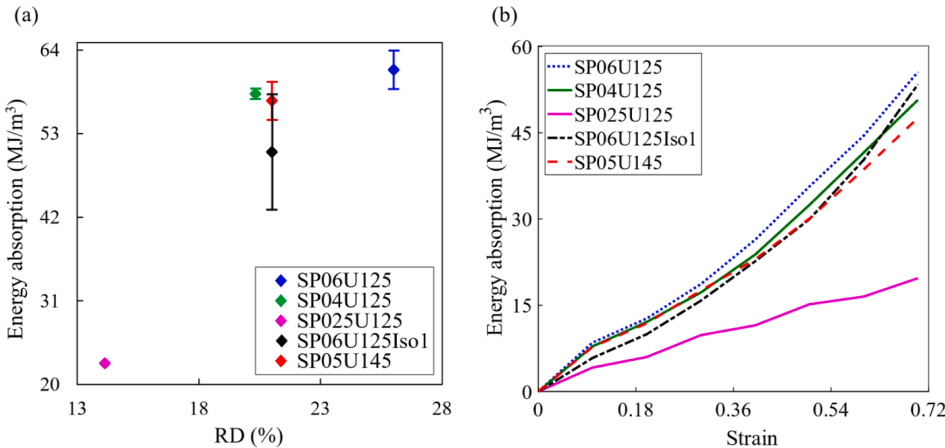


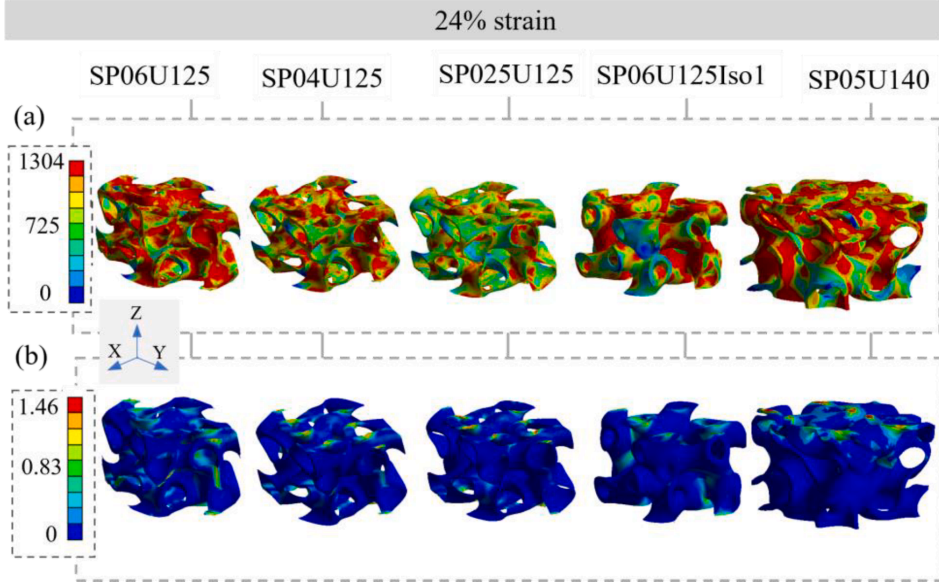
Fig. 10. Energy absorption of Split-P lattices (SP06U125, SP04U125, SP025U125, SP06U125Iso1, and SP05U145) subjected to compression load at different RD and strains up to the densification region; (a) Total energy absorption up to the densification region of each lattice at different RD; (b) Energy absorption behavior of Split-P lattices vs strain.

3.4. Energy absorption

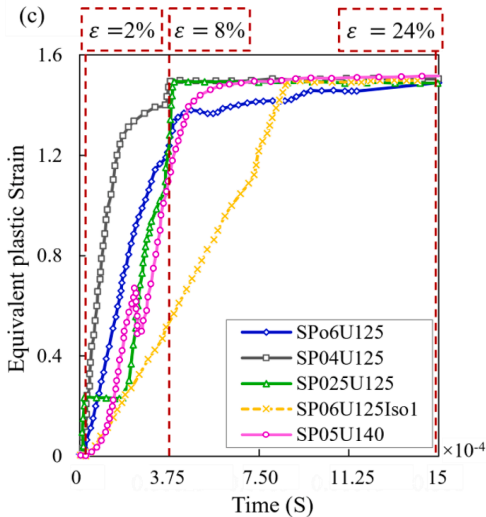
Fig. 10 shows the energy absorption versus RD and compressive strain. SP06U125 lattice reaches the highest energy absorption of  $61.41 \pm 2.52 \text{ MJ/m}^3$  while SP025U12 has the lowest value of  $22.82 \pm 0.86 \text{ MJ/m}^3$ . The energy absorption of SP06U125 is about 2.7 times that of P025U125, as shown in Fig. 10a. Thus, the effect of RD is more pronounced on the energy absorption capacity of the lattices. Comparison between SP05U140 and SP06U125Iso1 demonstrates that with the same RD, SP05U140 exhibits higher energy absorption ( $57.35 \pm 2.52 \text{ MJ/m}^3$ ), almost equal to the energy absorption of SP04U125 ( $58.22 \pm 0.69 \text{ MJ/m}^3$ ) with an RD of around 26%. Therefore, CM appears to have a strong effect on the amount of energy that can be absorbed. It is clearly visible that in the case of SP05U140, even with such a low density, the lattices have almost the same energy absorption as SP06U125Iso1. Fig. 10b presents the energy absorption curves of all Split-P lattices as a function of strain. All lattices exhibit a linear and steadily increasing trend, while SP025U125 shows an undulating curve with smooth fluctuations, which can be attributed to the collapse of the layers.

3.5. Numerical results

The mesh convergence study and a comparison of the numerical results of solid elements with the same size as shell elements are presented in Appendix D. As a result, solid and shell meshes with the size of 0.2 mm were selected to perform numerical simulation. Fig. 11 shows the contours of the equivalent von Mises stress and the plastic strain within the Split-P unit cells at 24% strain 24% for five topologies and RD. According to Fig. 11a, all Split-P unit cells exhibit a stress distribution across the surfaces, indicating better load-bearing capacity and a good stress transfer. In contrast, for SP05U125Iso1, the stress increases at the strut connection sites that are parallel to the load direction, demonstrating that solid network Split-P lattices can be effective in load-bearing capacity. Cells with different RD and morphologies show



**Fig. 11.** Distribution of von Mises stress and equivalent plastic strain of Split-P unit cells SP06U125, SP04U125, SP025U125, SP06U125Iso1, SP05U140 under compression test at a strain of 24%.



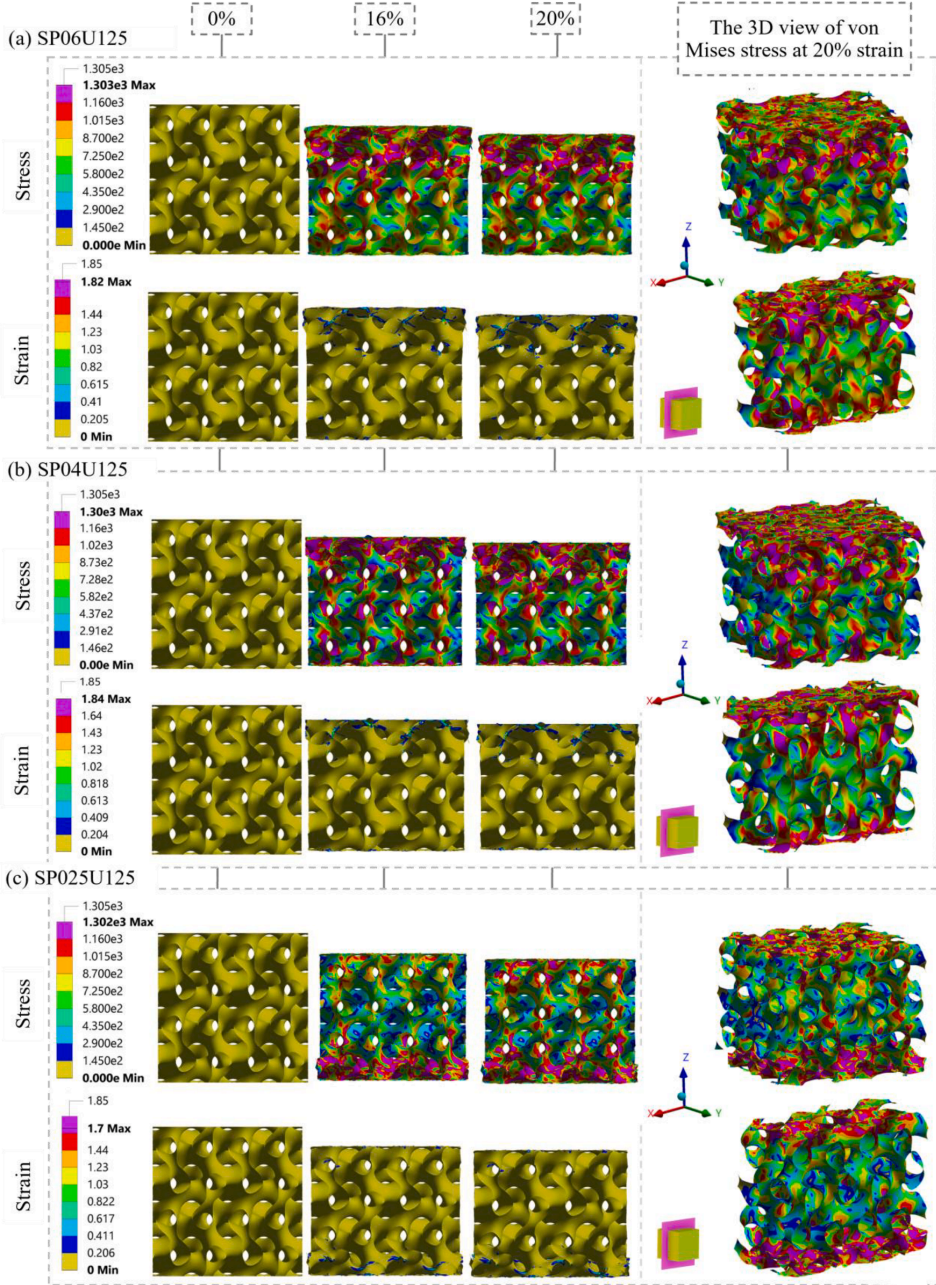
**Fig. 12.** Equivalent plastic strain vs. time of proposed Split-P unit cells named SP06U125, SP04U125, SP025U125, SP06U125Iso1, and SP05U140 under compression test at a strain of 24%.

yielding behavior at different strain levels. The contour of the equivalent plastic strain, seen in Fig. 11b, indicates high failure potential regions. SP05U125Iso shows the most localization of plastic deformation at the strut connection sites. In the case of SP025U125, the area of high plastic deformation is observed in the uppermost and lowermost layers. At a strain of 2%, the connection areas of SP06U125, SP04U125, and SP025U125 reach plasticity, while no significant signs of plasticity can be seen in the middle layers. SP05U140 also exhibits plastic deformation starting in the uppermost layers.

According to the strain-time curves in Fig. 12, all lattices show an upward trend in plastic behavior up to 2% strain. At 2% strain, SP025U125 has a different failure mode, indicating the first layer (bottom layer) reaches yield. Then, the plastic strain increases uniformly within the unit cell, followed by the second layer. All lattices exhibit an increasing trend between 2% and 8% strain except SP05U140. One drop can be seen in the SP05U140 curve, indicating the failure of the first layer (top layer). Among all lattices, SP05U125Iso has lowest slope at 8% strain, showing the longer time needed to reach yield. At  $3.75 \times 10^{-4}$  s, SP04U125 reaches its high plastic strain level, followed by SP025U125. SP06U125 reach to the high plasticity value at around  $15 \times 10^{-4}$  s while SP05U140, SP06U125Iso shows the maximum plasticity at around 6 and 8 s.

Fig. 13. represents the results of the numerical simulation for lattice structures showing that the deformation agrees well between computations and experiments. The von Mises stress distributions and equivalent plastic strains of Split-P TPMS lattice structures with an overall strain of 0%, 16%, and 20% are presented in Fig. 13 for SP06U125, SP04U125, and SP025U125 and in Fig. 14 for SP06U125Iso1 and SP05U140. The distributions of von Mises stresses in Fig. 13a show the largest stress concentrations in the layers and the connection sites depending on the lattice type. Ultimate stress is clearly more concentrated in the upper and bottom layers of SP025U125 and SP04U125. The upper layers of SP06U125 show higher stresses than the bottom layers, causing the main failure. In SP05U140, stress concentration regions in the top and bottom layers are clearly visible. Stress concentration can also be seen in the middle layers. Finally, in SP06U125Iso1, high stress is found in the middle of the connection struts. By increasing strain during compression, more stress is concentrated in the lattice, resulting in fractures. The fracture may transfer between layers as the stress concentration region shifts from one layer to the next. In according to the equivalent plastic strain distributions in all lattices in Figs. 13 and 14, most of the plastic deformations occur in the uppermost layers, leading to the initial collapse of SP06U125, SP04U125, and lower layers in SP025U125. However, several signs of plasticity are also observed in the middle layers of SP05U140 lattices. In SP025U125, first, the bottom layer reaches plasticity first, then the plastic strain increases uniformly





**Fig. 13.** Equivalent stress and plastic strain distributions of Split-P lattices at different strain level of 0%, 16%, and 20% and their 3D views of von Mises stress distribution at 20% strain, (a) SP06U125, (b) SP04U125, (c) SP025U125.

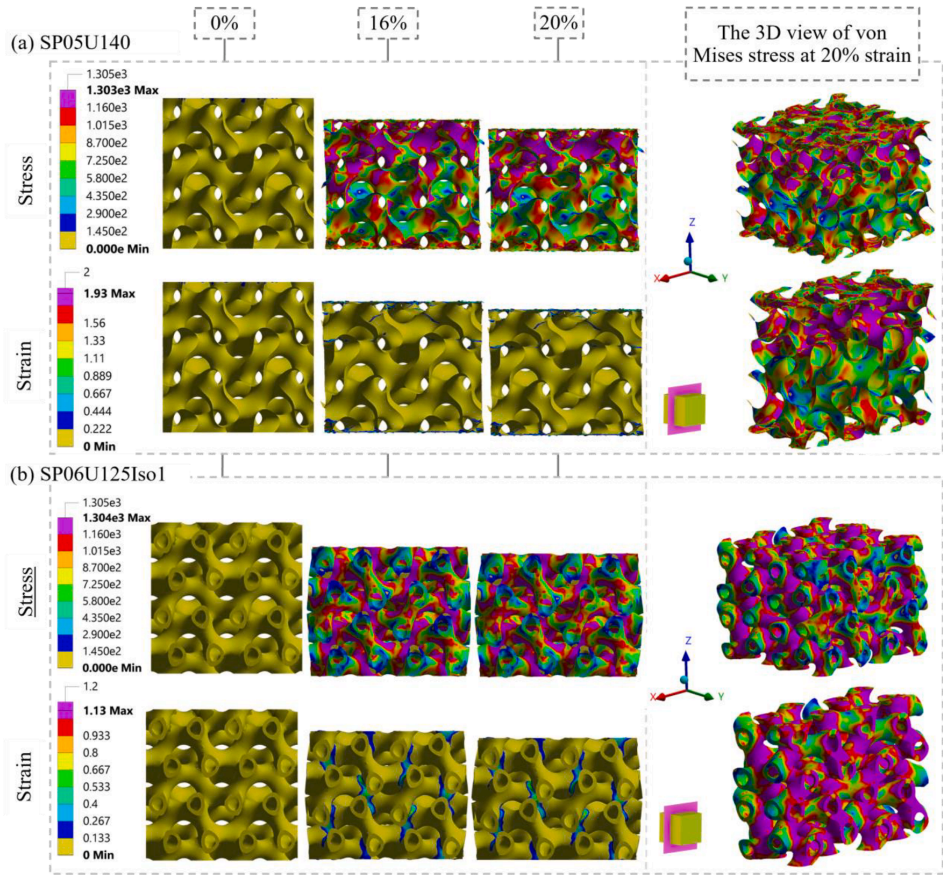
within the lattices, followed by the second layer. In SP06U125Iso1, most strut joints show localization of deformation, which increases the possibility of collapse.

As mentioned earlier, for all lattices except SP06U125Iso1, shell elements were used for numerical simulations. Shell elements are time-saving in numerical simulations due to the reduced number of elements [32]. The reliability of the FE method in the prediction of

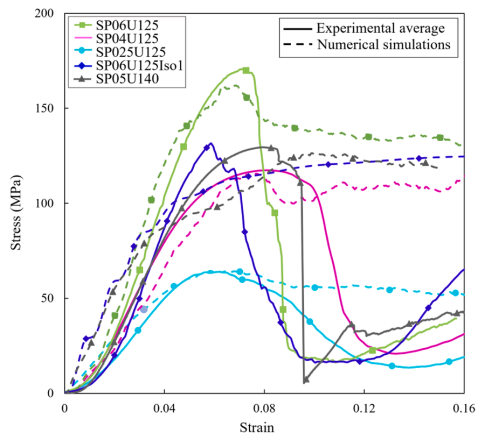
mechanical properties in terms of elastic modulus and yield strength was investigated by the relative error of the numerical simulation and experimental results, as shown in Fig. 15 and summarized in Table 7.

### 3.6. Lattice anisotropy comparison

In this section, Split-P lattices are compared with other TPMS



**Fig. 14.** Equivalent stress and plastic strain distributions of Split-P lattices at different strain level of 0%, 16%, and 20% and their 3D views of von Mises stress distribution at 20% strain; (a) SP05U140, and (b) SP06U125Iso1.



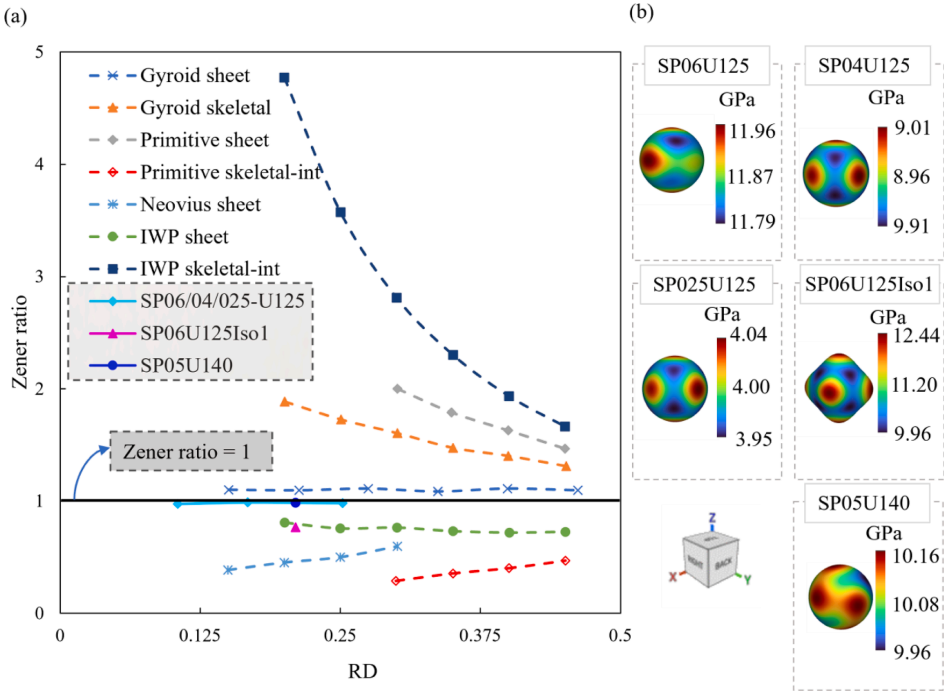
**Fig. 15.** Comparison of the computational and experimental stress-strain behaviors of SP06U125, SP04U125, SP025U125, SP05U140, and SP06U125Iso1 at 16% strain.

**Table 7**  
Comparison of the mechanical properties (elastic modulus and yield strength) of Split-P lattices in experiment and numerical simulation.

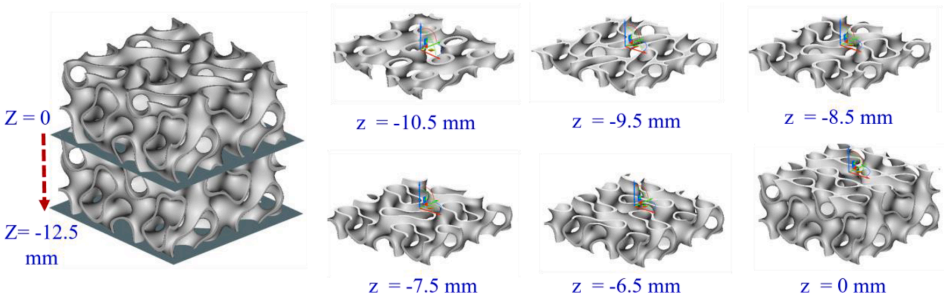
lattice	E (GPa)			$\sigma_y$ (MPa)		
	FE	Exp.	Error (%)	FE	Exp.	Error (%)
SP06U125	2.99	3.48	13.85	128.34	152.74	15.97
SP04U125	1.69	2.50	32.40	75.85	83.19	8.82
SP025U125	1.28	1.55	17.42	44.47	57.95	23.26
SP06U125Iso 1	2.86	3.49	18.05	82.76	116.02	28.67
SP05U140	2.47	2.63	6.08	97.47	100.88	3.38

structures by describing them in terms of Zener ratio. The comparison is shown in Fig. 16 for different RD. SP06U125, SP04U125, SP025U125, and SP05U140 have a Zener ratio close to 1. The Zener ratio of SP06U125Iso1 is lower, indicating anisotropy in the elastic properties of this lattice.

The obtained Zener ratios for SP06U125, SP04U125, SP025U125, SP05U140, and SP06U125Iso1 are 0.97, 0.99, 0.98, 0.98, and 0.76, respectively. The modulus surface illustrates the degree of anisotropy graphically. SP06U125Iso1 shows the highest degree of anisotropy due to its apparent protrusion into three principal directions. Other Split-P lattices have approximately isotropic moduli. Among the Split-P lattices, the SP04U125 lattice shows the highest Zener ratio (closest to 1).



**Fig. 16.** (a) Zener anisotropy index of Split-P lattices in the current study compared to different types of TPMS unit cells with different RD [57], (b) 3D elastic modulus surface of Split-P unit cells.



**Fig. 17.** Variety of pore shapes and pore sizes in Zdirection at different section views of Split-P lattice in the specific morphology (SP05U140) designed in the current study.

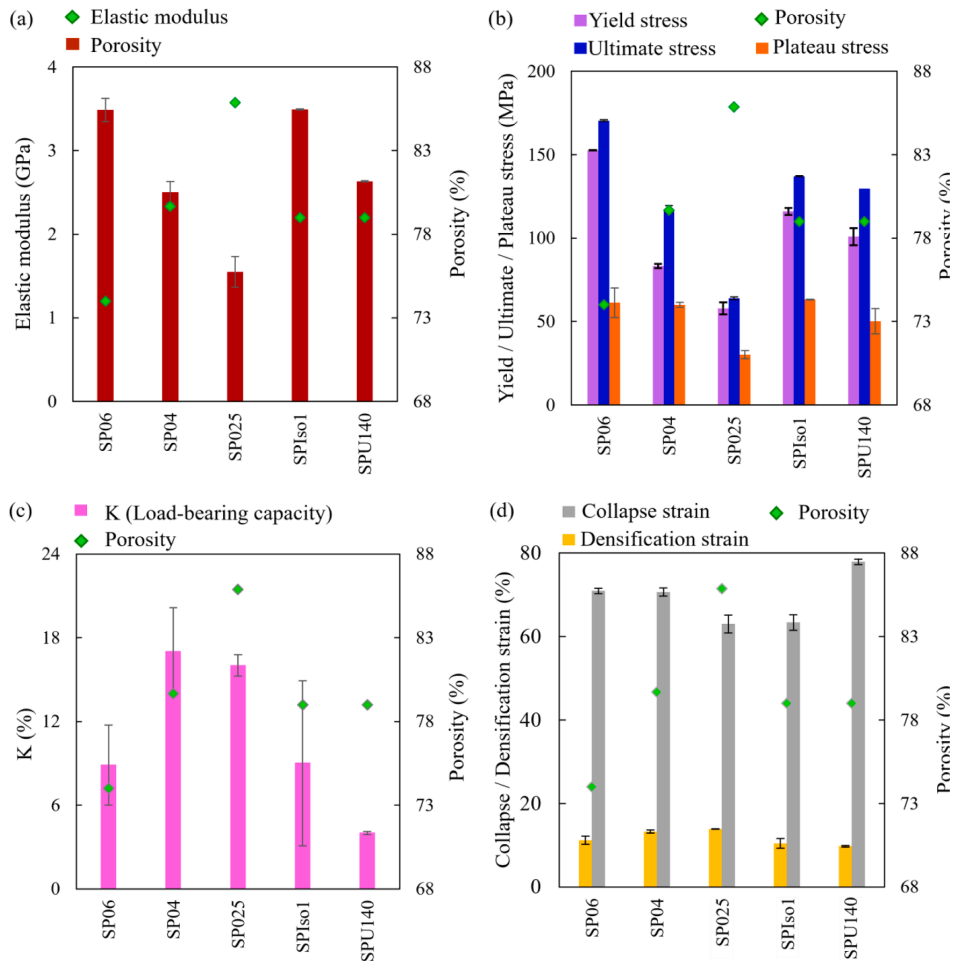
#### 4. Discussion

This study investigates SLM fabricated Split-P TPMS lattices with different porosities and CM as potential bone substitutes for the first time. The SLM process was used to fabricate Ti6Al4V Split-P lattices demonstrating that AM technologies can fabricate Split-P lattices on specific structural supports, depending on RD and thickness. We found that for some porosities and CM, it is essential to consider support structures to secure overhanging features and parts of the build platform.

##### 4.1. Structural advantages of split-p lattices

A large surface area facilitates cell adhesion and proliferation, and a larger pore size leads to enhanced permeability of the implant,

influencing bone ingrowth. Consequently, implants' surface area and pore size are important biological parameters [18]. A low porosity results in a reduction of bone growth, while a high porosity promotes it. The preferred pore size that supports new bone formation is 100–300  $\mu\text{m}$  [58]. Split-P lattices, which have a high surface area compared to other TPMS (Table 1), show a wide variety of pore shapes and pore sizes, as seen in Fig. 17, illustrating the different section views of the SP05U140 lattice structure. The pore size can be adjusted by increasing or decreasing the corresponding unit cell size and thickness to be within the required range for bone growth. Therefore, adjustment of structural parameters, such as cell size and isovalue, plays a critical role in controlling surface area and maintaining mechanical properties.



**Fig. 18.** Comparison of the mechanical properties of Split-P lattices vs porosity; SP06 (SP06U125), SP04 (SP04U125), SP025 (SP025U125), SP1so1 (SP06U125Iso1), and SP140 (SP05U145); (a) Elastic modulus, (b) Yield, ultimate and plateau stress, (c) Load-bearing capacity (K), and (d) Collapse and densification strain.

**Table 8**  
Comparison of mechanical properties of Split-P TPMS porous AM biomaterials with human bone tissue. Dash (–) indicates an absence of data.

	Split-P TPMS	Unknown different region of human bone	Proximal tibia	Iliac crest	Femoral neck	Skull
$E(\text{GPa})$	1.50–3.45	0.01–1.57 [84]	0.2–2.8 [43]	3–4.63 [85]	0.75–4.5 [40]	2–6 [82]
$\sigma_y(\text{MPa})$	55–128	–	–	–	55.3± [43]	–
$\sigma_U(\text{MPa})$	62–170	1.5–38 [84]	–	–	–	–

4.2. Structural morphology of fabricated Ti6Al4V split-p lattices

To improve the quality of 3D printing and increase the dimensional accuracy of the as-built samples, appropriate supports were added to the CAD model of the Split-P lattices as shown in Appendix B, Fig. B.1. In Split-P structure, self-supporting of the lattice depends on the size of the unit cells and wall thickness. With large-size unit cells, the suspended

area in the air and consequently the risk of unsuccessful 3D printing can increase. By increasing the thickness of the lattice, the suspended area can be reduced and a self-supporting Split-P lattice can be achieved. Among the designed lattices in this study, the SP06U125 lattices has natural connections and does not require any additional support.

The current study shows RD discrepancies between as-built lattices and CAD designs. These differences may be due to the unmolten powder particles attached to the lattice surfaces, leading to high surface roughness. Split-P lattice has the highest surface area among Gyroid, Diamond, and Primitive TPMS (Table 1). The large surface area intensifies the interaction between the powders and the consolidating base materials [40]. Therefore, in Split-P structures, the particles of partially melted metal powder adhering to the surface of the specimen may affect the measured RD, as reported in [18]. Blockage-free samples confirm SLM’s capability to fabricate Split-P TPMS lattices. The experimental results of the actual (fabricated) RD are fitted to those of the CAD model with a mathematical relationship of  $RD_{Actual} = 1.24(RD_{CAD}) - 7.55$  with a coefficient of determination of  $R^2 = 0.98$ , as shown in Appendix E, Fig. E.1. Accordingly, the correlation can be used as a guideline for the design of Split-P lattices.



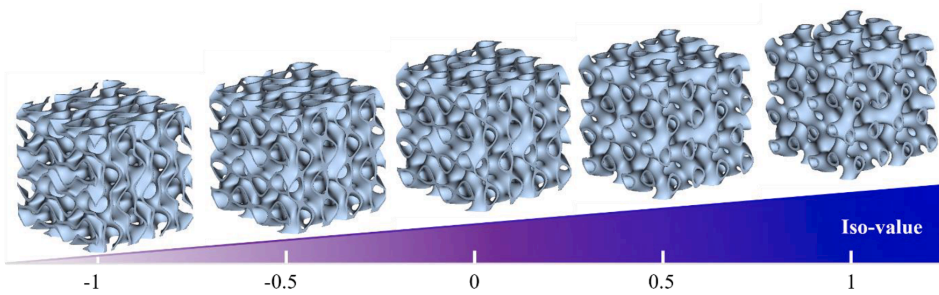


Fig. A.1. The effect of varying the iso-value on the resulting Split-P TPMS.

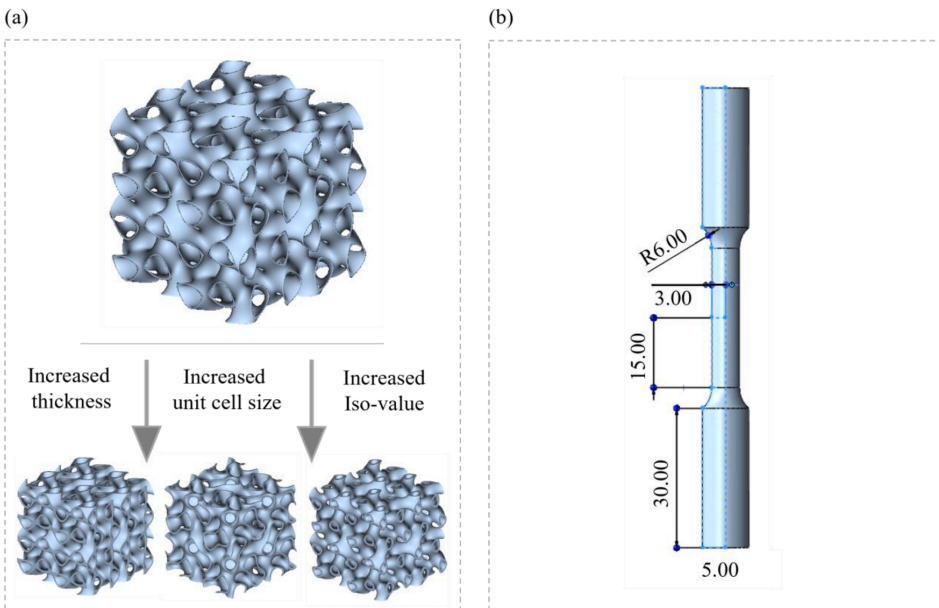


Fig. A.2. The procedure of the designed Split-P lattices with changing the thickness, unit cell size and iso-value and CAD model of solid tensile specimens; (a) CAD models of Split-P lattices; (b) CAD model of tensile specimen (dimensions in mm).

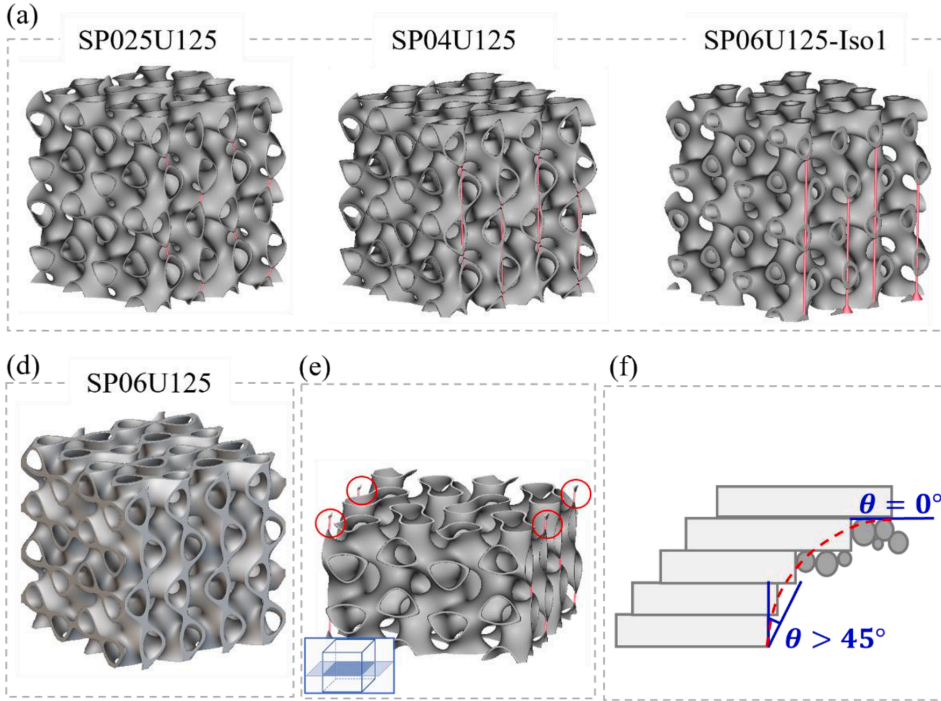
#### 4.3. Effect of structural morphology on compressive behavior and mechanical properties

This section discusses the results of Sections 3-2, 3-3, and 3-4. Porous scaffolds respond to compressive loading differently depending on their morphological parameters, such as porosity and pore shapes [59]. As a result of wall elements collapsing and load-bearing struts fracturing, all stress-strain responses of cellular lattices drop sharply after the first maximum strength, which is related to a brittle failure of struts in SLM processed Ti6Al4V lattice [60]. A significant drop can be seen for all lattices after reaching the ultimate strength, which is affected by the RD. This first sharp drop is at approximately 7%, 10%, and 6% compressive strains for SP06U125, SP04U125, and SP025U125, respectively.

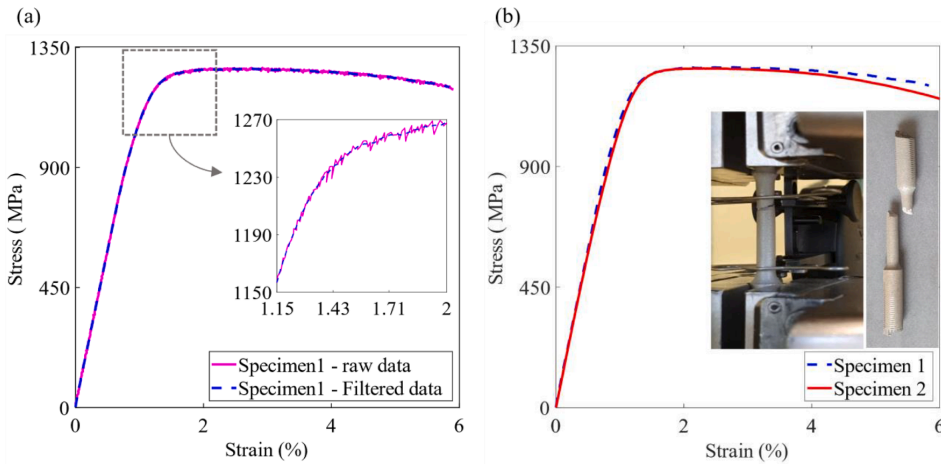
The load-bearing capacity  $K$  of lattice structures is also influenced by the structure's morphology and RD [61] and depends on the first minimum stress value after the initial plastic failure and the ultimate stress. The minimum load-bearing capacity was recorded for SP06U125. SP025U125 and SP04U125 exhibits the highest load-bearing capacity, almost 50% greater than SP06U125. The compressive response of Split-P

lattices indicates that the lattice with a lower porosity can behave like a solid block, resulting in higher shear stresses and a decreased load-bearing capacity, as reported in [61]. Therefore, the lattice's RD can influence load-bearing performance. Tables 5 and 6 show that CM strongly influences mechanical properties. SP06U125Iso1, with lower RD than SP06U125, shows higher elastic modulus and strain collapse with almost the same load-bearing capacity. SP05U140 and SP04U125 have nearly the same elastic modulus, while the RD of SP04U125 is less than the RD of SP05U140 by about 13%. The yield strength, ultimate strength, and load-bearing capacity of SP06U125Iso1 are greater than those of SP04U125. Among the five lattices, SP025U125 and SP06U125 have the lowest and highest elastic modulus, yield strength, and ultimate strength. The load-bearing capacity is highest for SP04U125 and lowest for SP05U140.

In the plateau region, all lattices show stress values below the ultimate strength, indicating that most of the energy is released during the first failure. However, the comparison between the stress-strain curves of different lattices shows that the plateau region demonstrates strain hardening and exhibits undulatory growth of stress due to the densification stage. The layer-by-layer failure behavior of the lattice in the



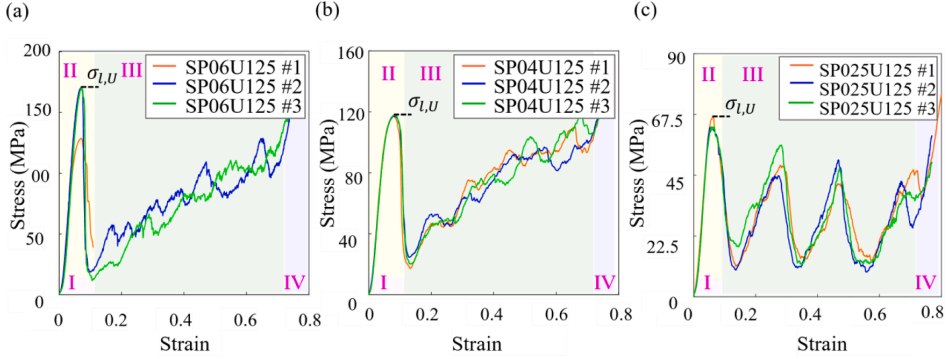
**Fig. B.1.** CAD designs of the Split-P lattices and the regions that need support to avoid collapsing during AM processes; (a) SP025U125, (b) SP04U125, (c) SP06U125-Iso1, (d) SP06U125 (e) Sectional view of Split-P lattice structure and areas that do not need self-supports, and (f) The influence of overhangs in bonded metal particles can result in deformation and collapse of the structure.



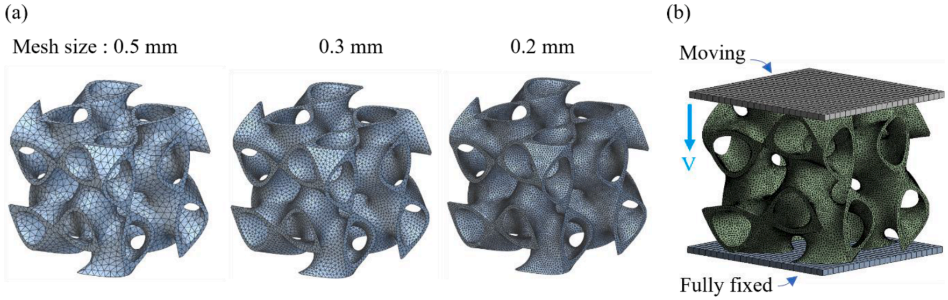
**Fig. C.1.** Stress-strain curves of as-built Ti6Al4V tensile specimens under quasi-static tensile test at strain rate of  $1\text{mm/min}$ , (a) Raw and filtered tensile test data of specimen 1, (b) Filtered tensile test data of specimens 1 and 2.

lower RD causes noticeable stress fluctuations in the plateau stage. The significant magnitude of fluctuations in the stress-strain curve is due to the failure of the individual layers and buckling of the local unit cells. In the cases of SP06U125 and SP04U125, the plateau region demonstrates some strain hardening and exhibits undulatory growth of stress up to the densification stage. In contrast, SP025U125 exhibits severe fluctuations with four noticeable stress fluctuations. The deformation behavior of

SP025U125 shows layer-by-layer collapse. Nevertheless, all samples densify at the end of the plateau stage, demonstrating an upward trend in stress-strain curves and reaching their initial peaks. Then, as the layers become denser at the end of the plateau, stress-strain behavior shows an increasing trend. The denser lattice structure exhibits a sharp increase in the elastic region, indicating high elastic modulus, high yield strength, and a large plateau region. It can be concluded that the



**Fig. C.2.** Stress-strain curves of each group of Ti6Al4V Split-P lattice subjected to quasi-static compression test at strain rate of 1 mm/min, (a) Stress-strain response of three tested lattices of SP06U125, (b) Stress-strain response of three tested lattices of SP04U125, (c) Stress-strain response of three tested lattices of SP025U125.



**Fig. D.1.** Different mesh sizes used in the FE analysis for the unit cell of SP04U125 with a size of 12.5 mm and RD of 16.74%; (a) Variation in solid mesh sizes varying from 0.5 mm to 0.2 mm (b) Applied boundary conditions used in numerical simulations.

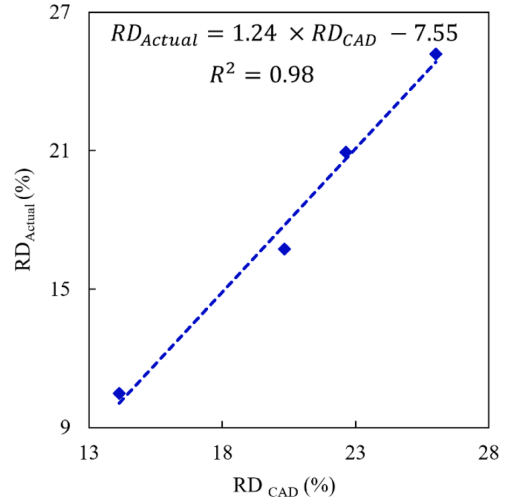
**Table. D.1**

The convergence results performed for the elastoplastic response of SP04U125 unit cell for solid elements in different sizes and shell elements.

Average mesh size	Total number of elements	Difference in Ewith previous iterations
Solid mesh	0.5 18,130	–
	0.3 67,631	0.11
	0.2 282,673	0.11
Shell mesh	0.2 44,578	0.17

morphology of the unit cell, the thickness, and, thus, RD strongly influence failure mechanisms since a denser structure exhibits fewer fluctuations of the stress-strain curve and homogeneous behavior, leading to collapse as a compact material. Therefore, depending on the architecture, the lattices undergo different failure mechanisms [62]. A low RD leads to a layer-by-layer failure, while in structures with a high RD, the shear band is observed, as reported in [63]. We found that the Split-P TPMS lattices exhibit stretching and shearing in some areas due to their complex shapes, and the designed RD also influences failure behavior.

The Gibson-Ashby model presents the relationship between the mechanical properties (elastic modulus and yield strength) and RD. The obtained value of the exponent  $n$  is close to 1, indicating stretching-dominated deformation [51]. Therefore, equations  $E_l/E_s = 0.04 RD^{1.32}$  and  $\sigma_{l,Y}/\sigma_{s,Y} = 0.04 RD^{1.32}$  establish the mathematical relationship between structural parameters and mechanical properties of Split-P TPMS. Accordingly, the actual mechanical properties of the 3D printed Ti6Al4V



**Fig. E.1.** The correlation between the CAD designed and actual (fabricated) RD of Split-P lattices at an iso-value of 0.

Split-P TPMS lattices can be predicted directly from the structural parameters ( $C, n$ ). For Split-P lattices, when the modulus is expressed as a function of RD, the stretching deformation behavior becomes more

evident as the curve approaches a straight line [64]. For the same RD, lattices with stretching-dominated deformation modes exhibit higher elastic modulus and strength, making them desirable for lightweight structures, such as orthopedic implants [65].

According to Fig. 18, among all Split-P lattices, SP025U125 has the lowest mechanical properties (elastic modulus, yield stress, ultimate stress, and plateau stress); however, its load-bearing capacity is among the highest. Changing unit cell size (CM) and isovalue leads to a significant change in mechanical properties [60]. Comparison between SP06U125 and SP06U125Iso1 shows that a 5% increase in porosity for SP06U125Iso1 results in the same elastic modulus but leads to a decrease in yield stress and ultimate stress. Both lattices show nearly the same plateau stress. SP04U125 and SP05U140 have almost the same elastic modulus while the porosity of SP04U125 is 4% higher than that of SP05U140. Yield stress and ultimate stress of SP05U140 are higher than those of SP04U125. SP05U140 has the lowest value of the plateau stress. SP04U125 has the highest load-bearing capacity among all Split-P lattices and SP05U140 shows the minimum value. SP025U125 exhibits maximum collapse strains, which can also be attributed to its load-bearing capacity. We conclude that the morphology of the unit cell strongly influences mechanical properties.

The energy absorption capacity, representing the material's resistance to load without severe failure, is an important property in the design of orthopedic structures [66]. This property is influenced by several parameters, such as RD, pore size, unit cell size, and unit cell type, while the most influential is RD [20]. A lattice structure as an energy absorber, should be able to withstand large deformations under relatively constant stress to prevent the lattice from being subjected to excessive stress [67] to provide long-term endurance and the ability to withstand impact load [68]. In addition, reducing fluctuations can significantly increase energy absorption [67] as can be seen in the comparison of mechanical responses in Figs. 8, and 10. According to Fig. 10, the energy absorption capacity increases gradually with increasing RD. The major factors affecting the energy absorption characteristics of a lattice structure are its plateau stress and densification strain; higher and longer plateau stress can improve the energy absorption [69].

Across all lattices investigated in the current study, high energy absorption (Fig. 10) was observed for SP06U125, SP04U125, and SP06U125Iso1, all of which showed high densification strain and high plateau stress (Fig. 18). Therefore, lattices have potential to be used for energy absorption applications. The energy absorption capacity of the lattices is in the range of 22.82 to 61.41 MJ/mm<sup>3</sup>.

Finally, high standard deviation can be seen in some mechanical properties of the experimentally tested lattices, similarly as reported in [70]. More samples could be used for the cases with high standard deviation. Nevertheless, this study shows the ability of SLM to produce Ti6Al4V Split-P lattices under specific structural supports, considering existing errors.

#### 4.4. Numerical simulations

Numerical simulations can predict the mechanical performance of additively manufactured lattice structures. However, the results do not agree ideally with the experimental data due to structural complexity and imperfect melting of the powder, as documented in previous studies [71]. Harrysson et al. [72] reported an error of 10.6–14.8% between experimental and computational results for the elastic modulus. An error of 30% between numerical and experimental results has been reported in [73]. Ma et al. investigated the mechanical properties of Gyroid structures by experiment and FEA. Their results showed prediction accuracy ranging from 30% to 56%. The authors' prior study [40] also reported the high difference between FEA and experiment, with deviation percentages ranging from 8% to 41% for elastic modulus and 32% to –24% for yield stress.

A discrepancy between the computational results and the

experimental test results is also found in the current study. These differences can be attributed to the SLM additive manufacturing technique and insufficient melting of metal powders [74,75], which is high in Split-P lattices due to large surface area leading to partially melted powder adhering to the surfaces. The deviation between the experiment and numerical simulation may also be due to the assumed friction contact in FEA [76]. A maximum relative error of 32.40% was observed in the elastic moduli and 23.26% in yield stresses in this study. Our study shows acceptable error rates for mechanical properties compared to the previous literature.

#### 4.5. Lattice anisotropy comparison

The current study used a numerical homogenization method to analyze the anisotropic elastic behavior of Split-P TPMS lattices. Isotropic lattices with appropriate porosity and mechanical properties are highly preferred for bone implantation [77,78]. In other types of TPMs, including Gyroid, Diamond, Schwarz P, F-RD, and Fischer-Koch S, increasing porosity leads to an increase in the deviation of the Zener ratio from 1 [79]. Increasing porosity and changing the unit cell morphology (i.e., increasing unit cell size and isovalue) increases anisotropy in axial directions. In all lattices, especially SP06U125Iso1, the stiff and soft directions are oriented axially and diagonally, respectively. Future work can seek to investigate methods to control anisotropy [78].

#### 4.6. Human bone and split-p lattices

Human cancellous and cortical bone have an elastic modulus of 0.1–4.5 to 3–20 GPa and yield strength of 2–17 to 33–193 MPa, respectively [80]. The elastic modulus of the skull is in the range of 2–6 GPa [81,82]. In the current study, 3D-printed Ti6Al4V Split-P lattices have mean elastic moduli of 1.55–3.48 GPa, lower than those of human cortical bone, and yield strengths of around 57–152 MP, which are comparable to those of cortical bone. Among all Split-P lattices, the elastic modulus and yield stress of SP025U125 are in the range and higher than those of cancellous bone, while the others are more suitable for use in the cortical bone and cortical part of the skull bone. Thus, SLM Ti6Al4V Split-P lattices are suitable structures for load-bearing applications due to their combination of high yield strength and low elastic modulus to eliminate stress shielding [83].

Finally, the current study has some limitations. More samples could be included in the analysis. Also, biocompatibility experiments were not conducted. Future work could explore biocompatibility and integration with bone. Additionally, functionally graded Split-P lattices were not considered in the current work. Future studies could address functionally graded Split-P lattices.

## 5. Conclusions

This study, for the first time, investigated experimentally and computationally the compressive behavior of Ti6Al4V SLM-manufactured Split-P TPMS lattices with different relative densities (RD) and cell morphologies (CM) for trabecular and cortical bone substitutes.

The present study found that the size of the unit cells and the thickness of the walls can affect the manufacturability of Split-P lattices. With the large size of the unit cell, low wall thickness, and specific porosities, the suspended area in the air and consequently the risk of an unsuccessful 3D printing process can increase. Therefore, appropriate supports should be added to the lattice. By increasing the thickness of the lattice, the suspended area can be connected and the Split-P lattice can become a self-supporting structure. However, the SLM-fabricated Ti6Al4V structures in this study show 9% to 34% higher RD than their CAD models.

Under a compression test, the Split-P lattices exhibit a modulus of



elasticity (1.55 to 3.48 GPa) and compressive yield strength (57.95 to 152.74 MPa), in the range of human bone. Among Split-P lattices with the same CM, SP06U125 exhibits higher elastic modulus, yield strength, and ultimate strength than SP04U125 and SP025U125. SP04U125 and SP025U125 have highest plateau stress and load-bearing capacity, approximately 50% higher than SP06U125. Gibson-Ashby model also indicates stretching-dominated deformation mechanisms in Split-P TPMS. In the group with the same RD and different CM including SP06U125Iso1 and SP05U140, the elastic modulus, yield strength, ultimate strength, plateau stress, and load-bearing capacity of SP06U125Iso1 are approximately 22%, 13%, 5%, 20%, and 55% higher than those of SP05U140.

The comparison between these two groups and the investigation of the effect of CM and RD on mechanical properties concludes that solid-based Split-P lattice structure (SP06U125Iso1) with 79% porosity shows almost equal mechanical properties to SP06U125 with 74.81% porosity. The same can be seen for SP05U140 with a porosity of 79%, in terms of elastic modulus in comparison with SP04U125 with a porosity of 83%. Comparing mechanical properties including yield strength, ultimate strength, plateau stress, and load-bearing capacity between SP04U125 and SP05U140 shows that changing CM strongly increases mechanical performance. Lattices exhibit an energy absorption of 22 to 61 MJ/m<sup>3</sup>, signifying high plastic deformation capacity. SP04U125 demonstrates energy absorption similar to SP05U140. SP06U125 shows the highest energy absorption, while SP025U125 shows the lowest. The comparison between SP05U140 and SP06U125Iso1 shows that solid-based Split-P lattices absorb energy 12% better than sheet-based lattices. Sheet-based lattices with the same cell morphology including SP06U125, SP04U125, SP025U125, and SP05U140, show two different failure behaviors, shear and layer-by-layer deformation. Significant 45° shear deformation is found in SP06U125Iso1 lattice with solid-based morphology indicating that CM and RD can greatly influence the compressive deformation.

The simulation results were confirmed through the compression tests on the samples and relatively errors were found between numerical and experimental results. Errors range from 6% to 32% and 3% to 28% in modulus of elasticity and yield strength respectively. In the von Mises stress and equivalent plastic strain distributions, Split-P lattice structures with different CM and RD show different stress and plastic strain concentrations. For the solid-based lattice structure SP06U125Iso1, the highest von Mises stress is concentrated at the connection sites. In other Split-P lattices most stress concentration occurs in the top and/or bottom

layer. Depending on the CM, stress concentration can also be seen dispersed in the middle layers. Homogenization study of the unit cells revealed a dependence between the Zener ratio and the CM. A sheet-based Split-P lattice exhibits almost isotropic moduli with a Zener ratio close to 1. SP06U125Iso1 showed the highest degree of anisotropy.

This study shows that Split-P lattices are potential candidates in load-bearing applications as they exhibit mechanical properties comparable to cortical or trabecular bone. The focus of this study, however, was only on the specific relative density with homogeneous pores size with constant wall thickness. Accordingly, future studies could investigate a sheet-based graded Split-P lattice structure with a variety of relative density variations. (Table 8)

#### CRedit authorship contribution statement

**Mansoureh Rezapourian:** Formal analysis, Investigation, Methodology, Software, Visualization, Writing – original draft. **Iwona Jasiuk:** Conceptualization, Data curation, Formal analysis, Methodology, Validation, Writing – review & editing. **Mart Saarna:** Investigation. **Irina Hussainova:** Conceptualization, Data curation, Formal analysis, Funding acquisition, Project administration, Resources, Supervision, Validation, Writing – review & editing.

#### Declaration of Competing Interest

The authors declare that they have no known competing financial interests or personal relationships that could have appeared to influence the work reported in this paper.

#### Data availability

Data will be made available on request.

#### Acknowledgments

This work was supported by the Estonian Research Council grant (PRG643, I. Hussainova). The authors wish to express their gratitude to Dr. Le Liu for his technical assistance in the additive manufacturing process and to Dr. Olga Volobujeva for SEM images.

## Appendix A. Design of Split-P lattices

### Mathematical equation of Split-P TPMS structure in the Cartesian coordinate system (X, Y, Z)

Mathematical form of Split-P lattice can be written as Eq. (A.1):

$$\varphi = 1.1 (\sin(2X)\cos(Y)\sin(Z) + \sin(2Y)\cos(Z)\sin(X) + \sin(2Z)\cos(X)\sin(Y)) - 0.2 (\cos(2X)\cos(2Y) + \cos(2Y)\cos(2Z) + \cos(2Z)\cos(2X)) - 0.4 (\cos(2Y) + \cos(2Z) + \cos(2X)) - t \quad (\text{A.1})$$

where,  $X, Y, Z = 2\pi n_i/L_i$ ,  $i = x, y, z$ , are the periodicities of the Split-P TPMS function,  $n_i$  indicates the number of unit cells along with the directions  $X, Y, Z$ , and  $L_i$  represents the unit size of the lattice structure in those directions.

### The effect of varying isovalue on the Split-P TPMS morphology

Changing isovalue in TPMS lattice can affect morphology of the lattices. In the case of Split-P TPMS, the isovalue of zero maximizes SA and SA/VR. Increasing the isovalue can create a solid-network lattice with lower SA and SA/VR that more closely resembles trabecular bone. Fig. A.1 shows the change in Split-P lattice morphology.

### CAD. model of designed Split-P lattices and tensile specimens

## Appendix B. Manufacturability of Split-P lattices

Fig. B.1 shows the CAD designs of the Split-P lattices and the regions that need support to avoid collapsing during AM processes. It is worth mentioning that all supports were carefully removed to perform compression tests on as-built lattices.

## Appendix C. Mechanical tests

### Engineering stress-strain curves of two tensile specimens

Fig. C.1 shows the engineering stress-strain curves of two tensile specimens obtained from quasi-static tensile tests. Raw data shows noisy data (Fig. C.1a). Therefore, a simple MAF algorithm is used to suppress the noises. Fig. C.1b represents the filtered data of two specimen tensile tests. The average values of modulus of elasticity, yield strength, and ultimate strength are  $114.7 \pm 3.7$  GPa,  $1182.8 \pm 8.7$  MPa, and  $1268 \pm 3.0$  MPa, respectively.

### Stress-strain curves of Ti6Al4V Split-P lattices at isovalue of 0

## Appendix D. Mesh convergence study

A mesh convergence study was performed for the unit cell of SP04U125 with a size of 12.5 mm under quasi static compression test up to 24% strain. The RD of the unit cell was set to 16.74% and solid mesh was generated using tetrahedral elements with the size of 0.5, 0.3, and 0.2 mm. Fig. D.1 portrays the variation in solid mesh sizes and applied boundary conditions in numerical simulations. All boundary conditions are considered according to the Section 2.4.

Table. D.1 summarizes the convergence results performed for the elastoplastic response of the unit cell. The results show that an average element size of 0.2 mm was adequate to obtain acceptable accuracy in the calculated responses and solid element of 0.2 mm can be used in numerical simulation of Split-P lattices. A comparison was also performed between the numerical results of 0.2 mm solid elements and shell elements, showing a good agreement. Thus, in the rest of this work the numerical simulations for lattice structures (not unit cells) used tetrahedral solid and shell elements of 0.2 mm. Depending on the lattice morphology, suitable element type was adopted. The solid elements were used for all unit cells and the SP06U125Iso1 lattice, while a shell mesh was used for the remaining lattices to reduce the computation time.

## Appendix E. Relationship between actual and designed RD of Split-P lattices

The correlation between designed and actual RD can be derived based on the result presented in Table 4 for SP06U125, SP04U125, and SP025U125. Fig. E.1 shows the correlation between actual RDs is well fitted to those of CAD designs with the coefficient of determination ( $R^2$ ) of 0.988.

## References

- [1] Goldberg V.M. Natural history of autografts and allografts. Bone Implant Graft 1992;9–12. [10.1007/978-1-4471-1934-0\\_2](https://doi.org/10.1007/978-1-4471-1934-0_2).
- [2] Zimmermann G, Moghaddam A. Allograft bone matrix versus synthetic bone graft substitutes. Injury 2011;42:S16–21. <https://doi.org/10.1016/j.injury.2011.06.199>.
- [3] Campana V, Milano G, Pagano E, Barba M, Cicione C, Salonna G, et al. Bone substitutes in orthopaedic surgery: from basic science to clinical practice. J Mater Sci Mater Med 2014;25:2445. <https://doi.org/10.1007/S10856-014-5240-2>.
- [4] O'Brien FJ. Biomaterials & scaffolds for tissue engineering. Mater Today 2011;14: 88–95. [https://doi.org/10.1016/S1369-7021\(11\)70058-X](https://doi.org/10.1016/S1369-7021(11)70058-X).
- [5] Sallent I, Capella-Monsonis H, Procter P, Bozo IY, Deev RV, Zubov D, et al. The few who made it: commercially and clinically successful innovative bone grafts. Front Bioeng Biotechnol 2020;8:952. <https://doi.org/10.3389/FBIOE.2020.00952/BIBTEX>.
- [6] Bohner M. Resorbable biomaterials as bone graft substitutes. Mater Today 2010;13: 24–30. [https://doi.org/10.1016/S1369-7021\(10\)70014-6](https://doi.org/10.1016/S1369-7021(10)70014-6).
- [7] Bazaka O, Bazaka K, Kingshott P, Crawford R.J., Ivanova E.P. Metallic implants for biomedical applications 2021;3:1–98. [10.1039/9781788019828-00001](https://doi.org/10.1039/9781788019828-00001).
- [8] Koons GL, Diba M, Mikos AG. Materials design for bone-tissue engineering. Nat Rev Mater 2020;5(5):584–603. <https://doi.org/10.1038/s41578-020-0204-2>.
- [9] Mastrogiacomo M, Scaglione S, Martinetti R, Dolcini L, Beltrame F, Cancedda R, et al. Role of scaffold internal structure on in vivo bone formation in macroporous calcium phosphate bioceramics. Biomaterials 2006;27:3230–7. <https://doi.org/10.1016/j.biomaterials.2006.01.031>.
- [10] Nguyen TD, Kadri OE, Sikavitsas VI, Voronov RS. Scaffolds with a high surface area-to-volume ratio and cultured under fast flow perfusion result in optimal O2 delivery to the cells in artificial bone tissues. Appl Sci 2019;9:2381. <https://doi.org/10.3390/AP9112381>.
- [11] Davoodi E, Montazerian H, Esmailizadeh R, Darabi AC, Rashidi A, Kadkhodapour J, et al. Additively manufactured gradient porous Ti-6Al-4V hip replacement implants embedded with cell-laden gelatin methacryloyl hydrogels. ACS Appl Mater Interfaces 2021;13:22110–23. [https://doi.org/10.1021/ACSAMI.0C20751/ASSET/IMAGES/MEDIUM/AMOC20751\\_M008.GIF](https://doi.org/10.1021/ACSAMI.0C20751/ASSET/IMAGES/MEDIUM/AMOC20751_M008.GIF).
- [12] Hayashi K, Kato N, Kato M, Ishikawa K. Impacts of channel direction on bone tissue engineering in 3D-printed carbonate apatite scaffolds. Mater Des 2021;204: 109686. <https://doi.org/10.1016/J.MATDES.2021.109686>.
- [13] Tanzer M, Chuang PJ, Ngo CG, Song L, TenHuisen KS. Characterization of bone ingrowth and interface mechanics of a new porous 3D printed biomaterial. Bone Joint J 2019;101-B:62–7. <https://doi.org/10.1302/0301-620X.101B6.BJJ-2018-1472.R1>.
- [14] Surmeneva MA, Surmenev RA, Chudinova EA, Koptioug A, Tkachev MS, Gorodsha SN, et al. Fabrication of multiple-layered gradient cellular metal scaffold via electron beam melting for segmental bone reconstruction. Mater Des 2017;133: 195–204. <https://doi.org/10.1016/J.MATDES.2017.07.059>.
- [15] Yang L, Li Y, Wu S, Chen P, Wu H, Su J, et al. Tailorable and predictable mechanical responses of additive manufactured TPMS lattices with graded structures. Mater Sci Eng A 2022;843:143109. <https://doi.org/10.1016/J.MSEA.2022.143109>.
- [16] Kelly CN, Kahra C, Maier HJ, Gall K. Processing, structure, and properties of additively manufactured titanium scaffolds with gyroid-sheet architecture. Addit Manuf 2021;41:101916. <https://doi.org/10.1016/J.ADDMA.2021.101916>.
- [17] Al-Ketan O, Rowshan R, Abu Al-Rub RK. Topology-mechanical property relationship of 3D printed strut, skeletal, and sheet based periodic metallic cellular materials. Addit Manuf 2018;19:167–83. <https://doi.org/10.1016/J.ADDMA.2017.12.006>.
- [18] Liu Z, Gong H, Gao J, Liu L. Topological design, mechanical responses and mass transport characteristics of high strength-high permeability TPMS-based scaffolds. Int J Mech Sci 2022;217:107023. <https://doi.org/10.1016/J.IJMECHSCI.2021.107023>.
- [19] Poltue T, Karuna C, Khruaeuangkham S, Seehanam S, Promopattum P. Design exploration of 3D-printed triply periodic minimal surface scaffolds for bone implants. Int J Mech Sci 2021;211:106762. <https://doi.org/10.1016/J.IJMECHSCI.2021.106762>.
- [20] Fan X, Tang Q, Feng Q, Ma S, Song J, Jin M, et al. Design, mechanical properties and energy absorption capability of graded-thickness triply periodic minimal surface structures fabricated by selective laser melting. Int J Mech Sci 2021;204: 106586. <https://doi.org/10.1016/J.IJMECHSCI.2021.106586>.

- [21] Yang L, Yan C, Han C, Chen P, Yang S, Shi Y. Mechanical response of a triply periodic minimal surface cellular structures manufactured by selective laser melting. *Int J Mech Sci* 2018;148:149–57. <https://doi.org/10.1016/j.jimecs.2018.08.039>.
- [22] Chen H, Han Q, Wang C, Liu Y, Chen B, Wang J. Porous scaffold design for additive manufacturing in orthopedics: a review. *Front Bioeng Biotechnol* 2020;8:609. <https://doi.org/10.3389/fbioe.2020.00609/BIBTEX>.
- [23] Abueidda DW, Elhebeary M, Shiang CS (Andrew), Abu Al-Rub RK, Jasiuk IM. Compression and buckling of microarchitected Neovius-lattice. *Extrem Mech Lett* 2020;37:100688. <https://doi.org/10.1016/j.eml.2020.100688>.
- [24] Rezapourian M, Kamboj N, Jasiuk I, Hussainova I. Biomimetic design of implants for long bone critical-sized defects. *J Mech Behav Biomed Mater* 2022;134:105370. <https://doi.org/10.1016/j.jmbbm.2022.105370>.
- [25] Zhang L, Feih S, Daynes S, Chang S, Wang MY, Wei J, et al. Energy absorption characteristics of metallic triply periodic minimal surface sheet structures under compressive loading. *Addit Manuf* 2018;23:505–15. <https://doi.org/10.1016/j.addma.2018.08.007>.
- [26] Liu L, Wang S, Liu J, Deng F, Li Z, Hao Y. Architectural design of Ti6Al4V scaffold controls the osteogenic volume and application area of the scaffold. *J Mater Res Technol* 2020;9:15849–61. <https://doi.org/10.1016/j.jmrt.2020.11.061>.
- [27] Al-Ketan O, Abu Al-Rub RK, Rowshan R. The effect of architecture on the mechanical properties of cellular structures based on the IWP minimal surface. *J Mater Res* 2018;33:343–59. <https://doi.org/10.1557/JMR.2018.1>.
- [28] Ali M, Sari RK, Sajjad U, Sultan M, Ali HM. Effect of annealing on microstructures and mechanical properties of PA-12 lattice structures proceeded by multi jet fusion technology. *Addit Manuf* 2021;47:102285. <https://doi.org/10.1016/j.addma.2021.102285>.
- [29] Miralbes R, Ranz D, Pascual FJ, Zouzias D, Maza M. Characterization of additively manufactured triply periodic minimal surface structures under compressive loading. *Mech Adv Mater Struct* 2020. <https://doi.org/10.1080/15376494.2020.1842948>.
- [30] Lehder EF, Ashcroft IA, Wildman RD, Ruiz-Cantu LA, Maskery I. A multiscale optimisation method for bone growth scaffolds based on triply periodic minimal surfaces. *Biomech Model Mechanobiol* 2020;20:2085–96. <https://doi.org/10.1007/s10237-021-01496-8>.
- [31] Maconachie T, Leary M, Lozanovski B, Zhang X, Qian M, Faruque O, et al. SLM lattice structures: properties, performance, applications and challenges. *Mater Des* 2019;183:108137. <https://doi.org/10.1016/j.matdes.2019.108137>.
- [32] Novak N, Al-Ketan O, Borovinsk M, Krstulovic-Opara L, Rowshan R, Vesjenjak M, et al. Development of novel hybrid TPMS cellular lattices and their mechanical characterisation. *J Mater Res Technol* 2021;15:1318–29. <https://doi.org/10.1016/j.jmrt.2021.08.092>.
- [33] El Elmi A, Melancon D, Asgari M, Liu L, Pasini D. Experimental and numerical investigation of selective laser melting-induced defects in Ti-6Al-4V octet truss lattice material: the role of material microstructure and morphological variations. *J Mater Res* 2020;35:1900–12. <https://doi.org/10.1557/jmr.2020.75>.
- [34] Mahbod M, Asgari M. Elastic and plastic characterization of a new developed additively manufactured functionally graded porous lattice structure: analytical and numerical models. *Int J Mech Sci* 2019;155:248–66. <https://doi.org/10.1016/j.jimecs.2019.02.041>.
- [35] Li D, Qin R, Xu J, Zhou J, Chen B. Topology optimization of thin-walled tubes filled with lattice structures. *Int J Mech Sci* 2022;227:107457. <https://doi.org/10.1016/j.jimecs.2022.107457>.
- [36] Zaidpoor AA, Maida J. Additive manufacturing of biomaterials, tissues, and organs. *Ann Biomed Eng* 2017;45:1–11. <https://doi.org/10.1007/S10439-016-1719-Y/FIGURES/8>.
- [37] Zhang J, Chen X, Sun Y, Yang J, Chen R, Xiong Y, et al. Design of a biomimetic graded TPMS scaffold with quantitatively adjustable pore size. *Mater Des* 2022;218:110665. <https://doi.org/10.1016/j.matdes.2022.110665>.
- [38] Bandyopadhyay A, Traxel KD, Lang M, Juhasz M, Eliaz N, Bose S. Alloy design via additive manufacturing: advantages, challenges, applications and perspectives. *Mater Today* 2022;52:207–24. <https://doi.org/10.1016/j.mattod.2021.11.026>.
- [39] Harun WSW, Kamariah MSIN, Muhamad N, Ghani SAC, Ahmad F, Mohamed Z. A review of powder additive manufacturing processes for metallic biomaterials. *Powder Technol* 2018;327:128–51. <https://doi.org/10.1016/j.powtec.2017.12.058>.
- [40] Zhou H, Zhao M, Ma Z, Zhang DZ, Fu G. Sheet and network based functionally graded lattice structures manufactured by selective laser melting: design, mechanical properties, and simulation. *Int J Mech Sci* 2020;175:105480. <https://doi.org/10.1016/j.jimecs.2020.105480>.
- [41] Sun Q, Sun J, Guo K, Wang L. Compressive mechanical properties and energy absorption characteristics of SLM fabricated Ti6Al4V triply periodic minimal surface cellular structures. *Mech Mater* 2022;166:104241. <https://doi.org/10.1016/j.jmechmat.2022.104241>.
- [42] Zhao M, Zhang DZ, Liu F, Li Z, Ma Z, Ren Z. Mechanical and energy absorption characteristics of additively manufactured functionally graded sheet lattice structures with minimal surfaces. *Int J Mech Sci* 2020;167:105262. <https://doi.org/10.1016/j.jimecs.2019.105262>.
- [43] Morgan EF, Bayraktar HH, Keaveny TM. Trabecular bone modulus–density relationships depend on anatomic site. *J Biomech* 2003;36:897–904. [https://doi.org/10.1016/S0021-9290\(03\)00071-X](https://doi.org/10.1016/S0021-9290(03)00071-X).
- [44] Wang X, Xu S, Zhou S, Xu W, Leary M, Choong P, et al. Topological design and additive manufacturing of porous metals for bone scaffolds and orthopaedic implants: a review. *Biomaterials* 2016;83:127–41. <https://doi.org/10.1016/j.biomaterials.2016.01.012>.
- [45] Maskery I, Sturm L, Aremu AO, Panesar A, Williams CB, Tuck CJ, et al. Insights into the mechanical properties of several triply periodic minimal surface lattice structures made by polymer additive manufacturing. *Polymer (Guildf)* 2018;152:62–71. <https://doi.org/10.1016/j.polymer.2017.11.049>.
- [46] Schaffler MB, Burr DB. Stiffness of compact bone: effects of porosity and density. *J Biomech* 1988;21:13–6. [https://doi.org/10.1016/0021-9290\(88\)90186-8](https://doi.org/10.1016/0021-9290(88)90186-8).
- [47] Designation: E8/E8M – 13a standard test methods for tension testing of metallic materials n.d. 10.1520/E0008.E0008M-13A.
- [48] Charles A, Elkaseer A, Paggi U, Thijs L, Hagemeyer V, Scholz S. Down-facing surfaces in laser powder bed fusion of Ti6Al4V: effect of cross formation on dimensional accuracy and surface texture. *Addit Manuf* 2021;46:102148. <https://doi.org/10.1016/j.addma.2021.102148>.
- [49] ISO13314:2011. Mechanical testing of metals - ductility testing -compression test for porous and cellular metals. *Int Organ Stand* 2011;2011.
- [50] Gibson LJ. Modelling the mechanical behavior of cellular materials. *Mater Sci Eng A* 1989;110:1–36. [https://doi.org/10.1016/0921-5093\(89\)90154-8](https://doi.org/10.1016/0921-5093(89)90154-8).
- [51] Tan XP, Tan YJ, Chow CSL, Tor SB, Yeong WY. Metallic powder-bed based 3D printing of cellular scaffolds for orthopaedic implants: a state-of-the-art review on manufacturing, topological design, mechanical properties and biocompatibility. *Mater Sci Eng C* 2017;76:1328–43. <https://doi.org/10.1016/j.msec.2017.02.094>.
- [52] Tran P, Peng C. Triply periodic minimal surfaces sandwich structures subjected to shock impact. *J Sandw Struct Mater* 2021;23:2146–75. <https://doi.org/10.1177/1099636220905551>.
- [53] Al Hassanieh S, A Alhantooobi, Khan KA, Khan MA. Mechanical properties and energy absorption characteristics of additively manufactured lightweight novel Re-entrant plate-based lattice structures. *Polym* 2021;13:3882. <https://doi.org/10.3390/POLYM13223882>.
- [54] Zhang L, Song B, Choi SK, Shi Y. A topology strategy to reduce stress shielding of additively manufactured porous metallic biomaterials. *Int J Mech Sci* 2021;197:106331. <https://doi.org/10.1016/j.jimecs.2021.106331>.
- [55] Chen Z, Xie YM, Wu X, Wang Z, Li Q, Zhou S. On hybrid cellular materials based on triply periodic minimal surfaces with extreme mechanical properties. *Mater Des* 2019;183:108109. <https://doi.org/10.1016/j.matdes.2019.108109>.
- [56] Xu S, Shen J, Zhou S, Huang X, Xie YM. Design of lattice structures with controlled anisotropy. *Mater Des* 2016;93:443–7. <https://doi.org/10.1016/j.matdes.2016.01.007>.
- [57] Chatzigeorgiou C, Piotrowski B, Chemisky Y, Laheurte P, Meraghni F. Numerical investigation of the effective mechanical properties and local stress distributions of TPMS-based and strut-based lattices for biomedical applications. *J Mech Behav Biomed Mater* 2022;126:105025. <https://doi.org/10.1016/j.jmbbm.2021.105025>.
- [58] Karageorgiou V, Kaplan D. Porosity of 3D biomaterial scaffolds and osteogenesis. *Biomaterials* 2005;26:5474–91. <https://doi.org/10.1016/j.biomaterials.2005.02.002>.
- [59] Feng J, Fu J, Yao X, He Y. Triply periodic minimal surface (TPMS) porous structures: from multi-scale design, precise additive manufacturing to multidisciplinary applications. *Int J Extrem Manuf* 2022;4:022001. <https://doi.org/10.1088/2631-7990/AC5BE6>.
- [60] Kadhodapour J, Montazerian H, Darabi AC, Zargarian A, Schmauder S. The relationships between deformation mechanisms and mechanical properties of additively manufactured porous biomaterials. *J Mech Behav Biomed Mater* 2017;70:28–42. <https://doi.org/10.1016/j.jmbbm.2016.09.018>.
- [61] Zhao M, Liu F, Fu G, Zhang D, Zhang T, Zhou H. Improved mechanical properties and energy absorption of BCC lattice structures with triply periodic minimal surfaces fabricated by SLM. *Materials (Basel)* 2018;11:2411. <https://doi.org/10.3390/ma11122411>.
- [62] du Plessis A, Razavi SMJ, Benedetti M, Murchio S, Leary M, Watson M, et al. Properties and applications of additively manufactured metallic cellular materials: a review. *Prog Mater Sci* 2022;125:100918. <https://doi.org/10.1016/j.pmatsci.2021.100918>.
- [63] Alaña M, Cutolo A, Ruiz de Galarreta S, Van Hooreweder B. Influence of relative density on quasi-static and fatigue failure of lattice structures in Ti6Al4V produced by laser powder bed fusion. *Sci Rep* 2021;11:1–15. <https://doi.org/10.1038/s41598-021-98631-3>.
- [64] Park SY, Kim KS, AlMangour B, Grzesiak D, Lee KA. Effect of unit cell topology on the tensile loading responses of additive manufactured CoCrMo triply periodic minimal surface sheet lattices. *Mater Des* 2021;206:109778. <https://doi.org/10.1016/j.matdes.2021.109778>.
- [65] Al-Ketan O, Abu Al-Rub RK. Multifunctional mechanical metamaterials based on triply periodic minimal surface lattices. *Adv Eng Mater* 2019;21:1900524. <https://doi.org/10.1002/adem.201900524>.
- [66] Hassan IM, Enab TA, Fouda N, Eldeouky I. Design, fabrication, and evaluation of functionally graded triply periodic minimal surface structures fabricated by 3D printing. *J Brazilian Soc Mech Sci Eng* 2023;45:1–11. <https://doi.org/10.1007/S40430-022-03972-3/TABLES/4>.
- [67] Sharma D, Hiremath SS. Bio-inspired repeatable lattice structures for energy absorption: experimental and finite element study. *Compos Struct* 2022;283:115102. <https://doi.org/10.1016/j.compstruct.2021.115102>.
- [68] Yang L, Han C, Wu H, Hao L, Wei Q, Yan C, et al. Insights into unit cell size effect on mechanical responses and energy absorption capability of titanium graded porous structures manufactured by laser powder bed fusion. *J Mech Behav Biomed Mater* 2020;109:103843. <https://doi.org/10.1016/j.jmbbm.2020.103843>.
- [69] Habib FN, Iovenitti P, Masood SH, Nikzad M. Fabrication of polymeric lattice structures for optimum energy absorption using multi jet fusion technology. *Mater Des* 2018;155:86–98. <https://doi.org/10.1016/j.matdes.2018.05.059>.

- [70] Liu Z, Gong H, Gao J. Enhancement in the fatigue resistances of triply periodic surfaces-based scaffolds. *Int J Mech Sci* 2023;245:108119. <https://doi.org/10.1016/j.ijmecsci.2023.108119>.
- [71] Ma S, Tang Q, Han X, Feng Q, Song J, Setchi R, et al. Manufacturability, mechanical properties, mass-transport properties and biocompatibility of triply periodic minimal surface (TPMS) porous scaffolds fabricated by selective laser melting. *Mater Des* 2020;195:109034. <https://doi.org/10.1016/j.matdes.2020.109034>.
- [72] Harrysson OLA, Cansizoglu O, Marcellin-Little DJ, Cormier DR, West HA. Direct metal fabrication of titanium implants with tailored materials and mechanical properties using electron beam melting technology. *Mater Sci Eng C* 2008;28:366–73. <https://doi.org/10.1016/j.msec.2007.04.022>.
- [73] Hazlehurst K, Wang CJ, Stanford M. Evaluation of the stiffness characteristics of square pore CoCrMo cellular structures manufactured using laser melting technology for potential orthopaedic applications. *Mater Des* 2013;51:949–55. <https://doi.org/10.1016/j.matdes.2013.05.009>.
- [74] Kladovasilakis N, Charalampous P, Tsongas K, Kostavelis I, Tzetzis D, Tzovaras D. Experimental and computational investigation of lattice sandwich structures constructed by additive manufacturing technologies. *J Manuf Mater Process* 2021;5:95. <https://doi.org/10.3390/JMMP5030095>.
- [75] Mulhi A, Dehgahi S, Waghmare P, Qureshi A. Dimensional assessment of uniformly periodic porosity primitive TPMS lattices using additive manufacturing laser powder bed fusion technique. *Int J Adv Manuf Technol* 2022;1–22. <https://doi.org/10.1007/S00170-022-10578-5/FIGURES/19>.
- [76] Cantaboni F, Ginestra P, Tocci M, Colpani A, Avanzini A, Pola A, et al. Modelling and FE simulation of 3D printed Co-Cr lattice structures for biomedical applications. *Procedia CIRP* 2022;110:372–7. <https://doi.org/10.1016/j.procir.2022.06.066>.
- [77] Feng J, Liu B, Lin Z, Fu J. Isotropic octet-truss lattice structure design and anisotropy control strategies for implant application. *Mater Des* 2021;203:109595. <https://doi.org/10.1016/j.matdes.2021.109595>.
- [78] Khaleghi S, Dehnavi FN, Baghani M, Safdari M, Wang K, Baniassadi M. On the directional elastic modulus of the TPMS structures and a novel hybridization method to control anisotropy. *Mater Des* 2021;210:110074. <https://doi.org/10.1016/j.matdes.2021.110074>.
- [79] Lu Y, Zhao W, Cui Z, Zhu H, Wu C. The anisotropic elastic behavior of the widely-used triply-periodic minimal surface based scaffolds. *J Mech Behav Biomed Mater* 2019;99:56–65. <https://doi.org/10.1016/j.jmbbm.2019.07.012>.
- [80] Zhang XY, Fang G, Xing LL, Liu W, Zhou J. Effect of porosity variation strategy on the performance of functionally graded Ti-6Al-4V scaffolds for bone tissue engineering. *Mater Des* 2018;157:523–38. <https://doi.org/10.1016/j.matdes.2018.07.064>.
- [81] Zhang J, Shen Y, Sun Y, Yang J, Gong Y, Wang K, et al. Design and mechanical testing of porous lattice structure with independent adjustment of pore size and porosity for bone implant. *J Mater Res Technol* 2022;18:3240–55. <https://doi.org/10.1016/j.jmrt.2022.04.002>.
- [82] Rahmoun J, Auperrin A, Delille R, Naceur H, Drazetic P. Characterization and micromechanical modeling of the human cranial bone elastic properties. *Mech Res Commun* 2014;60:7–14. <https://doi.org/10.1016/j.mechrescom.2014.04.001>.
- [83] Shimko DA, Shimko VF, Sander EA, Dickson KF, Nauman EA. Effect of porosity on the fluid flow characteristics and mechanical properties of tantalum scaffolds. *J Biomed Mater Res Part B Appl Biomater* 2005;73B:315–24. <https://doi.org/10.1002/JBM.B.30229>.
- [84] Gu XN, Zheng YF. A review on magnesium alloys as biodegradable materials. *Front Mater Sci China* 2010;4:111–5. <https://doi.org/10.1007/S11706-010-0024-1>.
- [85] Kuhn JL, Goldstein SA, Choi R, London M, Feldkamp LA, Matthews LS. Comparison of the trabecular and cortical tissue moduli from human iliac crests. *J Orthop Res* 1989;7:876–84. <https://doi.org/10.1002/JOR.1100070614>.





#### **Paper IV**

Rezapourian, M., & Hussainova, I. (2023). Optimal mechanical properties of Hydroxyapatite gradient Voronoi porous scaffolds for bone applications — A numerical study. *Journal of the Mechanical Behavior of Biomedical Materials*, 148, 106232.





## Research paper

## Optimal mechanical properties of Hydroxyapatite gradient Voronoi porous scaffolds for bone applications — A numerical study

Mansoureh Rezapourian<sup>\*</sup>, Irina Hussainova

Department of Mechanical and Industrial Engineering, Tallinn University of Technology, Tallinn, Estonia

## ARTICLE INFO

## Keywords:

Finite element analysis  
 Voronoi-Tessellation  
 Hydroxyapatite  
 Maximum stress criteria  
 Bone substitutions  
 Irregular porous scaffold

## ABSTRACT

Irregular Voronoi-based lattice (IVL) structures in tissue engineering (TE) have significant potential for bone regeneration. These scaffolds can mimic natural human bone interconnectivity by gradually altering strut thickness (ST) and seed point space (PS), which affects both mechanical and biological characteristics. This paper investigates the impact of design parameters, ST and PS, on Hydroxyapatite (HA) ILV structures' mechanical properties (elastic modulus (E) and maximum compressive strength (MCS)) and geometrical characteristics (pore number, size, and distribution, surface area (SA), and surface area-to-volume ratio (SA/VR)). Four types of IVL scaffolds were designed; PC-TC (Constant PS-Constant ST), PC-TG (Constant PS-Gradient ST), PG-TC (Gradient PS-Constant ST), and PG-TG (Gradient PS-Gradient ST). The study, conducted through linear static structural finite element analysis (FEA) with maximum stress criteria, underscores the profound impact of irregularity and morphology on mechanical performance and geometrical features. Regarding SA and SA/VR, a comparison between PC-TC with other proposed scaffolds showed a minor improvement for PC-TG, while higher significant improvements were found for both PG-TG and PG-TC. In terms of pores distribution and number, no noticeable improvement was observed for the PC-TG scaffold compared to PC-TC. In contrast, PG-TC and PG-TG lattices demonstrated a variety of pore distributions and approximately doubled pore numbers. Studying mechanical properties, considering E and MCS, showcases substantial gains for PG-TC. It, however, revealed that for the rest of the scaffolds, no enhancement was observed regarding E. Based on these results, gradient PS proved to be more effective than gradient ST in enhancing mechanical performance and geometrical properties. Due to these improvements, this study holds promise for expediting bone regeneration and reducing postoperative complications in bone replacement applications.

## 1. Introduction

In bone tissue engineering (BTE), optimal restoration is ensured by efficient and rapid bone replacements using advanced alternatives such as scaffolds and implants instead of traditional methods (Alonzo et al., 2021). Bone integrity can be compromised by traumatic injuries, congenital defects, and degenerative diseases (Awad et al., 2014). By designing and fabricating three-dimensional scaffolds and/or implants, that closely mimic the interconnectivity and complexity of natural human bone, this challenge can be easily addressed (Amini et al., 2012). Tissue engineers harness these structures and the regenerative abilities of the body to develop bio-compatible alternatives that integrate easily with the host bone, and enhance life quality (Awad et al., 2014).

Recent advancements in BTE have witnessed remarkable progress in scaffold development, advancing the field of regenerative medicine. Researchers have been focusing on creating scaffolds that mimic the intricate architecture of natural bone, leading to more effective bone

regeneration (Vance et al., 2019; Robinson et al., 2021). Innovations in the field have included the use of advanced materials such as biodegradable polymers, hydrogels, and bioactive ceramics, which not only provide mechanical support but also facilitate cell adhesion and growth (Arjunan et al., 2020, 2021).

Cellular lattice structures mainly consist of regular and irregular morphologies. Arrays of the same units make up regular lattice structures, while random morphologies generate irregular ones (Okubo et al., 2023). Irregular lattice structures, as opposed to regular lattices, offer several distinct advantages and benefits in the context of bone implants. These advantages are gaining attention in orthopedics and bioengineering because of the enhanced biomimicry, improved stress distribution, high degree of customization, fracture resistance, controlled porosity, reduced material usage, and enhanced biological integration (Chen et al., 2021). However, not all cases can be handled by a regular structure as the human bone trabecular part

<sup>\*</sup> Corresponding author.

E-mail address: [mareza@taltech.ee](mailto:mareza@taltech.ee) (M. Rezapourian).

indicates non-uniformity in the diameter of the internal pores and struts (Syahrom et al., 2013) indicating irregularity as a characteristic of natural bone (Nie et al., 2017). Humans are also able to perform a variety of functions in all directions because of a specific anisotropy in bone structure (Chen et al., 2021). In other words, bionics depends on the bone's irregularity. In the case of neo-formed bone quantities, irregular scaffolds have also outperformed regular ones (Rodríguez-Montañó et al., 2019). In computed tomography (CT) images, the morphology of natural bone appears as a Voronoi tessellation inspiring the development of new methods for producing irregular scaffolds (Fantini and Curto, 2018). Among different types of lattice structures, irregular Voronoi tessellation pattern offers fascinating possibilities for bone substitution (Wang et al., 2018; Chao et al., 2023). A Voronoi tessellation structure mimics human bone's intricate patterns (Wu et al., 2023) by dividing a given space into cells defined by their proximity to a seed point (Gómez et al., 2016). The irregularity of these types of scaffolds enables us to adjust Voronoi cell size, shape, distribution, and randomness of seed points. Therefore, by tailoring design parameters, the required mechanical properties and desired geometrical features such as porosity, SA, and pore size can be easily met (Wang et al., 2018; Du et al., 2020). Through these specific customizations, cellular adhesion, proliferation, and differentiation can be promoted (Chao et al., 2023). This facilitates and increases nutrient diffusion and uptake within the lattice structure. Therefore, VTL structures can be effectively used in different kinds of medical applications since they show biomimetic and functional properties (Frayssinet et al., 2022; Bhate et al., 2019).

Among biomaterials, bio-ceramics stand out among all due to their biocompatibility (Ruiz Henao et al., 2021; Przybilla et al., 2023), excellent mechanical properties (Zhang et al., 2022; Charbonnier et al., 2020), and versatility (Kumar and Mohanty, 2022). HA as a ceramic is widely known as one of the most advantageous available choices among bio-ceramics due to the akin to the mineral components of human bone facilitating integration with surrounding tissue (Bellucci et al., 2015; Zhang et al., 2022; Zhao et al., 2023). Additionally, HA exhibits excellent biocompatibility and bioactivity for enhancing cell adhesion, proliferation, and osteointegration (Zhao et al., 2023; Jiao et al., 2022). Moreover, the gradual resorption of HA can occur concurrently with new bone growth transferring mechanical loads slowly from the implant to the regenerating tissue (Zhao et al., 2023; Dai et al., 2019; Ghiasi et al., 2020) with no loss of mechanical support, minimizing stress shielding and providing mechanical harmony with the host bone (Bellucci et al., 2015).

Graded-porosity (functionally graded) lattice structures have gained significant attention in orthopedic applications compared to their uniform porous counterparts due to their improved stress distribution between host bone and implant that results in stress transition seamlessly, minimizing stress shielding (Rana et al., 2023), improving load distribution, and reducing failure risks (Pagani et al., 2021). The tailoring of the design parameters in graded scaffolds such as pore size, strut thickness, and material composition can lead to mechanical and biological enhancements (Viet et al., 2023; Pompe et al., 2003) and boost cell growth (Zhao et al., 2022). These customizations give them specific applications in bone replacement. Additionally, the transition zone between chondral and osseous phases at the bone-cartilage interface can also be treated with functionally graded ceramics (Lowen and Leach, 2020). Functionally graded Voronoi tessellation (FGVT) lattice structures herald a new era in BTE (Abdullahi and Gao, 2020; Cheikho et al., 2022; Leong et al., 2008).

In addition to those mentioned previously, there are many factors to keep in mind when designing a mimicking scaffold, all of which have a direct impact on the others. In this regard, modeling an optimized lattice scaffold is challenging (Shirzad et al., 2021). This study employed a numerical method to investigate the influence of the constant/gradient mode of the design parameters, especially the variation in ST and PS, within IVL scaffolds on the mechanical properties and geometrical

features of HA-based lattices. Specifically, we aim to understand how changes in ST and PS influence SA, SA/VR, pore size, number, and distribution in the scaffolds. Additionally, we aim to determine how these variations affect the mechanical properties, including E and MCS using maximum stress criteria, and assess how these changes can enhance their potential for bone tissue regeneration.

## 2. Research gaps

In recent years, several studies have been conducted that implemented the Voronoi-tessellation method to generate porous scaffolds meant for BTE. Most of these researches normally focused on experimentally analyzing metallic and/or ceramic Voronoi-based porous structures and the effect of irregularity and graded porosity on the mechanical response. Wang et al. (2018) proposed a top-down design method to generate functionally graded porosity lattice scaffold based on Voronoi-tessellation investigating how graded porosity can affect mechanical properties. Fabricated lattice scaffold by Ti6Al4V was tested experimentally by a quasi-static compression test and the results showed that the mechanical properties were influenced by both irregularity and porosity. Du et al. (2020) conducted an experimental compression test for a metallic irregular Voronoi-tessellation porous scaffold, which achieved the desired porosity and pore size range and met the elastic modulus and compression strength in the range of human bone to achieve implant requirements. Jiao et al. (2022) fabricated 15 groups of Voronoi-based lattice scaffolds using HA and zirconia by digital light processing (DLP). Experimentally tested manufactured scaffolds under compression test, showed comparable mechanical properties with human bone and proved the direct effect of irregularity on the mechanical response and conducted numerical simulation showed good agreements with experiments. Frayssinet et al. (2022) conducted a study on the assessment of the biomimetic capabilities of Voronoi-based scaffolds in comparison with human bone in the case of histomorphometric and elastic modulus. Mimetic microstructures were found to have histomorphometric features and elastic properties comparable to natural human bone, demonstrating the capability of Voronoi-based microstructures in bone application. Liu et al. (2021) developed a 3D-printed beta-tricalcium phosphate Voronoi-based biomimetic scaffold with different pore sizes and porosities by DLP. Experimental tests and finite element simulations were carried out to assess how geometrical parameters affect compressive strength, equivalent stress distribution, and deformation response of 3D Voronoi porous materials.

Few studies have employed failure criteria numerically to calculate optimal mechanical properties and geometrical features of ceramic-based Voronoi lattice scaffolds. To address this research gap, this study presents a numerical method using maximum failure criteria to investigate how transitioning from constant to gradient of the design parameters like ST and PS can improve geometrical features (SA, SA/VR, pores size, number and distribution) as well as mechanical properties (E and MCS) of HA IVL scaffolds.

## 3. Materials and methods

### 3.1. Voronoi-based porous structure design

Voronoi-based lattice morphology can have random seed point distributions resulting in regular or irregular pores distributions (Nikolić et al., 2018; Wang et al., 2018). The first step in creating Voronoi-based porous structures is generating initial seed points randomly distributed within the specified volume. Each initial point corresponds to one polyhedron generated in the volume. Afterward, the distance between each polyhedron's centroid point and the initial point is determined. Tessellation occurs when the distance between two points is less than a threshold. Otherwise, the centroid points will be considered new seed points, and tessellation will proceed until the distance value is less than the threshold. Afterward, beams can be generated along the edges

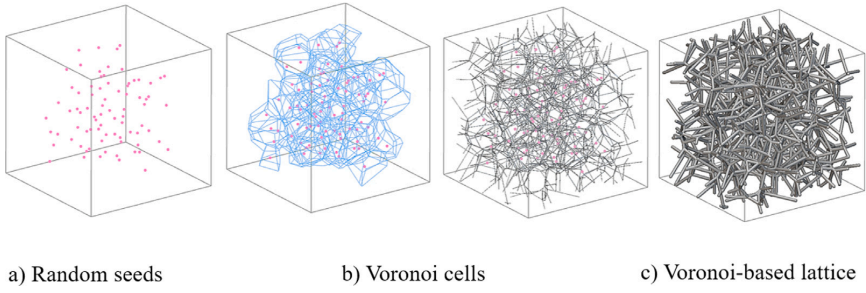


Fig. 1. Graphical representation of Voronoi lattice structure including random points, polyhedrons, and final IVL scaffold.

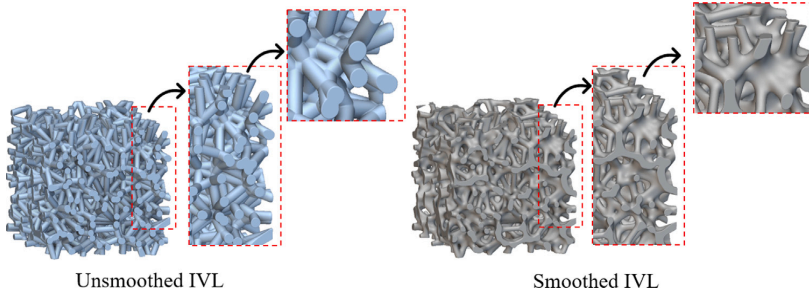


Fig. 2. Unsmoothed and smoothed irregular Voronoi scaffold.

of the polyhedrons resulting in a scaffold that mimics bone (Deering et al., 2021). When designing VTL structures, the number of points (PN), PS, and ST are the most influential parameters leading to design lattices with different percentages of porosity and pore sizes, and interconnections between pores resulting in different structural lattice geometries. The Voronoi tessellation can be described by the following equations; An  $m$ -dimensional Euclidean space has a set of points as below (Chow et al., 2007; Wang et al., 2018):

$$P = p_1, \dots, p_n \subset R^m, 2 \leq n \leq \infty, p_i \neq p_j, i, j \subset I_n = \{1, \dots, n\} \quad (1)$$

Space can be divided into two parts by the line between  $p_i$  and  $p_j$ , where  $H_i(p_i, p_j)$  is the part that includes  $p_i$ , then:

$$V(p_i) = \{x \mid \|x - p_i\| \leq \|x - p_j\|\} = \bigcap_{j \in I_n \setminus \{i\}} H(p_i, p_j) \quad (2)$$

$p_i$  represents the seed points in the  $R_m$  space in  $m$  dimensions and Voronoi diagram will be determined by  $Y(p) = \{V(p_1), \dots, V(p_n)\}$ . Depending on the number and distribution of seeds, Voronoi diagrams are formed.

The present study includes irregular pore distributions for all Voronoi-based lattices. Fig. 1 shows a sample of random points, Voronoi polyhedrons within the volume, and the final IVL scaffold.

In This study, IVL structures in uniform and graded PS and ST were designed using nTopology software (Version 4.7.3). Four types of IVL scaffolds were generated with tailorable pore size by adjusting the input parameters (PS and ST) in the design stage while keeping the number of seed points constant at 100. The design volume was considered a cube with a length of 10 mm and a porosity of 73%. Additionally, in IVL structures, the strut connections show sharp edges that can affect mesh quality in FEA leading to errors in the final mechanical properties results and causing stress concentrations. Therefore, all connection sites were smoothed with a 0.1 mm grid size, using “Smoothen body block” in nTopology software to eliminate all sharp edges. Greater local curvature leads to more osteoblast differentiation (Rumpler et al., 2008). Fig. 2 shows an IVL before and after the smoothing body.

Table 1

Design parameters and geometrical features of IVL structures; Constant(C), Gradient(G).					
Lattices	PS-ST	PS (mm)	ST (mm)	SA (mm <sup>2</sup> )	SA/VR (1/mm)
PC-TC	C-C	2.50	0.70	1187.90	4.45
PC-TG	C-G	2.50	0.46–1.41	1204.87	4.62
PG-TC	G-C	2.50–0.80	0.50	1618.86	6.07
PG-TG	G-G	2.50–0.70	0.45–0.60	1645.13	6.23

SA and SA/VR were also calculated with the related blocks in nTopology software. The design parameters of four types of smoothed IVL scaffolds are outlined below in Table 1.

Furthermore, Fig. 3 also depicts lattices and corresponding porous scaffolds of different regularities. Moreover, note that the distribution gradient of PS and ST is just regulated from the  $X$ -axis.

### 3.2. Maximum principal stress criteria

Maximum principal stress theory is considered an acceptable index of failure for brittle materials, including ceramics (Darwich et al., 2023; Gulec et al., 2017). Therefore, in this research, the maximum principal stress theory was applied to determine material failure. Each stress component is evaluated against the respective ultimate strength allowable of the material. For three-dimensional problems, the maximum stress criteria are as follows (Knight and Reeder, 2006):

$$\begin{aligned} e_1^t &= \sigma_{11}/X_T \text{ for } \sigma_{11} \geq 0; e_1^c = |\sigma_{11}|/X_C \text{ for } \sigma_{11} \leq 0 \\ e_2^t &= \sigma_{22}/Y_T \text{ for } \sigma_{22} \geq 0; e_2^c = |\sigma_{22}|/Y_C \text{ for } \sigma_{22} \leq 0 \\ e_3^t &= \sigma_{33}/Z_T \text{ for } \sigma_{33} \geq 0; e_3^c = |\sigma_{33}|/Z_C \text{ for } \sigma_{33} \leq 0 \\ e_4 &= \tau_{12}/S_{12}; e_5 = \tau_{23}/S_{23}; e_6 = \tau_{13}/S_{13} \end{aligned} \quad (3)$$

Where  $\sigma_{11}$ ,  $\sigma_{22}$ , and  $\sigma_{33}$  is the stress component in X, Y, and Z directions for each lattice structure,  $X_{T/C}$ ,  $Y_{T/C}$ , and  $Z_{T/C}$  are the compressive(C)/tension(T) material normal strengths (or allowable stresses) of the material in three directions,  $\tau$  and  $S$  are the shear stress component

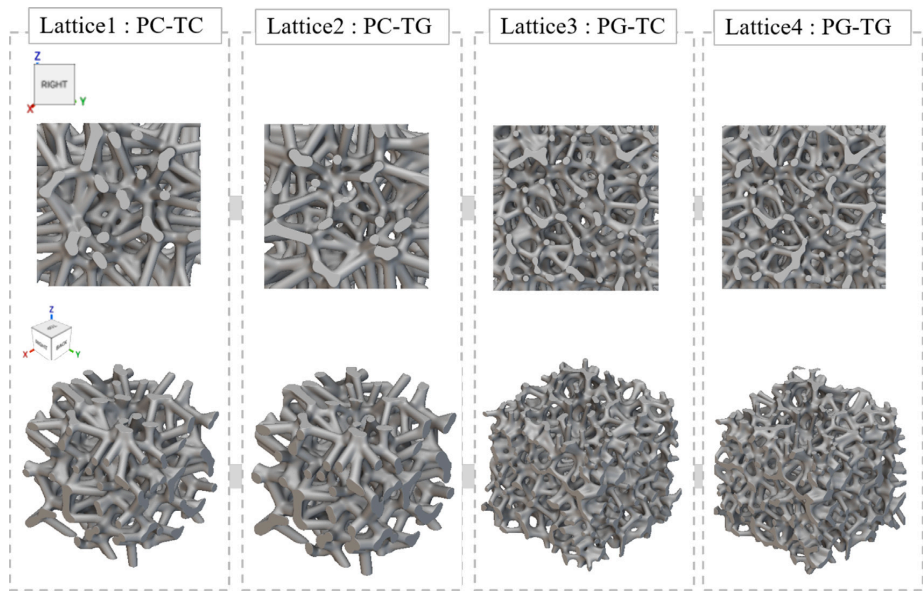


Fig. 3. Four types of smoothed IVL scaffold designed by varying ST and PS in a constant/gradient manner.

Table 2  
Representation of the elements and nodes in the converged structural FE model.

Design	Scaffolds			
	PC-TC	PC-TG	PG-TC	PG-TG
Elements	555 108	553 442	578 607	555 615
Nodes	842 703	850 453	929 544	888 860

of the lattice in X, Y, and Z directions, and material shear strength (or allowable) respectively.  $e_i^{f/c}$ , is the ratio of stress components of the material to the allowable value. Degradation occurs if the ratio exceeds the unity, which initiates failure in the material. At different load levels, different components may fail independently. In the current study, to implement failure criteria a UMAT code was incorporated into ABAQUS to compile the analysis.

3.3. Finite element simulation of IVL scaffolds

To study the effect of the uniform and gradient PS and ST on the mechanical properties of IVL structures, linear static structural analysis was employed, and maximum stress criteria were applied. Two important parameters including E and MCS ( $\sigma_c$ ) were calculated. ABAQUS (6.19) software incorporated with a UMAT code was used to assess the compressive behavior of the designed scaffolds. Two rigid plates were placed on the top and the bottom of all scaffolds. To define boundary conditions (BC), a 1 KN axial load was applied on the top plate in the Z direction and all degrees of freedom except the displacement normal to load were fixed, while the bottom plate's BC was fully constrained in all directions. In addition, the type of contact between the rigid plates and all scaffolds was designed to be frictional with a friction coefficient of 0.1 to avoid any rotation. Quadratic tetrahedral elements were assigned for all lattice structures.

Mesh sensitivity analysis was conducted and three different mesh sizes of 0.25 (M25), 0.20 (M20), and 0.15 (M15) mm were selected for mesh refinements based on the convergence of E. The details about the elements and nodes in the converged structural FE Model are listed in Table 2. FE analysis in this study was performed using an AMD Ryzen 9 3900X- 12 Core Processor 3.79 GHz with 64 GB RAM.

Table 3  
Mesh sensitivity analysis results.

Mesh size (mm)	E (MPa)	Discrepancy (%)	Solution time (hr:min)
0.25	198.45	0.00	01:27
0.20	212.25	6.90	02:38
0.15	211.01	0.59	05:07

FE simulation in this study was performed considering the 35% vol% HA (35% HA, 13.98% Resin, 35.75% HDDA, and 15.27% Dispersant) with mechanical properties of a 4 GPa elastic modulus, an 8 MPa breaking strength, and a 0.27 Poisson's ratio. More detail about the preparation material was provided in Kang et al. (2022).

4. Results and discussions

4.1. Verification of FEA and mesh sensitivity analysis

FE analysis was carried out on the different IVL scaffolds to find out the relationship between scaffolds' irregularity and mechanical properties. To verify the FE results, CS scaffold was selected from research (Kang et al., 2022) and a compression test was performed numerically. With maximum errors of 1.4% and 2.1%, elastic modulus and compressive strength were found to be in good agreement.

The mesh sensitivity results are presented in Table 3. Upon comparing the convergence of the E, a significant discrepancy was observed between the E values for mesh sizes M25 and M20, with an error of 6.9%, while M15 exhibited a much lower error of only 0.59%. These findings indicate that coarser meshes result in less accurate E values, whereas finer meshes lead to convergence. Therefore, mesh sizes of 0.15 and 0.20 mm are recommended for the final scaffold design. Although the solution time for M20 is shorter than that of M15, with a reduction of approximately 50%, when dealing with IVL structures featuring gradient ST, opting for the smaller element size ensures better element alignment with curves and surfaces, making an element size of 0.15 mm the preferable choice for all porous scaffolds in this study.



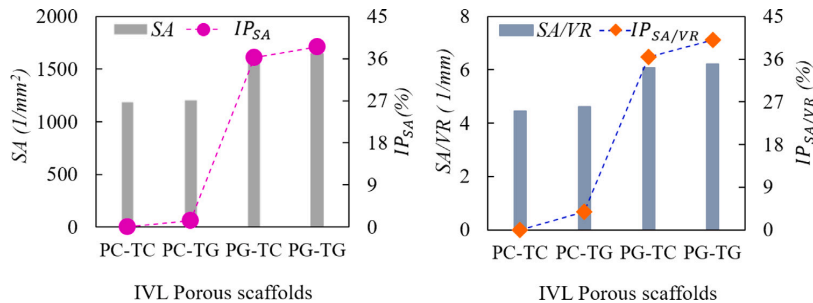


Fig. 4. An illustration of the SA and SA/VR of four designed IVL scaffolds and their improvements over PC-TC lattices.

Table 4  
SA and SA/VR of the designed IVL scaffolds and the percentage improvements of SA and SA/VR in comparison with PC-TC lattice.

Lattices	SA (mm <sup>2</sup> )	SA/VR (1/mm)	IP <sub>SA</sub> (%)	IP <sub>SA/VR</sub> (%)
PC-TC	1187.90	4.45	0.00	0.00
PC-TG	1204.87	4.62	1.43	3.82
PG-TC	1618.86	6.07	36.28	36.40
PG-TG	1645.13	6.23	38.49	40.00

4.2. Irregularity effect on the SA and SA/VR

SA and SA/VR are two of the most interesting geometrical features especially for bone replacement applications which affect both scaffold’s biological and mechanical performance (Yoo, 2014). Growth factors, nutrient exchange, and the interactions between surrounding cells are directly influenced by these two factors (Nguyen et al., 2019). Due to SA/VR’s effect on fluid permeability, a higher SA/VR indicates greater growth and more optimal adherence of cells (Vijayavenkataraman et al., 2018). A scaffold with a higher SA/VR led to a higher collision of O<sub>2</sub> molecules with cells, leading to an increased O<sub>2</sub> transformation and consumption in the scaffold which results in a higher flow rate to improve O<sub>2</sub> delivery to the cells (Vijayavenkataraman et al., 2018). It was found that gradient mode directly influences SA and SA/VR of IVL scaffolds. Table 4 shows SA and SA/VR values and their improvement percentages (IP<sub>SA</sub> and IP<sub>SA/VR</sub>) in comparison to the PC-TC scaffold.

In lattices with constant PS, changing ST to the gradient mode can increase SA and SA/VR by about 1.43% and 3.82% respectively, which is not much. By switching PS from constant to the gradient mode, the scaffold with constant ST shows improvements of 36.28% and 36.40% respectively, and when it comes to gradient thickness, improvements increase by 38.49% and 40.00%. As the results indicate in Fig. 4, the highest increase in SA and SA/VR can be seen in the scaffold with both gradient PS and ST while the lowest one is related to the scaffold with constant PS and ST, followed by the lattice with constant PS and gradient ST. It is found that generally higher SA and SA/VR lead to a higher percentage of cell attachment (Murphy and O’Brien, 2010).

These two factors significantly impact the success and effectiveness of BTE for a variety of reasons as follows: providing larger SA leading to promoting cell attachment and proliferation, facilitating nutrient exchange due to the diffusion of nutrients and oxygen, enhancing interaction between the newly formed bone and the adjacent native bone, development of vascular network due to more development of blood vessels (Henkel et al., 2013), and expediting regeneration speed by providing more space and controlling and customizing SA/VR leading to improve effectiveness in bone tissue regeneration (Melchels et al., 2010).

4.3. Irregularity effect on pore size, pore numbers, and pores distribution

A study into porous implants demonstrated that the largest pore size (350um) facilitated higher cell proliferation in vitro post-seeding (Murphy and O’Brien, 2010). Another research, also reported that the preferred pore size selection for trabecular bone based on irregular Voronoi lattice structure is in the range of 458.80–989.10 um (Li et al., 2022). According to recent studies, the desired pore size for simulating cell proliferation and differentiation should be in the range of 20–1200 μm (Liang et al., 2022; Biemond et al., 2011; Baksh et al., 1998). As a result, the pore size distributions must belong to a variety of ranges (Zhao et al., 2018). As shown in Fig. 5, the scaffolds in this study showed a good assortment of sizes that make them suitable for bone replacement.

Fig. 5 displays the color bar of the lower and upper bounds of the pore size. Fig. 6 also depicts the point maps of each pore inside each IVL structure, the indicator spheres that display the pores, their diameter with the center of the points, and the number of pores. Each colored point on the map in Fig. 6 represents a pore whose diameter can be read from the colored bar in Fig. 5. As can be seen in Figs. 5 and 6, applying the gradient option in the design of IVL structures leads to an increase in the number of pores that increases the pores with the desired size which are in the range of human bone. The highest pore number of 847 is observed in the PG-TG scaffold with gradient PS and ST followed by the PG-TC scaffold with 780 pores, and the lowest one is reported in the PC-TG scaffold with 320 pores followed by the PC-TC lattice with 322 pores.

It was found that applying a gradient to both PS and ST can increase the number of pores with desirable size. This results in an increase in SA and SA/VR, both of which are essential factors in bone growth and cell adhesion.

4.4. The effect of gradient on numerically estimated mechanical properties

von Mises stress distribution and displacement for each Voronoi scaffold are shown in Fig. 7 and 8. For all Voronoi scaffolds, von Mises stress distribution was observed in the connection sites and there is no sign of stress concentration in any area. As it is visible, most area of PC-TC and PC-TG scaffolds undergoes stress but in the case of PG-TC and PG-TG, the intensity of the stress distribution is less than others and more stable. Results confirmed the importance of geometry on the load distribution on the Voronoi porous scaffolds. The risk of failure is higher in the PC-TC and PC-TG scaffolds due to large stress distribution in connection sites. Among all Voronoi porous scaffolds, PC-TC exhibited the lowest displacement in the load direction while the maximum value was observed for PC-TG followed by PG-TC and PG-TG.

Mechanical properties of the designed porous scaffold such as elastic modulus and maximum compressive strength are summarized in Table 5 and Fig. 9 shows the stress–strain curves of the lattice structures.



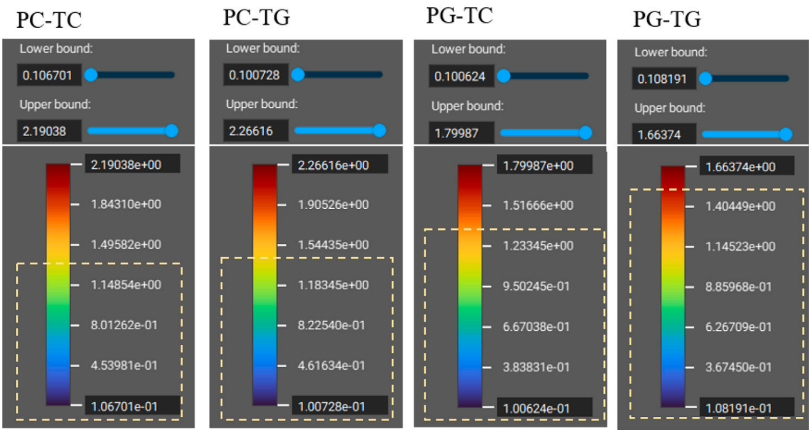


Fig. 5. Pore size of the four types of designed IVL structure with the lower and upper band; Dimensions in (mm).

	Point maps	Indicator spheres	Indicator spheres inside scaffolds	Number of pores
PC-TC				322
PC-TG				320
PG-TC				780
PG-TG				847

Fig. 6. Point maps, indicator spheres, indicator spheres inside the scaffolds, and the number of pores.

These results confirmed that in compression with TC-PC lattice, keeping constant the PS and applying a gradient on the ST has a diminishing effect of  $-11.04\%$  on the elastic modulus but an improvement of  $135\%$  can be seen in maximum compressive strength.

In the field of BTE, E and MCS are critical mechanical properties. All factors of mechanical mimicry, preventing stress shielding, cell differentiation, and implant stability depend on the elastic modulus of designed scaffolds (Li et al., 2019; Jiang et al., 2015; Fu et al., 2013).

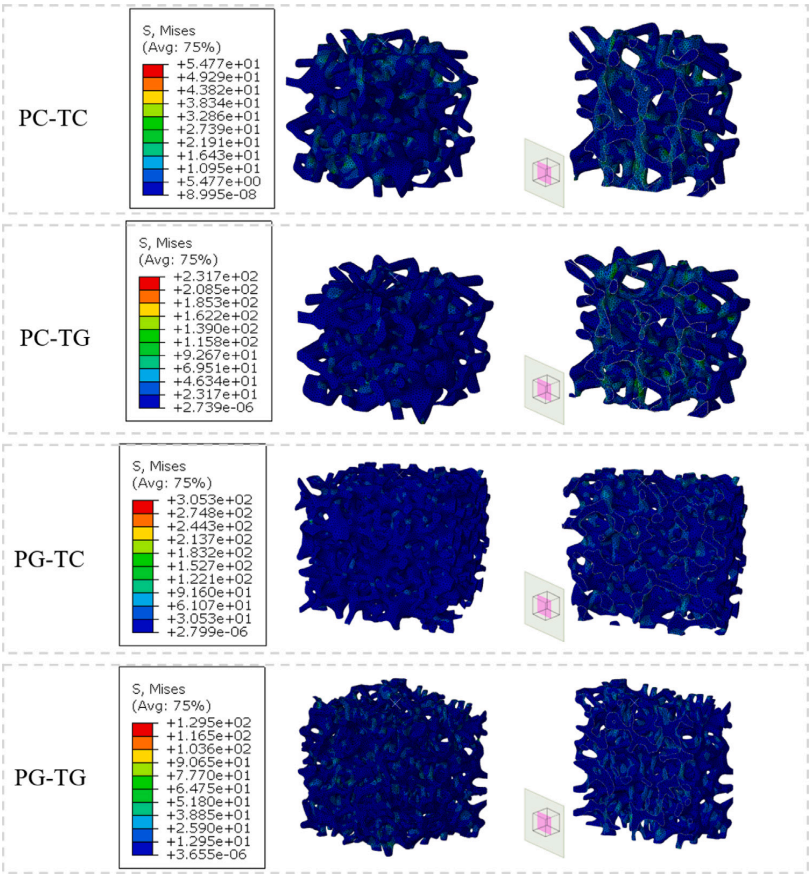


Fig. 7. Von Mises stress distribution of IVL scaffolds under compression load..

**Table 5**  
Elastic modulus and maximum compressive strength of the Voronoi-based scaffolds.

Lattices	$E$ (MPa)	$\sigma_c$ (MPa)	$IP_E$ (%)	$IP_{\sigma_c}$ (%)
PC-TC	238.58	0.60	0.00	0.00
PC-TG	212.24	1.41	-11.04	135.00
PG-TC	271.23	1.61	13.68	168.33
PG-TG	241.02	1.07	1.02	78.33

Elastic modulus represents the ability of the scaffold to resist deformation when subjected to an applied load to ensure structural support and maintain the appropriate load-bearing characteristics. A well-matched elastic modulus helps distribute loads more evenly between the implant and the surrounding bone reduces the risk of stress shielding and promotes healthy bone remodeling (Li et al., 2019). An appropriate elastic modulus can influence cell behavior, including differentiation into osteoblasts (bone-forming cells). Mesenchymal stem cells are also sensitive to mechanical cues. Therefore, it is essential to have an appropriate elastic modulus that encourages the desired cell responses and bone formation (Li et al., 2019; Jiang et al., 2015). For load-bearing applications, such as hip or knee replacements, an implant's elastic modulus is crucial for its long-term stability. A mismatch in elastic modulus between the implant and the surrounding bone can lead to implant loosening and failure (Li et al., 2019). Load-bearing capacity, scaffold durability, and reduction of post-operative complications are other factors that can be achieved by ensuring maximum compressive

strength to prevent implant failure, loosening, or bone loss (Fu et al., 2013; Zhang et al., 2018).

Applying gradient on the PS causes improvement in both elastic modulus and compressive strength about 13.68% and 168.33% respectively. Gradient mode also improves mechanical properties when both PS and ST are graded. The highest improvements were reported for the PG-TC scaffold with 13.68% and 168.33% in elastic modulus and compressive strength. Fig. 9 shows the stress-strain curves of four Voronoi porous scaffolds in this study. In the literature, the elastic modulus of cancellous bone was reported in the range of 0.4 to 4.5 GPa, and the yield strength of the spine, tibia, and proximal femur was reported in the range of 0.56 to 55.3MPa (Kang et al., 2022). In this research, all the scaffolds showed mechanical properties in the range of human bone and among them PG-TC scaffold shows the best performance in terms of strength and stiffness.

4.5. Clinical implications

The findings of our study bear significant clinical implications for the field of bone substitution therapies. The optimization of IVL structure through the manipulation of design parameters, such as PS and ST, provides an opportunity to enhance the mechanical properties of bone implants. By maximizing the elastic modulus and maximum compressive strength while adhering to the maximum stress criteria, our research supports the development of scaffolds that can better withstand

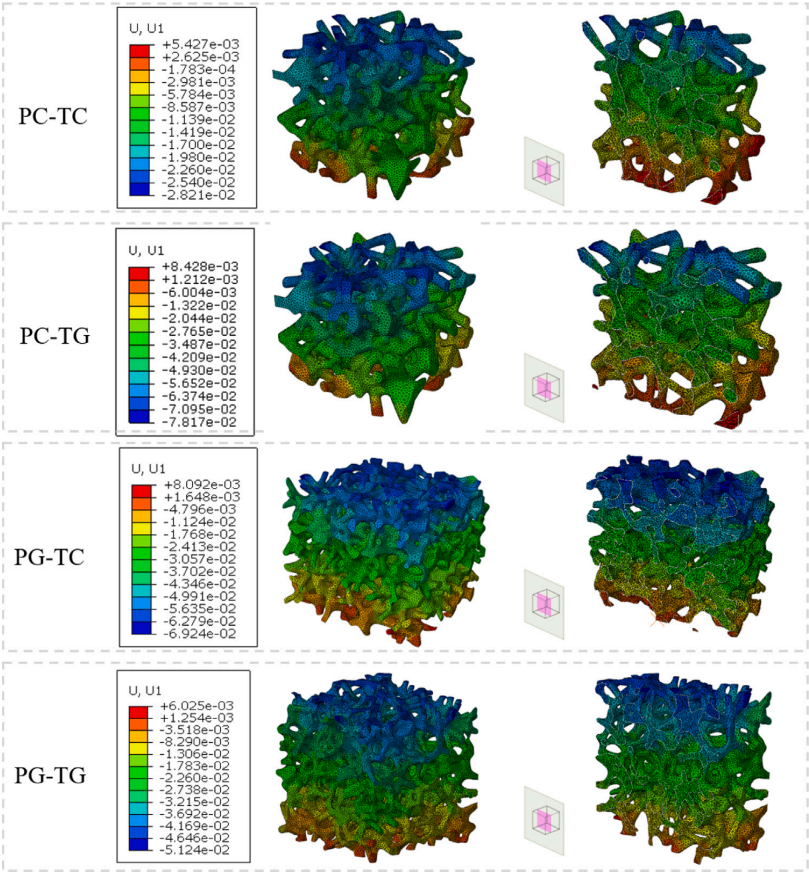


Fig. 8. Displacement of IVL structures under compression load.

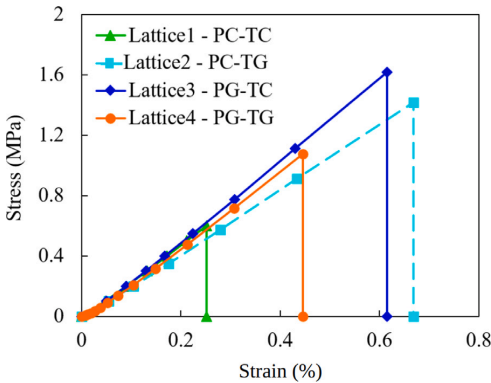


Fig. 9. Stress-Strain curve of all Voronoi-based lattice structures.

compressive loading. These improvements can translate into reduced risk of implant/scaffold failure and fracture, decreased post-operative complications or the need for early implant removal, a longer lifespan for the implant/scaffold due to the stability of implant/scaffold, and ultimately, improved patient outcomes (Prasadh and Wong, 2018).

Furthermore, our optimized lattice design, which simultaneously maximizes SA and SA/VR, pore size, and pores distribution, offers the potential for enhanced tissue integration and osseointegration. This aspect is of paramount importance in bone substitution therapies, as it promotes faster healing and the establishment of a strong and durable connection between the implant/scaffold and the surrounding bone tissue (Wang and Yeung, 2017). Consequently, our findings provide a basis for the design of more effective bone implants that can contribute to the successful and sustainable restoration of bone function in clinical practice.

#### 4.6. Limitations

The success of bioengineered scaffolds for bone regeneration purposes is strongly dependent on proper scaffold design to promote mechanical and biological performance. Several studies have investigated lattice structures to achieve predefined mechanical properties. Those studies were often aimed at maximizing scaffold stiffness and strength while imposing a suitable porosity for mimicking bone properties. Most of the studies primarily employed periodic designs that were repeated in three directions to generate scaffolds (Rezapourian et al., 2023, 2022, 2021). However, human bone has no homogeneous structure. It is necessary to optimize/improve mechanical properties by analyzing irregular lattice structures such as Voronoi tessellation lattice scaffolds, particularly investigating how designed parameters such as

PS, ST, and PN affect mechanical properties using maximum stress failure criteria. Despite this, this study has several limitations.

Recent advances in bone biomechanics have led to the development of FE modeling as an effective tool. However, it is not without limitations. The validation test of the scaffolds was performed by FEA using a redesigned scaffold and referenced material properties (Kang et al., 2022). Detecting mechanical properties revealed a discrepancy between validation results and reference analysis with maximum errors of 1.42% and 2.12%, for elastic modulus and compressive strength respectively. The results of FEA in this study may be affected by this error.

Due to the limitations of the analysis method, we did not directly observe or predict the specific failure modes in the lattice structures. The analysis primarily focused on assessing the elastic response and maximum compressive stress. To gain insights into the failure modes and fracture behavior of these lattice structures, a more comprehensive analysis, such as dynamic or fracture mechanics analysis, would be required.

We also need to determine the manufacturability of the scaffolds with HA or other ceramic materials and check how well the manufactured scaffolds are matched to the designed lattice structures. The complexity of the optimized/improved scaffold architectures requires specific AM/3D printing techniques to increase the accuracy of fabricated lattices. Each 3D printing technique has limitations depending on which material is used. This work is also limited by the lack of experimental compression tests to fully investigate the mechanical and damage behavior of different morphologies and biological tests to investigate the effect of geometrical features on cell growth. Therefore, in this study, the AM of the proposed lattice scaffolds with bioceramic material was one of the limitations.

Finally, scaffolds can be limited in their application. The implants cannot be used in all areas of the body, as their mechanical properties limit their use to the spine, tibia, and proximal femur.

## 5. Conclusions

In this study, we conducted a comprehensive investigation into the effects of varying design parameters including ST and PS, on HA-based IVL scaffolds for BTE based on static structural FEA and maximum stress criteria. The main findings of the current study provide valuable insights into the potential for enhancing the scaffolds' mechanical properties and geometrical characteristics. Results demonstrated that the morphology and irregularity of the IVL scaffolds can directly affect the geometrical properties, such as pore sizes, distributions, and numbers, as well as SA, and SA/VR, and mechanical properties such as E and MCS. Following is the summary of the main findings of this study:

We observed that transitioning from constant ST to a gradient mode had a negligible effect on SA and SA/VR. In contrast, altering PS from constant to gradient demonstrated substantial improvements. The most significant enhancements were achieved when both PS and ST were subjected to gradient changes. In summary, PS and ST play a key role in optimizing geometrical features that result in enhanced bone regeneration.

Additionally, the investigation of pore number and distribution within the scaffolds revealed that specific designs, such as the PG-TG lattice, yielded the highest pore count and diverse pore size and distributions, closely followed by the PG-TC scaffold. Conversely, scaffolds with constant PS and gradient ST showcased lower corresponding values. These results highlighted the capacity to customize scaffold porosity to mimic the interconnected nature of natural bone. By increasing pore numbers, we can improve SA and SA/VR, which are two factors that contribute to better biological performance. Gradient PS combination with gradient/constant ST increases the pores in the range of human bone. A greater variety in the number of pores and their size was observed in PG-TG followed by PG-TC, PC-TG, and PC-TC.

In terms of mechanical properties, shifting from constant PS to gradient PS decreased E while improving MCS noticeably. Similarly,

the combination of gradient PS and constant ST yielded noteworthy enhancements of E and an impressive gain in MCS. Conversely, gradient PS combined with gradient ST, resulted in a negligible E improvement and minimum MCS enhancement among others. Furthermore, considering only gradient ST had a negative effect on E while improving MCS. These outcomes underscore the critical role of design parameters in optimizing scaffold mechanical performance.

When considering the effects of irregularity on the stress distribution and displacement, the PG-TC lattice shows less area subjected to stress followed by PG-TG. The worst candidates were PC-TC and PC-TG in which more struts and curves had to deal with greater stress. Moreover, PC-TC had the least displacement in the load direction among all Voronoi porous scaffolds, followed by PC-TG, PG-TC, and PG-TG.

In total, PG-TC offered the best performance considering both geometrical and mechanical properties among the presented morphologies. It showed the importance of implementing gradients in the design parameters to achieve better geometrical and mechanical characteristics.

This study shows that all the designed Voronoi lattices are potential candidates for bone replacements as they exhibited mechanical and geometrical properties comparable to the trabecular bone of the spine, tibia, and proximal femur.

## 6. Future research directions

Looking ahead, the findings from this study illuminate promising opportunities for future research in the field of tissue engineering and scaffold design. Based on the insights gained from the analysis of IVL structures, researchers can explore the potential for customizing these scaffolds even further.

Future investigations might delve into the precise relationships between ST, and PS, and even other designed factors such as PN and their effects on biological and mechanical performance. Additionally, there is scope to expand the study to include a broader range of materials beyond HA and investigate the implications of diverse material properties including metals and other bioceramics.

To acquire a deeper understanding of the failure patterns, structural fracture characteristics, and damage behavior of the designed IVL lattices, it is essential to involve quasi-static or dynamic analysis and incorporate other constitutive models, such as Johnston-Holmquist (JH) into commercial finite element codes for in-depth investigation of how these types of lattice structures behave mechanically, and how the designed parameters will affect other mechanical properties such as energy absorption, load-bearing capacity.

Furthermore, as the field of tissue engineering advances, integrating advanced computational methods, such as artificial intelligence and machine learning, can offer a novel dimension in optimizing these types of scaffold designs.

To investigate the manufacturability of the proposed Voronoi lattice in the present study, additive manufacturing techniques, especially selective laser melting (SLM), would be used to conduct experimental tests and compare mechanical properties with FEA calculations of HA, other bioceramics, or metals. The future endeavors hold the promise of enhancing the effectiveness and suitability of Voronoi lattices in bone regeneration and other tissue engineering applications, advancing this field and contributing to its potential clinical applications.

## CRediT authorship contribution statement

**Mansoureh Rezapourian:** Writing – original draft, Visualization, Validation, Software, Methodology, Investigation, Formal analysis, Conceptualization. **Irina Hussainova:** Writing – review & editing, Validation, Supervision, Resources, Project administration, Funding acquisition, Formal analysis, Data curation, Conceptualization.



# Declaration of competing interest

The authors declare that they have no known competing financial interests or personal relationships that could have appeared to influence the work reported in this paper.

# Data availability

Data will be made available on request.

# Acknowledgments

This work has been supported by the Estonian Research Council, Estonia, under Grant PRG643 (I. Hussainova), and M-ERA.Net project “BiLaTeX” MNHA23020.

# References

Abdullahi, H.S., Gao, S., 2020. A novel multi-cell square tubal structure based on Voronoi tessellation for enhanced crashworthiness. *Thin-Walled Struct.* 150, 106690.

Alonzo, M., Primo, F.A., Kumar, S.A., Mudloff, J.A., Dominguez, E., Fregoso, G., Ortiz, N., Weiss, W.M., Joddar, B., 2021. Bone tissue engineering techniques, advances, and scaffolds for treatment of bone defects. *Curr. Opin. Biomed. Eng.* 17, 100248.

Amini, A.R., Laurencin, C.T., Nukavarapu, S.P., 2012. Bone tissue engineering: Recent advances and challenges. *Crit. Rev.™ Biomed. Eng.* 40 (5).

Arjunan, A., Baroutaji, A., Praveen, A.S., Robinson, J., Wang, C., 2020. Classification of Biomaterial Functionalities. Elsevier.

Arjunan, A., Baroutaji, A., Robinson, J., Praveen, A.S., Pollard, A., Wang, C., 2021. Future Directions and Requirements for Tissue Engineering Biomaterials. Elsevier.

Awad, H.A., O'Keefe, R.J., Lee, C.H., Mao, J.J., 2014. Bone tissue engineering: clinical challenges and emergent advances in orthopedic and craniofacial surgery. In: *Principles of Tissue Engineering*. Elsevier, pp. 1733–1743.

Baksh, D., Davies, J., Kim, S., 1998. Three-dimensional matrices of calcium polyphosphates support bone growth in vitro and in vivo. *J. Mater. Sci.: Mater. Med.* 9 (12), 743–748.

Bellucci, D., Sola, A., Anesi, A., Salvatori, R., Chiarini, L., Cannillo, V., 2015. Bioactive glass/hydroxyapatite composites: Mechanical properties and biological evaluation. *Mater. Sci. Eng.: C* 51, 196–205.

Bhate, D., Penick, C.A., Ferry, L.A., Lee, C., 2019. Classification and selection of cellular materials in mechanical design: Engineering and biomimetic approaches. *Designs* 3 (1), 19.

Biemond, J.E., Aquarius, R., Verdonchot, N., Buma, P., 2011. Frictional and bone ingrowth properties of engineered surface topographies produced by electron beam technology. *Arch. Orthopaedic Trauma Surg.* 131, 711–718.

Chao, L., He, Y., Gu, J., Xie, D., Yang, Y., Shen, L., Wu, G., Wang, L., Tian, Z., Liang, H., 2023. Design of porous structure based on the Voronoi diagram and stress line for better stress shielding relief and permeability. *J. Mater. Res. Technol.*

Charbonnier, B., Manassero, M., Bourguignon, M., Decambon, A., El-Hafci, H., Morin, C., Leon, D., Bensidoun, M., Corsia, S., Petite, H., et al., 2020. Custom-made macroporous bioceramic implants based on triply-periodic minimal surfaces for bone defects in load-bearing sites. *Acta Biomater.* 109, 254–266.

Cheikh, K., Laurent, C., Ganghoffer, J., 2022. An advanced method to design graded cylindrical scaffolds with versatile effective cross-sectional mechanical properties. *J. Mech. Behav. Biomed. Mater.* 125, 104887.

Chen, H., Liu, Y., Wang, C., Zhang, A., Chen, B., Han, Q., Wang, J., 2021. Design and properties of biomimetic irregular scaffolds for bone tissue engineering. *Comput. Biol. Med.* 130, 104241.

Chow, H., Tan, S., Sze, W., 2007. Layered modeling of porous structures with Voronoi diagrams. *Comput.-Aided Des. Appl.* 4 (1–4), 321–330.

Dai, C., Li, Y., Pan, W., Wang, G., Huang, R., Bu, Y., Liao, X., Guo, K., Gao, F., 2019. Three-dimensional high-porosity chitosan/honeycomb porous carbon/hydroxyapatite scaffold with enhanced osteoinductivity for bone regeneration. *ACS Biomater. Sci. Eng.* 6 (1), 575–586.

Darvich, A., Aljareh, A., Kanout, C., Nazha, H., 2023. Effect of onlay material and preparation design on fatigue behavior and stress distribution in molars: 3D-FEA. *J. Stomatol.* 75 (1).

Deering, J., Dowling, K.I., DiCecco, L.-A., McLean, G.D., Yu, B., Grandfield, K., 2021. Selective Voronoi tessellation as a method to design anisotropic and biomimetic implants. *J. Mech. Behav. Biomed. Mater.* 116, 104361.

Du, Y., Liang, H., Xie, D., Mao, N., Zhao, J., Tian, Z., Wang, C., Shen, L., 2020. Design and statistical analysis of irregular porous scaffolds for orthopedic reconstruction based on Voronoi tessellation and fabricated via selective laser melting (SLM). *Mater. Chem. Phys.* 239, 121968.

Fantini, M., Curto, M., 2018. Interactive design and manufacturing of a Voronoi-based biomimetic bone scaffold for morphological characterization. *Int. J. Interact. Des. Manuf. (IJIDeM)* 12, 585–596.

Frayssinet, E., Colabella, L., Cislino, A.P., 2022. Design and assessment of the biomimetic capabilities of a Voronoi-based cancellous microstructure. *J. Mech. Behav. Biomed. Mater.* 130, 105186.

Fu, Q., Saiz, E., Rahaman, M.N., Tomsia, A.P., 2013. Toward strong and tough glass and ceramic scaffolds for bone repair. *Adv. Funct. Mater.* 23 (44), 5461–5476.

Ghiassi, B., Sefidbakht, Y., Mozaafari-Jovin, S., Gharehcheloo, B., Mehrarya, M., Khodadadi, A., Rezaei, M., Ranaei Siadat, S.O., Uskoković, V., 2020. Hydroxyapatite as a biomaterial—a gift that keeps on giving. *Drug Dev. Ind. Pharm.* 46 (7), 1035–1062.

Gómez, S., Vlad, M., López, J., Fernández, E., 2016. Design and properties of 3D scaffolds for bone tissue engineering. *Acta Biomater.* 42, 341–350.

Gulec, L., Ulusoy, N., et al., 2017. Effect of endocrown restorations with different CAD/CAM materials: 3D finite element and weibull analyses. *BioMed Res. Int.* 2017.

Henkel, J., Woodruff, M.A., Epari, D.R., Steck, R., Glatt, V., Dickinson, I.C., Choong, P.F., Schuetz, M.A., Hutmacher, D.W., 2013. Bone regeneration based on tissue engineering conceptions—a 21st century perspective. *Bone Res.* 1 (1), 216–248.

Jiang, X.-f., Yang, K., Yang, X.-q., Liu, Y.-f., Cheng, Y.-c., Chen, X.-y., Tu, Y., 2015. Elastic modulus affects the growth and differentiation of neural stem cells. *Neural Regen. Res.* 10 (9), 1523.

Jiao, C., Xie, D., He, Z., Liang, H., Shen, L., Yang, Y., Tian, Z., Wu, G., Wang, C., 2022. Additive manufacturing of bio-inspired ceramic bone scaffolds: Structural design, mechanical properties and biocompatibility. *Mater. Des.* 217, 110610.

Kang, J.-H., Sakthiabirami, K., Jang, K.-J., Jang, J.-G., Oh, G.-J., Park, C., Fisher, J.G., Park, S.-W., 2022. Mechanical and biological evaluation of lattice structured hydroxyapatite scaffolds produced via stereolithography additive manufacturing. *Mater. Des.* 214, 110372.

Knight, Jr., N.F., Reeder, J.R., 2006. User-Defined Material Model for Progressive Failure Analysis. Tech. rep.

Kumar, R., Mohanty, S., 2022. Hydroxyapatite: A versatile bioceramic for tissue engineering application. *J. Inorganic Organometallic Polym. Mater.* 32 (12), 4461–4477.

Leong, K., Chua, S.C., Sudarmadji, N., Yeong, W., 2008. Engineering functionally graded tissue engineering scaffolds. *J. Mech. Behav. Biomed. Mater.* 1 (2), 140–152.

Li, J., Guo, D., Li, J., Wei, X., Sun, Z., Yang, B., Lu, T., Ouyang, P., Liu, W., He, X., et al., 2022. Irregular pore size of degradable bioceramic Voronoi scaffolds prepared by stereolithography: Osteogenesis and computational fluid dynamics analysis. *Mater. Des.* 224, 111414.

Li, L., Shi, J., Zhang, K., Yang, L., Yu, F., Zhu, L., Liang, H., Wang, X., Jiang, Q., 2019. Early osteointegration evaluation of porous Ti6Al4V scaffolds designed based on triply periodic minimal surface models. *J. Orthop. Translat.* 19, 94–105.

Liang, H., Chao, L., Xie, D., Yang, Y., Shi, J., Zhang, Y., Xue, B., Shen, L., Tian, Z., Li, L., et al., 2022. Trabecular-like Ti-6Al-4V scaffold for bone repair: A diversified mechanical stimulation environment for bone regeneration. *Composites B* 241, 110057.

Liu, S., Chen, J., Chen, T., Zeng, Y., 2021. Fabrication of trabecular-like beta-tricalcium phosphate biomimetic scaffolds for bone tissue engineering. *Ceram. Int.* 47 (9), 13187–13198.

Lowen, J.M., Leach, J.K., 2020. Functionally graded biomaterials for use as model systems and replacement tissues. *Adv. Funct. Mater.* 30 (44), 1909089.

Melchels, F.P., Barradas, A.M., Van Blitterswijk, C.A., De Boer, J., Feijen, J., Grijsma, D.W., 2010. Effects of the architecture of tissue engineering scaffolds on cell seeding and culturing. *Acta Biomater.* 6 (11), 4208–4217.

Murphy, C.M., O'Brien, F.J., 2010. Understanding the effect of mean pore size on cell activity in collagen-glycosaminoglycan scaffolds. *Cell Adhesion Migrat.* 4 (3), 377–381.

Nguyen, T.D., Kadri, O.E., Sikavitsas, V.I., Voronov, R.S., 2019. Scaffolds with a high surface area-to-volume ratio and cultured under fast flow perfusion result in optimal O<sub>2</sub> delivery to the cells in artificial bone tissues. *Appl. Sci.* 9 (11), 2381.

Nie, Z., Lin, Y., Tong, Q., 2017. Modeling structures of open cell foams. *Comput. Mater. Sci.* 131, 160–169.

Nikolić, M., Karavelić, E., Ibrahimbegović, A., Mišević, P., 2018. Lattice element models and their peculiarities. *Arch. Comput. Methods Eng.* 25, 753–784.

Okubo, S., Yamauchi, Y., Kitazono, K., 2023. Effects of random and controlled irregularity in strut lattice structure of PA12 on compression anisotropy. *Addit. Manuf.* 63, 103385.

Pagani, S., Liverani, E., Giavaresi, G., De Luca, A., Belvedere, C., Fortunato, A., Leardini, A., Fini, M., Tomesani, L., Caravaggi, P., 2021. Mechanical and in vitro biological properties of uniform and graded cobalt-chrome lattice structures in orthopedic implants. *J. Biomed. Mater. Res. Part B: Appl. Biomater.* 109 (12), 2091–2103.

Pompe, W., Worch, H., Epple, M., Friess, W., Gelinsky, M., Greil, P., Hempel, U., Scharnweber, D., Schulte, K., 2003. Functionally graded materials for biomedical applications. *Mater. Sci. Eng. A* 362 (1–2), 40–60.

Prasad, S., Wong, R.C.W., 2018. Unraveling the mechanical strength of biomaterials used as a bone scaffold in oral and maxillofacial defects. *Oral Sci. Int.* 15 (2), 48–55.

- Przybilla, P., Subkov, E., Latorre, S.H., Zankovic, S., Mayr, H.O., Killinger, A., Schmal, H., Seidenstuecker, M., 2023. Effect of 20  $\mu\text{m}$  thin ceramic coatings of hydroxyapatite, bioglass, GB14 and beta-tricalciumphosphate with copper on the biomechanical stability of femoral implants. *J. Mech. Behav. Biomed. Mater.* 105951.
- Rana, M., Karmakar, S., Bandyopadhyay, A., Roychowdhury, A., 2023. Design and manufacturing of patient-specific Ti6Al4V implants with inhomogeneous porosity. *J. Mech. Behav. Biomed. Mater.* 143, 105925.
- Rezapourian, M., Jasiuk, I., Saarna, M., Hussainova, I., 2023. Selective laser melted Ti6Al4V split-P TPMS lattices for bone tissue engineering. *Int. J. Mech. Sci.* 251, 108353.
- Rezapourian, M., Kamboj, N., Hussainova, I., 2021. Numerical study on the effect of geometry on mechanical behavior of triply periodic minimal surfaces. *IOP Conf. Ser.: Mater. Sci. Eng.* 1140, 012038.
- Rezapourian, M., Kamboj, N., Jasiuk, I., Hussainova, I., 2022. Biomimetic design of implants for long bone critical-sized defects. *J. Mech. Behav. Biomed. Mater.* 134, 105370.
- Robinson, J., Arjunan, A., Baroutaji, A., Martí, M., Molina, A.T., Serrano-Aroca, Á., Polard, A., 2021. Additive manufacturing of anti-SARS-CoV-2 copper-tungsten-silver alloy. *Rap. Prototyp. J.* 27 (10), 1831–1849.
- Rodríguez-Montaña, Ó.L., Cortés-Rodríguez, C.J., Naddeo, F., Uva, A.E., Fiorentino, M., Naddeo, A., Cappetti, N., Gattullo, M., Monno, G., Boccaccio, A., 2019. Irregular load adapted scaffold optimization: A computational framework based on mechanobiological criteria. *ACS Biomater. Sci. Eng.* 5 (10), 5392–5411.
- Ruiz Henao, P.A., Caneiro Queija, L., Mareque, S., Tasende Pereira, A., Liñares González, A., Blanco Carrion, J., 2021. Titanium vs ceramic single dental implants in the anterior Maxilla: A 12-month randomized clinical trial. *Clin. Oral Implants Res.* 32 (8).
- Rumpler, M., Woesz, A., Dunlop, J.W., Van Dongen, J.T., Fratzl, P., 2008. The effect of geometry on three-dimensional tissue growth. *J. R. Soc. Interface* 5 (27), 1173–1180.
- Shirzad, M., Zolfagharian, A., Matbouei, A., Bodaghi, M., 2021. Design, evaluation, and optimization of 3D printed truss scaffolds for bone tissue engineering. *J. Mech. Behav. Biomed. Mater.* 120, 104594.
- Syahrom, A., Kadir, M.R.A., Abdullah, J., Öchsner, A., 2013. Permeability studies of artificial and natural cancellous bone structures. *Med. Eng. Phys.* 35 (6), 792–799.
- Vance, A., Bari, K., Arjunan, A., 2019. Investigation of Ti64 sheathed cellular anatomical structure as a Tibia implant. *Biomed. Phys. Eng. Express* 5 (3), 035008.
- Viet, N., Waheed, W., Alazzam, A., Zaki, W., 2023. Effective compressive behavior of functionally graded TPMS titanium implants with ingrown cortical or trabecular bone. *Compos. Struct.* 303, 116288.
- Vijayavenkataraman, S., Zhang, L., Zhang, S., Hsi Fuh, J.Y., Lu, W.F., 2018. Triply periodic minimal surfaces sheet scaffolds for tissue engineering applications: An optimization approach toward biomimetic scaffold design. *ACS Appl. Bio Mater.* 1 (2), 259–269.
- Wang, G., Shen, L., Zhao, J., Liang, H., Xie, D., Tian, Z., Wang, C., 2018. Design and compressive behavior of controllable irregular porous scaffolds: Based on Voronoi-tessellation and for additive manufacturing. *ACS Biomater. Sci. Eng.* 4 (2), 719–727.
- Wang, W., Yeung, K.W., 2017. Bone grafts and biomaterials substitutes for bone defect repair: A review. *Bioact. Mater.* 2 (4), 224–247.
- Wu, Y., Wang, Y., Liu, M., Shi, D., Hu, N., Feng, W., 2023. Mechanical properties and in Vivo assessment of electron beam melted porous structures for orthopedic applications. *Metals* 13 (6), 1034.
- Yoo, D.-J., 2014. Advanced porous scaffold design using multi-void triply periodic minimal surface models with high surface area to volume ratios. *Int. J. Precis. Eng. Manuf.* 15, 1657–1666.
- Zhang, Q., Ma, L., Ji, X., He, Y., Cui, Y., Liu, X., Xuan, C., Wang, Z., Yang, W., Chai, M., et al., 2022. High-strength hydroxyapatite scaffolds with minimal surface macrostructures for load-bearing bone regeneration. *Adv. Funct. Mater.* 32 (33), 2204182.
- Zhang, B., Pei, X., Zhou, C., Fan, Y., Jiang, Q., Ronca, A., D'Amora, U., Chen, Y., Li, H., Sun, Y., et al., 2018. The biomimetic design and 3D printing of customized mechanical properties porous Ti6Al4V scaffold for load-bearing bone reconstruction. *Mater. Des.* 152, 30–39.
- Zhao, Y., Chen, H., Ran, K., Zhang, Y., Pan, H., Shangguan, J., Tong, M., Yang, J., Yao, Q., Xu, H., 2023. Porous hydroxyapatite scaffold orchestrated with bioactive coatings for rapid bone repair. *Biomater. Adv.* 144, 213202.
- Zhao, D., Huang, Y., Ao, Y., Han, C., Wang, Q., Li, Y., Liu, J., Wei, Q., Zhang, Z., 2018. Effect of pore geometry on the fatigue properties and cell affinity of porous titanium scaffolds fabricated by selective laser melting. *J. Mech. Behav. Biomed. Mater.* 88, 478–487.
- Zhao, Z., Li, J., Wei, Y., Yu, T., 2022. Design and properties of graded polyamide12/hydroxyapatite scaffolds based on primitive lattices using selective laser sintering. *J. Mech. Behav. Biomed. Mater.* 126, 105052.

# Curriculum Vitae

## 1. Personal data

Name	Mansoureh Rezapourian Ghahfarokhi
Date of birth	08 July 1988
Nationality	Iran

## 2. Contact information

Email	mareza@taltech.ee
LinkedIn	Mansoureh Rezapourian

## 3. Education

2019–2023	Tallinn University of Technology, Estonia Mechanical Engineering, Ph.D. student
2012–2015	Razi University, Kermanshah, Iran Mechanical Engineering, M.Sc.
2007–2011	ShahreKord University, Shahr-e Kord, Iran, Mechanical Engineering, B.Sc.

## 4. Language competence

Persian	Native
English	Fluent
Estonian	Basic
German	Basic

## 5. Field of research

- Biomedical

# Elulookirjeldus

## 1. Isikuandmed

Nimi	Mansoureh Rezapourian Ghahfarokhi
Sünniaeg	08 July 1988
Kodakondsus	Iraani

## 2. Kontaktandmed

E-post	mareza@taltech.ee
LinkedIn	Mansoureh Rezapourian

## 3. Haridus

2019–2023	Tallinna Tehnikaülikool, Eesti Masinaehitus, Ph.D.
2012–2015	Raziülikool, Kermanshah, Iraan, Masinaehitus, M.Sc.
2007–2011	ShahreKordiülikool, Shahr-e Kord, Iraan, Masinaehitus, B.Sc.

## 2. Keelteoskus

Pärsia	Emakeel
Inglise	Kõrgtase
Eesti	Algtase
Saksamaa	Algtase

## 5. Teadustöö põhisuunad

- Biomeditsiiniline



ISSN 2585-6901 (PDF)  
ISBN 978-9916-80-114-7 (PDF)